Spring 2016

Physical and numerical modeling of cross-flow turbines

Peter Bachant
University of New Hampshire, Durham

PHYSICAL AND NUMERICAL MODELING OF CROSS-FLOW TURBINES

BY

PETER BACHANT

B.S., Mechanical Engineering, University of Massachusetts Dartmouth, 2008
M.S., Mechanical Engineering, University of New Hampshire, 2011

DISSERTATION

Submitted to the University of New Hampshire
in Partial Fulfillment of
the Requirements for the Degree of

Doctor of Philosophy

in

Mechanical Engineering

May 2016

This dissertation has been examined and approved in partial fulfillment of the requirements for the degree of Doctor of Philosophy in Mechanical Engineering by:

Dissertation Director, Martin Wosnik,
Associate Professor, Mechanical Engineering

Kenneth Baldwin,
Professor, Mechanical Engineering

Diane Foster,
Professor, Mechanical Engineering

Thomas Lippmann,
Associate Professor, Earth Sciences

M. Robinson Swift,
Professor, Mechanical Engineering

Brian Polagye,
Associate Professor, Mechanical Engineering
University of Washington

on March 31, 2016.

Original approval signatures are on file with the University of New Hampshire Graduate School.

ACKNOWLEDGMENTS

First and foremost, thanks to my research advisor and mentor Martin Wosnik, without whose support none of this work would have even been undertaken. I'd also like to thank:

- My committee—professors Baldwin, Foster, Lippmann, Polagye, and Swift—for their expertise and guidance.
- Ashley, for trying to make sure I never worked too hard, and for understanding when I did.
- My parents for giving me a place to be creative growing up, my family for always asking "so when are you going to be done with school?", and Tom and Gramps for helping out the with tow tank.
- Paul Lavoie for many words of wisdom, and allowing for plenty of "third shift" time in the machine shop.
- Chris Ellis and Jim Mullin at SAFL for their advice regarding the tow tank linear guide system upgrades.
- Les Peabody, Craig Deady, Sean Mitchell from Minarik for their help with the upgraded tow tank motion system electronics.
- Lucid Energy Technologies, LLP, for materials used to build the UNH-RVAT turbine and experimental setup.
- All the open-source software projects, developers, and communities for sharing their skills and support: Python, Anaconda, NumPy, Matplotlib, Pandas, OpenFOAM (The OpenFOAM Foundation, Bruno Santos, Chris Sideroff, Vesselin Krastev), swak4Foam, Linux, Ubuntu, Linux Mint, Git, NREL (SOWFA), and more.
- Anders Goude for contributions to the turbinesFoam actuator line model.

- Matt Rowell and Vincent Lyon for their help conducting the experiments.

Finally, I'd like to aknowledge financial support from the US Department of Energy, from Dr. Geoffrey A. Prentice and the National Science Foundation (award 1150797), and Dr. Vincent S. Neary and Sandia National Labs.

TABLE OF CONTENTS

NOMENCLATURE

α	Blade element angle of attack.
ε	Actuator line element force Gaussian smearing width.
λ	Turbine tip speed ratio.
λ_0	Typical operating tip speed ratio, or that at which power coefficient is maximum.
ν	Fluid kinematic viscosity.
ω	Turbine shaft angular velocity.
ρ	Fluid density.
σ	Turbine rotor solidity or ratio of total planform area to swept area.
τ_w	Wall shear stress.
A	Turbine frontal area.
c	Foil or blade element chord.
C_D	Overall rotor drag (or thrust) coefficient.
C_d	Foil or blade element drag coefficient.
C_l	Foil or blade element lift coefficient.
C_m	Blade element pitching moment coefficient.
C_P	Turbine power coefficient.
C_T	Turbine torque coefficient.
D	Turbine rotor diameter.
F_d	Blade element drag force.
F_l	Blade element lift force.
Fr	Froude number.
H	Turbine rotor height.
k	Turbulence kinetic energy.

M	Blade element pitching moment.
N	Number of blades.
R	Maximum rotor radius.
Re_c	Reynolds number based on chord length.
Re_D	Reynolds number based on turbine rotor diameter.
T	Shaft torque.
u^*	Friction velocity.
U_∞	Free stream velocity.
y^+	Nondimensional wall distance.
ADV	Acoustic Doppler velocimeter.
AFT	Axial-flow turbine.
ALE	Actuator line element.
ALM	Actuator line model.
CAD	Computer-aided design.
CFD	Computational fluid dynamics.
CFT	Cross-flow turbine.
DAQ	Data acquisition.
DDES	Delayed detached eddy simulation
DES	Detached eddy simulation.
DMST	Double multiple streamtube.
DNS	Direct numerical simulation.
DOE	US Department of Energy.
GUI	Graphical user interface.
HAWT	Horizontal-axis wind turbine.
IDDES	Improved delayed detached eddy simulation.
LDV	Laser-Doppler velocimetry.
LES	Large eddy simulation.

MHK	Marine hydrokinetic.
NREL	National Renewable Energy Laboratory.
RANS	Reynolds-averaged Navier–Stokes.
RM2	Reference Model 2.
RNG	Renormalization group.
SGS	Subgrid-scale.
SNL	Sandia National Labs.
SST	Shear stress transport.
UNH	University of New Hampshire.
UNH-RVAT	University of New Hampshire Reference Vertical-Axis Turbine.
VAWT	Vertical-axis wind turbine.

LIST OF TABLES

LIST OF FIGURES

Figure **Page**

ABSTRACT

Physical and numerical modeling of cross-flow turbines

by

Peter Bachant

University of New Hampshire, May, 2016

Cross-flow (often vertical-axis) turbines (CFTs), despite being thoroughly investigated and subsequently abandoned for large scale wind energy, are seeing renewed interest for smaller scale wind turbine arrays, offshore wind, and marine hydrokinetic (MHK) energy applications. Though they are similar to the large scale Darrieus wind turbines, today's CFT rotors are often designed with higher solidity, or blade chord-to-radius ratios, which makes their behavior more difficult to predict with numerical models. Furthermore, most experimental datasets used for numerical model validation were acquired with low solidity rotors.

An experimental campaign was undertaken to produce high quality open datasets for the performance and near-wake flow dynamics of CFTs. An automated experimental setup was developed using the University of New Hampshire's towing tank. The tank's linear motion, control, and data acquisition systems were redesigned and rebuilt to facilitate automated cross-flow turbine testing at large laboratory (on the order of 1 meter) scale.

Two turbines were designed and built—one high solidity (dubbed the UNH Reference Vertical-Axis Turbine or UNH-RVAT) and one medium-to-low solidity, which was a scaled model of the US Department of Energy and Sandia National Labs' Reference Model 2 (RM2) cross-flow MHK turbine. A baseline performance and near-wake dataset was acquired for the UNH-RVAT, which revealed that the relatively fast wake recovery observed in vertical-axis wind turbine arrays could be attributed to the mean vertical advection of momentum and energy, caused by the unique interaction of vorticity shed from the blade tips.

The Reynolds number dependence of the UNH-RVAT was investigated by varying turbine tow speeds, indicating that the baseline data had essentially achieved a Reynolds number independent state at a turbine diameter Reynolds number $Re_D \sim 10^6$ or chord based Reynolds number $Re_c \sim$

10^5. A similar study was undertaken for the RM2, with similar results. An additional dataset was acquired for the RM2 to investigate the effects of blade support strut drag on overall performance, which showed that these effects can be quite significant—on the order of percentage points of the power coefficient—especially for lower solidity rotors, which operate at higher tip speed ratio. The wake of the RM2 also showed the significance of mean vertical advection on wake recovery, though the lower solidity made these effects weaker than for the UNH-RVAT.

Blade-resolved Reynolds-averaged Navier–Stokes (RANS) computational fluid dynamics (CFD) simulations were performed to assess their ability to model performance and near-wake of the UNH-RVAT baseline case at optimal tip speed ratio. In agreement with previous studies, the 2-D simulations were a poor predictor of both the performance and near-wake. 3-D simulations faired much better, but the choice of an appropriate turbulence model remains uncertain. Furthermore, 3-D blade-resolved RANS modeling is computationally expensive, requiring high performance computing (HPC), which may preclude its use for array analysis.

Finally, an actuator line model (ALM) was developed to attempt to drive down the cost of 3-D CFD simulations of cross-flow turbines, since previously, the ALM had only been investigated for a very low Reynolds number 2-D CFT. Despite retaining some of the disadvantages of the lower fidelity blade element momentum and vortex methods, the ALM, when coupled with dynamic stall, flow curvature, added mass, and end effects models, was able to predict the performance of cross-flow turbines reasonably well. Near-wake predictions were able to match some of the important qualitative flow features, which warrants further validation farther downstream and with multiple turbines. Ultimately, the ALM provides an attractive alternative to blade-resolved CFD, with computational savings of two to four orders of magnitude for large eddy simulation and RANS, respectively.

CHAPTER 1

INTRODUCTION

With the threat of anthropogenic climate change and the looming end to fossil fuel supplies, human civilization must reduce carbon emissions [94] and transition to a fully sustainable energy portfolio. Towards this end, natural fluid flows such as wind and water in river and tidal currents—a.k.a. marine hydrokinetic (MHK) energy—can contribute. It is estimated that there is 11,000 and 4,200 GW of capacity potential from on- and offshore wind in the US, respectively [118], while there is an estimated 50 GW of technically available MHK power capacity in the US [93, 155, 92]. For reference, the United States consumed on average about 438 GW of electric power in 2013, and only 13% of this was from renewable sources [188], which shows just how much work there is left to be done.

A turbine is the most common type of machine for extracting renewable energy from fluid flows, converting the energy to shaft work as the fluid applies torque on the rotor. Wind turbine designs have matured a lot over the past few decades, to the point where they are not changing much conceptually, though they are pushing forward by increasing size. MHK turbine designs on the other hand are quite immature despite taking much design influence from wind technology. Furthermore, MHK rotors will encounter approximately an order of magnitude greater torque compared to a wind turbine of the same size. This means MHK rotors are typically higher solidity—the ratio of blade planform area to swept area—to ensure structural integrity.

Turbine rotor concepts can essentially be divided into two classes—axial-flow and cross-flow—describing the relative orientation of the rotor axis to the nominal flow direction. The ubiquitous horizontal-axis wind turbine (HAWT) is an example of an axial-flow turbine (AFT), while the egg-beater shaped Darrieus vertical-axis wind turbine (VAWT), patented in 1931 [68], is an example

of a cross-flow turbine (CFT). Note that a cross-flow turbine can accept flow from any direction perpendicular to its rotation, meaning the axis can be horizontal, vertical, or anything in between.

The most well-known CFT, the Darrieus vertical-axis wind turbine, examples of which are shown in Figure 1.1, was investigated in the late 1970s through the early 1990s by groups including Sandia National Laboratories (SNL) in the US and the National Research Council (NRC) in Canada [148]. Sandia's efforts culminated in their 34 m diameter Test Bed, shown in Figure 1.1a. The lessons and knowledge gained from this research turbine eventually helped bring about the moderate commercial success of the FloWind Darrieus wind turbine array, shown in Figure 1.1c. The highest power output of any VAWT—in the 1–4 MW range—was achieved by the Canadian Lavalin Eole 64 m diameter research turbine, constructed in 1986 [148], and shown in Figure 1.1b.

Ultimately the three-bladed, horizontal-axis propeller-type axial-flow turbine (AFT) concept—shown in Figure 1.2 became the design of choice for large scale onshore wind—and for good reasons. Axial-flow turbines are easier to analyze since their operating principle can essentially be idealized as steady flow over a foil in an unstalled condition. AFTs also have the benefit of research "inertia"—a lot has been invested and a lot of knowledge has accumulated already. As a result, the designs are quite mature, for wind energy at least. In contrast, the CFT has been studied and applied significantly less, though there have been cases where CFTs have performed nearly equally as well as AFTs. However, CFTs are more difficult to design, since their blades are continuously changing their angles of attack throughout the turbine's rotation, often undergoing dynamic stall as part of normal operation [148], which makes blade loading hard to predict. Beside their unpredictability, the highly oscillatory blade loading presents significant design challenges for avoiding fatigue—a main cause for failure or premature retirement of the large Darrieus wind turbines.

Despite these engineering challenges, CFTs may have advantages over AFTs under certain conditions. They are simpler, omni-directional machines, which do not require yawing or pitching mechanisms. There were considerations in the 2010s by DEEPWIND in Europe [149] and SNL [159] in the US for using large scale floating VAWTs for offshore wind, since along with the omni-directionality, a vertical shaft allows placement of the generator and gearbox lower in the machine,

(a) Sandia 34 m diameter Test Bed, from [138].

(b) Lavalin Eole 64 m diameter VAWT. Photo by Paul Gipe. All rights reserved.

(c) FloWind VAWT array. Photo by Paul Gipe. All rights reserved.

Figure 1.1: Large scale Darrieus wind turbines: Sandia 34 m Test Bed (a), Lavalin Eole 64 m (b), and FloWind VAWT array (c).

Figure 1.2: Vestas V100 1.8 MW three-bladed axial-flow, a.k.a horizontal-axis wind turbine. Courtesy of Vestas Wind Systems A/S.

which lowers center of gravity. In the onshore wind arena, CFTs show promise for projects where space is limited, e.g., urban environments, as adjacent turbines sometimes interact "constructively" to increase each other's power outputs [115]—a trait not possessed by AFTs. It has been claimed that arrays of VAWTs can potentially provide an order-of-magnitude increase in the power output per land area of a wind turbine array, since the devices can be spaced more closely than HAWTs [66]. Field measurements have shown that their wakes recover more quickly than those of AFTs, and this cannot be entirely attributed to higher turbulence generation [104]. This phenomenon is investigated in later chapters.

In the built, i.e., suburban and urban environments, wind resources are less understood, more variable in terms of direction, speed, and turbulence levels [172]. Kooiman and Tullis [106] observed that a cross-flow turbine in an urban environment was indeed insensitive to changes in wind direction, and was only adversely affected by temporal variations in wind speed when turbulence intensity was above 15%. The lack of need for yawing can help lower cost of energy from CFTs versus AFTs by reducing complexity, e.g., by eliminating slip rings. Cross-flow turbines may also have an advantage in the urban environment since they must be designed for high fatigue loads anyway. Recently, the Eiffel tower in Paris, France has been outfitted with two 5.3 m tall, 3.2 m diameter helical vertical-axis cross-flow turbines, which will produce at least 10 MWh/yr, or approximately 1 kW on average, which is expected to power the entire first floor of the facility [119].

For MHK development, a field much less mature than wind power, the cross-flow turbine concept is playing a major role thanks to its omni-directionality and flexibility with respect to frontal area shape, allowing for more precisely tuned fitment in channels with complex bathymetry or installed structures. Chosen by the Ocean Renewable Power Company (ORPC) for their Turbine Generator Unit (TGU), integrated as part of their TidGen system, a cross-flow turbine was the first grid-connected tidal energy device in the US, which was installed in Cobscook Bay, ME [145]. Today, ORPC is working on improving their turbine's performance, and planning for the installation of 4 more turbines [142].

CFTs are also being considered for micropower applications, such as powering remote underwater instrumentation packages that currently rely on batteries [152]. They are also being used in riverine applications, for example, in ORPC's RivGen project in the Kvichak River just downstream of the village of Igiugig, AK [82]. Instream energy has also installed a 25 kW CFT in the Roza irrigation canal in Yakima, WA [91].

It could be argued that the failure of cross-flow turbines in the utility scale onshore wind industry is the result of less-than-adequate predictive capability in the engineering process. That is, issues such as lackluster performance and fatigue could have been overcome. In order for modern cross-flow turbines to be effective, these predictive or modeling capabilities must be enhanced, for both individual devices and arrays, which is a primary motivation for this research.

1.1 Principles of cross-flow turbine operation

Blade element theory, originally conceived by Drzewiecki [72, 73], is the analysis of a rotor or propeller as a collection of 2-D foil sections, or blade elements, and can be employed to obtain a simplified view of the kinematics and dynamics of a CFT. Figure 1.3 shows the relevant velocity and force vectors on a CFT blade element. The relative velocity U_{re} and angle of attack α are calculated by adding the inflow velocity vector U_{in} to the opposite of the blade element velocity ωr, where ω is the shaft angular velocity and r is the element radius, which for a straight-bladed turbine is equal to the maximum rotor radius R. In the relative velocity coordinate system, the lift (F_l) and drag (F_d) forces are then oriented normal and tangential to the relative velocity, respectively. These forces, combined with the blade element pitching moment M ultimately produce the shaft torque, and in turn the shaft power.

The shaft's angular velocity ω is nondimensionalized as the tip speed ratio

$$\lambda = \frac{\omega R}{U_\infty}, \tag{1.1}$$

where U_∞ is the free stream velocity. The turbine's shaft torque, T, is characterized by the nondimensional torque coefficient

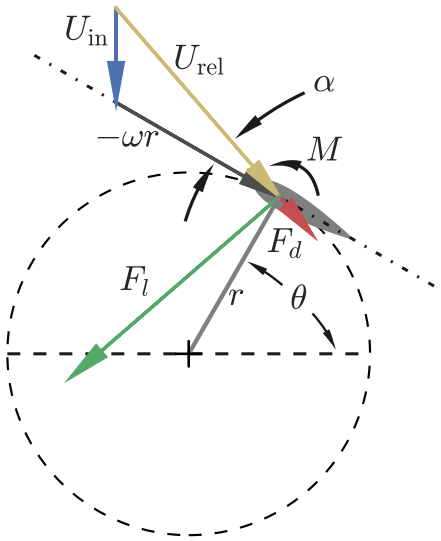

Figure 1.3: Vector diagram of velocity and forcing on a cross-flow turbine blade element. Note that the free stream velocity U_∞ is oriented from top to bottom (identical to U_{in} for purely geometric calculations), the blade chord (dash-dotted line) is coincident with the tangential velocity (i.e., zero preset pitch, which would offset the geometric angle of attack α), and the drag vector is magnified by a factor of two (approximately, relative to the lift vector) to enhance visibility.

$$C_T = \frac{T}{\frac{1}{2}\rho A R U_\infty^2}, \tag{1.2}$$

where ρ is the fluid density and A is the turbine's frontal area. Similarly, the turbine power $P = T\omega$ and overall rotor drag F_D are normalized as the power coefficient

$$C_P = \frac{T\omega}{\frac{1}{2}\rho A U_\infty^3}, \tag{1.3}$$

and the rotor drag (a.k.a. thrust) coefficient

$$C_D = \frac{F_D}{\frac{1}{2}\rho A U_\infty^2}. \tag{1.4}$$

It is also worth noting that $C_P = \lambda C_T$.

So why then, is it so difficult to analyze these machines? A first glimpse can be seen in Figure 1.4, where the geometric angle of attack and relative velocity magnitude are plotted over one turbine revolution for various tip speed ratios. Note that by considering geometry alone, we are neglecting the effect of the blade element forcing on the local inflow velocity vector—the so-called induction—which will most significantly decrease the inflow and angle of attack on the downstream half of the blade path, i.e., for $180 < \theta < 360$. If we imagine a typical high solidity $\sigma = Nc/R$ turbine, where N is the number of blades, operating at an optimal tip speed ratio $\lambda_0 = 2$, for example [96] (note that solidity and λ_0 are inversely correlated [182]), we see that geometric angles of attack can be very high even in optimal conditions.

As shown in Figure 1.3, the blade's lift to drag ratio and angle of attack can be thought of as the quantities to maximize in order to develop shaft torque. However, beyond a threshold angle of attack, i.e., the static stall angle, C_l/C_d drops. Predicting foil characteristics (lift, drag, pitching moment) is difficult beyond the static stall angle, where boundary layer separation becomes dominant over most of the foil suction surface, which reduces lift and increases drag dramatically. For example, Figure 1.5 shows measured lift and drag coefficients for an S826 airfoil at $Re_c = 145,000$ compared with 2-D and 3-D Navier–Stokes CFD simulations from Cakmakcioglu et al. [51]. The

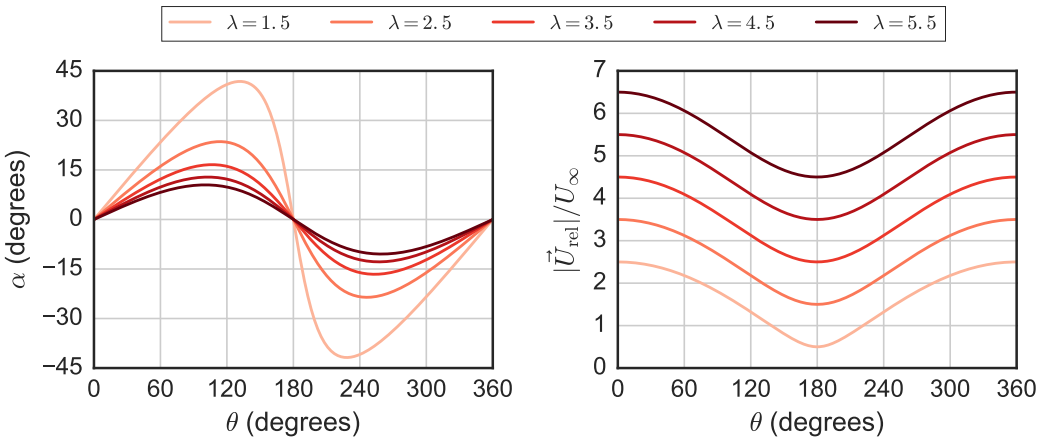

Figure 1.4: Geometric angle of attack (left) and relative velocity (right) versus azimuthal angle at various tip speed ratios.

linear lift slope region and static stall angle are predicted well enough, but the peak C_l/C_d is massively overestimated, due to both an overprediction of lift and underprediction of drag. This may not be an issue for a machine designed to operate at relatively fixed and/or pre-stall α, e.g., airplane wings, propellers, or axial-flow wind turbines, but a cross-flow turbine will most likely encounter post-stall regimes, cf. Figure 1.4, making even high-fidelity CFD analysis an uncertain prospect for accurate blade load prediction.

1.1.1 Unsteady aerodynamics and dynamic stall

Up until now we have only considered the static behavior of foils, which may be sufficient to model the steady performance of an axial-flow turbine, since angles of attack for all rotor blade elements are meant to remain constant in ideal conditions. The rotation of a cross-flow turbine, however—with its constantly changing angle of attack (also changing in sign mid-rotation) and relative velocity—produces an unsteady environment for the blade elements, even in an idealized case.

Unsteady foil behavior has been studied extensively in rotorcraft research [112]. In the absence of stall, even a helicopter rotor airfoil will deviate from static behavior due to cyclic pitching, along with changes in relative velocity as the blade advances and retreats. Thus, the wealth of knowledge available from the helicopter literature provides insight into the cross-flow turbine case.

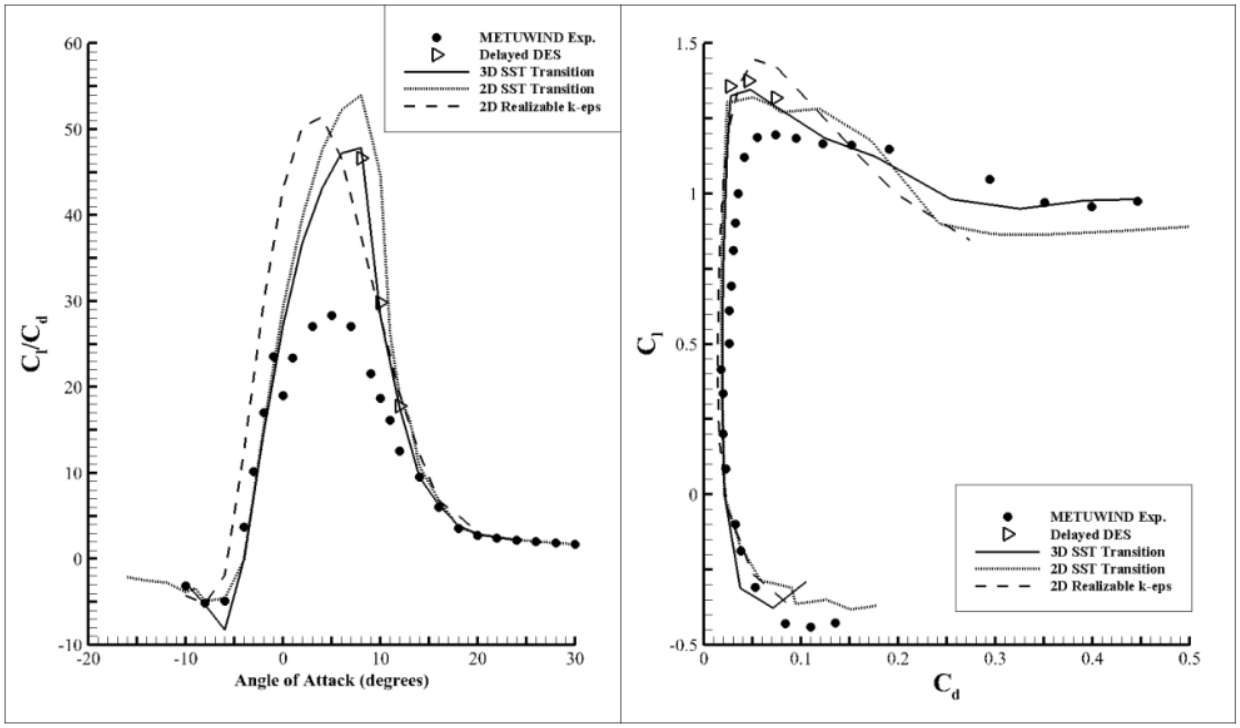

Figure 1.5: Characteristics of an S826 airfoil at $Re_c = 145,000$, from [51].

The first consideration is the attached behavior of unsteady airfoils. As one might expect, in these cases either the angle of attack or relative velocity is varying, but dramatic flow separation, i.e., stall, is never encountered. The unsteadiness is characterized by a reduced frequency [112]

$$k = \frac{\omega c}{2U_\infty}, \tag{1.5}$$

which assumes the free stream velocity is constant. Unsteady effects begin to become significant for $k > 0.05$, and can become dominant for $k \geq 0.2$ [112].

For a cross-flow turbine reduced frequency can be reformulated in terms of the tip speed ratio as

$$k = \frac{\lambda c}{2R}, \tag{1.6}$$

which is then also a function of solidity or chord-to-radius ratio c/R. As an example, a large scale, relatively low solidity Darrieus turbine such as the Sandia 34 m diameter Test Bed, with an

equatorial blade chord of 0.91 m [138], a reduced frequency $k = 0.16$ is encountered based solely on angle of attack oscillations at $\lambda = 6$. For a smaller scale CFT, e.g., with $c/R = 0.25$, operating at $\lambda = 2$, the reduced frequency is 0.25. It follows that unsteady effects will be significant for cross-flow turbines even in the absence of nonlinear effects such as stall.

In the unsteady regime, when a foil's angle of attack exceeds the static stall angle, it encounters dynamic stall. The effects on foil loading are different from those of static stall in that they are time dependent and include hysteresis or lag effects. The dynamic stall process in general can be described as [128], depicted in Figure 1.6:

1. Attached flow with a thin boundary layer.

2. Separation begins. A large leading edge vortex is formed, which causes an overshoot in lift beyond the static case in a linear fashion.

3. The vortex is advected downstream, causing additional lift and negative pitching moment.

4. The vortex advects towards the trailing edge. Lift and moment decay rapidly after reaching peak values.

5. Secondary vortices may be shed, leading to additional lift and moment peaks.

6. Forces slowly return to the linear regime as flow reattaches.

Based on Figure 1.4, we expect dynamic stall to play an important role in governing overall blade loading for a cross-flow turbine. Therefore, it is necessary to either accurately model dynamic stall, or employ CFD methods that can resolve unsteady effects in the foil boundary layer, both of which will be explored in later chapters.

1.2 The state of engineering tools for CFTs

1.2.1 For individual devices

Presently, the most reliable predictor of turbine performance is physical modeling (building prototypes or copying existing designs that have been field-tested), so long as important dynamical

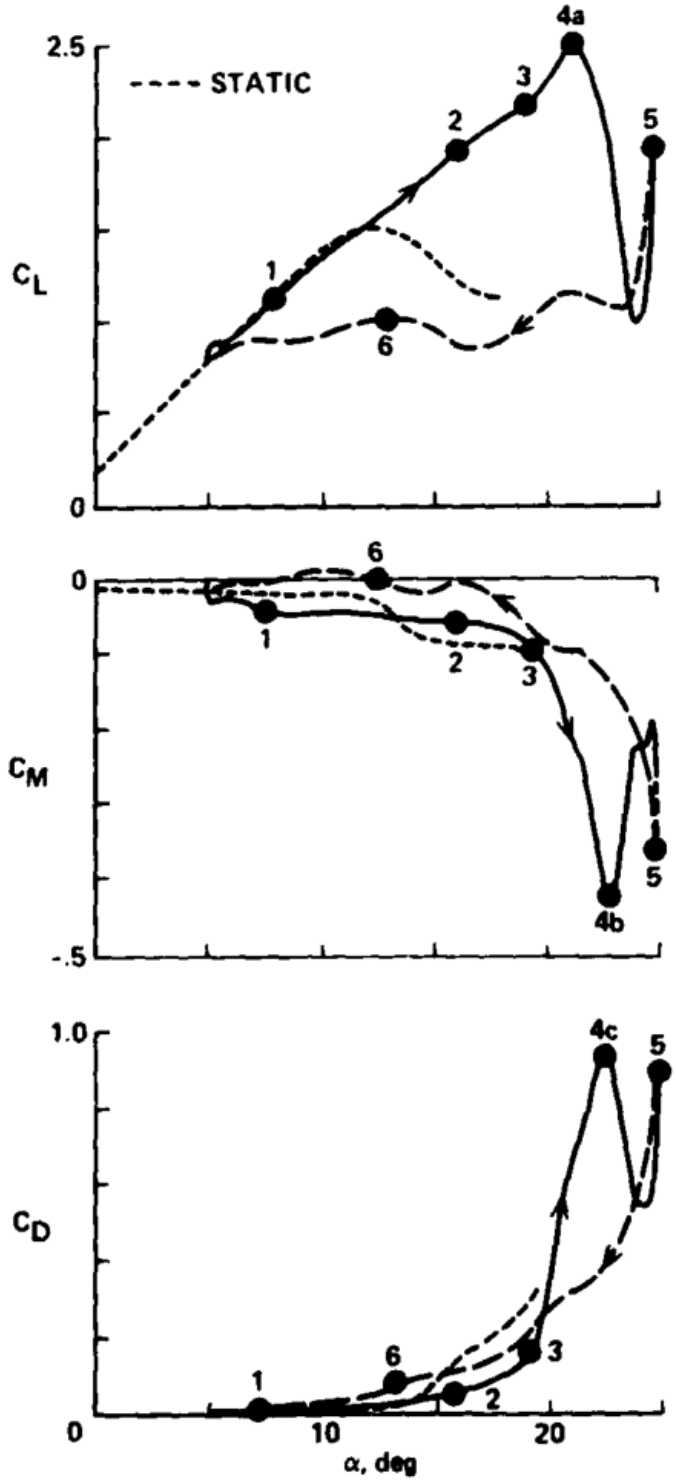

Figure 1.6: Dynamic stall events for a Vertol VR-7 airfoil, taken from [128].

scales (Reynolds number, mainly) are sufficiently matched. It has been shown that performance becomes essentially Reynolds number independent at an approximate blade chord Reynolds number $Re_c \approx \lambda U_\infty c/\nu = O(10^5)$ [49], which is investigated further in Chapter 4. However, experiments at this scale can be quite expensive. For example, a turbine with a 1 m diameter and 10 cm chord would need to be tested in a flow on the order of 1 m/s in water and 10 m/s in air. For a turbine this large it is typically impractical to manufacture many prototypes to find the optimal design, so numerical modeling is preferred. There exists a large spectrum of numerical modeling techniques with widely varying computational cost and fidelity, and sometimes only the most complex and computationally expensive are trustworthy.

Momentum models are the simplest and computationally least expensive, where the turbine blades are discretized into blade elements, for which 2-D static lift and drag data are tabulated. The relative velocity and angle of attack for a blade element are calculated by seeking a balance between forces computed from the static foil data and the rate of change of momentum of the fluid passing by the blade element, computed within a single or multiple "streamtubes." Momentum methods break down for large streamwise forces, i.e., "induction factors"—common in water and high solidity turbines—and must be corrected empirically. Despite their deficiencies, these models can do a reasonable job for low solidity rotors when combined with corrections for dynamic loading, the most prominent cause of which is dynamic stall [148], but fail for high solidity [103]. A double multiple streamtube (DMST) momentum model can compute a full turbine performance curve in seconds on a modern desktop computer.

Vortex line methods are similar to momentum models, except blade element local velocity is computed using potential flow theory, where lifting bodies are bound vortex lines that shed vortex wake elements whose influences are combined via the Biot–Savart law [179]. Sandia National Labs' CACTUS is one example of a vortex line code [138]. CACTUS has been tested against experimental data from large, low-solidity wind turbines (those for which momentum models do well), but has been shown to fail for smaller turbines in water, which are typically higher solidity [136]. Regarding computing effort, vortex line methods can compute a full turbine performance

curve for a simple geometry in minutes—longer than the DMST method, but still quite fast. However, in some cases vortex methods can become quite expensive, e.g., when turbines contain many bound vortex elements, and/or the simulation must be run for long times, where the number of shed vortices becomes large. The increase in accuracy of the flow field prediction and the robustness with respect to high turbine loading justify the slightly higher expense of the vortex line method.

A more sophisticated vortex model is the so-called panel method, where turbine geometry can be specified arbitrarily as potential flow boundary elements, negating the need for sectional foil coefficient tables. This is a significantly more computationally expensive model—see for example [69]—in spite of its increased generality. Furthermore, boundary layer models are necessary to predict the occurrence and consequences of dynamic stall [195], and since the fluid dynamics are still assumed to be governed by potential flow, effects of turbulence are not resolved.

The most computationally expensive models solve the Navier–Stokes equations, with turbulence modeled with Reynolds-averaging (RANS) or large eddy simulation (LES)—the former being relatively less expensive, since LES directly solves a larger portion of the energy spectrum of turbulence. If a body-fitted grid is used, the actual turbine geometry is included as part of the computational domain, and the mesh is generally refined next to the solid surfaces to resolve the boundary layer, i.e., with cells adjacent to walls having a nondimensional wall distance $y^+ = u^* y/\nu \sim 1$, where u^* is the friction velocity, defined as $u^* = \sqrt{\tau_w/\rho}$, where τ_w is the wall shear stress. When only run in two dimensions, RANS methods are affordable enough to be run on a single CPU, computing a single turbine operating point in hours. However, 3-D effects are important enough that 2-D simulations are not reliable, at least as predictors of absolute performance [114]. 3-D simulations with a body-fitted grid are very expensive (especially for LES), therefore are practically limited to high performance computing (HPC) clusters. Even with the high computational expense, these models are not perfect and results can deviate significantly from experimental measurements, especially when using RANS models [114].

Actuator line modeling (ALM), first used by Sorensen and Shen [174], is a hybrid of the blade element and Navier–Stokes methods. The turbine is not part of the mesh, but is represented by lines

that move through the flow, acting as momentum sinks, where the resultant force is computed using 2-D foil data. Negating the needs for a body-fitted grid and resolving the boundary layer removes a significant amount of computational effort, but the flow field is still computed more accurately than with momentum or vortex methods, since nonlinear effects and turbulence are included in the RANS or LES equations. Removing the need for complex grids is also an advantage with respect to mesh generation, which is arguably the largest impediment to automation in CFD [170]. Computational effort is also significantly reduced since the ALM does not need a rotating mesh.

To the author's knowledge, at the time of this writing there has only been one study in the literature investigating the ALM for CFTs [164], which was performed for a 2-D rotor at very low Reynolds number, for which performance predictions were not reported. Assessing its effectiveness is therefore of interest in the present work.

1.2.2 For arrays

Effective turbine array engineering directly depends on accurate prediction of turbine wake generation, evolution and interaction, along with the impact of various types of turbulent inflow on power production of each device. Like for individual turbines, physical modeling is an option for predicting array performance, though it becomes even more expensive to match relevant dynamical scales. For this reason, turbine arrays are mainly designed using numerical methods.

The contemporary industry standard method for predicting array performance involves the superposition of prescribed wakes [176]. Evolution can be dependent on a single expansion coefficient chosen by the free stream turbulence intensity [101, 60] or computed by a solution of the linearized RANS equations with an empirically derived constant eddy viscosity closure [3]. While these models may be acceptable for analyzing HAWT farms, in light of the CFT's unique near-wake dynamics, the validity of these models for application to CFT arrays is questionable. At the very least they would need to be recalibrated for CFTs, though their applicability is limited in the near-wake of any turbine, meaning they are generally inappropriate for closely-spaced arrays.

The next step up in complexity is the actuator disk method, where a constant body force is added to the Navier–Stokes equations. This method can be computationally cheap with RANS, or

quite expensive and thorough with LES. The ORPC turbine array in Cobscook Bay, Maine is being laid out using the SNL-EFDC code, which uses a constant uniform force applied to the RANS equations, where the turbine injects turbulence kinetic energy and dissipation for the model's k–ε closure [142]. The ability of actuator disk models to predict the near-wakes of CFTs is of interest in this work.

At present simulations with body-fitted grids are limited to one or two turbines due to computational cost, which means they are impractical for full array simulations. Thus the actuator line method, when combined with LES, is the most complex model being used today. The ALM has the benefit of resolving unsteady flow features created by periodic blade forcing and end effects, ultimately producing the most accurate parameterization for turbine induced forces in Navier–Stokes simulations. It has been shown in blind axial-flow turbine modeling tests that ALM/LES methods fair better when predicting turbine induced turbulence, and therefore will be more accurate at predicting flow within a turbine array [108].

1.3 Goals and objectives

At the most basic level, the goal this research is to work towards the ability to predict the performance of and flow though an array of cross-flow turbines, to allow for the evaluation of array layouts, and the prediction of overall power output and potential environmental effects. The strategy for meeting this goal includes the following objectives:

1. To improve the understanding of both high and low solidity cross-flow turbine wakes, most importantly the apparent increased rate of momentum and energy recovery compared with axial-flow turbines. This will establish our flow modeling targets.

    (a) To evaluate the ability of actuator disk models to predict the wakes of cross-flow turbines.

2. To assess the allowable scale mismatch at which physical models can provide results relevant to full-scale devices and arrays.

3. To evaluate the ability of high-fidelity blade-resolved computational fluid dynamics and high performance computing to supplement or possibly replace experimental work.

4. To investigate actuator line modeling to potentially reduce the required computing power necessary for engineering work with CFTs.

An additional overarching goal is to release all research products—data, code, CAD models, simulation case files—as openly as possible to enable reproducibility and maximize reuse.

1.4 Contributions to science and engineering

Cross-flow turbines are simple machines made from common shapes, i.e., foils, but they can produce very complex flows. Despite their failure in the large scale wind industry, and beyond their contemporary adoption in marine hydrokinetics, there is scientific and engineering value to better understanding their behavior. The flow problem—unsteady foil behavior involving dynamic stall, finite blade span end effects in curvilinear flows—is complex yet general enough to be applicable to other unsteady turbomachinery and/or foil flows, e.g., Voith Schneider propellers, Cyclogyros, or even conventional helicopter rotors.

The experiments performed as part of this work have helped elucidate the unique wake features of cross-flow turbines [29] and establish scaling guidelines for physical modeling and numerical model validation [31]. This is especially important for CFTs since typical designs for small wind and MHK use have not yet been established. This means that in order to be robust, numerical models must be tested against measurements from turbines with varying design parameters, notably the solidity and aspect ratio, which affect the unsteadiness and significance of 3-D effects, respectively. There is a danger that validating against the most ubiquitous Darrieus turbine experiments may result in models that fail with newer, more unique designs.

In addition to conventional publications, the datasets collected and analyzed have been provided openly [27, 34, 36], both for a high and low-to-medium solidity turbine. These datasets will help others evaluate their numerical models, and since their availability also includes processing code, other researchers may find new knowledge to glean from them.

Lastly, the effectiveness of state-of-the-art Navier–Stokes based numerical modeling techniques was evaluated, and an actuator line model was developed and validated against performance and wake measurements for three-dimensional cross-flow turbines operating at Reynolds numbers relevant to full scale. Software tools here have also been made open-source, e.g., [22], have been made available to the public throughout all phases of development, and have benefited from open collaboration as well.

CHAPTER 2

DEVELOPMENT OF AN EXPERIMENTAL SETUP FOR MEASURING THE PERFORMANCE AND NEAR-WAKE OF CROSS-FLOW TURBINES AT LARGE LABORATORY SCALE

In 2011, a turbine test bed was developed for measuring the performance (mechanical power and overall rotor drag or thrust) of large laboratory scale ($O(1)$ m^2 frontal area) cross-flow turbines in the University of New Hampshire (UNH) tow tank [12], a 36.6 m long, 3.66 m wide, and 2.44 m deep facility, pictured in Figure 2.1, which was capable of towing up to approximately 1.4 m/s. The turbine-specific instrumentation consisted of a mounting frame built from NACA 0020 hydrofoil struts, a hydraulic disk brake for turbine loading, an Interface T8 200 Nm capacity rotary torque transducer, and a 54 pulse-per-rev magnetic pickup for measuring shaft speed. The frame was mounted to the carriage via streamwise-oriented linear bearings and was held in place by a pair of Sentran ZB3 2224 N capacity load cells that allowed measurement of total streamwise rotor drag.

Despite its usefulness in collecting a relatively small amount of data for two helical cross-flow turbines [30], this "first generation" system had some issues to be addressed:

- No control over turbine shaft angular velocity. This made operation at tip speed ratio below peak torque impossible.
- Fully manual starting and load application. This limited resolution of the applied torque, and took considerable effort to perform experiments on the order of 100 tows, since a person had to ride on the tow carriage to adjust and apply the load torque.
- Open loop speed and manual position control of the tow carriage. This also took considerable effort to operate experiments, since the operator had to estimate braking distance to ensure the carriage did not hit the tank ends.

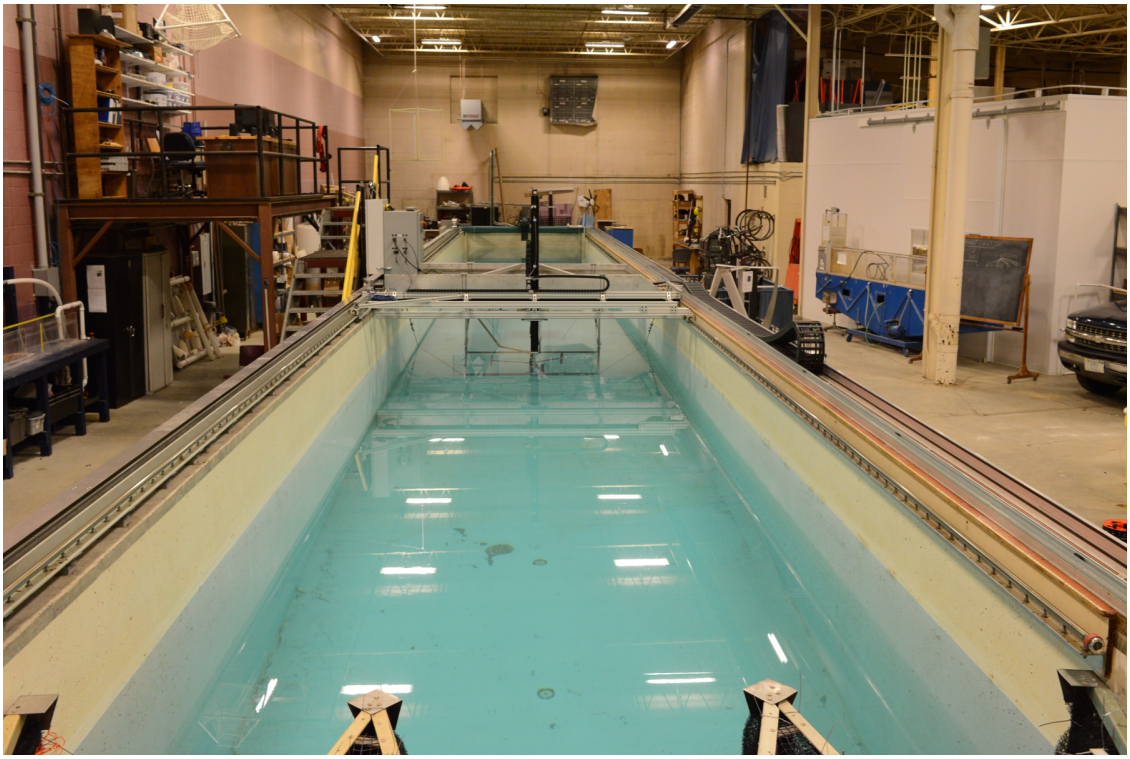

Figure 2.1: The University of New Hampshire's wave and tow tank, located in the Jere A. Chase Ocean Engineering Laboratory.

Spec	Old system	Target
Maximum speed	1.4 m/s	3.0 m/s
Maximum acceleration	0.1 m/s^2	2.0 m/s^2
Control system	Open loop velocity only	Closed loop position/velocity
Onboard power	4×12 V batteries	Continuous 120 and 220 VAC

Table 2.1: Specifications summary for existing and upgraded tow tank systems.

- Low carriage acceleration. The carriage acceleration was on the order of 0.1 m/s^2, which limited the steady state turbine operating duration to a few seconds.

- Low frequency resonance in the tow member. A long 0.25 inch diameter wire rope was used to tow the carriage, which resonated longitudinally with the significant variation of streamwise forces from the turbine.

In addition to the above issues, in order to meet the data acquisition goals, it was necessary to measure turbine wake flows. These concerns required major renovations, upgrades, and additions to the tow tank and turbine test bed motion, control, and data acquisition systems. Furthermore, it was desirable to automate the entire system to increase both data quality and quantity. These changes were made possible thanks to an infrastructure grant from the US Department of Energy (DOE).

2.1 Modifications to the UNH tow tank

The "foundation" of the experimental setup was the tow tank, which was addressed first. The main goals for the tow tank upgrades were to increase max speed and acceleration, add closed-loop positioning and velocity control, stiffen the tow member to reduce longitudinal resonance, and add onboard power and networking to the carriage for data acquisition and other peripherals. A summary of the old system and new target specifications is shown in Table 2.1.

2.1.1 Linear guides

The previous linear guide system, shown in Figure 2.2a, consisted of a "master" guide constructed from 4×4 inch fiberglass tubing, and a "slave" guide constructed from aluminum angle, on which

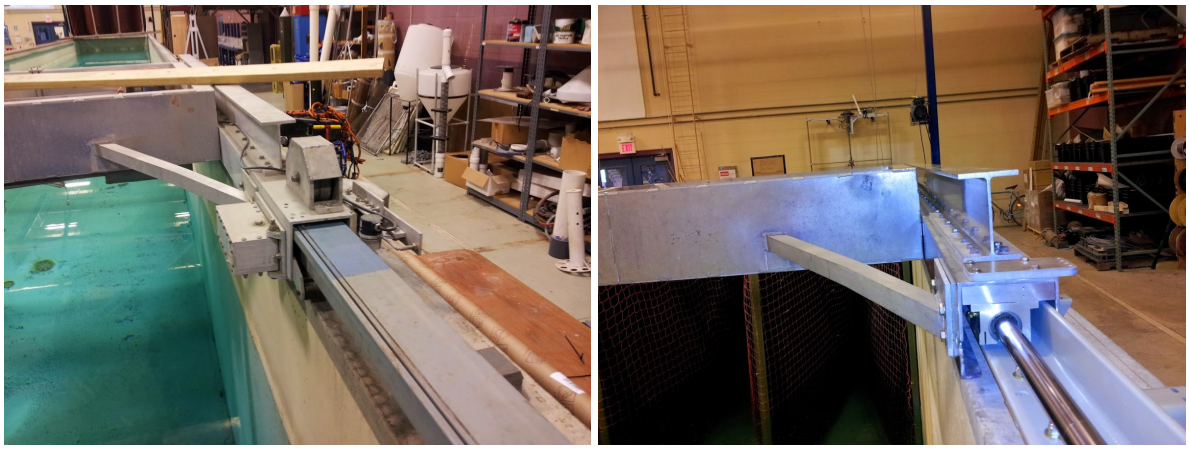

(a) Previous linear guide system. (b) Upgraded linear guides.

Figure 2.2: Linear guide system (on "master" side) (a) before and (b) after upgrades.

plastic wheels rode. Over time, the fiberglass tubing had failed structurally and was covered with stainless steel bars fixed with double-sided tape. These bars shifted around considerably during towing and were a source of noise in the measurements.

A new set of linear guides was designed from 1.25 inch diameter Thomson 440C stainless steel linear shafts and super self-aligning linear bearings, shown in Figure 2.2b. The existing carriage was modified to retrofit the linear bearings, and a series of parts were designed to adapt the stainless shafts to the existing quasi-level mounting surfaces, which helped keep cost down. The shafts were mounted via 3/8-24 inch threaded rods in oversized holes to allow adjustment in all three dimensions, a concept which was inspired by similar linear guide setups at the University of Minnesota's Saint Anthony Falls Laboratory (SAFL). The shafts were aligned in the cross-tank direction using a piece of monofilament line stretched along the path. The vertical alignment was set by spacing the shaft from its mounting surface equally along the path via machined blocks. When the existing level surfaces were set in 1996, these were measured to be level within $\pm 1/16$ inches [67].

2.1.2 Motion and control

The tow tank's previous motion system consisted of a 10 horsepower AC induction motor powered by a Yaskawa V7 variable frequency drive. The motor was coupled to a speed reducing gearbox, on which a pulley was mounted to drive a 0.25 inch diameter wire rope. It was seen in previous testing that this system had very low acceleration (~ 0.1 m/s^2), which severely reduced steady state towing durations. The relatively low spring constant of the wire rope tow member also gave the system a low natural frequency, which resonated due to cross-flow turbines' cyclic forcing. Furthermore, the system was only velocity-controlled, and in an open-loop manner. This meant positioning was done manually, which took a skilled operator, and reduced usable tank length further to allow for coasting to a stop.

These issues were addressed by changing the motor to a 26.1 maximum horsepower Kollmorgen AKM82 permanent magnet servo motor and 10:1 gearbox, shown installed in Figure 2.3, which was sized to tow turbines with 1 m^2 frontal area up to 3 m/s, while accelerating at 2 m/s^2. The motor was powered by a Kollmorgen S700 servo drive, controlled by an 8-axis ACS NTM EtherCAT master controller, providing closed loop position and velocity control. A series of emergency stop buttons were also installed to increase the safety of the system.

A 7.5 cm wide steel-reinforced polyurethane timing belt was chosen as the new drive member. The most robust timing belt profile—an ATL20—was chosen for maximum stiffness per unit width. Custom timing belt and pulley housings were designed to move both the upper and lower runs of the belt above the tank wall, shortening the overall length, which when combined with the higher specific stiffness belt increased the total drive member spring constant roughly by a factor of 7.

2.1.3 Data acquisition and onboard accessories

The previous generation tow tank data acquisition (DAQ) system was based around an onboard PC, powered by a set of four 12 V automotive batteries. This was done to avoid the complexity of running power out to the carriage [67]. The DAQ PC was accessed wirelessly via Windows Remote Desktop to control any DAQ applications. The PC that sent the control signal to the

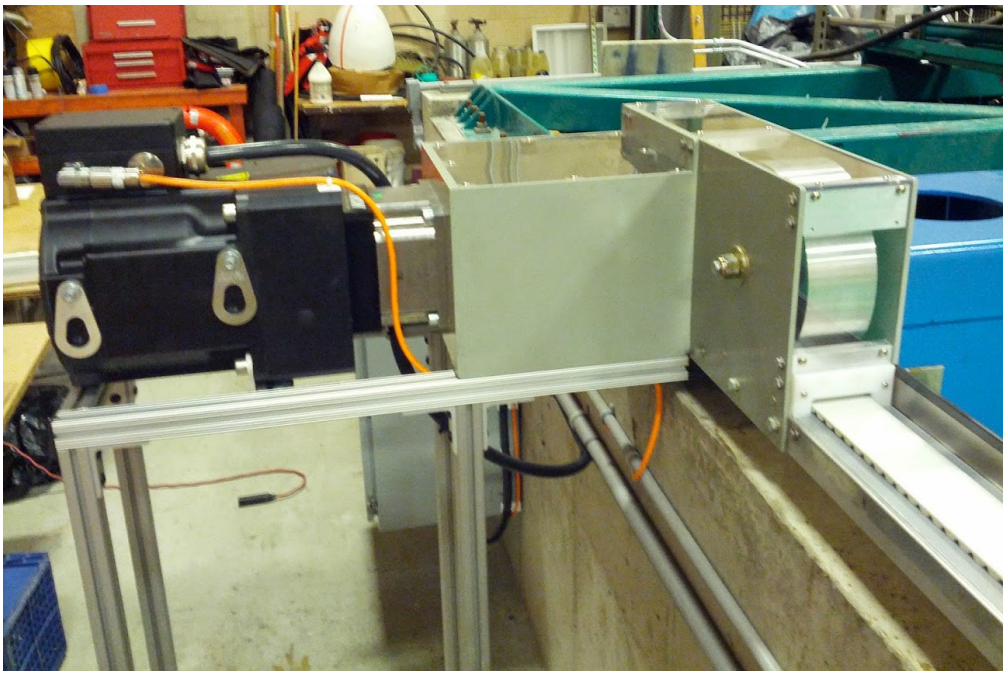

Figure 2.3: Upgraded tow system servo motor, gearbox, and custom-designed timing belt pulley housing.

inverter drive was a separate machine, which meant users had to work with at least two interfaces to specify DAQ and motion parameters. This also made it difficult to synchronize motion with data acquisition, e.g., triggering data collection at a certain location.

A new DAQ system was designed based around a National Instruments (NI) 9188 Compact-DAQ Ethernet chassis. NI 9237, 9205, 9401, and 9411 modules were installed for analog bridge, analog voltage, digital, and quadrature encoder signals, respectively. A single CAT5e cable was dedicated for this system. Additional cables were run for the EtherCAT and Internet connectivity on the carriage. An 8-port Ethernet-serial server was installed for accessing serial devices, e.g., the Nortek Vectrino+, described later. For measuring carriage speed, and therefore inflow velocity, a Renishaw LM15 linear encoder with 10 μm resolution was installed and connected to the NI 9411 module. Networking, power, and control signal cables were run through an igus cable carrier, installed along the "slave" or $+y$ side of the tank.

Requirements for onboard power were derived from the goal of fully automating both motion and data acquisition. It was also determined that the UNH ME department's high frame rate particle

image velocimetry (HFR-PIV) system would be used on the carriage at some point, which included laser power supplies and a laser chiller that could not be powered by the previous generation's isolated battery/inverter system.

An onboard electronics cabinet was designed by Minarik, Inc. as part of the upgraded motion system. A 45 amp, 120 VAC circuit and 20 amp, 240 VAC single phase power cable were run through the cable carrier to power outlets on the side of the onboard electronics cabinet. An additional 240 VAC three-phase supply was connected to a Kollmorgen AKD servo drive, also installed in the cabinet, which was sized to power a servo motor to control turbine shaft position and speed. The AKD drive's digital outputs were setup for triggering instrumentation, e.g., the NI 9188 chassis, via the main motion controller.

2.2 Upgraded turbine test bed

For this work, the turbine test bed was kept mostly intact, but modified for fully-automated operation. To reduce low frequency resonance in the frame caused by turbine side forces, and help redistribute some of the streamwise force from turbines towed at higher speeds, two pairs of steel guy wires were added. These solutions were chosen based on a finite element analysis (FEA) of the turbine mounting frame, which showed more improvement regarding stiffening in the desired directions compared to simply adding 45 degree flat bar braces in the corner joints. To ensure drag from the outer guy wires was included in the overall streamwise force measurement, an additional set of linear bearings was added to the carriage for their connection.

Summaries of turbine test bed sensors and instrumentation are presented in Table 2.2 and Table 2.3, respectively. A drawing and photo of the test bed are shown in Figure 2.4. Details on each subsystem are presented in following sections.

2.2.1 Turbine loading, speed control, torque, and drag measurement

In order to control turbine shaft angular velocity, a Kollmorgen AKM62Q servo motor and 20:1 ratio gearhead were added with a custom retrofit mounting plate and housing. Two zero-backlash R+W EKH/300/B curved jaw couplings were added above and below the rotary torque transducer.

Measured quantity	Device type	Mfg. & model	Nominal accuracy
Carriage position	Linear encoder	Renishaw LM15	10 μm/pulse [157]
Turbine angle	Servo encoder output	Kollmorgen AKD	10^5 pulse/rev [105]
Turbine torque	Rotary transducer	Interface T8-200	$\pm$0.5 Nm [97]
Turbine torque (2)	Load cell (& arm)	Sentran ZB3-200	$\pm$0.2 Nm [163]
Drag force, left	Load cell	Sentran ZB3-500	$\pm$0.6 N [163]
Drag force, right	Load cell	Sentran ZB3-500	$\pm$0.6 N [163]
Fluid velocity	ADV	Nortek Vectrino+	$\pm$0.5% $\pm$1 mm/s [144]

Table 2.2: Turbine test bed sensor details. Note that "(2)" denotes a secondary redundant measurement. "Turbine torque (2)" nominal accuracy estimated by combining load cell accuracy and arm machining tolerances ($\pm 1 \times 10^{-4}$ m) as root-sum-square.

Measured quantity	Device type	Mfg. & model
Carriage position	Differential counter	NI 9411
Carriage velocity (2)	Motion controller	ACS NTM
Turbine angle	Differential counter	NI 9411
Turbine RPM (2)	Motion controller	ACS NTM
Turbine torque	Analog voltage input	NI 9205
Turbine torque (2)	Analog bridge input	NI 9237
Drag force, left	Analog bridge input	NI 9237
Drag force, right	Analog bridge input	NI 9237

Table 2.3: Details of the instrumentation used to perform experiments with the turbine test bed. Note that "(2)" denotes a secondary redundant measurement.

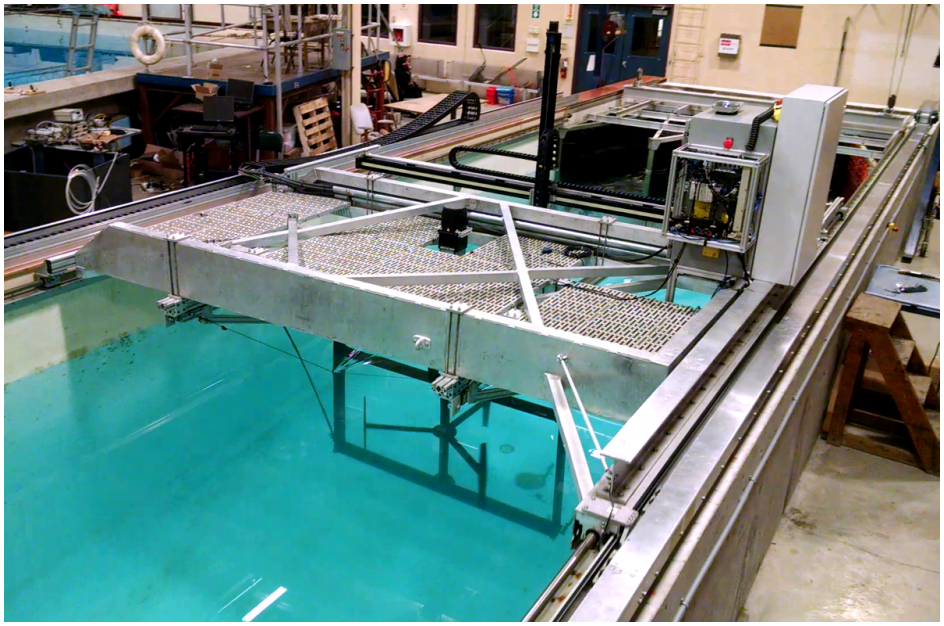

(a)

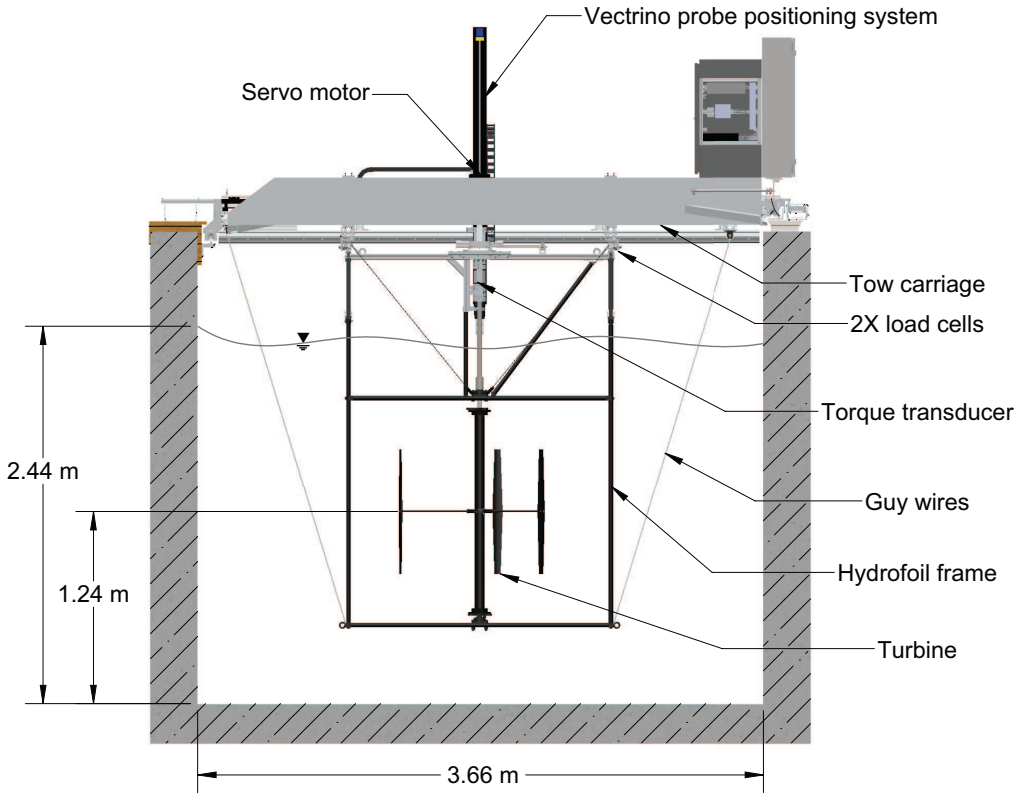

(b)

Figure 2.4: Turbine test bed photo (a) and drawing (b).

An additional torque measurement system was added by mounting the servo/gearhead assembly to a slewing ring bearing, and holding its mounting housing in place by a Sentran ZB3 890 N capacity load cell attached at a fixed distance by a 0.406 m long arm. This system served as a redundant torque measurement for values up to 200 Nm, and extended the maximum torque range to approximately 360 Nm.

Turbine shaft angle was measured via the AKD drive's emulated encoder output, set to 5×10^3 (pre-gearbox) or 1×10^5 (post-gearbox) lines-per-rev in an A-quad-B configuration. This signal was sampled by either the NI 9401 (experiments reported in Chapter 3) or the NI 9411 (experiments reported in Chapters 4 and 5) modules. Shaft speed was computed by differentiating the angle time series with a second order central difference scheme. A moving average filter $\sim$10 samples wide was applied to smooth the resulting ω time series such that it agreed nearly identically with the shaft RPM measured by the servo motor's resolver feedback as sampled by the motion controller.

The two drag slide assemblies for overall streamwise drag or thrust measurement were retained from the previous setup, which is described in [12]. All turbine performance related signals were sampled by modules in the NI 9188 CompactDAQ chassis at a 2 kHz sample rate.

2.2.2 Wake measurement system

In order to characterize turbine wakes, a Nortek Vectrino+ acoustic Doppler velocimeter (ADV) was purchased with a Hubbard Fund grant from UNH. An ADV is capable of measuring three components of velocity at a single point in space (technically over a small volume), and the Vectrino+ was set to sample at 200 Hz. This system was considered desirable compared with hot wire or hot film anemometry as it required no calibrations, and the sensor element is significantly more robust. Spatial resolution is typically lower—the Vectrino's measurement volume is 6 mm in diameter [144]—but this is still small compared with the typical length scale of a turbine model. ADV was also preferable to laser Doppler velocimetry (LDV) in this case since the tow carriage is a high vibration environment, which would make LDV alignment a challenge.

A y–z axis positioning system was designed for the Vectrino probe. This system consisted of two Velmex BiSlide linear stages—the y-axis driven by belt and the z-axis by ball screw. Both

drive systems were powered by stepper motors with approximately 0.001 inch resolution. These motors were driven by an ACS UDMlc EtherCAT drive, connected to the tow tank's main motion controller for integrated synchronous motion.

When operating the Vectrino, the tank was seeded with 11 μm mean diameter hollow glass spheres. Seeding was added along the tank length, generally at the surface, and was mixed by towing the turbine through the tank. This process was repeated until the Vectrino's signal-to-noise ratio (SNR) was approximately above 12 dB. Seeding was added throughout experiments as necessary—totaling approximately 1–5 cups (dry) per day. Note that while acquiring ADV data the y- and z-axis stepper drive had to be disabled to reduce noise. The axes were re-enabled to position the probe before each run.

2.2.3 Software

Software was developed to automate the entire turbine testing process. Dubbed TurbineDAQ, the desktop application was written in Python due to its reputation as a good "glue" language for systems integration. The graphical user interface (GUI), shown in Figure 2.5, was built using the PyQt bindings to the Qt framework. Communication with the tow tank's motion controller, data acquisition system, and ADV were integrated into a single application. This, combined with the ability to load and automatically execute test matrices in comma-separated value (CSV) format, allowed for experiments consisting of thousands of tows, where the previous generation test bed could only realistically achieve around 100. Note that the software was developed after the experiments in Chapter 3, for which turbine tip speed ratio, Vectrino positioning, and data collection parameters were input manually. However, TurbineDAQ was developed before and employed for both the larger experiments described in Chapter 4 and Chapter 5.

2.2.4 Tare drag and torque compensation

The drag and torque measurement systems were set up in such a way that raw measurements for drag would include all submerged gear and torque would include all friction below the transducer along with the turbine shaft torque. To compensate, tare torque and drag runs were performed to measure the shaft bearing friction torque and turbine mounting frame drag, respectively. Tare

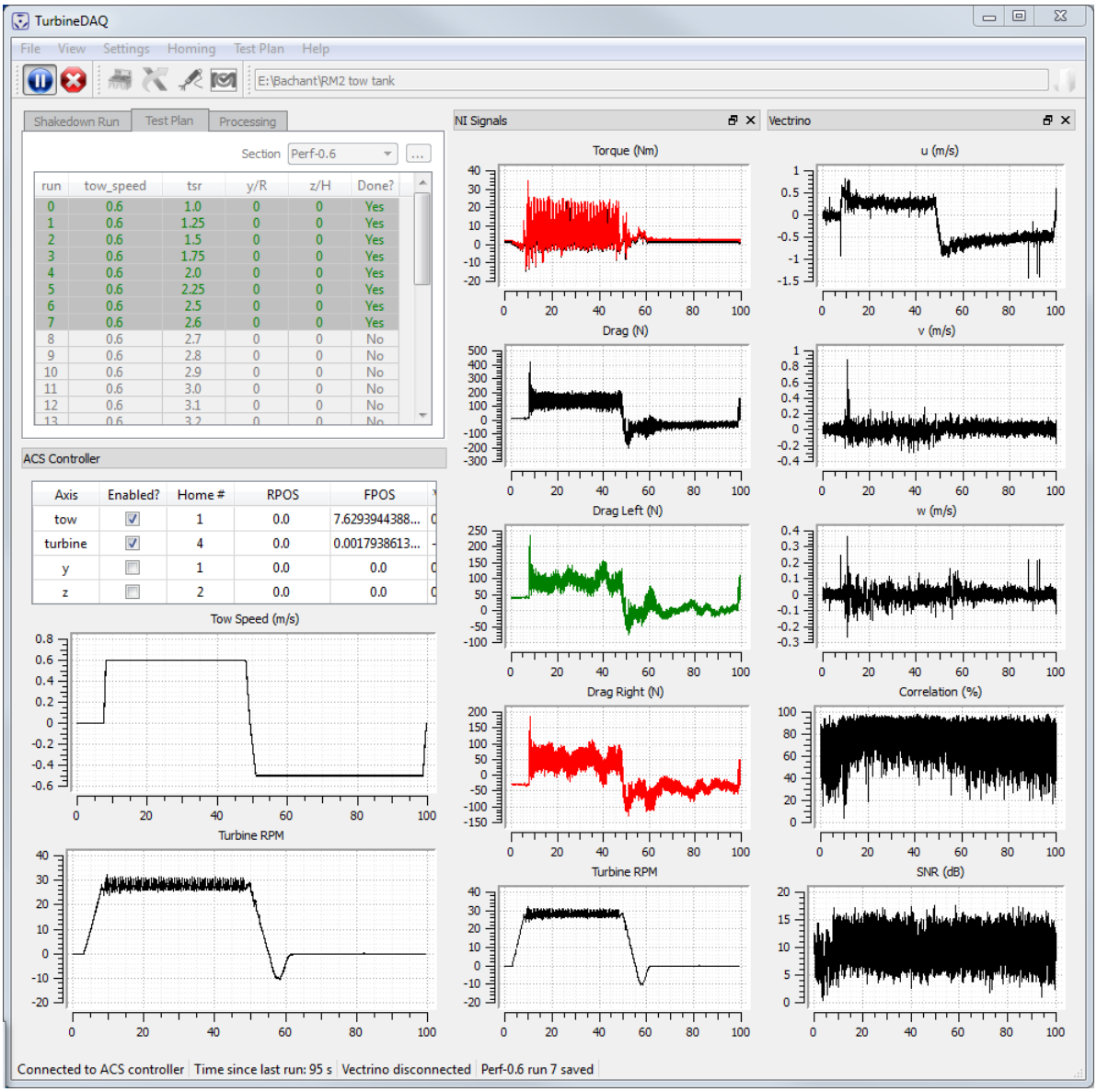

Figure 2.5: TurbineDAQ turbine test bed experiment automation software graphical interface.

drag runs were performed for each tow speed in each experiment, for which the mean value was subtracted in data processing to estimate rotor drag alone. Tare torque runs were performed by rotating the turbine shaft (without blades) in air at constant angular velocity for a specified duration, over the range of angular velocities used throughout the experiment. Tare torque was then fit with a linear regression versus shaft angular velocity, and added to the measured turbine torque in post-processing.

2.2.5 Synchronization of instrumentation subsystems

The three data acquisition instrumentation subsystems—motion controller, NI DAQ (performance measurements), and Vectrino+ (wake velocity measurements)—were set to begin sampling at precisely the same time each run, after being triggered by a TTL pulse created by the motion controller. This strategy retains synchronization for all performance signal samples (tow speed, torque, drag, angular velocity), ensuring precise calculation of, e.g., power coefficient. Since there is also synchronization of the initial sample from each three subsystems, correlation of events in the performance and wake signals is also possible.

2.2.6 Calibrations

Factory calibrations for all instrumentation were used for the experiments described in Chapters 3 and 4. The drag slide and torque arm assemblies were calibrated out of the tank using the fixtures shown in Figure 2.6, in which a Sentran ZB3 500 lbf capacity load cell and indicator were used for input values. The reference load cell and indicator were calibrated as a full system from the factory and remained connected to each other at all times. The drag slide and torque arm fixtures were loaded incrementally using a 3/4-16 inch threaded rod, nut, and self-lubricating thrust bearing.

Before the RM2 experiment described later in Chapter 5, traceable calibration certificates were obtained for the Interface T8-200 torque transducer and NI 9205 and NI 9237 modules. In 2014, the drag slide and torque arm assemblies were recalibrated using the same fixture and Sentran ZB3 load cell and indicator described above, for which a new traceable calibration certificate was obtained. Values before and after the recalibration are presented in Table 2.4.

(a)

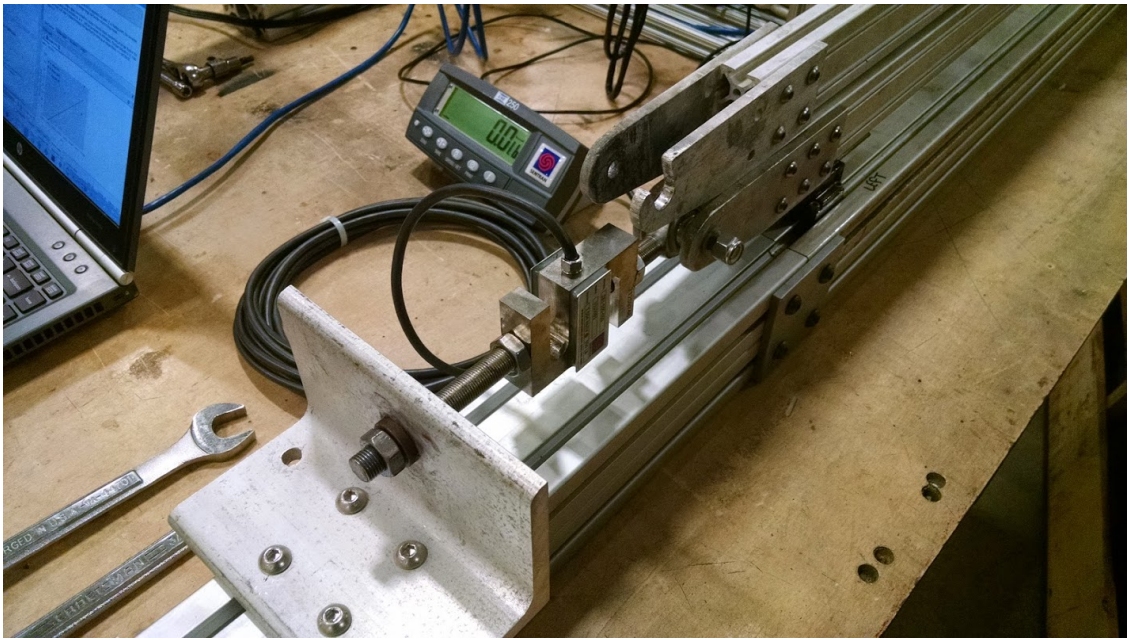

(b)

Figure 2.6: Torque arm (a) and drag slide (b) calibration fixtures. Note that the same load cell, indicator, and thrust bearing are used for both setups.

Signal	Calibration 1	Calibration 2	Difference
Torque trans.	40.0000 Nm/V	39.8380 Nm/V	-0.4 %
Torque arm	122531 Nm/V/V	123437 Nm/V/V	0.7 %
Drag left	743104 N/V/V	742830 N/V/V	-0.1 %
Drag right	740137 N/V/V	742400 N/V/V	0.3 %

Table 2.4: Calibration slopes used for experimental measurements. Calibration 1 was used for the experiments described in Chapter 3 and Chapter 4. Calibration 2 was used for those in Chapter 5.

2.3 Determining tank settling time

For each experiment, sample turbine tows were performed at each speed to determine the amount of time taken between runs such that the tank has settled adequately, i.e., background turbulence and any large scale mean flows have been dissipated. This was assessed by towing the turbine, bringing the carriage back to mid-tank, and allowing the Vectrino to continue recording velocity data, monitoring the mean and standard deviation of the signals.

Turbulence intensity tended to decay quickly, while the lower frequency fluctuations were damped with the help of the tank's "beach," designed for absorbing waves created by the paddle-style wavemaker. Settling times ranged from 140 seconds for tows at 0.3 m/s up to 360 seconds for those at 1.4 m/s. These values were then included in the experiment configuration—one value for each tow speed, to be used by TurbineDAQ as wait times between automated runs.

2.4 Blockage

Placing a turbine in a confined environment such as a towing tank will force flow through the turbine at higher velocity compared with a free case, where streamlines are allowed to diverge. Consequently, higher levels of blockage will lead to increased turbine performance, and a shift in optimal operating parameters, i.e., tip speed ratio. In order to for experiments to be relevant to others in the literature, blockage effects must either be corrected for, or the blockage ratio should be kept to a typical value seen in other studies.

Most numerical models have the ability to include finite domains or walls, which makes uncorrected applicable to validation; applying blockage corrections may even complicate validation

efforts. Furthermore, blockage will be non-zero in most MHK cases, where turbines are placed in rivers or channels, the effects of which need to be predicted as well. Since a definitive blockage correction for CFTs has not yet been established [55, 70], and a 1 m^2 turbine creates a reasonably low blockage—on the order of 10%—no corrections were applied.

2.5 Turbine models

Two physical turbine models were designed and built. The first was intended to be a geometrically simple—not necessarily very efficient—high-solidity turbine. This simplicity was achieved with symmetrical foil profiles, square frontal rotor area, and a rectangular blade planform. This turbine was constructed from materials donated by Lucid Energy Technologies, LLP, and dubbed the "Reference Vertical-Axis Turbine" or UNH-RVAT.

The second turbine was designed and built as part of a measurement task for Sandia National Laboratories (SNL), in collaboration with the US Department of Energy (DOE), which is described in more detail later in Chapter 5. The so-called "Reference Model 2" (RM2) was developed by SNL to be a standard cross-flow turbine for which modelers could validate their predictions [141]. The RM2 was designed using Sandia's CACTUS vortex line code [40], and its low-to-medium solidity made it a nice complement to the UNH-RVAT for testing the robustness of numerical models to varying solidity.

2.5.1 UNH-RVAT

The UNH-RVAT turbine was constructed from straight 14 cm chord length NACA 0020 extrusions, used for both the blades and struts. The blades were mounted at mid-chord, mid-span, and zero preset pitch, with a length or height of 1 m and placed at 1 m diameter, giving the rotor an aspect ratio of unity. These parameters gave the rotor a relatively high solidity $Nc/(\pi D) = 0.13$ and a large chord-to-radius ratio $c/R = 0.28$.

The support struts were also constructed from 14 cm chord NACA 0020 profiles, and attach the turbine to a 9.5 cm diameter shaft. A drawing of the turbine rotor is shown in Figure 2.7a and

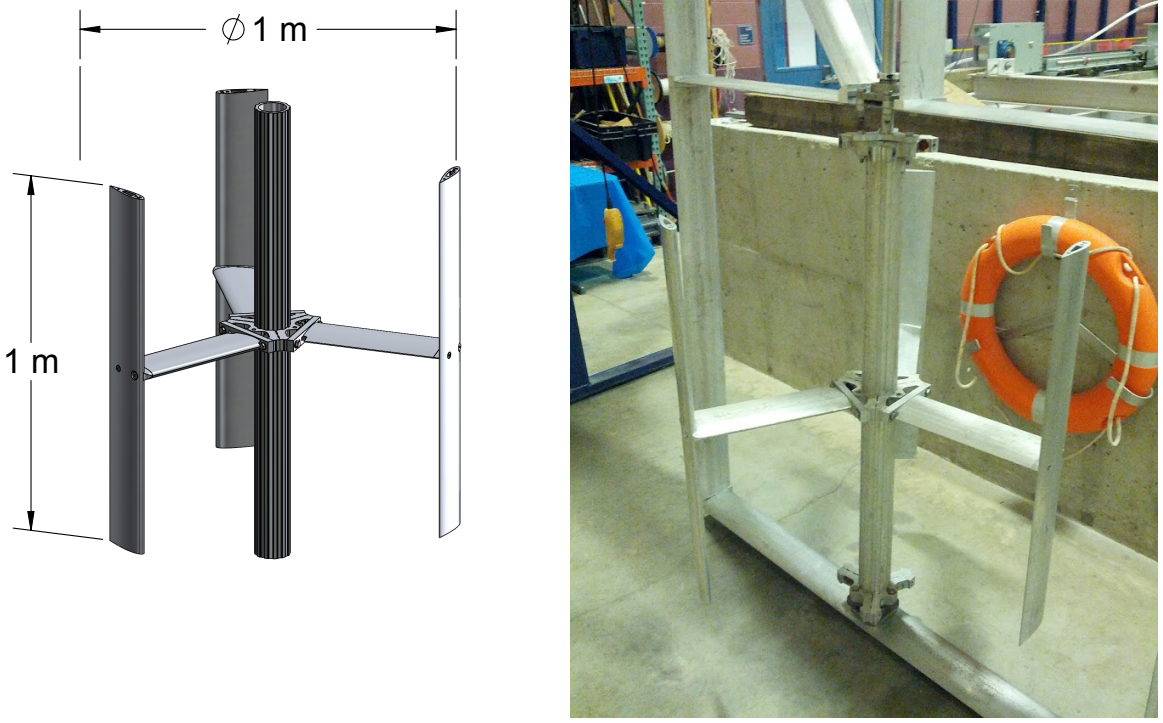

(a) (b)

Figure 2.7: Drawing (a) and photo (b) of the UNH-RVAT vertical-axis cross-flow turbine. Note that the upper and lower mounting flanges (and the area of the shaft they cover) have been excluded in the drawing. These were included in the tare drag measurements for the experiments in Chapter 4, but excluded for those in Chapter 3.

CAD models are available from [28]. The turbine is shown outside of the tank installed in the test bed mounting frame in Figure 2.7b.

2.5.2 DOE/SNL RM2

The RM2 rotor was designed as a 1:6 scale model of that described in the RM2 "rev 0" design report [40], with the exception of the shaft diameter, which was scaled from the SAFL RM2 shaft [95]. The hub design is also similar to the SAFL model. A drawing of the turbine design is shown in Figure 2.8a and a photo of the RM2 installed in the turbine test bed mounting frame is shown in Figure 2.8b. The rotor has tapered blades with $c/R = 0.12$ at the roots (mid-span) and $c/R = 0.07$

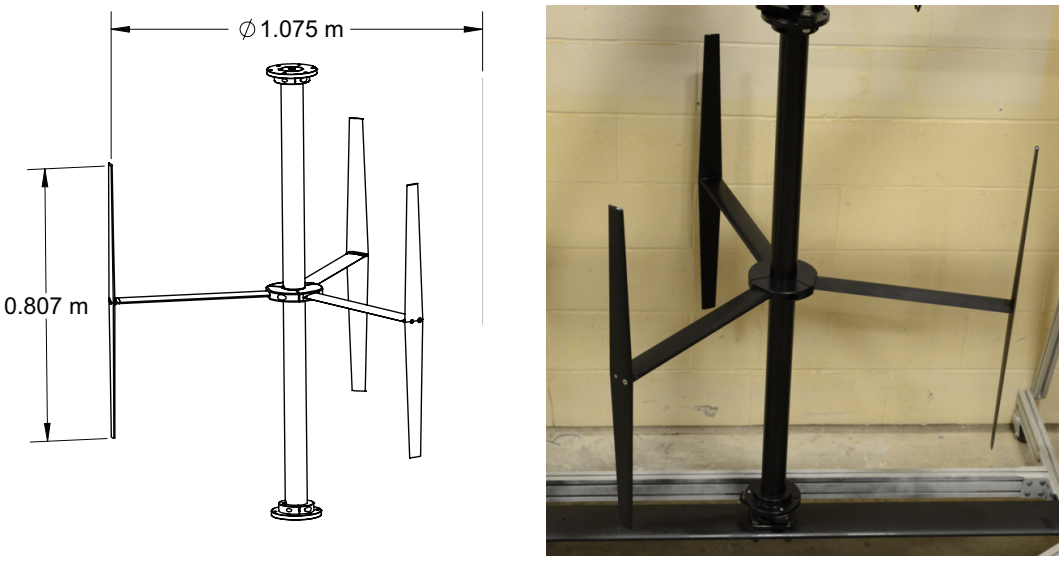

(a) (b)

Figure 2.8: Drawing (a) and photo (b) of the 1:6 RM2 scaled physical model cross-flow turbine.

at the tips, which uniquely gives it a medium-high solidity for a wind turbine and low solidity for an MHK turbine. The RM2 is discussed in more detail in Chapter 5.

2.6 Summary and conclusions

An upgraded test bed for measuring the performance and near-wake flows of large laboratory scale ($O(1)$ m^2 frontal area) cross-flow turbines was developed for the UNH tow tank. To acquire adequate amounts of data and to achieve significant lengths of steady state operation with a limited tank length, the tow tank's linear motion, control, and data acquisition systems had to be redesigned, rebuilt, and upgraded to allow fully automated operation, along with higher carriage speed and acceleration. Integrating carriage, turbine, and Vectrino probe positioning, along with synchronized data acquisition from performance measurement, Vectrino, and motion controller systems increased the number of tows possible per experiment by essentially an order of magnitude, while simplifying data processing and increasing data quality and repeatability. CAD files for the tow tank and turbine test bed are available from [23].

Two turbine models were designed and fabricated. The UNH-RVAT turbine was designed to be more geometrically simple, but higher solidity, while the RM2 turbine is lower solidity, with tapered blades. The differences between these rotors provide an opportunity for direct comparison within the same experimental setup, and will provide validation data to test numerical models' predictive capabilities with varying levels of flow curvature (from higher c/R) and end effects (blade aspect ratio and taper).

CHAPTER 3

BASELINE EXPERIMENTAL CHARACTERIZATION OF A HIGH SOLIDITY CROSS-FLOW TURBINE

As an initial baseline experiment with the turbine test bed, the performance and near-wake velocity of the high solidity UNH-RVAT were measured. Note that the results presented here have been published in [24, 29].

The first task was to assess the rotor's characteristic performance (power and drag coefficient versus tip speed ratio) curves. Next, a typical operating set point tip speed ratio was established, at which the near-wake was examined in detail to gain insight into the mechanisms that improve CFT wake recovery rates compared with AFTs (allowing closer spacing, cf. [104]) or other axisymmetric turbulent wakes, with the ultimate goal that these mechanisms can be replicated in simpler models for use in simulations of large turbine arrays, where resolving actual turbine geometry is prohibitively expensive. The ability of one such model—an actuator disk inside a Reynolds-Averaged Navier–Stokes (RANS) simulation—to predict those defining characteristics was also assessed.

The dominant scales within the turbine's near-wake were evaluated for their relative importance, loosely following the conceptual framework presented in Chamorro et al. [56], where the turbine was treated as an "active filter." However, by extending this concept it should be cautioned that this filter could also be nonlinear, i.e., the spectral modifications of the inflow are dependent on the spectral distribution itself, not a superposition of effects at each individual scale. It is also expected that a CFT will introduce even stronger large (turbine) scale variance into the flow, due to its cyclical forcing from oscillatory blade angles of attack and relative velocity. The experiments presented here were performed in a towing tank, providing a very low turbulence intensity inflow (at least as low as the instrumentation noise floor), which provides an excellent baseline case for

spectral content added to the flow by the turbine, without any modulation of a turbulent inflow spectra.

Previous detailed experimental studies with CFTs were generally limited in terms of Reynolds number due to small geometric scale. On the other hand, as expected, large-scale measurements were typically performed with lower resolution instrumentation, and with less control of inflow conditions [189]. Brochier et al. [50] employed laser-Doppler velocimetry (LDV) to acquire detailed flow measurements of a small-scale, quasi-2-D CFT in dynamic stall. Their study was similar in scope to the work presented here, but was conducted at very low Reynolds number—approximately two orders of magnitude smaller than the study presented here. More recently, Tescione et al. [184] performed a detailed experimental campaign, using particle image velocimetry to illuminate vortex structures in the wake, and how these interact with each other. However, the question still remains as to why the CFT wake would recover more quickly than that of an AFT. The study reported here also examined the three-dimensionality of the wake, as turbine blade end effects will no doubt affect interaction with the free stream.

To summarize, the goals of this experiment were:

1. To identify the essential features of the near-wake of a cross-flow turbine.

2. To assess the relative importance of mean and turbulent dynamics on the transport of momentum and kinetic energy in the wake.

3. To compare the measured CFT wake to numerical predictions from a uniform actuator disk force parameterization implemented inside a RANS model, to evaluate its prospects for representing CFTs in array simulations.

3.1 Experimental test plan

All experiments were performed at a tow speed of 1 m/s, resulting in a Reynolds number based on turbine diameter of $Re_D = U_\infty D/\nu = 1 \times 10^6$, or an approximate blade chord Reynolds number of $Re_c \approx \lambda U_\infty c/\nu = 2.7 \times 10^5$ for $\lambda = 1.9$, where tip speed ratio $\lambda = \omega D/(2U_\infty)$. Note that this

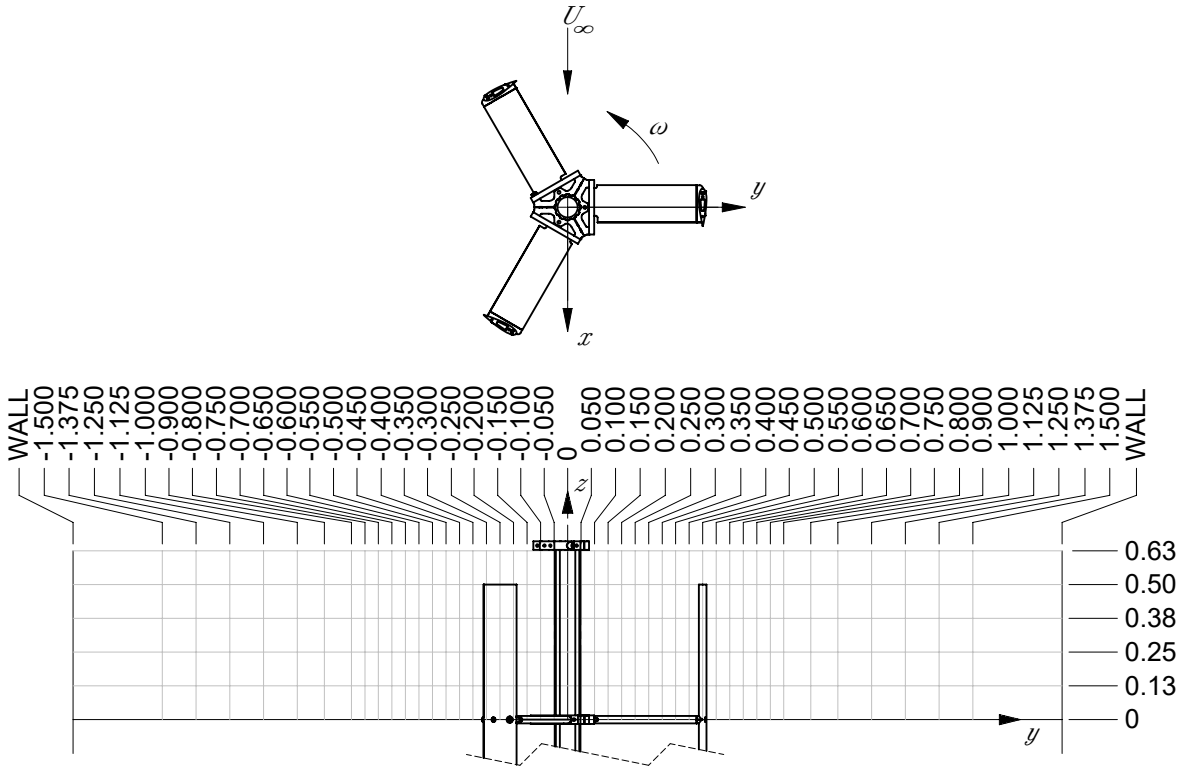

Figure 3.1: Wake measurement coordinate system and grid.

Reynolds number is high enough to be considered operating in a *Re*-independent regime [49, 26, 31], which is examined in more detail in Chapter 4.

The performance of the turbine was measured first by operating at a range of tip speed ratios, which were held constant during individual tows, and varied from almost zero to just above that where power becomes negative, i.e., where the motor has to drive the rotor. From the C_P–λ curve, the optimal tip speed ratio λ_0 was selected for characterizing the wake at one rotor diameter downstream of the rotor axis. The flow measurements mapped out the upper half of the turbine wake over 3 m in the spanwise direction, centered within the 3.66 m tank width, the coordinate system and locations for which are shown in Figure 3.1.

For the power and drag measurements, the ADV was placed at the quarter height $z/H = 0.25$, with $z/H = 0$ corresponding to the turbine center. A duplicate set of measurements were also taken for $z/H = 0$ to show how quarter height and center line measurements differ as a function

of tip speed ratio. One additional transverse wake profile was then acquired at $z/H = 0.25$ for a lower-than-optimal tip speed ratio to increase the effects of dynamic stall.

3.2 Results and discussion

3.2.1 Data processing

Data from each tow were extracted where the quantities of interest—torque, drag, and velocity—had reached an approximately stationary mean value. The time series were then trimmed further such that they correspond to an integer number of turbine blade passages, to minimize bias from periodicity. Wake data collection runs included 30 blade passages, which corresponds to approximately 16.5 seconds or 3300 velocity samples at each measuring station. Drag from the mounting structure, a.k.a. tare drag, was measured by towing with the turbine removed, and then subtracted from the turbine measurements to provide a better estimate of the overall drag on the turbine rotor and shaft alone. Similarly, tare torque was measured by driving the turbine support shaft and bearings in air and regressing these values linearly with respect to shaft angular velocity. This tare torque was then added to the measured turbine torque in post-processing to provide a more accurate estimate for the true hydrodynamic torque.

As described in Chapter 2, the tank was seeded with 11 μm mean diameter hollow glass spheres to achieve adequate beam correlation and signal-to-noise ratios. No filtering was used on the velocity data, i.e., statistics were computed using all raw samples from the measurement interval. For computing partial derivatives of velocity quantities, a central difference scheme was employed. For the boundaries of the measurement plane, an inward-facing second-order scheme was used. The data processing and plotting code, along with the reduced dataset are available from [27].

3.2.2 Turbine performance

Performance curves showing the overall power and drag coefficients of the turbine are shown in Figure 3.2. The drag coefficient monotonically increases with increasing tip speed ratio over the entire range tested, and the power coefficient reaches a maximum of 26% around a tip speed ratio $\lambda = 1.8$–1.9, where the drag coefficient is 0.96. These curves informed the selection of the optimal

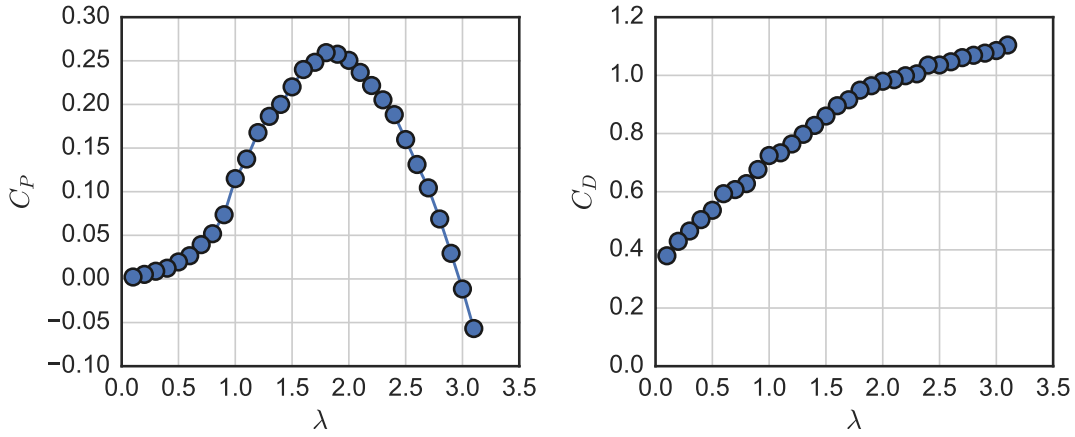

Figure 3.2: Mean turbine power (left) and drag (right) coefficients plotted versus tip speed ratio.

tip speed ratio $\lambda_0 = 1.9$ as the operating point for detailed near-wake characterization. We expect that at this tip speed ratio the turbine blades will be operating in dynamic stall over a part of the turbine rotation [160], reaching maximum angles of attack of approximately 35 degrees, and that this will be a significant contributor to the near-wake structure. Note that the maximum power coefficient could likely be improved with simple geometric modifications, e.g., changing the blade pitch [79], but for this study the geometry was meant to be as simple as possible, therefore the blade pitch was left at zero.

3.2.3 Wake characteristics

The near-wake of the turbine was described in terms of its mean velocity, streamwise vorticity, Reynolds stresses, and turbulence kinetic energy. Dominant time scales were identified and evaluated for their contribution to the turbulent spectra. Finally, the processes that lead to replenishment of momentum and energy in the wake were investigated, with the goal of explaining the CFT's relatively fast wake recovery.

3.2.3.1 Momentum and vorticity

The mean velocity measured in the wake at one turbine diameter downstream is shown in Figure 3.3. The most obvious characteristics are the asymmetry and three-dimensionality of the flow field. The peak momentum deficit is shifted towards the right side of the turbine (looking up-

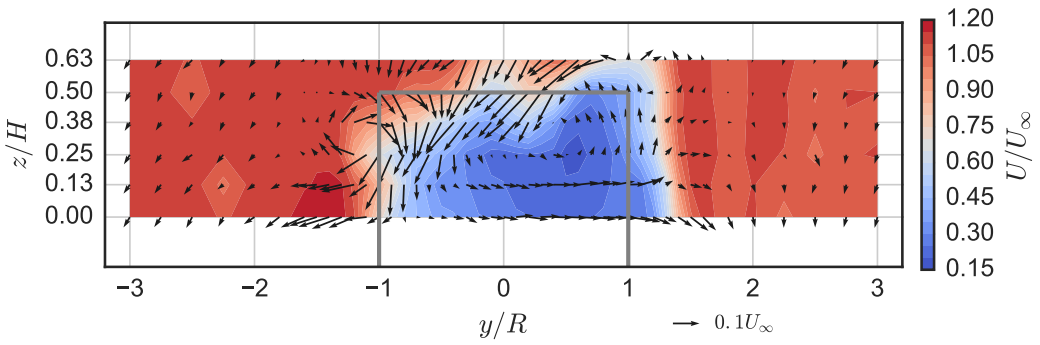

Figure 3.3: Mean velocity at $\lambda = 1.9$. Vectors are cross-stream and vertical velocities; contours are streamwise velocity. View is looking upstream, with the turbine frontal area indicated by the solid gray lines.

stream). We can also see the effects of blade tip vortex shedding, where flow is moving downward and to the left, creating strong streamwise mean vorticity near the blade tip at $y/R = -1$, contours for which are shown in Figure 3.4. The asymmetry may explain observations of counter-rotating turbine pairs helping speed wake recovery [66].

The generation of streamwise vorticity with opposing directions highlights once again the three-dimensionality of the wake of this turbine, and its difference from an axisymmetric swirling wake such as that of an axial-flow turbine. The two regions of counter-rotating vorticity act like an asymmetrical doublet, propelling fluid downward towards the turbine centerline.

Compared with the rotating cylinder wake measurements of Lam [110], we see a similar asymmetry in the mean streamwise velocity. The wake is less asymmetrical with respect to the wake centerline for the turbine compared to the rotating cylinder for the same non-dimensional rotation rate, although some of these differences may be due to the cylinder experiments' lower Reynolds numbers. Compared with the end effects of a finite cylinder wake [181], we do see generation of a counter-rotating vortex pair, though for a non-rotating cylinder these are symmetric, which is not the case for the turbine wake, where the vortex pair seems to be tilted. The turbine's wake is also similar to a finite cylinder wake in a sense that there is a mean downward velocity directly behind the wake generator. These similarities and differences give some perspective regarding the

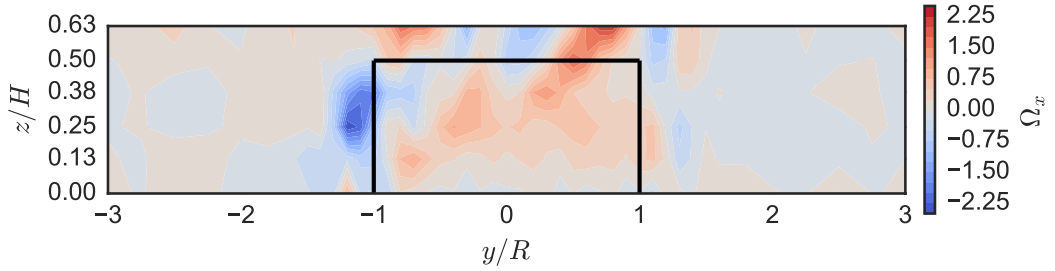

Figure 3.4: Contours of mean streamwise vorticity. Note that this perspective is looking upstream and therefore negative values indicate clockwise rotation.

use of cylinders for turbine simulators in physical model studies of arrays, which was considered by [150].

Compared with an axial-flow turbine wake [52], and a rotating actuator disk model [193], axisymmetric streamwise vorticity or swirl is not observed here, which is one of the reasons for the wakes' differing dynamics. This can be explained as a consequence of the conservation of angular momentum, where the AFT imparts a streamwise rotation along its axis due to torque generation, where the CFT imparts a torque that is perpendicular to the flow. The AFT mean swirl only propels fluid away from its axis, while the CFT induces mean flow into its momentum deficit region, albeit in a asymmetric fashion.

Reynolds shear stress contours, shown in Figure 3.5, quantify the replenishment of mean momentum by turbulent transport. Regions of high $\overline{u'v'}$ as well as the observed asymmetry correspond to the regions of high gradients of streamwise velocity, indicating regions of high turbulence production.

To quantify the relative importance of mean and turbulent transport processes, we rearrange the streamwise Reynolds-averaged momentum equation to isolate terms contributing to its streamwise derivative. Assuming the flow is stationary in the mean and incompressible, the equation becomes

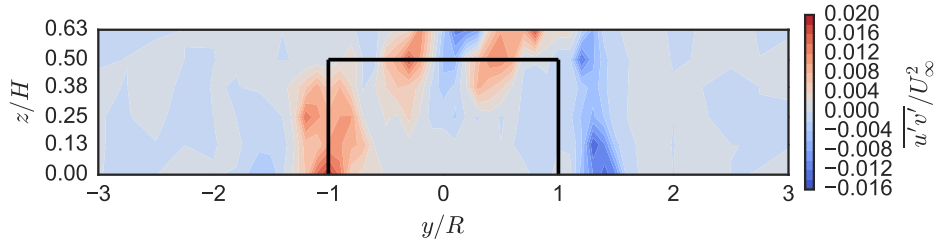

(a)

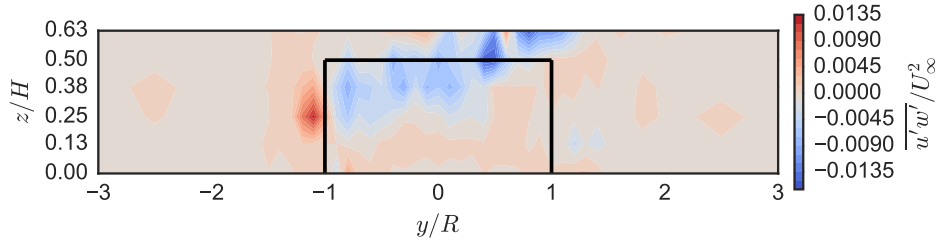

(b)

Figure 3.5: Contours of (a) streamwise–cross-stream and (b) streamwise–vertical Reynolds shear stress.

$$\begin{aligned}\frac{\partial U}{\partial x} = \frac{1}{U}\Bigg[& -V\frac{\partial U}{\partial y} - W\frac{\partial U}{\partial z} \\ & -\frac{1}{\rho}\frac{\partial P}{\partial x} \\ & -\frac{\partial}{\partial x}\overline{u'u'} - \frac{\partial}{\partial y}\overline{u'v'} - \frac{\partial}{\partial z}\overline{u'w'} \\ & +\nu\left(\frac{\partial^2 U}{\partial x^2} + \frac{\partial^2 U}{\partial y^2} + \frac{\partial^2 U}{\partial z^2}\right)\Bigg].\end{aligned} \tag{3.1}$$

From the experimental measurements, all of the terms on the right hand side were computed except for the streamwise pressure gradient and the streamwise (x) derivatives of the Reynolds and viscous stresses; the latter two terms are expected to be small under a thin shear layer assumption. Weighted averages for these terms, taken over the entire measurement plane and normalized by D/U_∞ to assess nondimensional mean momentum recovery per turbine diameter of downstream distance, are plotted in Figure 3.6. We see that as expected, viscous diffusion is almost negligible. The two Reynolds stress transport terms are both significant, but the vertical advection term

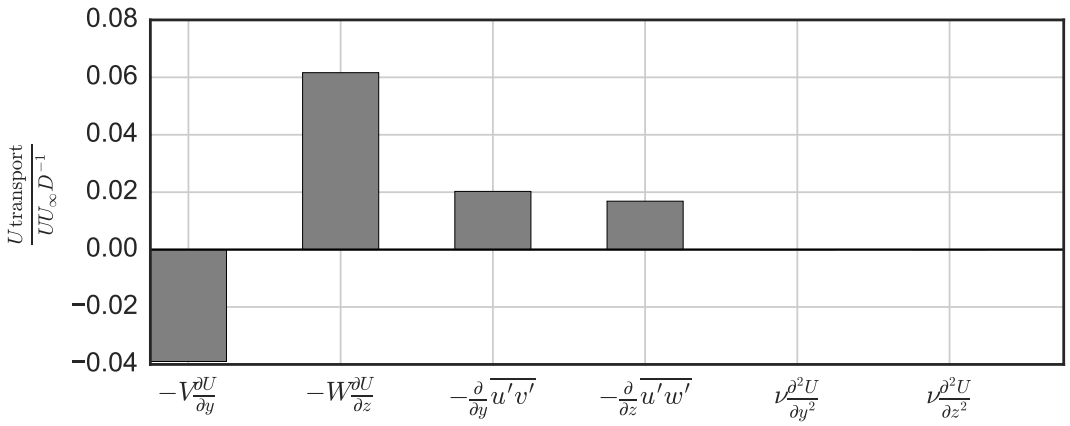

Figure 3.6: Estimates for the contributions to mean streamwise momentum recovery in the streamwise direction, multiplied by two (due to assumed symmetry), averaged over the measurement plane, and normalized by the average streamwise velocity, free stream velocity, and turbine diameter.

dominates, and the horizontal advection term contributes negatively, corresponding to streamlines diverging around the turbine. The flow essentially behaves like an inviscid three-dimensional, non-axisymmetric turbulent wake. If we sum all the terms we obtain a total wake recovery rate at $x/D = 1$ of 12% per turbine diameter, which would be interesting to compare with an axial-flow turbine in similar conditions.

3.2.3.2 Dominant time scales

Spectral densities were computed using a fast Fourier transform (FFT) based algorithm, with a Hanning window applied to the time series. Spectral values were averaged over 4 adjacent frequencies to reduce noise and increase confidence intervals. Figure 3.7a shows the peak frequency—normalized by the turbine angular frequency—of the cross-stream velocity energy spectra at each measurement point. We can see how unsteadiness in the flow is induced primarily at the blade passage frequency, or three times f_{turbine}. Note that some higher peak frequencies can also be seen in this plot, out in regions of low turbulence intensity. This is due to both the noise floor of the ADV and the wakes of the guy wire supports.

Spectral concentration Ψ is quantified by normalizing the peak value of the spectral density by the total variance of the signal multiplied by the spectrum's Fourier frequency interval Δf, i.e.,

$$\Psi = \frac{S_{\max}\Delta f}{\sigma^2}, \tag{3.2}$$

where $\Delta f = 1/(N\Delta t)$, N is the total number of samples, and Δt is the sampling interval. For a pure harmonic $\Psi = 1$, indicating all variance contained within a single frequency. This metric provides further characterization of the turbulence in terms of its range of scales, rather than the overall variance or turbulence intensity.

A plot of this concentration is also shown in Figure 3.7b, where it is evident that energy is more concentrated towards the side of the turbine where the blades move upstream, likely seeing lower angles of attack, and therefore boundary layer separation occurring further towards the trailing edge of the blade. This concentration is indicative of more coherent motion, or extraction of energy/momentum from the flow without intense separation, whereas on the opposite side of the turbine, turbulence generated by the dynamic stall process is increasing the diffusion of shed vorticity. This effect can be further illustrated looking at sample spectra for turbine torque coefficient and cross-stream velocity components at two points on opposite sides of the turbine, shown in Figure 3.8, where the cross-stream velocity at the side of the turbine inducing massive separation shows a smaller peak in its spectrum at the blade passage frequency.

3.2.3.3 Kinetic energy

Contours of turbulence kinetic energy are shown in Figure 3.9. The turbulence kinetic energy is concentrated near the top and left side of the turbine, as a result of the blade tip and dynamic stall vortex shedding, respectively. The lower turbulence kinetic energy on the $+y$ side of the turbine corresponds with the more concentrated spectral energy of velocity unsteadiness in this area. This can be interpreted as the lift-induced vorticity being shed with less separation compared to the $-y$ side of the turbine, where turbulence is being generated and redistributing energy across a

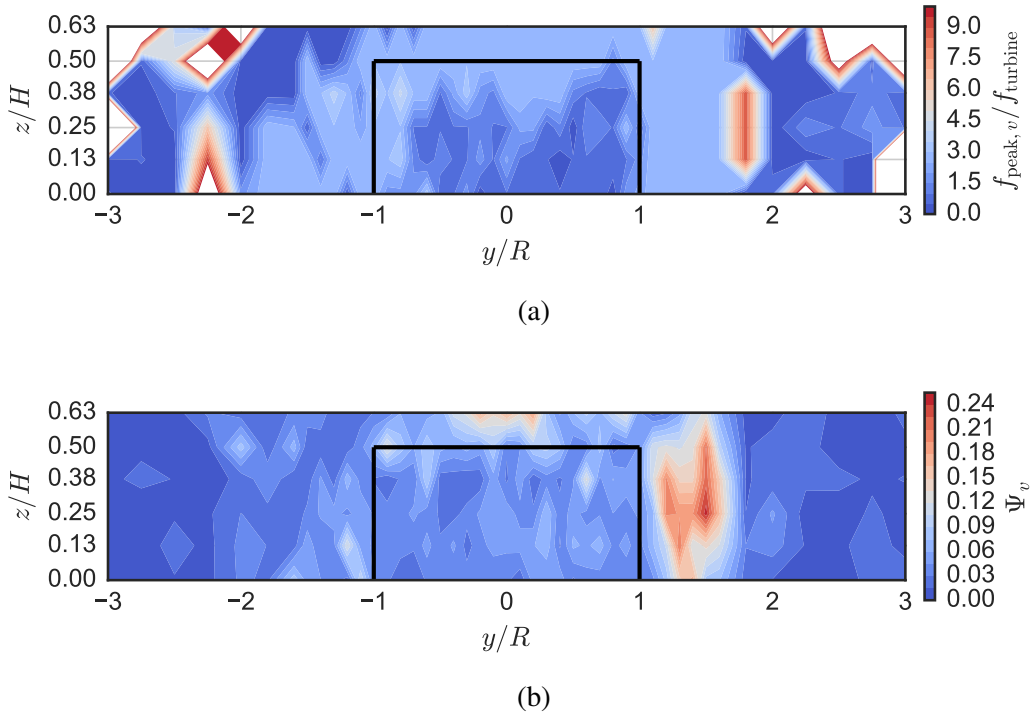

Figure 3.7: Cross-stream velocity energy spectra (a) peak frequency normalized by turbine angular frequency and (b) spectral concentration. Note that white regions have values higher than the maximum value of the color bar, caused by both noise and wakes of the guy wire supports.

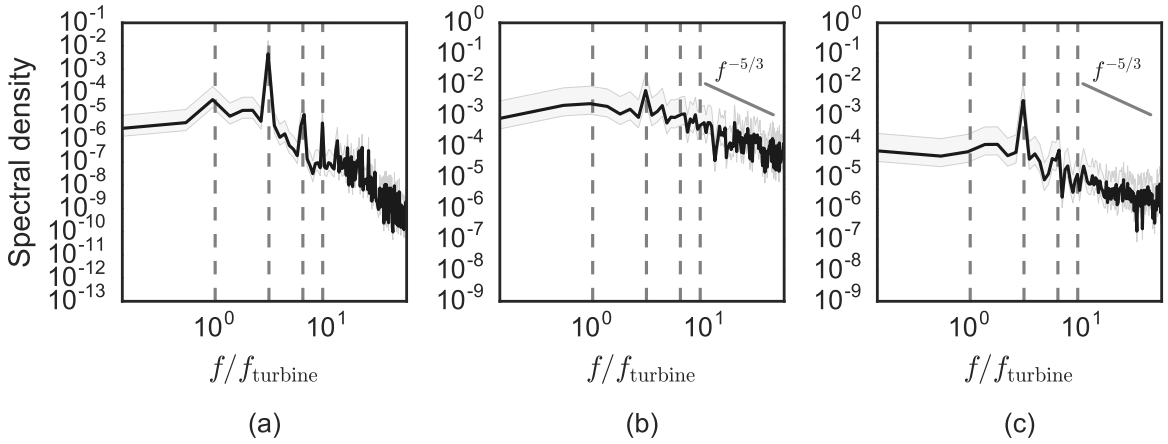

Figure 3.8: Spectral density for (a) torque coefficient, (b) cross-stream velocity at $y/R = -1$; $z/H = 0.25$, and (c) cross-stream velocity at $y/R = 1.5$; $z/H = 0.25$. Dashed vertical lines indicate $[1,3,6,9]$ times the turbine rotational frequency and the shaded gray region indicates the 95% confidence interval for a χ^2 variable with 8 degrees of freedom—twice the number of frequencies over which spectral values were averaged to reduce noise.

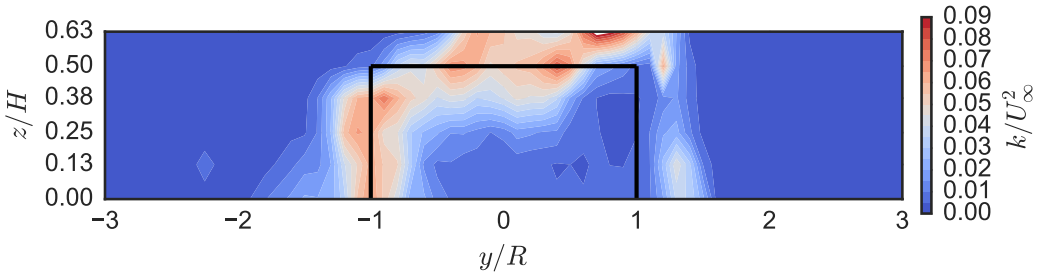

Figure 3.9: Contours of normalized turbulence kinetic energy. Turbine frontal area is indicated by solid black lines.

larger bandwidth. This brings up one potential improvement to actuator line models: Modulating turbulence fields at the occurrence of dynamic stall.

Like the analysis of the mean streamwise momentum, the mechanisms which play the most important role in mean kinetic energy recovery as the wake evolves in the streamwise direction are now examined. The transport equation for the kinetic energy K associated with the mean flow [183], rearranged to isolate the streamwise recovery ($\partial/\partial x$) can be written as

$$\frac{\partial K}{\partial x} = \frac{1}{U}\Bigg[\underbrace{-V\frac{\partial K}{\partial y}}_{y\text{-adv.}} \underbrace{-W\frac{\partial K}{\partial z}}_{z\text{-adv.}} - \frac{1}{\rho}\frac{\partial}{\partial x_j}PU_i\delta_{ij} + \frac{\partial}{\partial x_j}2\nu U_i S_{ij} \underbrace{-\frac{1}{2}\frac{\partial}{\partial x_j}\overline{u_i'u_j'}U_i}_{\text{Turb. trans.}} + \underbrace{\overline{u_i'u_j'}\frac{\partial U_i}{\partial x_j}}_{k\text{-prod.}} \underbrace{-2\nu S_{ij}S_{ij}}_{\text{Mean diss.}}\Bigg]. \tag{3.3}$$

The terms of interest are labeled—advection ("adv.") in the cross-stream and vertical directions, energy transport by turbulent fluctuations ("Turb. trans."), production of turbulence kinetic energy (k-prod.) through mean shear, and the dissipation due to mean viscous shear forces ("Mean diss."). For the tensor terms, streamwise derivatives were omitted, since the measurements were limited to a single streamwise distance. Table 3.1 lists all components kept for the computation of each transport term.

Figure 3.10 shows estimates of mean kinetic energy transport by turbulent fluctuations. The structure observed indicates that the turbulent fluctuations act mainly in regions with significant

Term in Eq. 3.3	Implementation
y-adv.	$-\frac{V}{U}\frac{\partial K}{\partial y}$
z-adv.	$-\frac{W}{U}\frac{\partial K}{\partial z}$
Turb. trans. (y)	$-\frac{1}{2U}\left[\frac{\partial}{\partial y}\overline{u'v'}U+\frac{\partial}{\partial y}\overline{v'v'}V+\frac{\partial}{\partial y}\overline{w'v'}W\right]$
Turb. trans. (z)	$-\frac{1}{2U}\left[\frac{\partial}{\partial z}\overline{u'w'}U+\frac{\partial}{\partial z}\overline{v'w'}V+\frac{\partial}{\partial z}\overline{w'w'}W\right]$
k-prod.	$\frac{1}{U}\left[\overline{u'v'}\frac{\partial U}{\partial y}+\overline{v'v'}\frac{\partial V}{\partial y}+\overline{w'v'}\frac{\partial W}{\partial y}\right.$ $\left.+\overline{u'w'}\frac{\partial U}{\partial z}+\overline{v'w'}\frac{\partial V}{\partial z}+\overline{w'w'}\frac{\partial W}{\partial z}\right]$
Mean diss.	$-\frac{2\nu}{U}\left[\left(\frac{\partial U}{\partial y}\right)^2+\left(\frac{\partial U}{\partial z}\right)^2+\left(\frac{\partial V}{\partial y}\right)^2\right.$ $\left.+\left(\frac{\partial V}{\partial z}\right)^2+\left(\frac{\partial W}{\partial y}\right)^2+\left(\frac{\partial W}{\partial z}\right)^2\right]$

Table 3.1: Terms used to compute contributions to mean kinetic energy recovery.

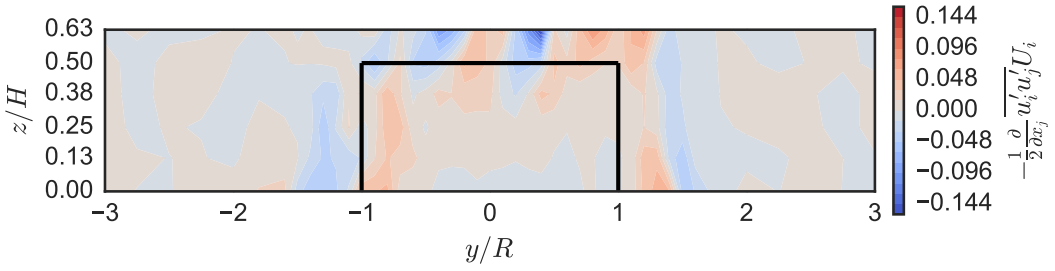

Figure 3.10: Contours of estimated mean kinetic energy transport by turbulent fluctuations, where streamwise derivatives are omitted. Turbine frontal area is indicated by solid black lines.

mean velocity gradients, as expected. The signs of the terms plotted here can be understood from Figure 3.5. Note that despite lower turbulence kinetic energy on the $+y$ side of the turbine, magnitudes of the turbulent transport are similar on both.

Like the streamwise momentum transport, contributions to mean kinetic energy recovery from various mechanisms were averaged over the measurement plane using the trapezoidal rule, weighted by the local measurement plane grid size, which was nonuniform (see Figure 3.1). Figure 3.11 shows the normalized sum of each quantity to show their relative size. As with the momentum, the cross-stream mean advection contributes negatively since the flow is accelerating around the turbine due to its pressure disturbance, where streamlines diverge.

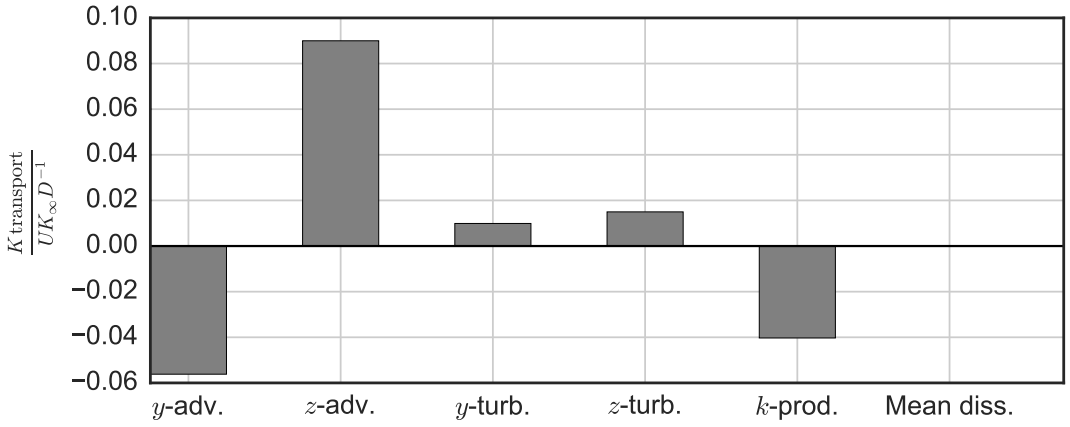

Figure 3.11: Estimates for the contributions to mean kinetic energy recovery in the streamwise direction, multiplied by two (due to assumed symmetry), averaged over the measurement plane, and normalized by the average streamwise advection velocity, free stream kinetic energy, and turbine diameter.

Viscous dissipation due to mean shear is essentially negligible compared to the other terms, which is to be expected in a high Reynolds number shear flow a short distance downstream of the shear flow (wake) generator (CFT).

Production of turbulence kinetic energy acts to reduce mean kinetic energy, as expected for the mean kinetic energy equation. The turbulent transport terms, separated by the direction of their divergence, i.e., "y-turb." is a sum of all terms with $\partial/\partial y$ in them and "z-turb." is a sum of all terms with $\partial/\partial z$ in them, are about the same order of magnitude, both roughly an order of magnitude smaller than the vertical advection term, which is the largest. It should be re-stated that the terms in Figure 3.11 were evaluated in the near wake, in a measurement plane at $x/D = 1$ shown in Figure 3.1.

Compared to the observations of Kinzel et al. [104], where the turbulent transport terms were found to be not large enough to replenish turbine power output, it can be seen here that it is most likely vertical advection that plays the most important role in enhancing the wake recovery, not the turbulence quantities. This is likely a consequence of the unique vorticity generation and interaction from lift production, (dynamic) stall vortices, and blade end effects.

3.2.4 Effects of tip speed ratio

Low tip speed ratio may occur temporarily during a gust inflow condition, may be caused by malfunctioning controls, or may be the optimal operating point for a high solidity turbine. From our measurements we can observe how mean velocities at two fixed points downstream of the turbine axis vary with tip speed ratio. These velocity components are plotted in Figure 3.12. Mean streamwise velocity deficit at $z/H = 0$ increases with tip speed ratio, which is expected in light of the drag measurements. However, the mean streamwise velocity deficit at the quarter height is highest at tip speed ratios corresponding to high power coefficient, but decreases at higher values of λ. Mean vertical velocity at the turbine center remains relatively constant across the entire operating envelope. However, mean vertical velocity at the quarter height shows a markedly higher downward component at higher λ, corresponding to the similar aforementioned trend of decreasing streamwise velocity deficit at that location. Asymmetry about $y/R = 0$ is seen in the mean cross-stream velocity at values of λ away from those of highest power output, with a mean component in the positive y-direction. Ultimately, these effects may be attributed to a shift in the blade position at which maximum loading occurs, therefore changing the strength and orientation of the blade tip vortices.

Next we want to look more closely at the effects of lowering λ, thereby increasing maximum blade angle of attack and inducing increased stalling behavior. Quarter height streamwise mean velocity profiles for the two tip speed ratios of interest are shown in Figure 3.13. Some similarities can be identified with the study by Brochier et al., namely the assymetry of the mean velocity profile and how its shape changes on the side of the turbine where the blade faces into the flow—positive y for our experiments and negative for theirs [50].

Figure 3.14 shows mean vertical velocity profiles for the two tip speed ratios of interest. The large gradient appearing at negative values of y, suspected to be the result of blade tip vortices, remains a approximately the same location. However, the peak seen at $y/R = 1.2$ is decreased for the lower tip speed ratio case.

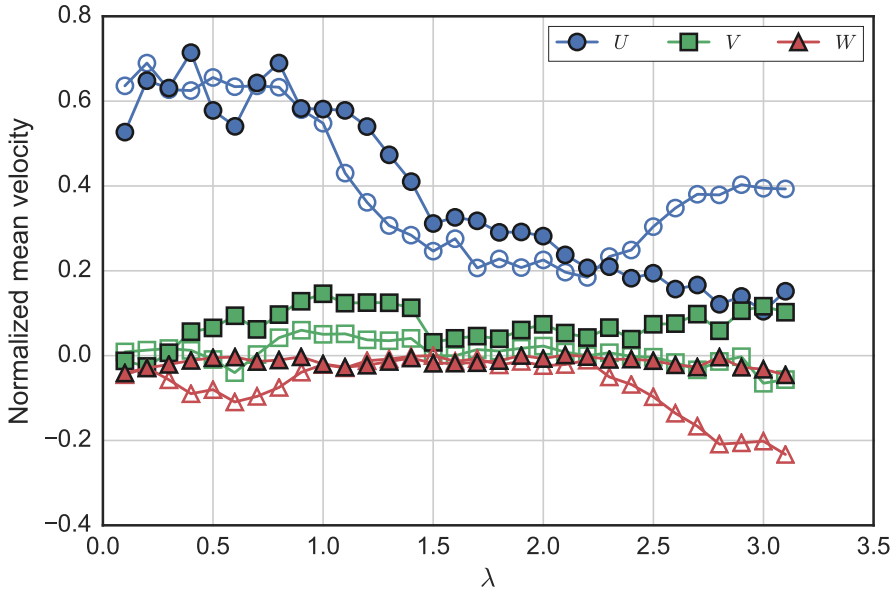

Figure 3.12: Normalized centerline mean velocity components at $x/D = 1$ versus tip speed ratio. Filled markers indicate measurements at $z/H = 0$, while open markers indicate those at $z/H = 0.25$.

Figure 3.15 shows profiles of mean cross-stream velocity for both λ values. Unlike the streamwise and vertical profiles, these show relatively large differences at our two tip speed ratios of interest, indicating significant fluid motion—on the order of 10% of the free stream velocity—to the left on the left edge of the rotor at $\lambda = 1.9$ and to the right at the right edge of the rotor at $\lambda = 1.4$. This shows how by changing tip speed ratio, and therefore the location of peak blade loading, there may be potential for control over transverse diversion of the flow in the near-wake.

Regarding turbulence kinetic energy in the wake, profiles of which for the two tip speed ratios are shown in Figure 3.16, we can make similar comparisons with the very low *Re* study of Brochier et al. [50]. Their results show two peaks on opposite sides of the rotor axis, with the lower tip speed ratio case having a relatively higher peak on one side, which should correspond to negative y values in our case. This is somewhat in agreement with our results, though the value at the origin for our case is relatively higher, which may be due to the larger shaft wake. However, when we compare our two profiles, we notice for the lower value of λ there is higher average turbulence levels

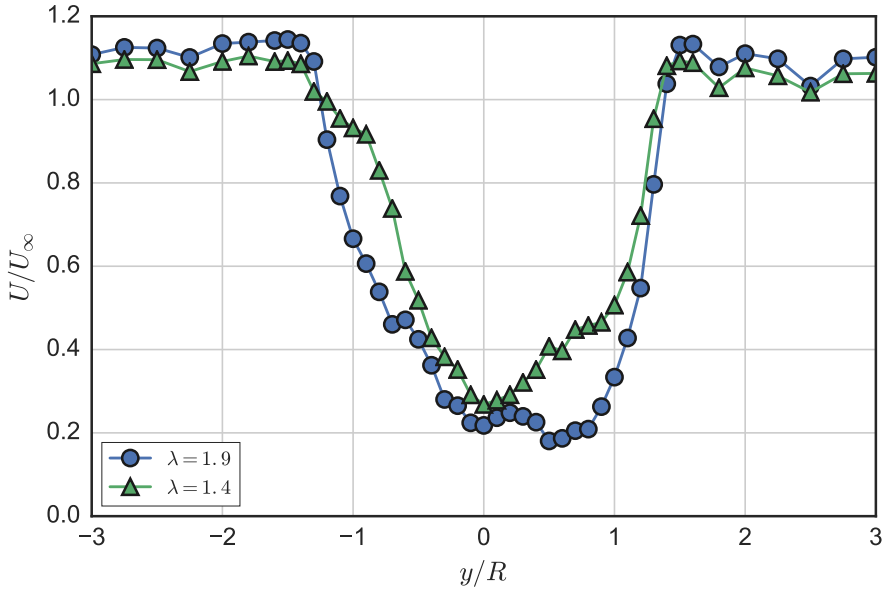

Figure 3.13: Streamwise mean velocity profiles for $\lambda = 1.9$ and $\lambda = 1.4$ at $x/D = 1$ and $z/H = 0.25$.

throughout the center region. This appears to be caused by more intense blade stall, beginning earlier along the upstream blade path, i.e., at higher positive values of y.

3.2.5 Comparison with an actuator disk

The actuator disk model, commonly used in modern large-eddy simulations of wind farms [177], parameterizes turbine forcing on the flow field as a steady streamwise force applied over the frontal area of the turbine. The model is attractive due to its relatively simple implementation; it does not require the meshing of actual turbine geometry, making it computationally feasible to simulate large turbine arrays. For example, the turbine array being installed by ORPC in Cobscook Bay, Maine was laid out with a RANS actuator disk model, where cross-flow turbines were represented inside the mesh over three cells [142]. Furthermore, the actuator disk force coefficients are not time dependent, allowing for simulation of, e.g., tidal cycles without the need for small time steps to resolve unsteady turbine forcing.

Here the experimental measurements are compared and contrasted with the near-wake of an actuator disk model, to illustrate how this model would represent a cross-flow turbine in an array

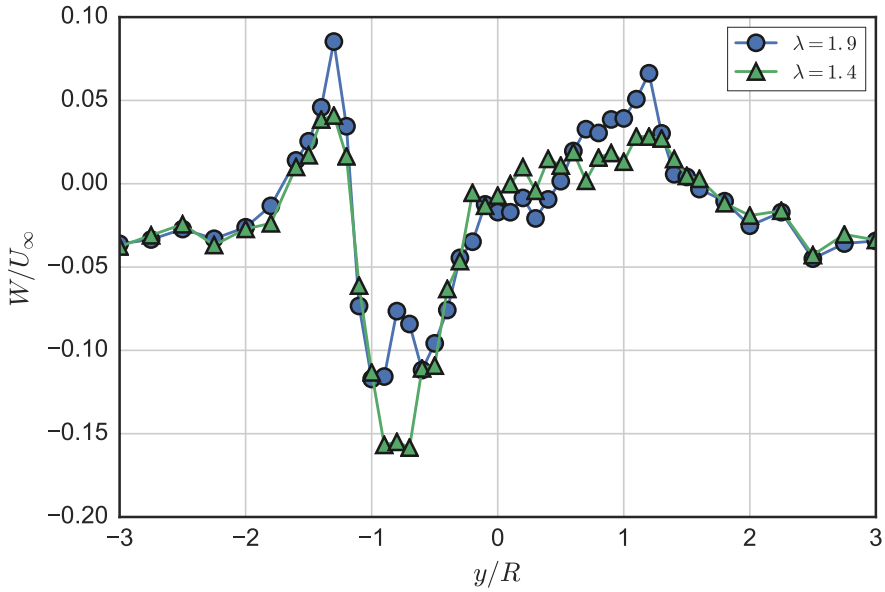

Figure 3.14: Mean vertical velocity profiles for $\lambda = 1.9$ and $\lambda = 1.4$ at $x/D = 1$ and $z/H = 0.25$.

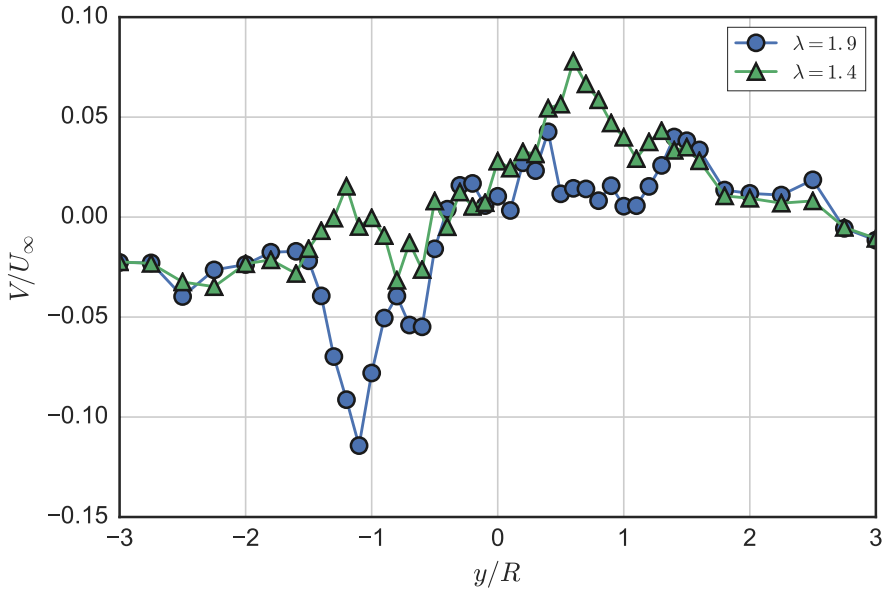

Figure 3.15: Mean cross-stream velocity profiles for $\lambda = 1.9$ and $\lambda = 1.4$ at $x/D = 1$ and $z/H = 0.25$.

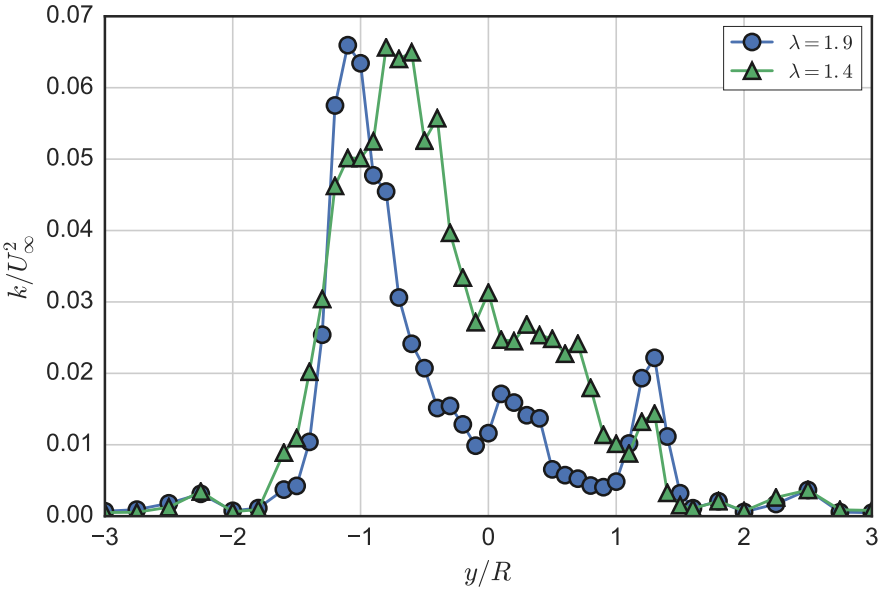

Figure 3.16: Turbulence kinetic energy for $\lambda = 1.9$ and $\lambda = 1.4$ at $x/D = 1$ and $z/H = 0.25$.

simulation. Since one of the potential benefits of cross-flow turbines is to be able to be spaced more closely in an array installation, the near-wake dynamics will be more important than those of an axial-flow turbine.

For axial-flow turbines, the actuator disk model can be enhanced with a rotating axial velocity component, which gives better results than a simple volume force [193], but to our knowledge this technique has not been applied (adapted) to cross-flow turbines. Nevertheless, in the present study the ability of a simple streamwise force distributed over a cylindrical volume to mimic the near-wake of a cross-flow turbine was evaluated. As described in previous sections, the asymmetry of the turbine's wake indicates that a uniform streamwise force from the actuator disk will likely not capture the wake accurately.

The open source CFD package OpenFOAM (v2.3.x) was used to solve the RANS equations with the turbine represented by an actuator disk, which was implemented as a force or sink in the momentum equation, parameterized by the power and drag (or thrust) coefficients, and applied over a selected volume of cells in the mesh.

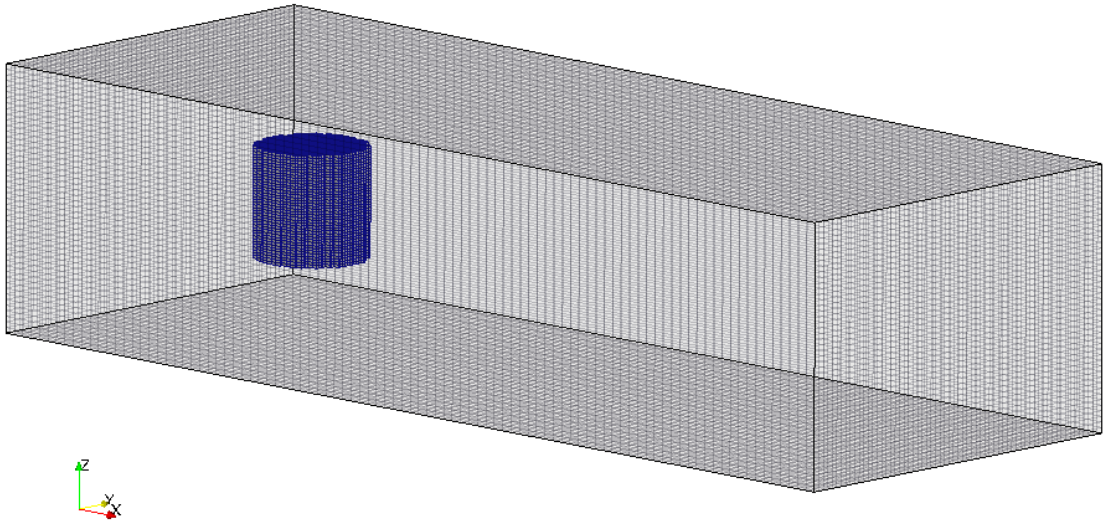

Figure 3.17: Snapshot of the computational mesh for the actuator disk RANS simulation. The cylindrical region indicates the cells in which the momentum source was added.

The cross-section of the domain was the same as that of the tow tank used for the experimental measurements. The actuator disk was technically not a disk, but a 1 m diameter by 1 m tall cylinder, mimicking the turbine swept area. The domain extended 2 m upstream and 8 m downstream. The background mesh consisted of 96, 64, and 48 points in the x, y, and z directions, respectively. The cells in the volume enclosed by the actuator disk region were refined by a factor of two, giving a total of approximately 3×10^5 hexahedral cells. A snapshot of the mesh is shown in Figure 3.17. Boundary conditions were set to approximate the tow tank environment, i.e., the velocity at the bottom and walls were set to the free stream value. The free surface was not modeled—the domain had a rigid lid with a slip velocity boundary condition—a reasonable approximation for low Froude numbers. Inputs to OpenFOAM's `actuationDiskSource` are given in Table 3.2, and the case files for this simulation are available from [25].

Cp	0.26
Ct	0.96
diskArea	1.0
upstreamPoint	(-1.0 0 0)

Table 3.2: Input parameters for the actuator surface using OpenFOAM's `actuationDiskSource`.

The turbulence is modeled with a standard k-ε closure, with relatively low levels of inlet turbulence kinetic energy and dissipation, 2×10^{-4} and 3×10^{-5}, respectively. These low free stream values were chosen to approximate the tow tank ambient conditions.

Results for the mean velocity field are presented in Figure 3.18, in a manner similar to that of Figure 3.3, for comparison. The vertical mean flow, which was determined to be an important driver of near-wake dynamics in the experiments, is absent. In fact, it contributes negatively to streamwise wake recovery. This means that all momentum and energy transport back into the deficit in the wake created by the turbine will need to be facilitated by turbulent transport (and viscous diffusion, to a much lesser degree). Note also how acceleration due to blockage is much lower compared to the experiments despite matching the overall drag coefficient.

Figure 3.19 shows the downstream evolution of the centerline streamwise velocity, and the terms that contribute to its streamwise derivative averaged over various constant-x planes. Note how very close to the turbine, the streamwise pressure gradient is contributing significantly to the increase in U, despite the fact that the turbine creates a positive pressure gradient along the centerline. The large pressure-driven increase in streamwise velocity makes sense considering the fact that the values are averaged over the entire cross-section of the domain, which includes a large area of flow acceleration around the turbine, where the streamwise pressure gradient is negative. Just after the turbine, $-\partial P/\partial x$ drops off very quickly and then acts to decrease streamwise momentum slightly as the static pressure recovers moving downstream.

We can see that the streamwise momentum recovers very slowly, only starting to recover around $x = 7D$, which can be mostly attributed to the low inflow turbulence levels, chosen to mimic the tow tank environment. This can be further understood by looking at the transport terms plotted on the

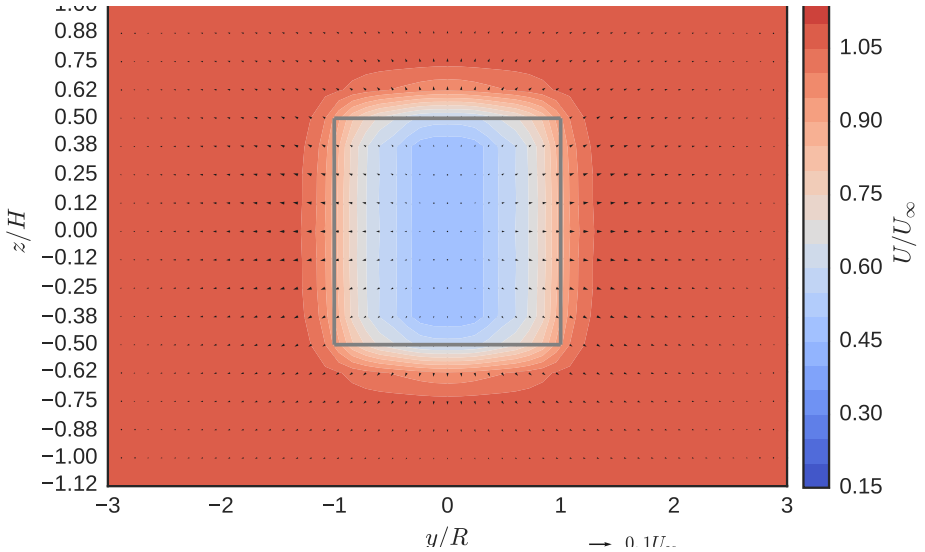

Figure 3.18: Mean velocity predictions at $x/D = 1$ from the RANS actuator disk numerical model. Vectors are cross-stream and vertical velocities; contours are streamwise velocity.

right in Figure 3.19, where we see all terms are quite small when compared with the experimental results from the turbine. Rather than the advection terms, which contribute negatively, the turbulent transport—here modeled using the k–ε eddy viscosity ν_t—is driving the streamwise evolution, despite being very small. One way to increase the wake recovery in such a model is to have the actuator disk "inject" turbulence quantities to increase the eddy viscosity [99, 142]. However, this will likely still not be sufficient to predict evolution and interaction in closely-spaced arrays of CFTs, since neither the significant vertical mean velocities in the CFT wake, nor any coherent vortical structures due to blade, shaft, or strut forces are captured by the actuator disk model.

It could be argued that the actuator disk model should not be judged this way as it is well known that it is a poor predictor of near-wake characteristics, however, these models are common in engineering practice when calculating performance of turbine arrays, as previously mentioned. The experiments reported here have shown that the use of these models would likely be a source of large uncertainty if applied to cross-flow turbine installations.

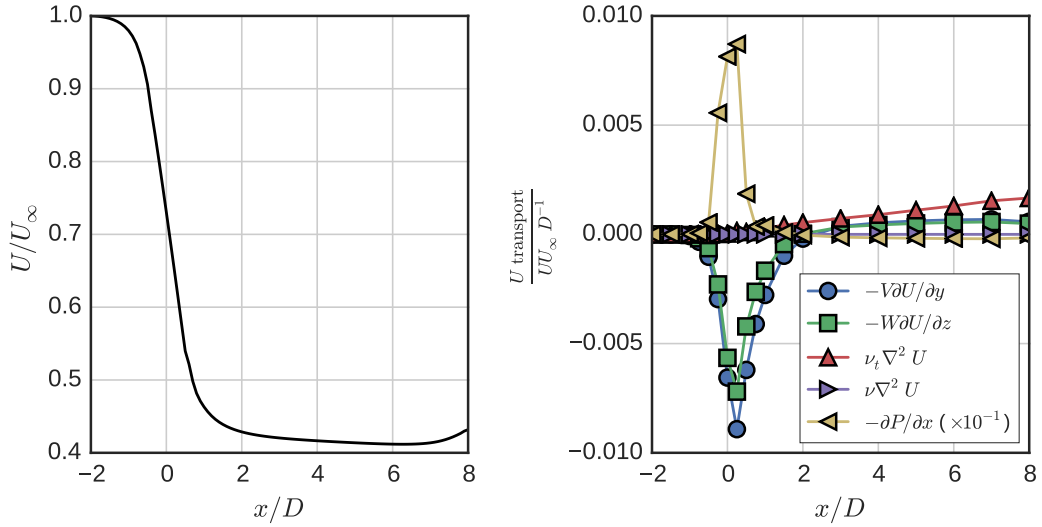

Figure 3.19: Downstream evolution of the centerline streamwise velocity (left) and normalized momentum transport terms (right) averaged over y–z slices from the actuator disk RANS simulation.

3.3 Conclusions

Detailed measurements were performed in the near-wake of a vertical axis cross-flow turbine operating at peak power coefficient. The following essential features were identified:

1. Asymmetry and three-dimensionality in the mean velocity field.

2. Mean streamwise swirling flow, or vorticity produced by blade tip and dynamic stall vortex shedding, which propels fluid towards the wake's center and makes mean vertical advection the largest contributor to streamwise momentum and mean kinetic energy recovery.

3. Asymmetric turbulence generation due to the effects of dynamic stall being more pronounced on one side of the turbine.

The most dominant timescale induced into the wake is the blade passage period. The $+y$ side of the turbine contains more coherent motion at this frequency, as stalling is less prevalent there. The reduced separation due to stall also leads to lower magnitudes of turbulence kinetic energy on the $+y$ side.

Regarding recovery of the mean streamwise momentum and kinetic energy, it was calculated from the wake velocity measurements that vertical advection is more than twice as large as transport by turbulent fluctuations, which may explain why CFT wakes entrain free stream kinetic energy more effectively than their AFT counterparts. The importance of the vertical flow created by the turbine showed that array flow simulations will need to be carried out in three dimensions to produce accurate results. Considering how high power coefficient estimates are in 2-D simulations [114], it logically follows that 3-D effects significantly decrease the power output of a single turbine, but this uncaptured power helps pull more power from outside the array. This also raises interesting questions with respect to how cross-flow turbine blades should be "terminated", i.e., reducing blade tip vortices by winglets or inhibiting them with end struts or end disks, as commonly done, may increase the performance of individual CFTs, however, free ends that produce tip vortices may be advantageous in an array setting to increase the wake recovery rate. Furthermore, it hints at the possibility of adding vortex generators to the nacelles of horizontal-axis or axial-flow turbines to help advect more mean kinetic energy downwards from above.

A commonly used, simple turbine forcing parameterization—an actuator disk—was assessed for predicting the near-wake characteristics of this turbine with a RANS simulation. The actuator disk model was found to be a poor representation of a CFT, despite its computational efficiency and use in research and industry. It is suggested that an actuator disk with a non-uniform force distribution or a collection of actuator lines [174, 164] may produce the asymmetry and unsteadiness that is characteristic of the CFT near-wake and will be necessary to predict performance of closely-spaced arrays that cross-flow turbines are thought to enable. The actuator line method is investigated later in Chapter 7.

CHAPTER 4

REYNOLDS NUMBER EFFECTS ON THE PERFORMANCE AND NEAR-WAKE OF A HIGH SOLIDITY CROSS-FLOW TURBINE

In this chapter, we investigate whether the results from Chapter 3 were obtained at a large enough scale to be considered relevant to full scale applications. Note that most of the content here has been reproduced or adapted from [31].

Scaled physical models are often used in science and engineering to approximate real-world systems. The principle of dynamic similarity allows for geometrically-scaled systems to be dynamically identical if certain nondimensional physical parameters are matched. In the case of fluid systems, the most important nondimensional parameter is often the Reynolds number, Re, which quantifies the importance of inertial forces over viscous forces on the flow physics [1]: $Re = Ul/\nu$, where U and l are characteristic velocity and length scales, respectively, and ν is the fluid kinematic viscosity. The other common dynamical scale, for systems with a free surface, is the Froude number $Fr = U/\sqrt{gl}$, where g is the gravitational acceleration. Matching both the Froude and Reynolds number is not possible for a scaled model in a given fluid, which is illustrated by the relation $Re = l^{3/2}g^{1/2}Fr/\nu$, since Re scales linearly with l, or the geometric scale. In general, the geometric scale of a physical model is not necessarily the same as its dynamical scale. As such, hereafter, we will use the word "scale" to refer to this dynamical scale or the Reynolds number and assume the Froude number is small enough to be negligible.

With regards to wind and marine hydrokinetic (MHK) turbines, scaled physical models are used to validate predictive numerical models, predict full-scale performance of individual turbines and design or investigate arrays of devices. Scaled models have the benefit of being significantly less expensive; however, a key question is whether or not an acceptable scale mismatch exists. Similarly, it is questionable whether numerical models validated with physical model data obtained

orders of magnitude away from prototype scale should be considered validated at all. An example of the errors that can result from the extrapolation of small-scale experiments can be found in [38].

The performance and wake characteristics of cross-flow (often vertical-axis) turbines (CFTs) depend on turbine solidity, blade profile (lift/drag, dynamic stall at reduced frequency of turbine rotation, symmetry, thickness, camber), blade pitch, number of blades, strut drag, operational parameters, such as tip speed ratio, and on the Reynolds number [148]. Note that an approximate average blade chord Reynolds number, $Re_{c,\text{avg}} = \lambda U_\infty c/\nu$—using geometric considerations, i.e., no induction—can be expressed in terms of tip speed ratio $\lambda = \omega R/U_\infty$, where U_∞ is the free stream velocity, c is the blade chord length, ν is the fluid kinematic viscosity, ω is the rotor's angular velocity, and R is the rotor radius. The value of λ at which a turbine reaches peak performance in general decreases with turbine solidity $Nc/(\pi D)$ [182], which roughly allows for the use of a simpler Reynolds number based on turbine diameter $Re_D = U_\infty D/\nu$, for comparing turbines with the same number of blades without knowing their operating tip speed ratios *a priori*.

Solidity often directly correlates with the chord-to-radius ratio c/R. Rotors with $c/R \geq 0.1$ are considered to have high solidity [79], for which so-called flow curvature or virtual camber effects become significant [137]. These effects arise from the blade sections' circular paths and can complicate the comparison with the behavior of an airfoil in a linear flow.

Blackwell et al. [45] investigated the effects of Reynolds number on the performance of a 2 m diameter Darrieus vertical-axis cross-flow wind turbine with NACA 0012 blades. By varying wind tunnel speed, the turbine was made to operate at an approximately constant blade chord Reynolds number Re_c ranging from 1×10^5 to 3×10^5. In this regime, the turbine power coefficient C_P was shown to be sensitive to Re_c, with sensitivity diminishing at the higher Reynolds numbers, especially for turbines of lower solidity (Nc/R, where N is the number of blades and R is the turbine's maximum radius). More recently, Polagye and Cavagnaro [152] observed significant Reynolds number sensitivity for a high solidity helical cross-flow turbine, and Bravo et al. [49] observed the power coefficient of a straight-bladed VAWT to become Reynolds number independent at $Re_c \approx 4 \times 10^5$. Bachant and Wosnik [26] observed Reynolds number independence of the

power coefficient at the optimal tip speed ratio for a high solidity cross-flow turbine at $Re_D \approx 10^6$ or $Re_{c,\text{avg}} \approx 2 \times 10^5$.

The wake of a 2-D cross-flow turbine in the dynamic stall regime has been studied via laser Doppler velocimetry by Brochier et al. [50] and in 3D with particle image velocimetry (PIV) by Fujisawa and Shibuya [83]. However, both of these studies were performed at very low Reynolds numbers: $Re_D = 10^4$ and 10^3, respectively. Tescione et al. [184] studied the wake of a vertical-axis wind turbine at its optimal tip speed ratio in a wind tunnel using stereo PIV at an approximate blade chord Reynolds number $Re_c = 1.7 \times 10^5$; very close to the *Re*-independence criteria reported in [26], though it was not confirmed if this was indeed a *Re*-independent state. The two lower *Re* experiments tended to focus on the effects of dynamic stall, whereas the higher *Re* experiment mostly concerned the mean velocity and tip vortex effects. Whereas the value of these studies was in elucidating the complex wake dynamics of cross-flow turbines, they also motivated the more systematic investigation of scale effects undertaken here.

Scale effects on axial-flow or horizontal-axis wind turbines are better understood, and investigators have methods for compensating. Krogstad and Adaramola [107] observed Reynolds number independence of the performance of a 0.9 m diameter axial-flow turbine rotor at $Re_D \approx 5 \times 10^5$ in wind tunnel tests. Their turbine blades had an S826 profile along their entire span, a profile chosen for its *Re*-independence. Walker et al. [190] similarly chose a NACA 63-618 foil for their axial-flow turbine tests in a towing tank, which were performed at a mid-span Reynolds number $Re_c = 4 \times 10^5$. McTavish et al. [131] showed how the near-wake expansion for an axial-flow rotor is increased at higher Reynolds numbers, concluding that physical models should be designed with *Re*-independence in mind if they are to be run at low *Re*. It is uncertain, however, if these methods work equally well for cross-flow turbines.

When designing or studying arrays, it is common to use very small (geometrically) scaled devices [58, 59]. It is therefore important to realize the limitations of evaluating both the power output of turbines and the wake recovery when the Reynolds number is very far from full scale. Sometimes, the models used are not turbines, but wake-generating objects, e.g., porous disks, that

are meant to replicate the wakes of real turbines [86]. In this case, it is of interest to determine at what Reynolds number one might be able to realistically study wake flows in an array and also to evaluate the effectiveness of a wake generator. In other words, a wake generator may do a fine job simulating a scaled turbine, but how well can it simulate a full-scale device? Note that for a porous disk, the Reynolds number of interest is based on diameter, since it is the scaling of the far-wake dynamics that matters.

Vertical-axis wind turbine array field experiments have revealed that improved wake recovery allows for closer spacing when compared to conventional axial-flow propeller-type turbines [66, 104]. In the last chapter, it was observed experimentally that a high solidity vertical-axis cross-flow turbine's near-wake produces a unique vertical mean velocity field, generated by blade tip vortex shedding, the advection by which is the largest contributor to streamwise momentum and energy transport or recovery [29]. In this study, we seek to replicate those same momentum and energy balance considerations at multiple Reynolds numbers, to examine the implications on how scaled, i.e., low Reynolds number experiments, may be used to study flows in turbine arrays.

4.1 Modes of Reynolds number dependence

It is of interest to examine how Reynolds number scaling affects both the blade loading, i.e., turbine performance, and the near-wake. Typically, static airfoil data show that the static stall angle increases with blade chord Reynolds number Re_c [98]. A review of Reynolds number effects on airfoil behavior is presented in [116]. In general, airfoil performance, often characterized by the profile's lift-to-drag ratio, is enhanced as the boundary layer on the foil transitions to turbulence closer to the leading edge, which enables it to advance further downstream against the adverse pressure gradient on the suction side, delaying separation to higher angles of attack. For smooth airfoils, this transition can cause a dramatic increase in foil performance at a blade chord Reynolds number on the order of 10^5 [130]. Note that there is a distinct lack of highly reliable data for airfoils in this transitional regime and below. An evaluation of the various databases relevant to cross-flow turbines is presented in [44].

Static foil performance does not tell the whole story for a cross-flow turbine. The azimuthal, and therefore, temporal, variation of α in a cross-flow turbine implies dynamic loading, encountering dynamic stall for tip speed ratios near and below those of maximum rotor torque [148]. Bousman [48] states that dynamic stall is relatively insensitive to Reynolds number for $Re = 1.0 \times 10^5$ to 2.5×10^5, judging from measurements on a pitching VR-7 foil in a wind and water tunnel, since the loading is dominated by vortex shedding. However, Singleton and Yeager Jr. [169] state that the effect of Reynolds number on dynamic stall remains an unsolved question.

Despite lower lift on the blades at lower Re, we expect stronger tip vortex shedding [194]. As mentioned previously, the dynamic stall vortex shedding is not expected to be highly sensitive to Reynolds number, though a larger separation bubble at lower Re may induce higher levels of turbulence as shed vortices become unstable and break down.

Chamorro et al. [57] showed that turbulence statistics in an horizontal-axis or axial-flow wind turbine wake became Re-independent at $Re_D \approx 1 \times 10^5$ and that mean velocity profiles became Re-independent slightly earlier at $Re_D \approx 5 \times 10^4$. Note that in this study, the tip chord Reynolds number was not reported, but is estimated to be $Re_c \approx 4 \times 10^4$ at $Re_D = 1 \times 10^5$. It is therefore our objective to observe similar scaling relationships for a cross-flow turbine near-wake.

4.2 Updates to experimental setup

After the baseline experiments performed in Chapter 3, the sodium hypochlorite solution in the tow tank induced mild corrosion on the UNH-RVAT rotor and test bed mounting frame's bare aluminum surfaces. To prevent subsequent surface roughening, the turbine and frame were cleaned, scoured, primed, and painted flat black. It should be noted that this did not appreciably change the baseline performance curve and wake characteristics, which were remeasured in this experiment.

4.3 Experimental test plan

Approximately 1500 tows were conducted for the study reported here; each tow was used for a single data point on either a performance curve or wake map. Each performance curve consisted

Tow Speed (m/s)	Re_D	$Re_{c,\text{ave}}$ ($\lambda = 1.9$)
0.3	0.3×10^6	0.8×10^5
0.4	0.4×10^6	1.1×10^5
0.5	0.5×10^6	1.3×10^5
0.6	0.6×10^6	1.6×10^5
0.7	0.7×10^6	1.9×10^5
0.8	0.8×10^6	2.1×10^5
0.9	0.9×10^6	2.4×10^5
1.0	1.0×10^6	2.7×10^5
1.1	1.1×10^6	2.9×10^5
1.2	1.2×10^6	3.2×10^5
1.3	1.3×10^6	3.4×10^5

Table 4.1: Turbine diameter and approximate blade chord Reynolds numbers for the tow speeds used in the experiment.

of 31 tows, where during each tow, the mean turbine tip speed ratio was held constant, ranging from 0.1 to 3.1 in 0.1 increments. Full performance curve data were acquired for tow speeds from 0.4 to 1.2 m/s in 0.2 m/s increments, for which the turbine diameter and approximate blade chord Reynolds number are presented in Table 4.1. Performance was also measured for $\lambda = 1.9$ at tow speeds $[0.3, 0.5, 0.7, 0.9, 1.1, 1.3]$ m/s for two tows each.

Each wake map was generated by positioning the ADV, which measured three components of velocity at a 200 Hz sampling frequency, at 270 different locations, varied in the cross-stream and vertical directions at one turbine diameter downstream ($x/D = 1$). These locations had vertical coordinates from the turbine centerline up to $z/H = 0.625$, ranging in the cross-stream direction $y/R = \pm 3$. These locations are shown in Figure 4.1.

4.3.1 Data processing

From each set of tows, a standard time interval was set, which allowed the turbine performance and wake to reach a quasi-periodic state. Each run was analyzed to compute statistics over this interval, truncating the end slightly to achieve an integer number of blade passages. Turbine shaft angular velocity and tow carriage speed were calculated using a second order central differencing

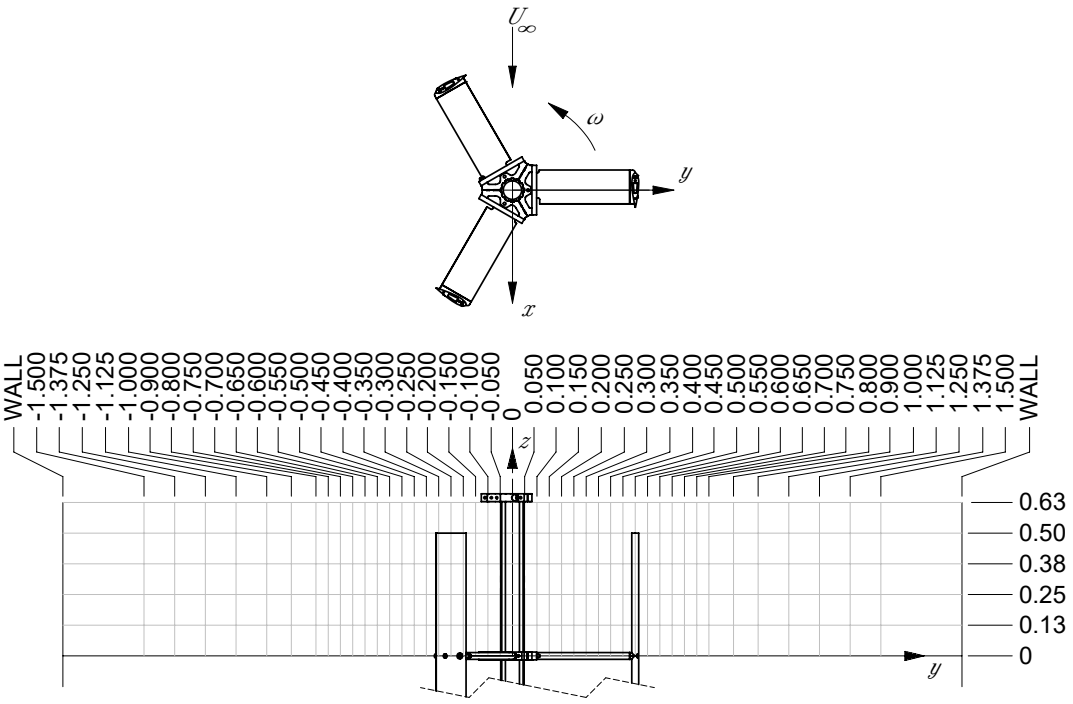

Figure 4.1: Wake measurement coordinate system and locations. Dimensions are in meters.

scheme on the respective position measurements. Power and drag coefficients were calculated as instantaneous quantities using the carriage speed as the free stream velocity.

Wake velocity data were filtered for spurious "spikes" by removing data points 8 standard deviations, or 0.9 m/s, from the mean. The experimental data and code for processing and visualization are available from [34].

4.3.2 Uncertainty

Uncertainties from systematic and random error were estimated and combined using the methods outlined in Appendix A. For the Reynolds number dependence of turbine performance, error bars are included on the plots. Expanded uncertainty estimates for mean wake velocities (averaged over all runs) are listed in Table 4.2.

U_∞ (m/s)	U (m/s)	V (m/s)	W (m/s)
0.4	1×10^{-2}	7×10^{-3}	6×10^{-3}
0.6	1×10^{-2}	8×10^{-3}	8×10^{-3}
0.8	2×10^{-2}	1×10^{-2}	1×10^{-2}
1.0	2×10^{-2}	1×10^{-2}	1×10^{-2}
1.2	2×10^{-2}	1×10^{-2}	1×10^{-2}

Table 4.2: Average expanded uncertainty estimates (with 95% confidence) for mean velocity measurements at each tow speed.

4.4 Results and discussion

4.4.1 Performance

Complete power and rotor drag (also known as thrust) coefficient curves for various Reynolds numbers are plotted in Figures 4.2 and 4.3, respectively. In general, maximum C_P increases with Reynolds number. The power coefficient curves also show a slight downward shift in the optimal tip speed ratio (peak performance) with increasing Reynolds number, from about $\lambda \approx 2.0$ to 1.9. This is caused by the stall delay from a more turbulent boundary layer on the blade suction side. There is essentially no change in the shape of the drag coefficient curves, merely a slight upward shift in C_D with increasing Re.

Mean power and drag coefficients at $\lambda = 1.9$ are plotted versus the Reynolds number in Figure 4.4. Note that the large error bars for C_P at low Re are dominated by systematic error estimates for the torque transducer, since torque values are at the lower end of its measurement range. However, the uncertainty due to random error or repeatability remains relatively low. There is a drastic improvement in C_P with increasing Reynolds number at the lower end of the Re range. The power coefficient then becomes essentially Re-independent at $Re_D = 0.8 \times 10^6$, which corresponds to an approximate average blade chord Reynolds number $Re_{c,\text{ave}} = 2.1 \times 10^5$. This threshold is consistent with the behavior of the blade boundary layer transitioning from laminar to turbulent, thereby promoting either the suppression or reattachment of the laminar separation bubble [116].

The behavior of the mean rotor drag coefficient C_D is similar, though the changes are less dramatic. This is likely due to cross-flow turbine geometry, where increases in blade drag at lower Re somewhat offset the reduction in lift, causing the total streamwise force to vary less than the

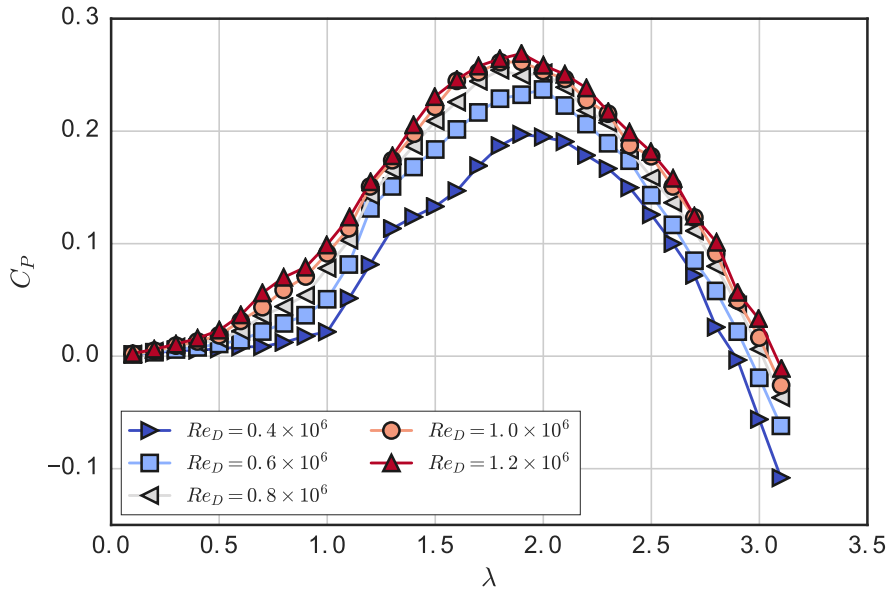

Figure 4.2: Mean power coefficient curves plotted for multiple Reynolds numbers.

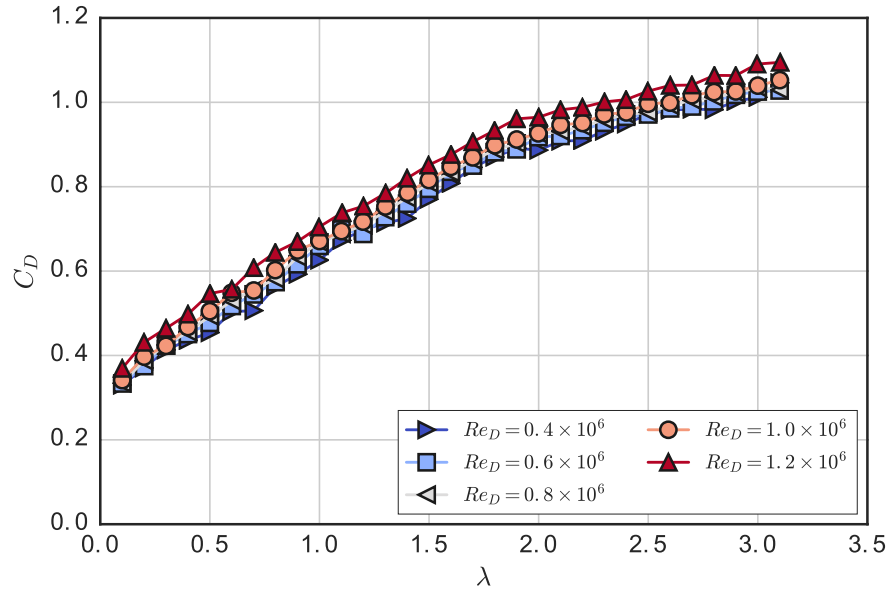

Figure 4.3: Mean rotor drag coefficient curves plotted for multiple Reynolds numbers.

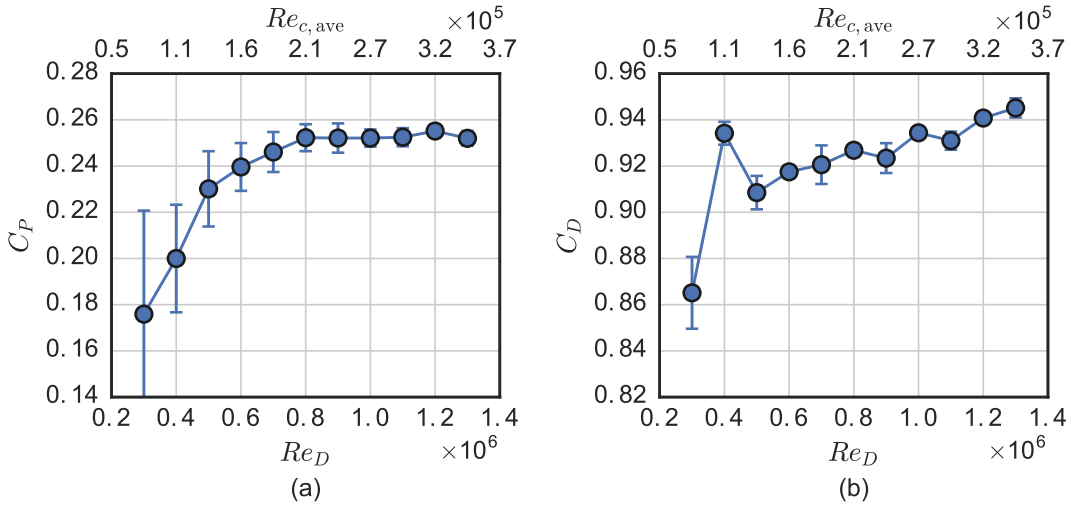

Figure 4.4: UNH-RVAT measured mean (a) power and (b) drag coefficients at $\lambda = 1.9$ plotted versus the Reynolds number. Error bars indicate expanded uncertainty estimates for 95% confidence, which for C_P is dominated by systematic error estimates from the torque transducer operating at the lower end of its measurement range.

rotor torque. The tendency for C_D to continue increasing with *Re* may also include the effects of an increasing Froude number (from faster tow speeds), which increases free surface deformation and wave drag during towing without increasing flow through the turbine.

4.4.1.1 Relation to static foil characteristics

To help understand, and possibly predict, the *Re*-sensitivity on turbine performance, a series of static foil coefficient datasets were computed with the viscous panel method code XFOIL [71], a commonly-used tool for airfoil analysis, e.g., [54, 190], implemented as part of the open source turbine design software QBlade [123]. Simulations were run for an angle of attack range of 0° to 40°, in increments of 0.5°. Solver parameters used were 100 panels, a fixed speed, zero Mach number, `NCrit=9` (default e^n transition criteria parameter for an average wind tunnel), and no forced boundary layer transition. Characteristics were computed for the approximate average blade chord Reynolds numbers encountered in the tow tank experiments.

To investigate the effects of the blades' "virtual camber" due to their circular path [137], the XFOIL calculations were performed for 20% thick foils with 0% (NACA 0020), 2% (NACA 2520),

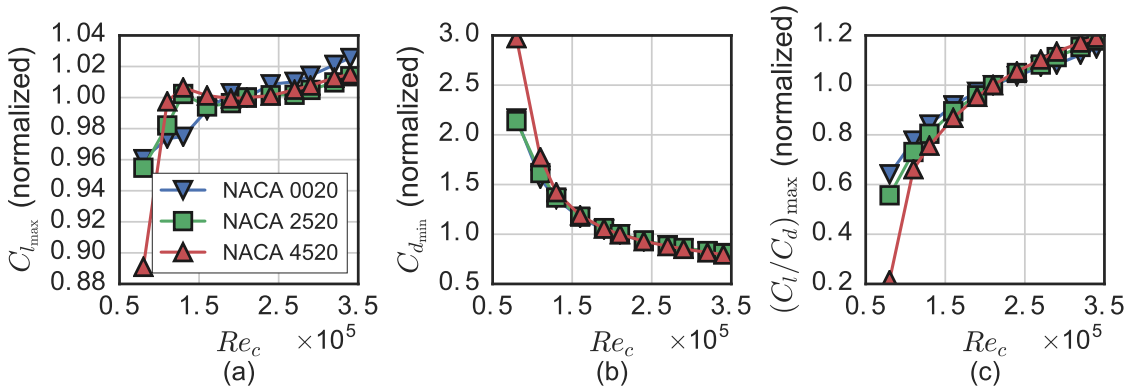

Figure 4.5: Normalized maximum (a) lift coefficient, (b) drag coefficient, and (c) lift-to-drag ratio computed by XFOIL at various Re_c for each profile.

and 4% (NACA 4520) camber about their half-chord location. A 4% camber approximates the maximum distance between the blade chord line and path for the UNH-RVAT, and the 2% camber takes into account the reduction in virtual flow curvature from the non-curved inflow velocity by dividing by the tip speed ratio $\lambda = 1.9$.

Results from the XFOIL calculations for the airfoil profiles are shown in Figure 4.5, where values of the maximum lift coefficient $C_{l_{\max}}$, minimum drag coefficient $C_{d_{\min}}$, and maximum lift-to-drag ratio are normalized (to visualize relative differences in scaling between the foils) and plotted versus Re_c. In general, larger camber is associated with decreased foil performance at lower Reynolds number. The data and processing code for these calculations is available from [33].

In conjunction with the cross-flow turbine blade kinematics, the foil coefficients were used to approximate turbine performance by calculating the peak torque coefficient on the upstream half of the blade path. The turbine torque coefficient C_T can be related to the blade section chordwise force coefficient C_c by:

$$C_T = \frac{C_c c}{2R} \frac{|U_{\text{rel}}|^2}{U_\infty^2}, \tag{4.1}$$

where the blade section chordwise force coefficient (for zero preset pitch) is given by:

$$C_c = C_l \sin\alpha - C_d \cos\alpha. \tag{4.2}$$

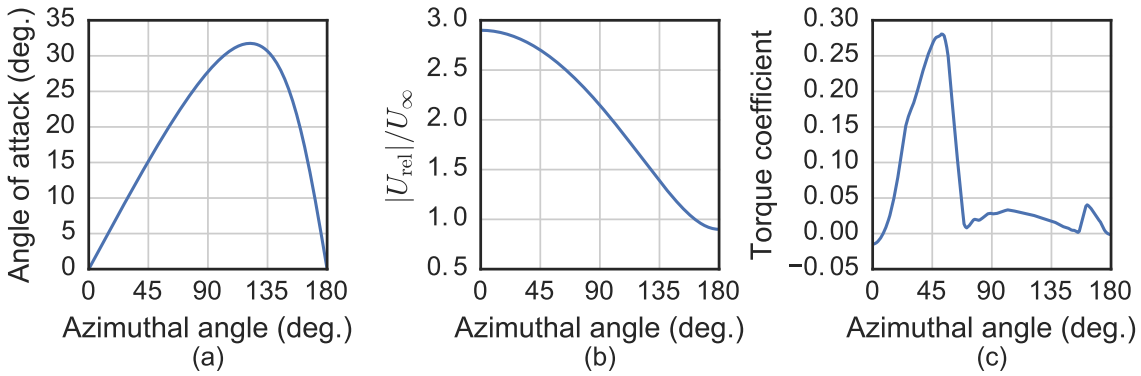

Figure 4.6: Geometric (a) angle of attack, (b) relative velocity , and (c) torque coefficient calculated with a NACA 0020 foil operating at $\lambda = 1.9$.

The relative blade velocity U_{rel} was calculated by vector addition of the free stream velocity and the opposite of the blade tangential velocity. Note that this neglects any induction, i.e., slowing of the free stream by the turbine forces, which would be present in reality or any numerical model, e.g., a momentum/streamtube model. Since the goal of this approach was not to predict absolute performance, but rather to gain insight into relative changes with *Re*, this method was deemed acceptable, as it is extremely simple and fast to compute.

Values for the blade angle of attack, relative velocity, and torque coefficient are plotted in Figure 4.6 for the upstream half of rotation of the turbine. The effects of static stall are clearly present in the torque coefficient plot, and by the time the angle of attack has decreased below the static stall angle, the relative velocity is so low that there is not much contribution to the torque coefficient.

Results for the normalized peak torque coefficient for each foil are plotted versus Re_c in Figure 4.7. It is interesting that the convergence of $C_{T_{\text{max}}}$ with increasing Reynolds number is more dramatic than any of the common foil performance characteristics plotted in Figure 4.5, meaning that the cross-flow turbine's unique kinematics must be taken into account when attempting to predict the effect of transitional Reynolds numbers on turbine performance.

From the peak torque coefficient metric plotted in Figure 4.7, the Reynolds number independence is achieved at lower values and more dramatically. We see that the trend of the (non-

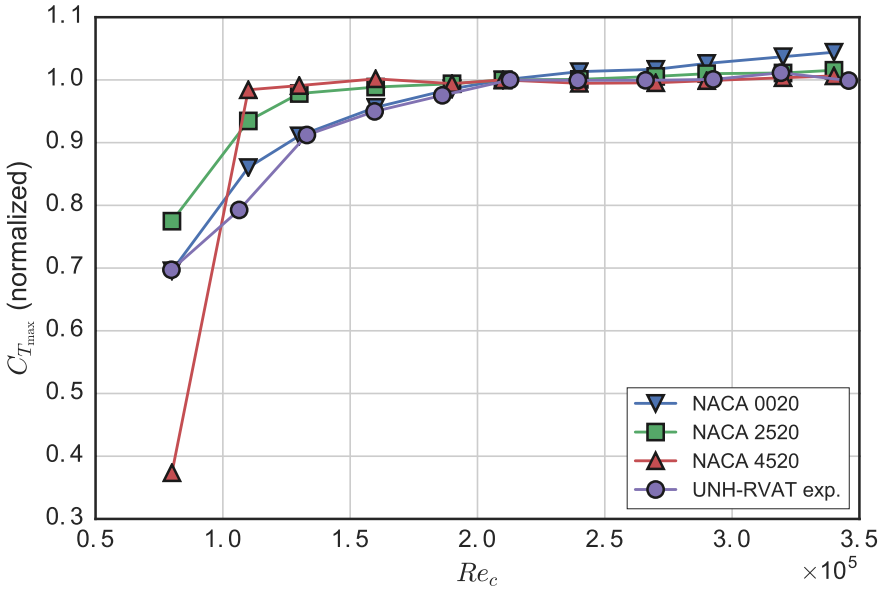

Figure 4.7: Reynolds number dependence of the normalized peak torque coefficient calculated from static foil coefficients and blade kinematics, compared to experimental data from a cross-flow turbine. Note that the experimental data represents the mean torque coefficient, not the maximum.

cambered) NACA 0020 curve matches almost perfectly up to $Re_c \approx 2.1 \times 10^5$, but then continues to increase slowly and linearly with Re. This is not matched by the experimental data, which at higher Re looks more like the cambered foil results. Though this method does not provide absolute predictions of turbine performance, it predicts the transitional Reynolds number regime for cross-flow turbine performance using only 2D static airfoil characteristics, i.e., the Reynolds number scaling of the peak C_T computed this way behaves much like that of the measured turbine performance.

4.4.2 Wake characteristics

The near-wake of this turbine at $x/D = 1$, $\lambda = 1.9$, along with momentum and kinetic energy balances at a $Re_D = 1.0 \times 10^6$ were discussed in [29]. Similar data were taken for the experiment here, and the results for the mean velocity field and turbulence kinetic energy calculated from wake maps of 270 individual measurements (tows) are shown in Figures 4.8 and 4.9, respectively, looking upstream towards the turbine. With respect to the mean velocity field, we see asymmetry

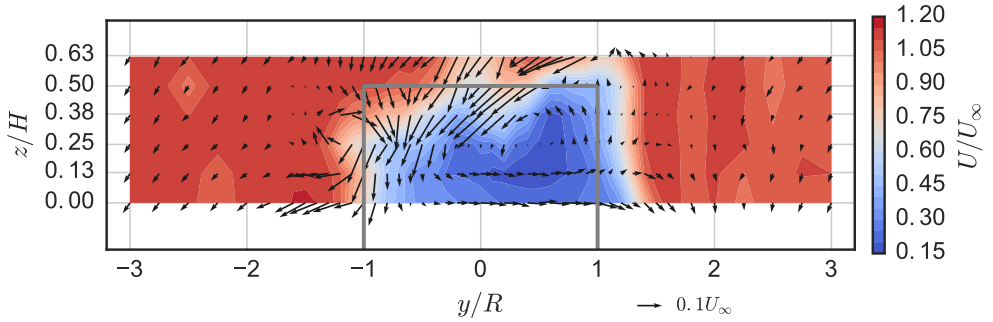

Figure 4.8: Mean velocity field at $x/D = 1$, $\lambda = 1.9$, and $Re_D = 1.0 \times 10^6$.

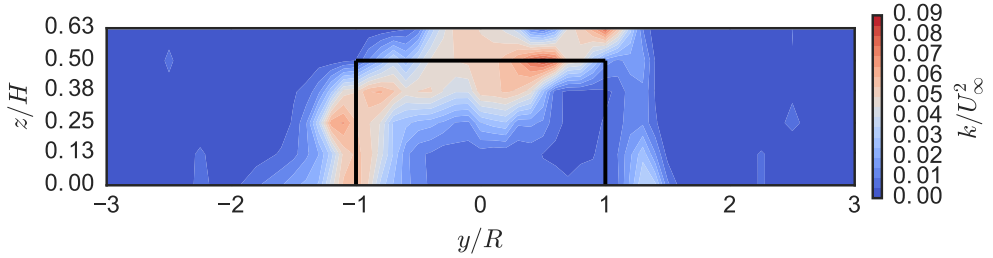

Figure 4.9: Turbulence kinetic energy at $x/D = 1$, $\lambda = 1.9$, and $Re_D = 1.0 \times 10^6$.

and a mean vortex structure created by blade tip vortex shedding. The effects of the tip vortices are also seen in the turbulence kinetic energy measurements, along with turbulence generated by the blades undergoing dynamic stall on the $-y$ side of the turbine.

These same wake maps were measured for $Re_D = 0.4 \times 10^6$, 0.6×10^6, 0.8×10^6, and 1.2×10^6. Qualitatively, these look very similar, so they have not been plotted here, though profiles at $z/H = 0.0$ are compared in Figure 4.10 to illustrate the subtlety of the differences at different Re. We will instead compare and contrast the wake behavior by examining spectra and wake transport terms in the equations that govern the downstream evolution of mean momentum and kinetic energy.

4.4.2.1 Dominant timescales and turbulence spectra

Spectra of the cross-stream velocity normalized by the free stream were computed using a fast Fourier transform-based method, applying a Hanning window and averaging over four adjacent frequency bands to decrease confidence intervals. These spectra are plotted in Figure 4.11 for

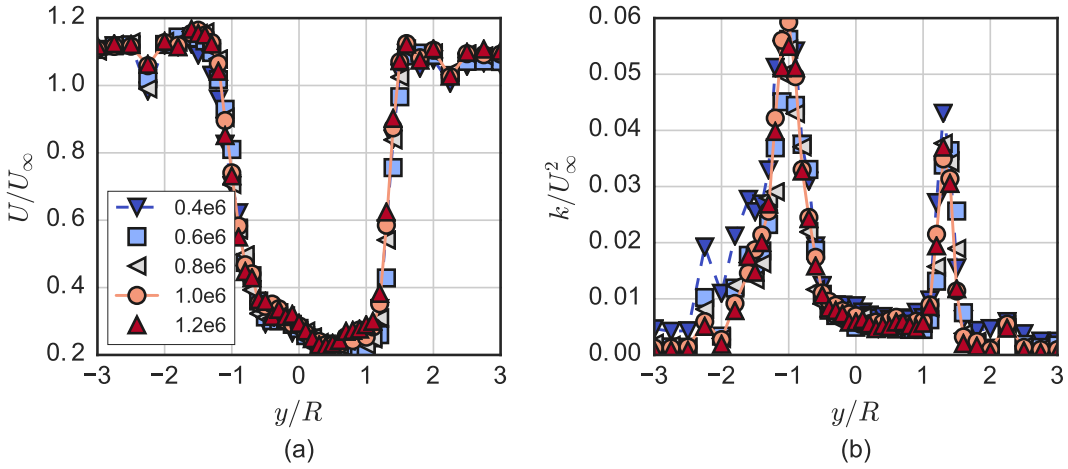

Figure 4.10: Mean streamwise velocity (a) and turbulence kinetic energy (b) profiles at $z/H = 0.0$. Turbine diameter Reynolds number Re_D is indicated by the legend.

regions on either side of the turbine. On the $-y$ side of the turbine, there is broadband turbulence produced by blade stall, and on the $+y$ side, there is a clear peak in the spectra caused by the blade passage. We see that on both sides, there is higher spectral energy at lower Reynolds numbers. On the $+y$ side of the turbine, we notice higher spectral energy at the blade passage frequency's first harmonic, or $6f_{\text{turbine}}$. This is likely due to the blade's shed vorticity being less stable at higher Re.

4.4.2.2 Transport of mean momentum and kinetic energy

Similar to the baseline analysis performed in Chapter 3, the relative importance of various physical processes on mean streamwise momentum and kinetic energy transport/recovery in the streamwise direction were assessed at each Reynolds numbers. The governing equations were rearranged to isolate the streamwise partial derivative ($\partial/\partial x$) for the quantities of interest [29], i.e., streamwise momentum and mean kinetic energy.

Results from the terms that can be computed from the experimental data i.e., excluding $\partial/\partial x$) from the right-hand sides of Equations (3.1) and (3.3) are plotted in Figures 4.12 and 4.13, respectively. Derivatives were computed using a second order finite difference scheme, with central differencing for interior points and inward facing schemes for the boundaries. A weighted average for each term was then calculated based on the grid spacing. We note that similar to [29], the

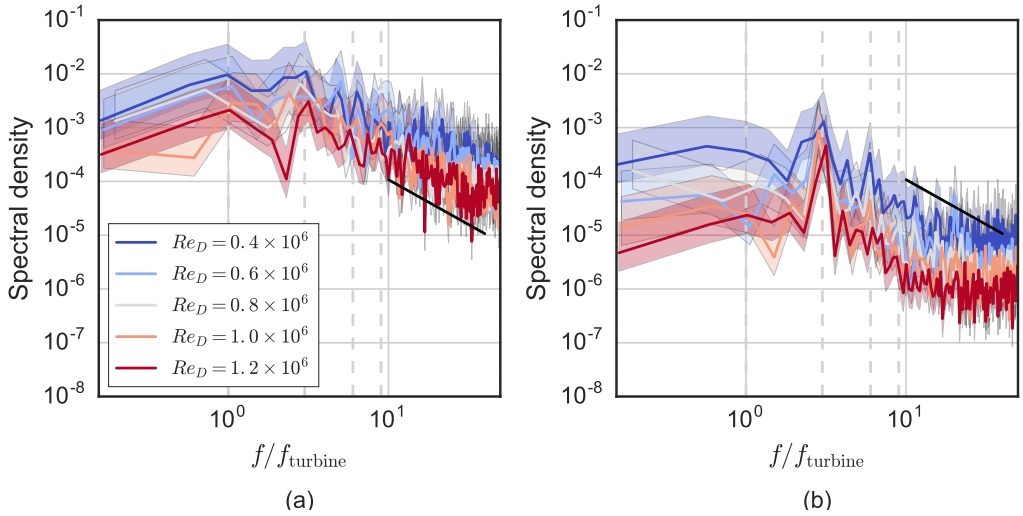

Figure 4.11: Cross-stream velocity (normalized by U_∞) spectra at $z/H = 0.25$, $y/R = -1.0$ (-0.5 m in Figure 4.1) (a) and $y/R = 1.5$ ($+0.75$ m in Figure 4.1) (b). Dashed vertical lines indicate $[1,3,6,9]$ times the turbine rotational frequency. Shaded regions indicate 95% confidence intervals assuming a χ^2 distribution.

vertical advection at this point in the wake is the dominant contributor to positive wake recovery, caused by the unique vortex pattern created by the blade tips and blade wakes.

We see that in general, levels of turbulent transport are slightly lower at larger Reynolds numbers. The viscous diffusion and dissipation, though still three orders of magnitude smaller than the other terms, do increase at low Reynolds numbers, which is consistent with the physical meaning of the Reynolds number itself. From these results, one might expect that the viscous effects will become significant to the wake dynamics as the Reynolds number is decreased below $Re_D \sim 10^4$.

Transport due to cross-stream advection appears to become more negative at higher Re. This could be a consequence of increasing free surface deformation (higher Fr), which then decreases the effective flow cross-sectional area downstream of the turbine, forcing more flow to accelerate around the sides of the turbine. Note that we also observe slightly higher drag coefficients at higher Re (potentially for the same reason), which also helps explain larger negative values of cross-stream advection.

The totals for all of the wake transport terms calculated in Figures 4.12 and 4.13 are plotted in Figure 4.14. We see that in general, the wake transport of both mean streamwise momentum and

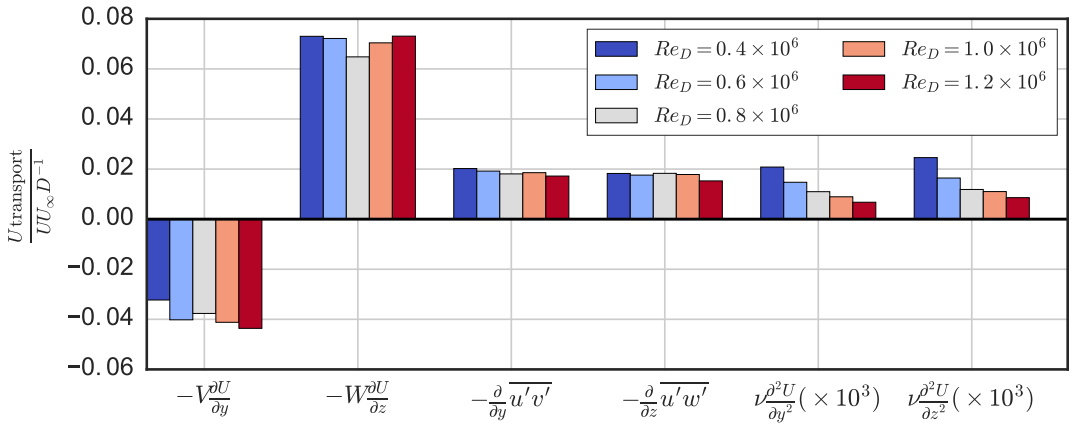

Figure 4.12: Normalized streamwise momentum transport quantities computed as weighted averages from Equation 3.1.

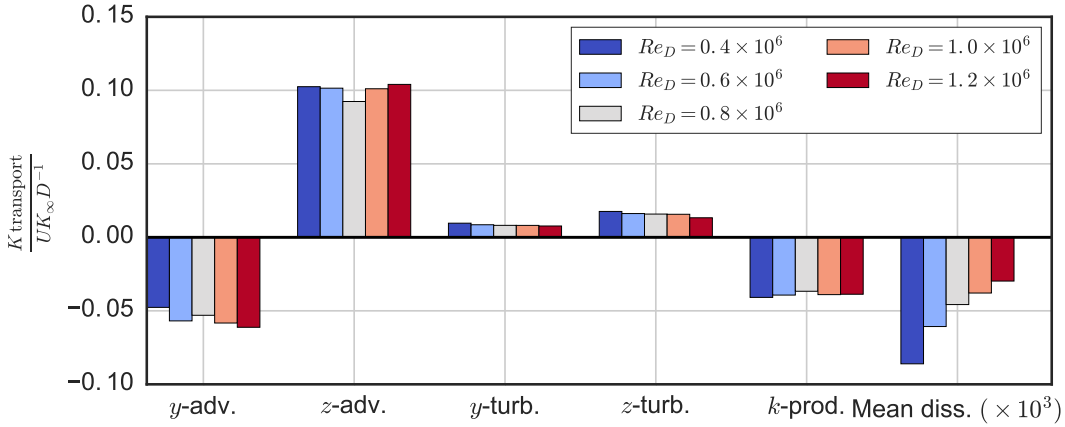

Figure 4.13: Normalized mean kinetic energy transport quantities computed as weighted averages based on Equation (3.3), omitting the non-measured streamwise derivatives. Note that directions of the turbulent transport terms refer to the directions of their partial derivatives.

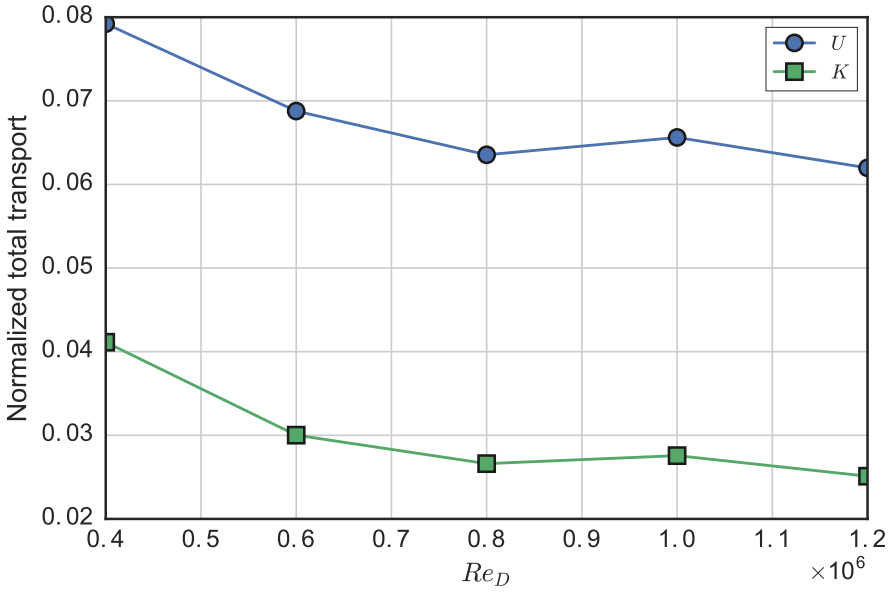

Figure 4.14: Normalized transport totals from Figures 4.12 (streamwise momentum, U) and 4.13 (mean kinetic energy, K) plotted versus the Reynolds number.

kinetic energy is enhanced at lower Reynolds numbers and levels off consistent with the behavior of the turbine power coefficient. This is an important consideration if studying sub-scale models of turbine arrays, where increased levels of wake recovery could motivate different ideal array configurations when compared to full-scale turbines if the scale model Reynolds number is too low.

4.5 Conclusions

In this study, it was demonstrated that the performance of a high solidity ($c/R = 0.28$) cross-flow turbine becomes essentially *Re*-independent at a Reynolds number based on the turbine diameter $Re_D \approx 10^6$ or an approximate Reynolds number based on the blade chord $Re_c \approx 2 \times 10^5$. The power coefficient values on the left-hand side of the C_P-λ curve are reduced more than those on the right-hand side at low *Re* due to deeper stalling. The *Re*-independent threshold corresponds to that at which the foil suction surface boundary layer becomes turbulent before having to recover static pressure against the adverse pressure gradient, highlighted in [116, 130, 53].

We propose a method for predicting the Reynolds number dependence of a cross-flow turbine using static airfoil characteristics and turbine blade kinematics:

1. Acquire static lift and drag coefficient data for the desired blade profile.

2. For azimuthal angles of 0 to 180 degrees and a given tip speed ratio, calculate the geometric angle of attack and relative velocity magnitude from the blade and undisturbed free stream velocity (taken as unity) vectors.

3. With arrays of geometric angle of attack and relative velocity magnitude, calculate the blade chordwise force and then the rotor torque coefficient from Equations (4.1) and (4.2), respectively.

4. Extract the maximum value of C_T, and repeat this process for static foil data at multiple Re.

It was shown that the peak torque coefficient computed this way shows similar Reynolds number sensitivity as the experimental results for an actual turbine, making it a better predictor than conventional quantifications of airfoil performance, e.g., the lift-to-drag ratio. Note that this method is not restricted to standard symmetrical NACA foils, though those evaluated here with higher camber were more sensitive at lower Re, but had smaller slopes in the linear regime.

In the near-wake of the turbine, we observed lower levels of turbulence with increasing Reynolds number, along with lower levels of turbulent transport with respect to mean streamwise momentum and mean kinetic energy recovery in the streamwise direction. Vertical advection, the largest transport mechanism measured, showed little Re-dependence, whereas the negative effects of cross-stream advection were enhanced at high Re, which may be due to larger free surface deformation effectively reducing the near-wake's cross-sectional area. Despite being orders of magnitude smaller than other transport processes, viscous diffusion increased rapidly with decreasing Re and is expected to become significant to the wake dynamics around $Re_D \sim 10^4$. Overall, the total wake transport measured leveled off at essentially the same Reynolds number that the performance did: $Re_D \approx 0.8 \times 10^6$.

From these results, we recommend that physical model tests of cross-flow turbines be performed at $Re_D \sim 10^6$ or greater to provide reasonable predictions of full-scale performance. This threshold also applies to the validation of predictive engineering models, especially for high-fidelity CFD models where the boundary layer is to be resolved, since transition to turbulence plays an important role in overall blade loading. Note that in our case, blockage, though reasonably low, may be increasing flow through the turbine compared to a free case, which could mean *Re* thresholds for free flows could be slightly higher, though a reliable blockage correction algorithm has not yet been agreed upon for CFTs [55].

If using scaled physical models to predict array performance, where turbine power output is measured, it may also be important to keep all turbines in the regime where the power coefficient varies linearly to avoid exaggerated power deficiencies for downstream turbines, despite similarities in wake characteristics. Results here also suggest that low Reynolds number physical model studies of turbine arrays may see exaggerated levels of wake recovery, leading to inadequate or inappropriate spacing or layouts.

Ultimately, these results show that our baseline data was indeed taken at sufficient Reynolds number. This will allow us to use the data for numerical model validation, and also to conceptualize models for predicting large scale array performance.

CHAPTER 5

EXPERIMENTAL CHARACTERIZATION OF THE DOE/SNL REFERENCE MODEL 2 CROSS-FLOW TURBINE

In the study described in this chapter, a DOE/SNL Reference Model 2 cross-flow MHK turbine was designed and built to 1:6 scale, then its performance, Reynolds number dependence, and near-wake characteristics were measured using the turbine test bed. Note most of the content here has been taken from [37].

The Reference Model Project (RMP), sponsored by the US Department of Energy (DOE), produced six marine hydrokinetic (MHK) technology point designs as reference models (RMs) to serve as non-proprietary test articles for open research development, and to benchmark performance and costs for technology developers [141, 140]. Open-source RMP products, along with supporting documentation, are available at the RMP website `http://energy.sandia.gov/rmp` to facilitate their use in future R&D studies by industry, academia, and national laboratories. These products include: Technical specifications and computer-aided design (CAD) files for each RM device to allow exact replication for physical and numerical modeling studies; resource site information used to design each RM device; and references to physical modeling data sets that can be used to validate numerical modeling design and analysis tools.

Reference Model 2 (RM2) is a dual-rotor, vertical-axis cross-flow hydrokinetic (river) turbine that was designed to operate in a reach of the lower Mississippi River near Baton Rouge, Louisiana [40, 139]. The rotor has three tapered blades and a relatively low solidity $Nc/(\pi D)$ or chord-to-radius ratio $c/R \approx 0.1$. A preliminary analysis with Sandia's CACTUS vortex line numerical model [138] predicted an individual rotor's full-scale performance coefficient to be $C_P = 0.47$ at 1 m/s flow speed and a tip speed ratio $\lambda = \frac{\omega R}{U_\infty} = 3.15$ [40], where ω and R are the rotor's angular velocity and radius, respectively. Note that the RM2 rotor solidity would be considered moderate to high for

a wind turbine, whose c/R values typically range from 0.05 to 0.09, but MHK rotors are typically higher solidity since they must withstand approximately an order of magnitude higher torque in typical flows, necessitating relatively larger blades to meet strength and fatigue life requirements.

An initial experimental measurement campaign with a 1:15 scale RM2 rotor conducted at the Saint Anthony Falls Laboratory (SAFL) at the University of Minnesota resulted in maximum power coefficient of approximately 5% at $\lambda = 2.2$ [95]. This discrepancy between numerical and physical model performance prompted the experimental measurements presented here, namely due to the low Reynolds number—$Re_D = U_\infty D/\nu$, where U_∞ is the free stream velocity, D is the rotor diameter, and ν is the fluid kinematic viscosity—of the 1:15 scale tests, which were performed at $Re_D \sim 10^5$.

The effect of Reynolds number on average power output was shown to be significant on the 2 m Sandia Research Darrieus turbine in wind tunnel testing [45]: The maximum power coefficient, $C_{P_{\max}}$, increased with Reynolds number, $Re_c = \lambda U_\infty c/\nu$ (based on blade chord rather than diameter, though these are approximately proportional since optimal tip speed ratio correlates inversely with solidity and therefore chord length), along with a shift of the location of $C_{P_{\max}}$ toward lower tip speed ratios due to delayed blade stall. The effects of Reynolds number were quite dramatic over a relatively small range of $Re_c \approx 1.1 \times 10^5$–$2.9 \times 10^5$. More recently, Bachant and Wosnik [26, 34] showed that performance and near-wake characteristics of a high solidity cross-flow turbine become Reynolds number independent at $Re_D \approx 10^6$ or $Re_c \approx 2 \times 10^5$.

As part of the engineering process it is generally less expensive to assess designs via numerical rather than physical models. However, it is important—especially when dealing with fluid dynamics where the "exact" physics cannot be resolved with even the most advanced computers—that numerical models be validated against experimental data. It is uncertain whether numerical models validated with physical model data obtained at low Reynolds numbers should be considered validated at all, since the scale at which the model will be applied for real world design problems is orders of magnitude larger. One way to overcome this uncertainty is to show that the scaled

physical model test has become Reynolds number independent, so validation efforts are relevant at full-scale, which was the strategy employed here.

The main objective of the present study was to acquire a new experimental dataset for the RM2 turbine at sufficiently high Reynolds numbers to be relevant to full-scale physical and numerical modeling. It was hypothesized that the parasitic losses from rotor blade support struts could play an important role in overall turbine performance, especially for a lower solidity turbine that operates at higher tip speed ratios. Thus, the parasitic torque from strut drag was measured without blades, then deliberately and significantly increased in the physical model to provide data to investigate its importance. The velocity field in the near-wake of the turbine was then measured to compare with measurements from a higher solidity rotor in the same experimental setup [29], and to provide validation data for numerical models that predict wake flows, which determine turbine–turbine interaction and optimal spacing for turbine arrays. This dataset, along with the code for processing and visualization, has been made publicly available (licensed via Creative Commons CC-BY for data and MIT license for code) as a Git repository on GitHub (`https://github.com/UNH-CORE/RM2-tow-tank`) and as a citable archive with a digital object identifier (DOI) [36].

5.1 Survey of validation data and usage

To provide perspective on where this investigation fits amongst past studies, including those in previous chapters, a selection of measured performance data in the literature and its usage in numerical model validation is presented in Table 5.1. Turbine diameter Reynolds numbers spanned from small laboratory scale ($Re_D \sim 10^5$) all the way to full scale ($Re_D \sim 10^7$). Individual blade forces were only measured in two of the experiments—Strickland et al. [178] and Laneville and Vitecoq [111]. There has been nearly equal attention given to the eggbeater-shaped Darrieus rotor and the straight-bladed H-rotor. The performance of a large scale H-rotor with tapered blades, the VAWT 850 [127], has also been measured.

In general, there have been more experiments done with low c/R rotors. These rotors are easier to model, since unsteady dynamic effects are less influential on the overall performance [178]. This

Name	Rotor type	N_b	c/R	Re_D	Used in
Sandia 2 m [45]	Darrieus	2–3	0.06–0.09	$\sim 10^6$	[158, 44]
Sandia 5 m [166]	Darrieus	3	0.08	$\sim 10^6$	[8, 44]
Sandia 17 m [192]	Darrieus	2	0.06	$\sim 10^7$	[147, 146, 44]
Sandia 34 m [11]	Darrieus	2	0.05	$\sim 10^7$	[117, 138, 44]
Strickland et al. [178]	H	1–3	0.15	$\sim 10^5$	[153, 161]
Laneville and Vitecoq [111]	H	2	0.13	$\sim 10^6$	[6]
Howell et al. [96]	H	2–3	0.33	$\sim 10^5$	[103]
Mertens [135]	H	2	0.21	$\sim 10^5$	[146]
VAWT 850 [127]	Tapered H	2	0.05	$\sim 10^7$	[138]
UNH-RVAT [27]	H	3	0.28	$\sim 10^6$	[136]
RM2 (present)	Tapered H	3	0.07–0.12	$\sim 10^6$	

Table 5.1: Selected measured performance data and its usage for numerical model validation. Note that individual blade forces were measured in the Strickland et al. and Laneville and Vitecoq experiments.

is apparent when examining the effectiveness of numerical models that rely on static foil coefficient input data, e.g., streamtube and vortex models, which are most applicable for $c/R \leq 0.1$. For example, Bedon et al. [44] used a double multiple streamtube momentum model without dynamic stall corrections to evaluate the effectiveness of various foil coefficient databases against the Sandia Darrieus turbine experimental data. Despite using such a simple model, performance predictions were quite accurate in most conditions except at low tip speed ratio for the 2 m turbine, which had the highest c/R of all the Sandia rotors, making the dynamic effects more important. This highlights the need for more validation data for higher solidity rotors to ensure numerical models are robust enough to explore unique cross-flow turbine designs, especially as the MHK concepts mature.

The UNH-RVAT, for which the performance, near-wake, and Reynolds number dependence of was investigated using the same experimental setup as the study here [29, 31], was an H-rotor of 1 m height and 1 m diameter. The UNH-RVAT experimental datasets are also openly available [27, 34], and provide an interesting comparison for the near-wake dynamics of a rotor similar in size to the 1:6 scale RM2, but with non-tapered blades and a high solidity $c/R = 0.28$.

	Full-scale	Model (1:6)
Diameter (m)	6.450	1.075
Height (m)	4.840	0.8067
Blade root chord (m)	0.4000	0.06667
Blade tip chord (m)	0.2400	0.04000
Blade profile	NACA 0021	NACA 0021
Blade mount	1/2 chord	1/2 chord
Blade pitch (deg.)	0.0	0.0
Strut profile	NACA 0021	NACA 0021
Strut chord (m)	0.3600	0.06000
Shaft diameter (m)	0.2540 [42] or 0.4160 [95]	0.06350

Table 5.2: RM2 turbine geometric parameters for full and 1:6 scale models.

5.2 Test bed external regeneration resistor modification

During the UNH-RVAT Reynolds number dependence experiment described in Chapter 4, it was noted that the turbine test bed's Kollmorgen AKD servo drive was nearly reaching its 200 W internal power dissipation limit for the higher speed tows. Since the RM2 was expected to produce more power, before this experiment an Kollmorgen BAR1000-15 external regeneration resistor was added to the system to bring the power dissipation capacity up to 1 kW, ensuring this would not be a limiting factor for testing the RM2 at higher tow speeds.

5.3 Turbine model details

Geometric parameters for the 1:6 scale RM2 rotor were taken from the RM2 design report [40], with the exception of the shaft diameter, which was scaled from the SAFL RM2 model [95]. Values for both the 1:6 and full-scale designs are presented in Table 5.2 and a drawing and photo of the turbine is shown in Figure 2.8. The rotor components—blades, struts, shaft, and center hub sections—were fabricated from 6061-T6 aluminum, which was hardcoat anodized per MIL-8625-A, type III, class 2 specifications. CAD models and manufacturing drawings for the turbine are available from [35]. Note that after fabrication the turbine parts were inspected both by the manufacturer and in-house to ensure parts were within the design tolerances, the results from which are available in the experimental repository [36].

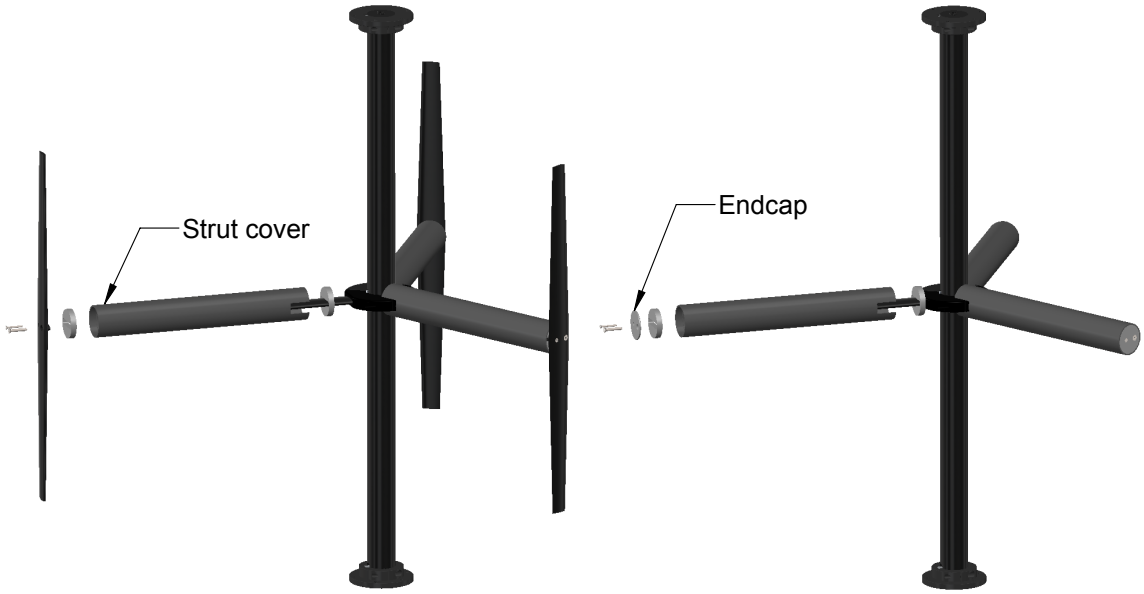

Figure 5.1: A drawing of the high drag strut cover configuration with and without blades.

The rotor was 1.075 m in diameter and 0.8067 m tall, presenting a 10% blockage in the tow tank cross-section based on frontal area. The blade chord lengths taper from 0.067 m at the roots, or half-span, to 0.04 m at the tips, varying the chord-to-radius ratio c/R from 0.12 to 0.07 (0.1 average). The rotor was therefore approximately at the threshold between high and low solidity [178, 79], which presents a unique validation case not yet seen in the literature. The RM2 is conceptually similar to the VAWT 850 [127] which also had tapered blades, but the RM2 has a moderately high c/R to more accurately represent typical MHK rotors, which presents a challenge for numerical modeling.

For investigating the effects of support strut drag losses, a set of cylindrical covers were designed to slip over the struts, which provided a deliberate and significant increase in strut drag. Endcaps were also fabricated to allow the high drag strut cover configuration to be operated without blades. A drawing of the strut covers is shown in Figure 5.1.

Tow speed (m/s)	Re_D	$Re_{c_{\text{tip}}}$	$Re_{c_{\text{root}}}$	$Re_{c_{\text{mid}}}$
0.4	4.3×10^5	5.0×10^4	8.3×10^4	6.6×10^4
0.6	6.5×10^5	7.4×10^4	1.2×10^5	9.9×10^4
0.8	8.6×10^5	9.9×10^4	1.7×10^5	1.3×10^5
1.0	1.1×10^6	1.2×10^5	2.1×10^5	1.7×10^5
1.2	1.3×10^6	1.5×10^5	2.5×10^5	2.0×10^5

Table 5.3: Turbine diameter and approximate average blade chord Reynolds numbers $Re_c = \lambda U_\infty c/\nu$ at blade tip, root, and mid-span, corresponding to various tow speeds at $\lambda = 3.1$.

5.4 Test parameters

Like the experiments described in Chapter 3 and Chapter 4, data collection runs were separated into individual tows, for which all independent variables—tow speed, tip speed ratio, velocity probe position—were held constant. These runs were grouped into logical test matrix "sections," in which typically a single independent variable was varied. Test matrix section names and descriptions are provided in the `README.md` file of the experimental data and code repository [36]. Tow speed and their corresponding turbine diameter and blade chord Reynolds numbers are presented in Table 5.3.

Wake measurements were all performed at 1 m downstream, which corresponds to $x/D = 0.93$. The cross-stream and vertical coordinates are shown in Figure 5.2. Altogether 750 tows were performed and included in the experimental database.

5.5 Data processing

For each tow speed, a relevant quasi-steady duration was selected by manually inspecting a plot of the C_P time series. This interval was then truncated to include a whole number of blade passages. Relevant statistics were then calculated over this duration.

To calculate turbine RPM from shaft angle, the encoder signal was differentiated using a second order central difference scheme, after which an 8 sample wide moving average smoothing filter was applied to match the noise level present in the redundant turbine RPM measurement from the motion controller. A similar approach was used for calculating tow carriage speed U_∞ from

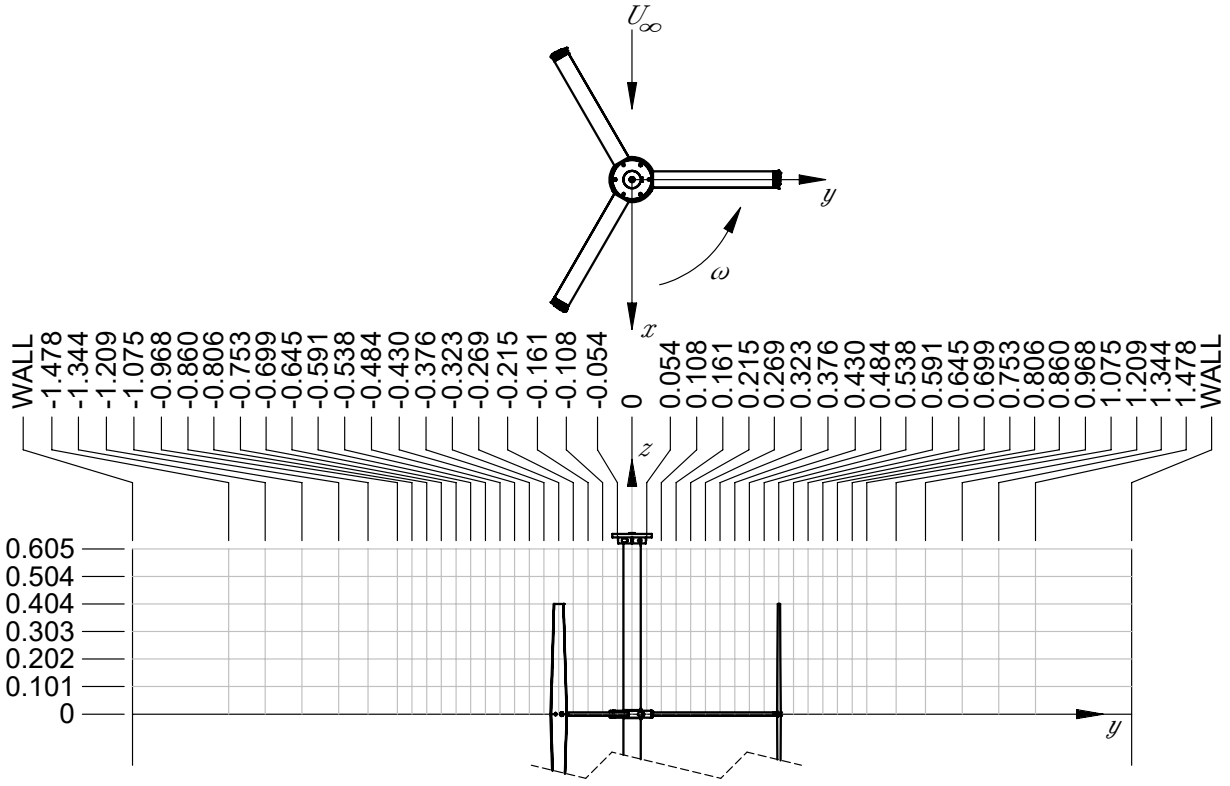

Figure 5.2: RM2 wake measurement coordinate system and cross-stream/vertical coordinates. All dimensions are in meters.

carriage position measurements. Power and drag coefficients were calculated as instantaneous quantities from the carriage speed as

$$C_P = \frac{T\omega}{\frac{1}{2}\rho A U_\infty^3} \tag{5.1}$$

and

$$C_D = \frac{F_{\text{drag}}}{\frac{1}{2}\rho A U_\infty^2}, \tag{5.2}$$

where ρ is the fluid density (assumed to be a nominal 1000 kg/m^3) and A is the turbine frontal area DH.

5.6 Results and discussion

5.6.1 Performance

Mean rotor power coefficients for multiple Reynolds numbers are plotted versus tip speed ratio in Figure 5.3. In general, C_P increases with Re, along with a reduction in the optimal tip speed ratio, due to the tendency of foils to stall at higher angles of attack at higher Re, and the higher angle of attack ranges seen by the blades at lower λ. These effects diminish with increasing Re, which is expected as the blade boundary layers transition to turbulence closer to the leading edge [116, 130, 34], which helps flow remain attached longer as it moves against the adverse pressure gradient on the suction side of the foil. For the experiment reported here, a maximum power coefficient $C_P = 0.37$ was reached at $Re_D = 1.3 \times 10^6$. Note how at lower tip speed ratios and Reynolds numbers, C_P becomes significantly negative, which was possible thanks to the speed control of the experimental setup's servo motor applying negative torque to the rotor.

Mean rotor drag coefficients are plotted versus tip speed ratio in Figure 5.4. These C_D curves show little difference compared to the power coefficient curves, which is most noticeable at low λ and low Re. The relative similarity could be attributed to the effects of stall, where the lift-to-drag ratio on the blades may drop, decreasing rotor torque, though the total resultant force due to high blade drag retains a similar component in the streamwise direction. When operating at maximum power coefficient, $\lambda_0 = 3.1$, and $Re_D = 1.3 \times 10^6$, a rotor drag coefficient $C_D = 0.84$ was measured.

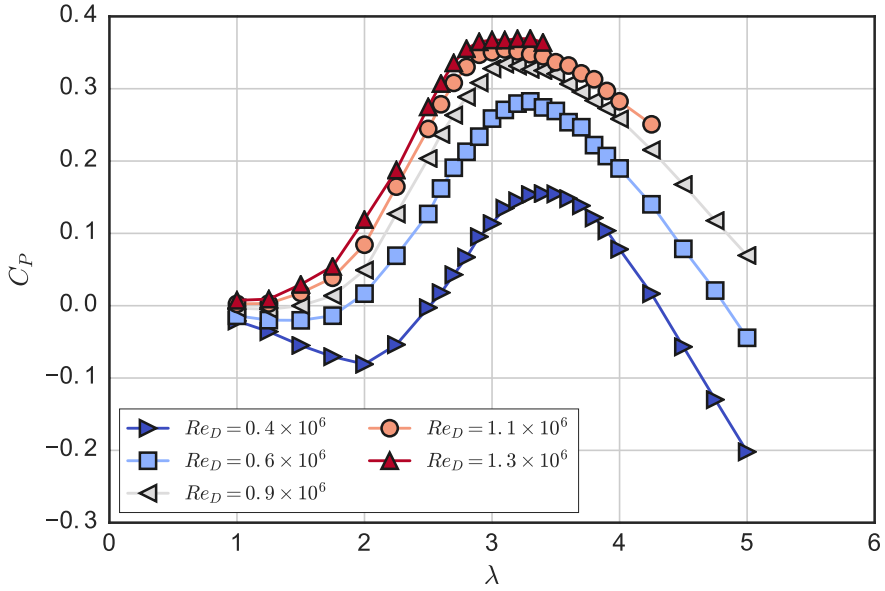

Figure 5.3: Mean rotor power coefficient plotted versus mean tip speed ratio for multiple Reynolds numbers.

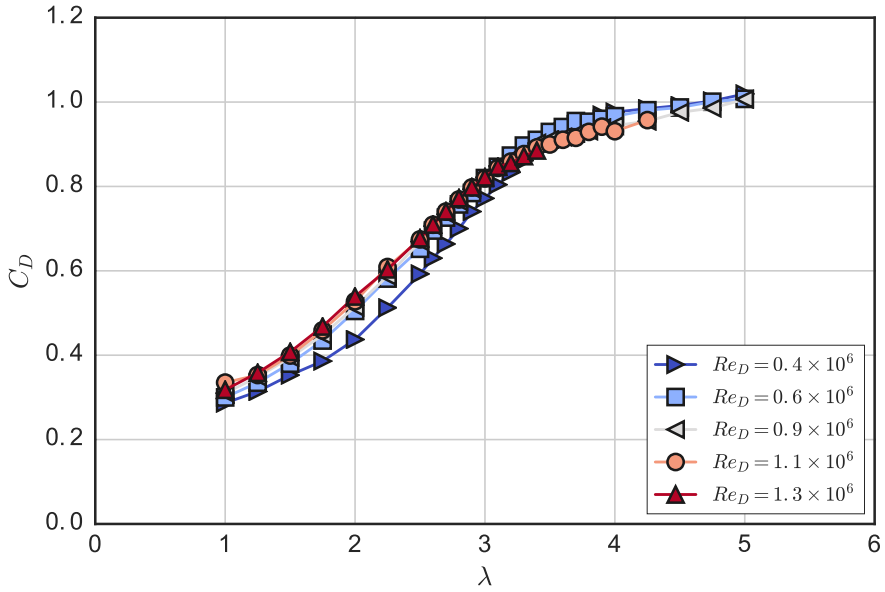

Figure 5.4: Mean rotor drag coefficient plotted versus mean tip speed ratio for multiple Reynolds numbers.

The power coefficient curves do not collapse exactly onto each other, indicating Reynolds number dependence, though the differences become relatively small as Re is increased. Note that the data collection was limited at higher Re and λ due to the unsteady turbine force resonating with the tow carriage drive belt. However, in contrast to the power coefficient data, the rotor drag coefficient curves nearly collapse onto each other for $Re_D \geq 0.6 \times 10^6$.

The effects of Reynolds number on the power and drag coefficients at $\lambda = 3.1$ are shown in Figure 5.5. The rotor drag coefficient C_D became more or less Reynolds number independent for $Re_D \geq 0.6 \times 10^6$. The power coefficient of the turbine increased dramatically below $Re_D = 1 \times 10^6$ or $Re_c = \lambda U_\infty c/\nu \approx 2 \times 10^5$, beyond which there appears to be a small, linear, positive trend. At the lowest Reynolds number, mean power coefficient even dropped below zero, which is consistent with the low performance of the 1:15 scale RM2 physical model study [95]. However, the blades of the 1:15 scale RM2 were mounted at approximately 58% of the chord from the leading edge, versus 50% for the present model, which helps explain the 1:15 scale model's positive power output at $\lambda = 2.2$ and $Re_D \sim 10^5$, since moving the blade mount point further back is equivalent to a "toe-out" preset pitch condition [79].

The tendency of C_P to continue increasing slightly could be an effect of flow curvature—caused by the finite c/R—which imparts a "virtual camber" [137], or can be thought of as producing a "lead" in angle of attack since cambered airfoils have non-zero lift at zero angle of attack [88]. The residual weak Re-dependence of the RM2 compared to the Re-independence of the higher c/R UNH-RVAT could be due to this virtual camber effect, since camber has been shown to cause earlier Re-convergence of the CFT's geometric torque coefficient when calculated from static foil coefficients given by a viscous panel method, whereas characteristics like lift-to-drag ratio do not converge as strongly [34].

5.6.2 Strut drag losses

Performance curves for the rotor with both NACA 0021 and cylindrical struts are shown in Figure 5.6. As expected, the high drag cylindrical struts reduce performance dramatically, producing an entirely negative C_P curve. The detrimental effects of the strut drag were more pronounced

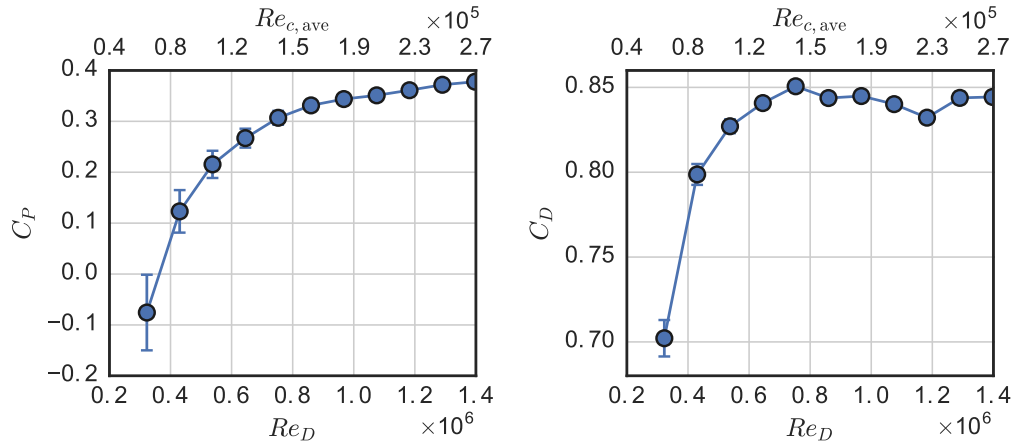

Figure 5.5: Power and drag coefficient at $\lambda = 3.1$ plotted versus turbine diameter and approximate average blade root chord Reynolds number.

at higher λ. This is in accordance with the measurements of Rawlings [156], though the strut losses in this case were larger due to the very high drag circular profile. In contrast to the dramatic effect strut drag had on C_P, overall rotor drag measurements were relatively similar for both the cylindrical and NACA 0021 strut cases.

Measurements for the power coefficient contributions of the strut drag losses are presented in Figure 5.7 for NACA 0021 and cylindrical struts—both in towed and stationary conditions. These are computed in the same fashion as the curves in Figure 5.3, but with the rotor blades removed. We see that strut drag losses increase with tip speed ratio to the power 2–3, which makes streamlined struts much more important for low solidity turbines, given the inverse correlation between solidity and λ_0 [182].

Strut drag losses did not change much for the streamlined NACA 0021 struts in the towed versus stationary configuration, which helps explain why overall rotor drag coefficients remained of comparable magnitude even at low Reynolds number, where C_P was dramatically reduced, or even negative. For the cylindrical struts, losses increased significantly when towed and operating in the mid range of tip speed ratios.

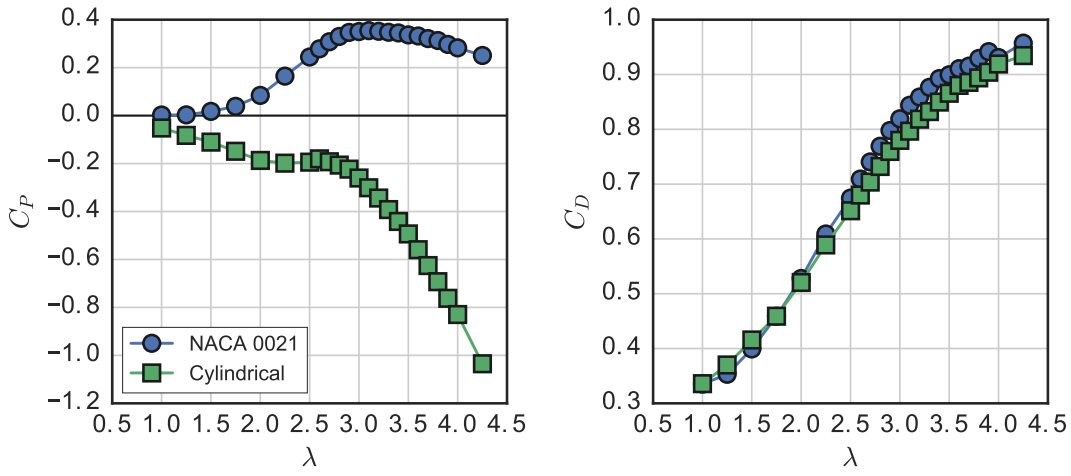

Figure 5.6: Turbine performance and rotor drag coefficient curves with both NACA 0021 and cylindrical struts.

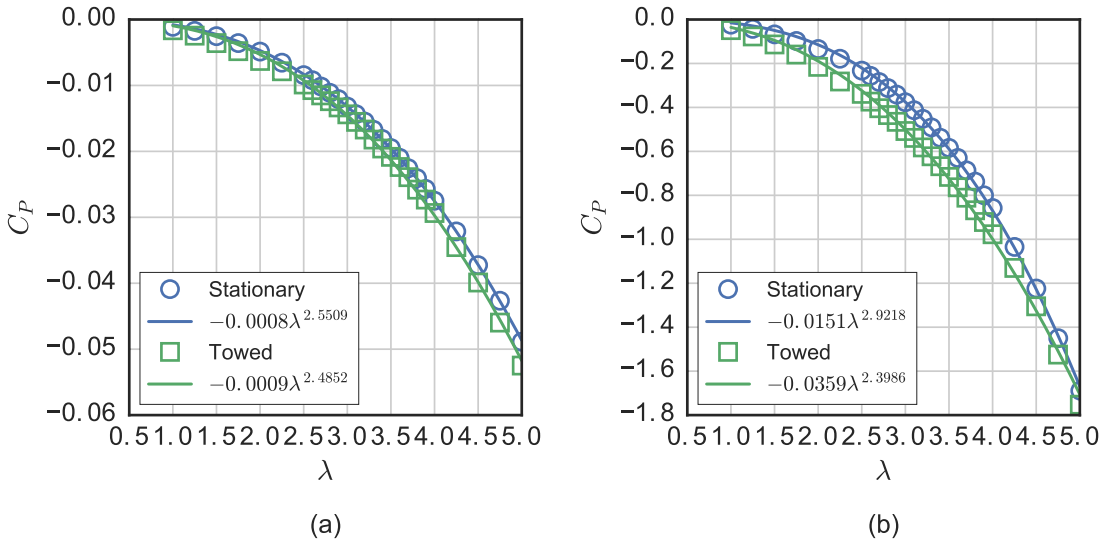

Figure 5.7: Measurements of the strut drag losses for (a) NACA 0021 and (b) cylindrical struts, both stationary and towed.

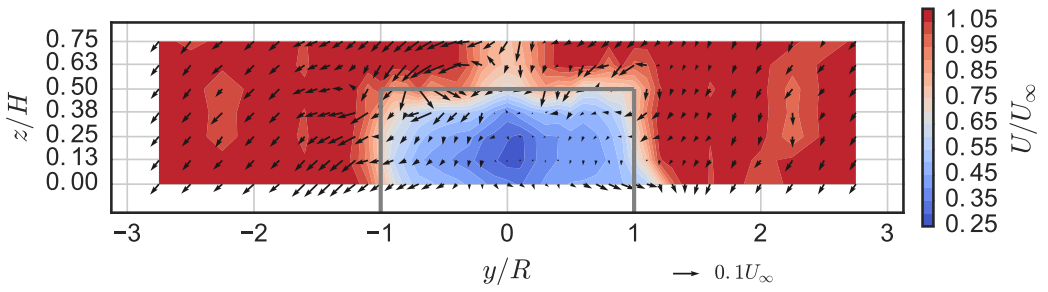

Figure 5.8: RM2 near-wake mean velocity field (looking upstream) at 1 m downstream ($x/D = 0.93$), $U_\infty = 1.0$ m/s, and $\lambda = 3.1$. Refer to Figure 5.2 for turbine axis orientation. Solid dark gray lines indicate turbine frontal area.

Though a real turbine would never use such high drag struts, with respect to numerical modeling, these measurements provide some interesting validation cases. Modelers can isolate and evaluate the ability to predict these losses independent of the blade loading by modeling combinations of the rotor with the high/low drag struts and with/without blades.

5.6.3 Near-wake characteristics

The mean velocity field at the chosen optimal tip speed ratio $\lambda_0 = 3.1$, 1 m downstream ($x/D = 0.93$) from the rotor axis is plotted in Figure 5.8. The mean streamwise velocity deficit is markedly more symmetric than that of the higher solidity UNH-RVAT, shown in Figure 3.3, with the RM2 inducing lower acceleration around the turbine due to the lower rotor drag coefficient and a slightly lower blockage ratio [29]. Tip vortex shedding is relatively weaker, which is likely an effect of the RM2's smaller blade chord length and tapered blades.

Figure 5.9 shows the turbulence kinetic energy in the turbine wake. We mainly see unsteadiness in the flow generated by the blade tip vortex shedding (the horizontal band around $z/H = 0.5$). Compared with the UNH-RVAT, shown in Figure 3.9, turbulence generation is lower overall, without the intense vertical band around $y/R = -1$, which indicates that the RM2 blades are operating further from stall—consistent with its higher optimal tip speed ratio.

As described in Chapter 3, analysis of the near-wake of the higher solidity UNH-RVAT turbine revealed that vertical advection was the largest contributor to streamwise recovery [29], a trait

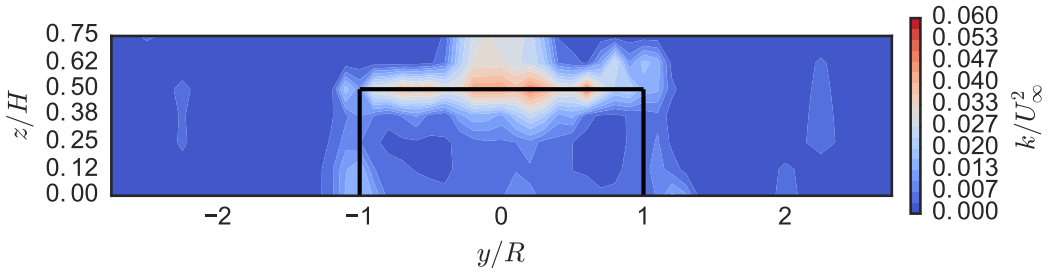

Figure 5.9: Turbulence kinetic energy in the RM2's near-wake (looking upstream) at 1 m downstream ($x/D = 0.93$), $U_\infty = 1.0$ m/s, and $\lambda = 3.1$. Solid black lines indicate turbine frontal area.

which is considered an advantage of cross-flow over axial-flow rotors in arrays [104]. A similar analysis was undertaken for the RM2 using Equation 3.3, the transport equation for mean kinetic energy, rearranged to isolate the streamwise partial derivative.

Terms that were able to be calculated from the experimental data are those that do not involve x-derivatives, since all wake measurement locations were at a fixed downstream distance. The available terms are the cross-stream advection (y-adv.), vertical advection (z-adv.), transport due to turbulent fluctuations (y-turb. and z-turb., separated by the direction of the derivative), production of turbulence kinetic energy (k-prod.), and the dissipation due to the mean velocity gradient (Mean diss.).

Derivatives were computed with a second order central difference scheme for interior points, and a second order inward-facing scheme for the edges, following the methodology in [29]. Weighted averages for these calculations are shown in Figure 5.10. Due to the weaker blade vortex shedding, transport due to vertical advection at this point in the wake was approximately 3 times lower than the higher solidity UNH-RVAT. Note that direct comparison is somewhat invalid, since the total measurement plane area was about 5% lower for this experiment. However, the differences observed are larger than the area ratio between the two experiments. We also see relatively lower levels of cross-stream turbulent transport due to the lack of blade stall vortex shedding. These results may have interesting implications regarding the application of turbines with lower power coefficient to possibly improve overall array performance through enhanced transport of kinetic

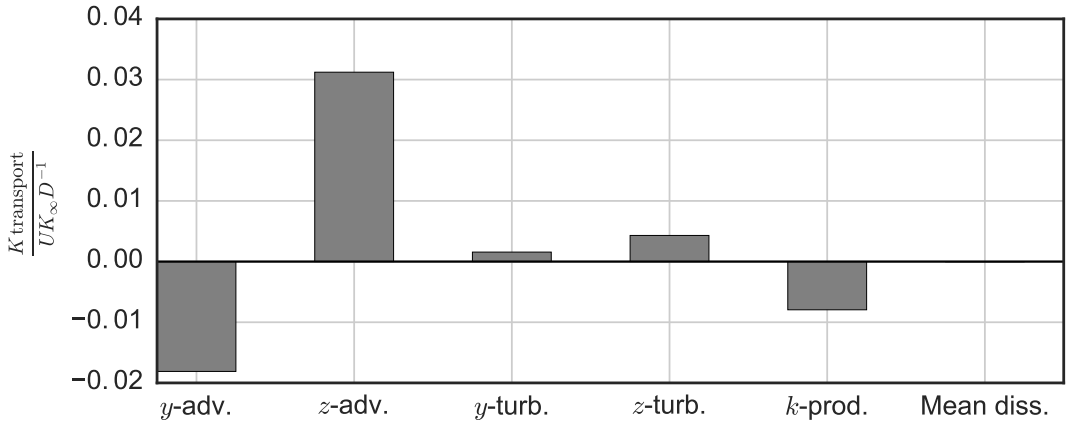

Figure 5.10: Weighted average estimates for terms contributing to streamwise recovery of mean kinetic energy, multiplied by two due to implied symmetry.

energy from the free stream, though evaluating these trade-offs will require a detailed analysis of the downstream evolution and turbine–wake interaction.

5.7 Conclusions

The performance and near-wake velocity of a 1:6 scale DOE Reference Model 2 cross-flow turbine were measured in a towing tank. A maximum power coefficient $C_P = 0.37$ and rotor drag coefficient $C_D = 0.84$ were observed at an optimal tip speed ratio $\lambda_0 = 3.1$.

Performance was assessed for Reynolds number dependence, showing a convergence to a weakly *Re*-dependent linear regime at approximately $Re_D \approx 1 \times 10^6$ or $Re_{c,\text{ave}} \approx 2 \times 10^5$. Comparison was made between this turbine and the higher solidity UNH-RVAT, tested in nearly identical conditions, which showed similar Reynolds number thresholds but a flatter linear regime, likely to due virtual camber of the higher chord-to-radius ratio of the UNH-RVAT blades. Nevertheless, these results indicate an important transitional scale threshold beyond which data should be taken for numerical model validation, in order to stay relevant to full scale devices.

The effects of parasitic drag from blade support struts on turbine performance were measured by rotating the turbine without blades while stationary and while towing. These losses—even for a streamlined hydrofoil strut—can become significant at higher tip speed ratios—up to an approxi-

mate 5 percentage point decrease in power coefficient at a tip speed ratio of 5. These measurements were repeated with a set of high-drag cylindrical struts, which as expected, prevented the turbine from producing any mechanical power at any tip speed ratio. Nevertheless these measurements provide useful validation data for both high and low fidelity numerical performance prediction models, allowing researchers and engineers to test predictions without blade effects.

While operating at its optimal tip speed ratio $\lambda = 3.1$ the wake at $x/D = 0.93$ downstream was shown to be relatively symmetrical and lacked the evidence of strong blade stall, both of which differentiate this near-wake from the higher solidity, lower λ_0 UNH-RVAT. Terms from the mean kinetic energy transport equation were also computed in this y–z plane, showing the relative importance of the vertical advection compared with turbulent transport terms at this location, which is qualitatively similar to the UNH-RVAT wake data. However, lower wake recovery totals were calculated. This indicates that although the RM2 is a more effective energy converter than the UNH-RVAT, its wake recovery may in fact be delayed due to weaker blade tip vortex shedding and lower levels of turbulence in the near-wake, which may present a trade-off when considering optimal array layouts.

This dataset, along with the code for processing and visualization, is provided openly via a Creative Commons license (MIT license for code), and is available as a Git repository from `http://github.com/UNH-CORE/RM2-tow-tank` or a citable archive [36]. Note that the processing code will automatically download raw data as necessary so users can perform a full reanalysis of the measurements presented here.

5.8 Acknowledgments

This study was carried out in collaboration with Sandia National Laboratories and was supported by the Department of Energy (DOE), Office of Energy Efficiency and Renewable Energy (EERE), Wind and Water Power Technologies Office (WWPTO). Sandia National Laboratories is a multi-program laboratory managed and operated by Sandia Corporation, a wholly owned subsidiary of

Lockheed Martin Corporation, for the U.S. Department of Energy's National Nuclear Security Administration under contract DE-AC04-94AL85000.

CHAPTER 6

ON THE USE OF BLADE-RESOLVED COMPUTATIONAL FLUID DYNAMICS

In this chapter we will evaluate the effectiveness of modern high-fidelity computational fluid dynamics (CFD) for predicting the performance and near-wake characteristics observed for the UNH-RVAT. The content presented here has been submitted for publication as [32].

Despite the development of many simple engineering models based on blade element momentum or vortex methods, it remains difficult to predict the performance of cross-flow turbines for all cases—namely when solidity, or blade chord-to-radius ratio is high—a common characteristic of smaller rotors, and those designed for marine hydrokinetic (MHK) applications. With computing power becoming evermore available and affordable, CFD based on the Reynolds-averaged Navier–Stokes (RANS) equations has become an attractive method for predicting the performance of cross-flow turbines. Since a direct numerical simulation (DNS) of all scales at realistic Reynolds numbers is not currently feasible, turbulence be modeled. However, with an appropriate turbulence model, blade-resolved RANS presents a more physically realistic first principles based approach versus simpler models based on momentum theory or potential flow. However, CFD can be computationally expensive when done in three dimensions, which may be necessary in some cases.

There are many examples in the literature of 2-D cross-flow turbine simulations with widely varying results. Balduzzi et al. [39] provides a summary of recent efforts and an attempt to standardize a methodology for using Reynolds-averaged Navier–Stokes (RANS) to correctly predict performance of a 2-D CFT. Howell et al. [96], performed both 2-D and 3-D simulations of a high solidity cross-flow turbine using a k–ε renormalization group (RNG) turbulence model. The results from the 2-D simulations over-predicted power coefficient, while the 3-D case matched well with wind tunnel measurements near the tip speed ratio of maximum power. In general, 3-D simulations

Author	Turbulence modeling	Perf. val.	Wake val.
Alaimo et al. [5]	k–ε RANS	N/A	N/A
Marsh et al. [122]	SST RANS	[156]	N/A
Orlandi et al. [146]	SST RANS	[4, 135]	N/A
Lam & Peng [109]	SST RANS & IDDES[1]	N/A	[184]
Nini et al. [143]	Spalart–Allmaras RANS	N/A	[41]
Boudreau & Dumas [46]	Spalart–Allmaras DDES[2]	N/A	N/A
Li et al. [114]	SST RANS & Smagorinsky–Lilly LES	[129]	N/A
Howell et al. [96]	k–ε RNG[3] RANS	[96]	N/A

Table 6.1: Selected 3-D blade-resolved cross-flow turbine simulations reported in the literature, turbulence modeling employed, and performance and/or wake studies used for validation. Note the Li et al. study used periodic boundary conditions and is technically considered 2.5-D.

are less common, but have begun to appear more frequently recently—a testament to the progress towards higher computing power.

An overview of 3-D blade-resolved cross-flow turbine simulations reported in the literature is presented in Table 6.1. The k–ω SST RANS turbulence model is shown to be a popular choice due to its success in predicting flows with adverse pressure gradients and separation [134]. Higher fidelity methods that resolve the large scales of turbulence, such as large eddy and detached eddy simulation have also been used. Note that for all the studies listed, model validation was performed for either performance or wake predictions—not both—and in some case omitted entirely.

Modeling the boundary layer flows on cross-flow turbine blades is essential to predicting the blade loading. This flow condition presents a challenge due to the dynamically changing inflow velocity and angle of attack—which often exceeds static stall values and causes dynamic stall. Furthermore, the ability to predict the occurrence and interdependence of boundary layer transition to turbulence and separation can have dramatic influence on the blade loading and therefore the predicted turbine power output. These challenges present significant obstacles to the prospect of using CFD to replace wind tunnel or tank testing of physical models.

[1] Improved delayed detached eddy simulation.

[2] Delayed detached eddy simulation.

[3] Renormalization group.

To date, little computational work has been done to attempt to design arrays of CFTs, despite their prospects for closer spacing compared with axial-flow turbines (AFTs). For example, Araya et al. [9] modeled the flow through a VAT array using "leaky Rankine body" potential flow singularities, which was able to rank relative—though not absolute—performance of array configurations. Goude and Agren [89] used a 2-D vortex method to simulate a farm of cross-flow turbines, though this was not validated with experiments. Durrani et al. [74] used 2-D CFD to model a group of cross-flow turbines, observing higher power output for a staggered configuration, but also did not compare with experimental results. Giorgetti et al. [84] took a similar approach for 2-D array analysis using turbine pairs inspired by Dabiri [66], but again experimental validation was not performed. Li and Calisal [115] used a 3-D vortex line method to show mutually improved power output from two adjacent turbines, though the simulations over-predicted the effects by approximately 5% compared with experiments. Antheaume et al. [8] used a blade element approach coupled with a 3-D RANS solver to also show how close spacing can improve power output of CFTs.

In this study we set out to model the performance and near-wake of the high solidity University of New Hampshire Reference Vertical-Axis Turbine (UNH-RVAT) using the Reynolds-averaged Navier–Stokes equations using the open-source finite volume CFD package OpenFOAM, version 2.3.x. Though studies in the literature generally focus on predicting the turbine loading and the local blade boundary layer, we seek to model both this and the larger scale flow produced by the rotor, i.e., the near-wake, which is of interest for this particular turbine since it has been shown experimentally that the near-wake's momentum and energy transport processes are dominated by vertical advection [29]. It logically follows that a 2-D simulation, which omits the vertical dimension, would not correctly predict wake recovery and turbine–turbine interaction. However, it is of interest to determine how wrong a 2-D model may be, since the lower computational cost of 2-D simulations is attractive.

We seek to validate 2-D and 3-D blade-resolved RANS models against the UNH-RVAT mechanical power and near-wake measurements. If the blade loading and velocity in the near-wake

match well enough, the flow field can potentially be inspected in greater detail, i.e., we may be able to make observations of quantities not measured experimentally, e.g., pressure, and gain greater insight into where the dominant flow structures originate. This will ultimately help develop and evaluate low-order wake generator models for use in turbine array modeling. In summary, the questions we hope to answer here are:

1. Can 2-D RANS be used for individual turbine and/or array design?

2. How accurately can 3-D RANS predict performance?

3. Do the flow fields predicted by 3-D RANS match the experimental wake measurements well enough to provide insight for developing new low-order wake generators to represent CFTs?

4. Does 3-D RANS realize the correct proportions of wake recovery mechanisms, i.e., are the 3-D blade-resolved results a good reference case or "target" for those a low-order model should produce?

6.1 Numerical setup

In this study the UNH-RVAT baseline tow tank experiment was simulated using a mean rotor tip speed ratio $\lambda = 1.9$, which corresponds to the maximum measured power coefficient, cf. Figure 3.2. The tow speed or free stream velocity $U_\infty = 1.0$ m/s gives a turbine diameter Reynolds number $Re_D \approx 10^6$, which corresponds to the Re-independent state for both performance and near-wake characteristics, as determined from previous experimental measurements [26, 31], cf. Figures 4.2 and 4.4.

The turbine CAD geometry was prepared or "cleaned" for CFD by removing details determined to be unnecessary, e.g., screw heads and axial shaft grooves, which would complicate the meshing process and contribute very little to the overall loading or flow modulation. A drawing of the physically and numerically modeled geometries is presented in Figure 6.1.

To close the RANS equations, two different turbulence models were used: Menter's k–ω SST [132] and the Spalart–Allmaras (SA) one equation model [175]. Both closures use the eddy-

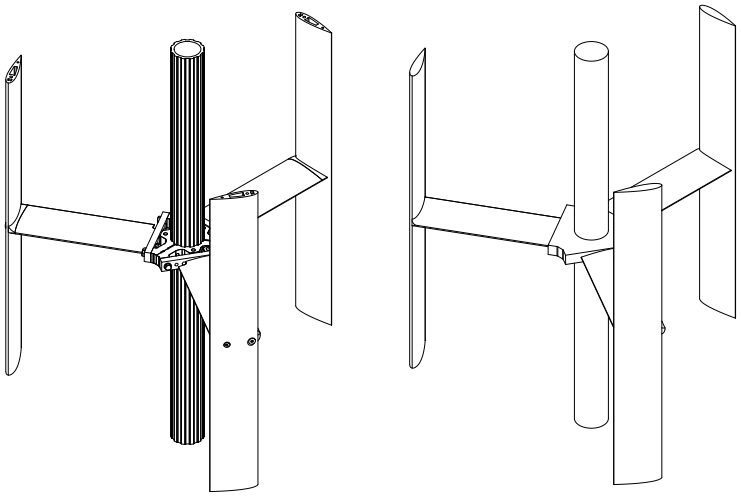

Figure 6.1: CAD drawings of the UNH-RVAT cross-flow turbine as designed and built (left) versus cleaned for simulation (right).

viscosity approach—the SA employing a single additional scalar transport equation for an eddy-viscosity-like quantity $\tilde{\nu}$ and the SST solving equations for the turbulence kinetic energy k and specific dissipation ω—see Appendix D for the model details. The SST model was chosen due to its prominence in the literature for simulating separating flows, which we assumed to be present in the current problem in the form of dynamic stall. The SA model was shown by Ferreira et al. [78] to match experimental particle image velocimetry (PIV) results for a CFT in dynamic stall, though this was a somewhat low Reynolds number case ($Re_c \approx 6 \times 10^4$). Further justification for using the SA model for this case comes from Crivellini and D'Alessandro [65], where they successfully modeled the laminar separation bubble and subsequent boundary layer transition to turbulence at Reynolds numbers similar to those investigated here.

6.1.1 Computational mesh

The computational domain was a rectangular volume 3.66 m long, 3.66 m wide, and 2.44 m tall (for 3-D), with the turbine located 1.52 m from the inlet, and centered vertically with a vertical axis, designed to match the tow tank dimensions for comparison with previous experiments. The rotor geometry was located at the center of a cylindrical sliding mesh interface, which rotated at

a mean tip speed ratio $\lambda = 1.9$ with a sinusoidal oscillation at the blade passage frequency—with and amplitude of 0.19 and the first peak at 1.4 radians—to mimic the slight deviation from the mean tip speed ratio observed in the experiments. The 2-D mesh overview is shown in Figure 6.2 and the blade mesh detail is shown in Figure 6.3.

Meshes were generated using OpenFOAM's blockMesh and snappyHexMesh utilities. Mesh topology consists of a background hexahedral mesh, which is refined in all three directions by a factor of 2 in a rectangular region containing the turbine and near-wake (0.9 m upstream, 1.3 m downstream, $\pm$0.9 m cross-stream, and $\pm$0.8 m vertically). Cells adjacent to the turbine shaft and struts are refined by a factor of 4, while cells adjacent to the blades are refined by a factor of 6. To capture the boundary layer, 20 layers were added next to the blades with an expansion ratio of 1.2. Overall mesh refinement is controlled by a single parameter—the number of cells in the streamwise direction, N_x.

6.1.2 Solver

Simulations were run using OpenFOAM's pimpleDyMFoam solver, which uses a hybrid PISO-SIMPLE algorithm for pressure-velocity coupling and is compatible with dynamic meshes. An Euler scheme was used to advance the simulation forward in time. The case files required to replicate the simulations are available from [16, 15, 18, 17].

6.1.3 Initial and boundary conditions

Initial and boundary conditions were set to match those of the tow tank as well as possible. The velocity at the inlet, bottom, and side walls was fixed to 1 m/s to match the tow tank case, while the top boundary condition was a slip velocity condition. Pressure was held fixed at the outlet while a zero-gradient boundary condition was applied at the inlet (a typical velocity-inlet/pressure-outlet case). Note that in 2-D the top and bottom boundary conditions are "empty," which is an OpenFOAM convention to indicate two-dimensionality.

Since the mesh was only refined next to the blade surfaces in order to resolve the boundary layer profile, no wall functions were used. However, wall functions were used for the other turbine surfaces, i.e., struts, hub, and shaft, and for the tank sidewalls, bottom, and top.

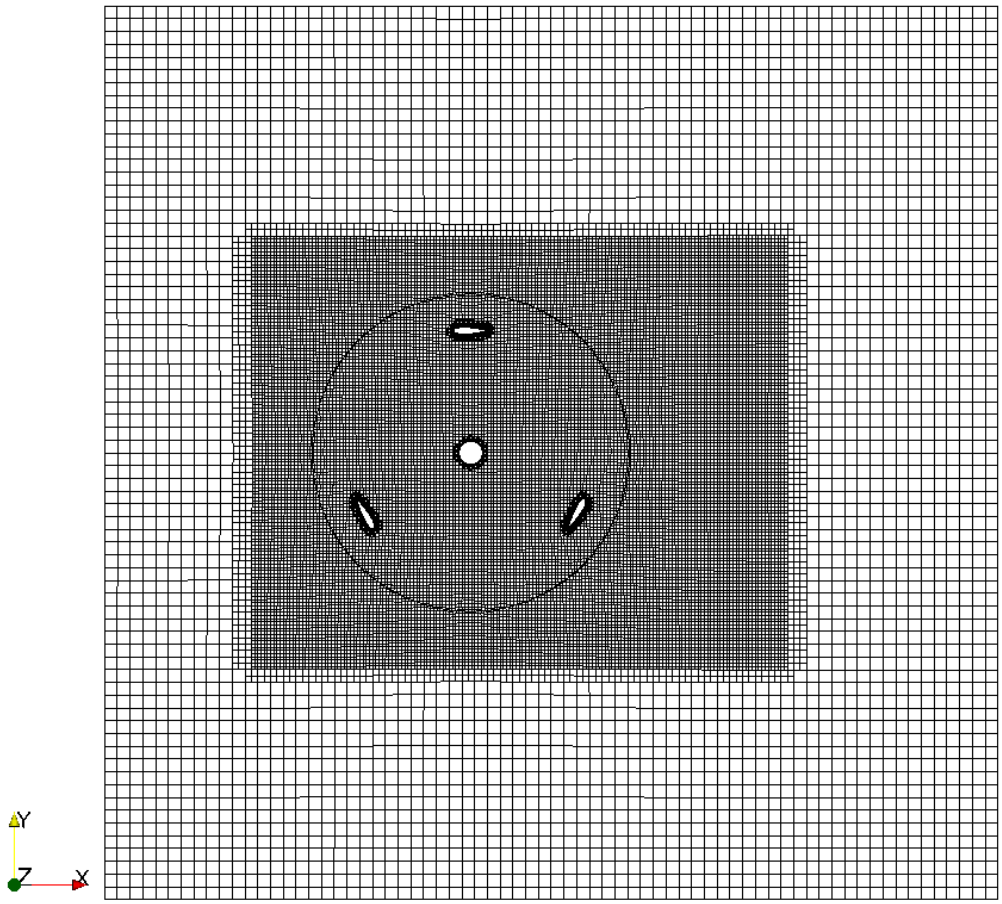

Figure 6.2: Overview of the 2-D computational mesh.

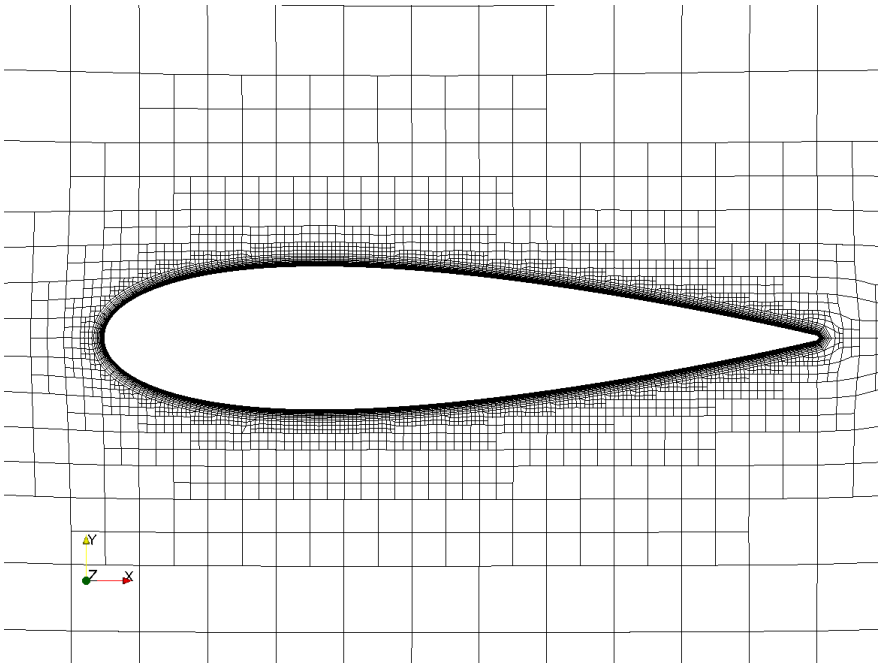

Figure 6.3: Detailed view of the 2-D computational mesh near the blades.

6.2 Model verification

Both the k–ω SST and Spalart–Allmaras RANS model cases were verified for convergence of the turbine mean power coefficient with respect to grid spacing and time step using 2-D domains. The grid topology was fixed, but the number of cells per domain length was scaled proportionally, maintaining the same background mesh cell aspect ratio. Results for this parameter sweep are shown in Figure 6.4, from which the final number of streamwise grid points $N_x = 70$ was chosen, which resulted in a nondimensional wall distance $y^+ = u^* y/\nu \sim 1$, where u^* is the friction velocity, defined as $u^* = \sqrt{\tau_w/\rho}$, where τ_w is the wall shear stress. This mesh resolution gave a total cell count of approximately 5×10^4 for the 2-D cases and 16 million for the 3-D case. Sensitivity to domain length was assessed as well, showing a 2% increase in mean power coefficient for the 2-D SST case with the domain extended an additional two rotor diameters downstream.

Time step dependence was evaluated using the 2-D $N_x = 70$ grid, the results from which are shown in Figure 6.4. It was seen that the Spalart–Allmaras model converged well with decreasing time step, leading to a final time step of 0.001 s. The results from the SST model show a local

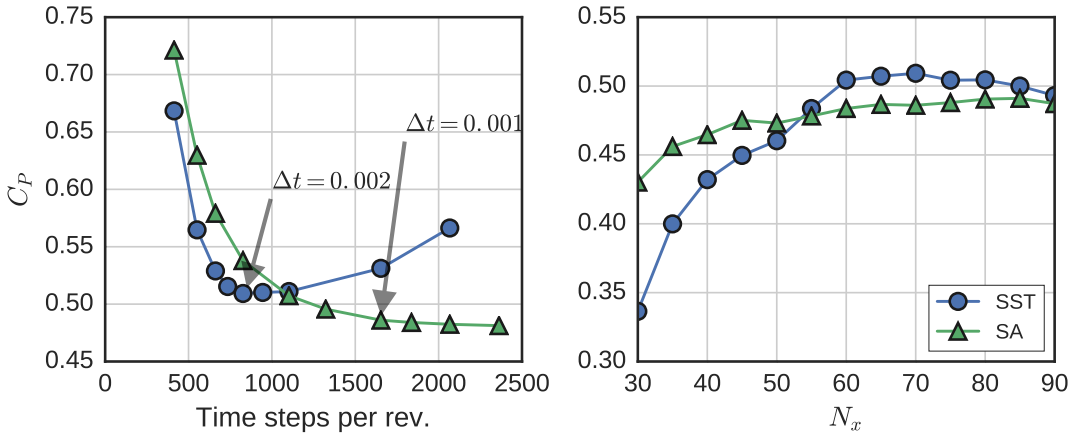

Figure 6.4: Time step (left) and grid size (right) dependence for the 2-D case with both the SST and SA turbulence models. Time step dependence was carried out with $N_x = 70$ and grid size dependence with the time steps annotated for each turbulence model.

minimum at $\Delta t = 0.002$ s, with some divergence for smaller time steps. The local minimum was chosen as the final time step to run the simulations. Note that the SST model's convergence behavior may be due to its specific implementation in OpenFOAM, and not indicative of the nature of the model equations. Verification studies for CFTs with this level of detail in the literature are not common, though the final time step is comparable to others [39].

6.3 Results

Turbine operation in all cases was simulated for 10 seconds, or approximately six rotor revolutions. Computations for the 3-D cases were run on 192 processes (24 nodes $\times$ 8 cores each on Sandia National Labs' Red Mesa high performance computing cluster) and took on the order of 1,000 CPU hours per second of simulated time. The 2-D simulations were run on a single processor and took on the order of one CPU hour per second.

Performance statistics were computed after the first revolution onward and flow statistics were calculated over the time interval spanning 5–10 seconds, or approximately three rotor revolutions, from time series downsampled to 50 Hz. It is assumed that the downsampling frequency is high

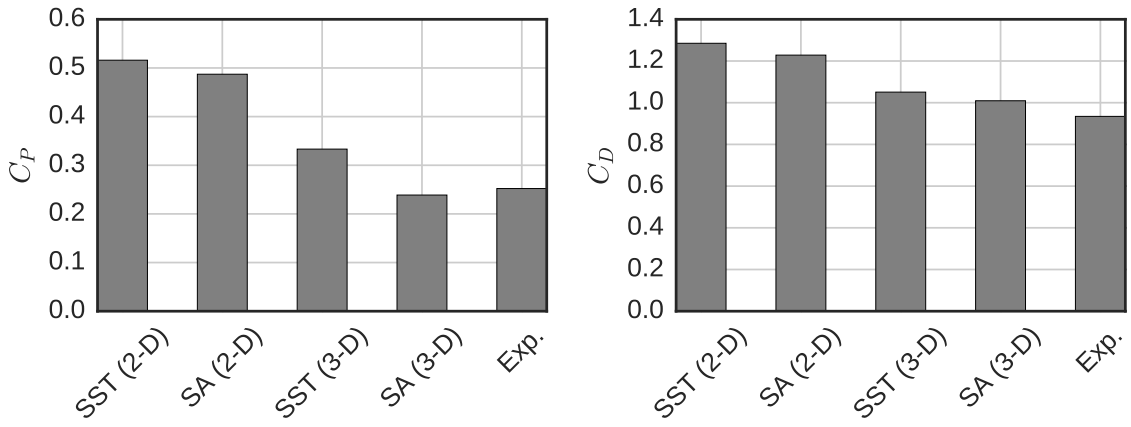

Figure 6.5: Power (left) and drag (right) coefficient predictions from experiments and each numerical model.

enough above the blade passage frequency such that differences from the variance (for computing turbulence statistics) in the original velocity will be negligible.

6.3.1 Performance prediction

Predictions for both the mean rotor power and drag coefficients are shown in Figure 6.5. In general, the 2-D CFD cases both significantly overpredict turbine loading and therefore mechanical power output, which is due to their increased blockage ratio, unresolved blade end effects, and lack of blade support struts.

The 3-D simulations matched the experimental measurements more closely. The Spalart–Allmaras model's mean power coefficient was 0.24 while the SST's was 0.33, which represent a 6% under- and 30% overprediction, respectively, compared with the experiments. Some of the apparent overprediction of rotor drag coefficient could also be an effect of the experimental procedure, where the "tare drag" from the turbine mounting structure was measured without a turbine installed, then subtracted in post-processing. With the turbine installed, flow past the mounting frame will be higher due to blockage, meaning the tare drag would be underestimated, and the CFD results for C_D should be slightly higher than the experimental measurements.

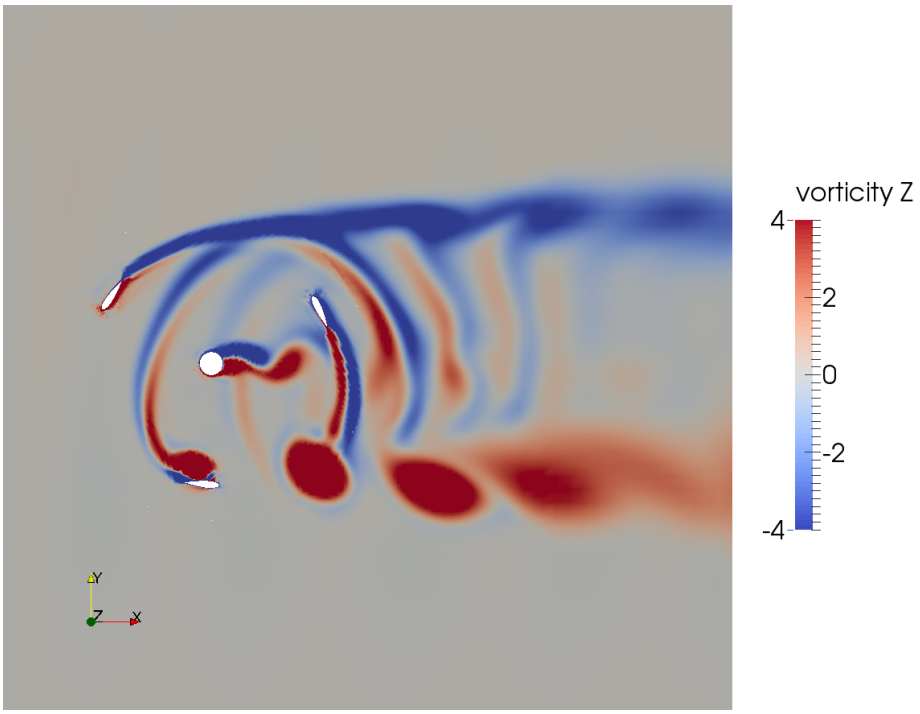

Figure 6.6: Instantaneous vorticity contours (at $t = 9.64$ s) computed for the 2-D Spalart–Allmaras case.

6.3.2 Wake characteristics

Visualizations of the complex vorticity field generated by the turbine are presented for the 2-D and 3-D Spalart–Allmaras cases in Figure 6.6 and Figure 6.7, respectively. It can be seen how the upstream blade—as it turns back into the streamwise direction—is shedding a large amount of spanwise vorticity due to the separated flow. In the 3-D case, strong tip vortices are also present, which trace the "contracting" wake flow on the $-y$ side of the turbine associated with the induced vertical velocity field. The 3-D dynamic stall vortex also shows asymmetry about the x–y mid-rotor plane; once again highlighting the importance of three-dimensional effects on wake dynamics.

Mean velocity profiles at one turbine diameter downstream are shown in Figure 6.8. The 2-D results suffer from a blockage mismatch, i.e., keeping the proximity of the walls constant increases the blockage ratio. The 3-D results, however, show good agreement with the experiments.

Turbulence kinetic energy profiles are also shown in Figure 6.8. The turbulence kinetic energy for the unsteady RANS models was calculated as

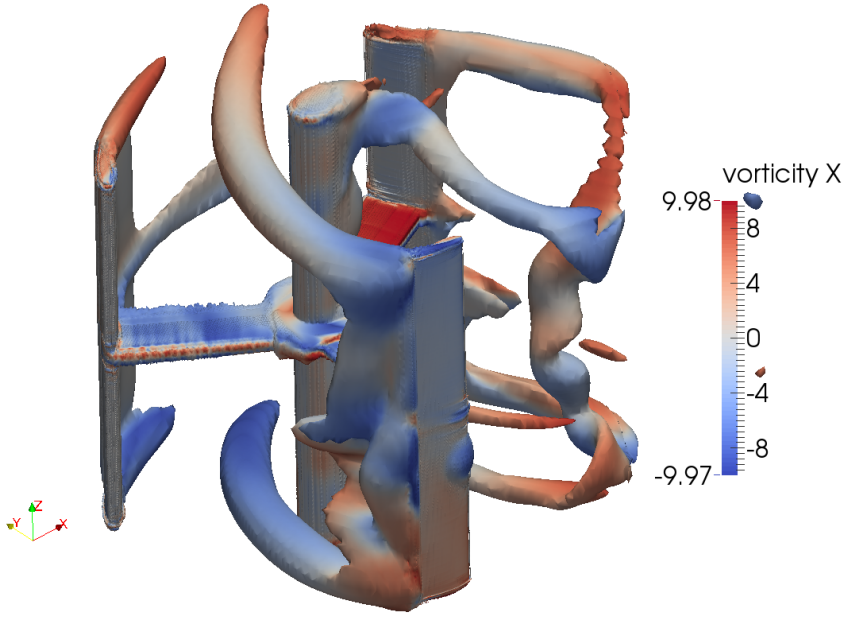

Figure 6.7: Iso-vorticity contours (at $t = 9.64$ s) colored by the streamwise component of vorticity for the 3-D Spalart–Allmaras case.

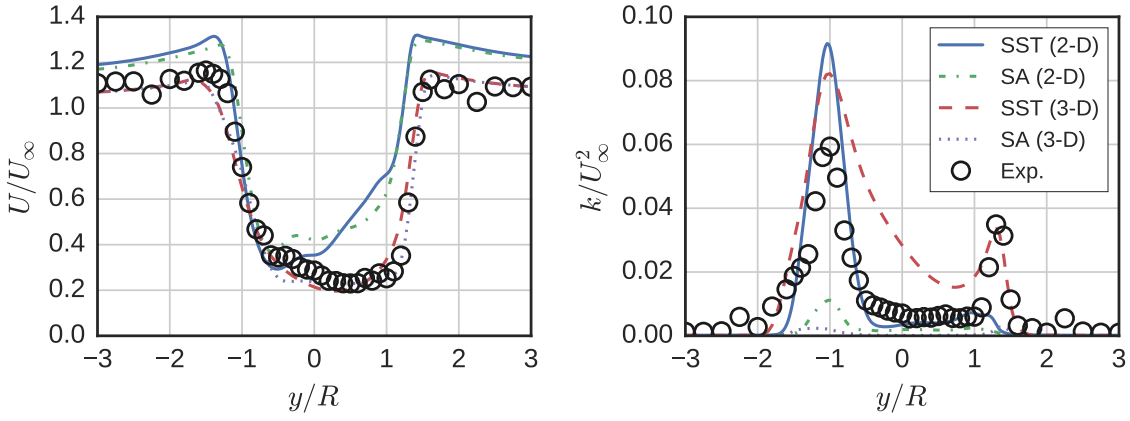

Figure 6.8: Mean velocity (left) and turbulence kinetic energy (right) profiles at $x/D = 1$ from 2-D simulations, 3-D simulations ($z/H = 0$), and experiments [29].

$$k = k_{\mathrm{RA}} + \frac{1}{2}\left(\overline{U'}^2 + \overline{V'}^2 + \overline{W'}^2\right), \tag{6.1}$$

where $U' = U - \overline{U}$ (the resolved velocity fluctuations) and k_{RA} is the kinetic energy calculated by the turbulence model, which is zero for the SA model.

Both Spalart–Allmaras cases did a poor job predicting the turbulence kinetic energy in the flow, since it must be resolved as variance in the velocity field. The 2-D SST model did a good job predicting the peak in k at $y/R = -1$, though is missing the smaller peak at $y/R = -1$. This is once again likely due to blockage issues, where local tip speed ratio is decreased, increasing the blades' instantaneous angle of attack at this location on the downstream passage. In contrast, the 3-D SST model predicts the $+y$ peak in turbulence kinetic energy very well, though the $-y$ peak magnitude is overpredicted by about 30%. We also see some smearing of k across the center of the rotor, which is likely due to exaggerated levels of the turbulent eddy viscosity.

6.3.2.1 Mean velocity in three dimensions

In order to visualize the mean velocity field, vector arrows for the mean cross-stream and vertical components are superimposed on top of contours of the streamwise component at $X/D = 1$ in Figure 6.9. Both CFD models predict the general structure of the mean velocity well, though the SA case has a slightly larger vertical mean flow component, which could be due to stronger tip vortex generation, or lower diffusivity compared with the SST model.

6.3.2.2 Turbulence kinetic energy contours

Turbulence kinetic energy contours for the experimental measurements and each CFD case at $x/D = 1$ are presented in Figure 6.10. As seen in the profiles in Figure 6.8, the SA model was not able to resolve the majority of the unsteadiness in the flow. In contrast, the SST model did a good job predicting the locations and magnitudes of various peaks in k. These are generated along the top of the turbine via tip vortex shedding, and the $-y$ side of the turbine via dynamic stall. We do however see the smearing effect from the dynamic stall vortex centered around $z/H = 0$, which is likely more of an issue with wake evolution rather than wake generation.

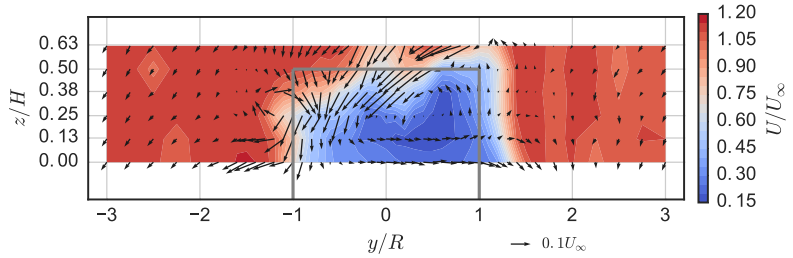

(a) Mean velocity field at $x/D = 1$ from experiments [34].

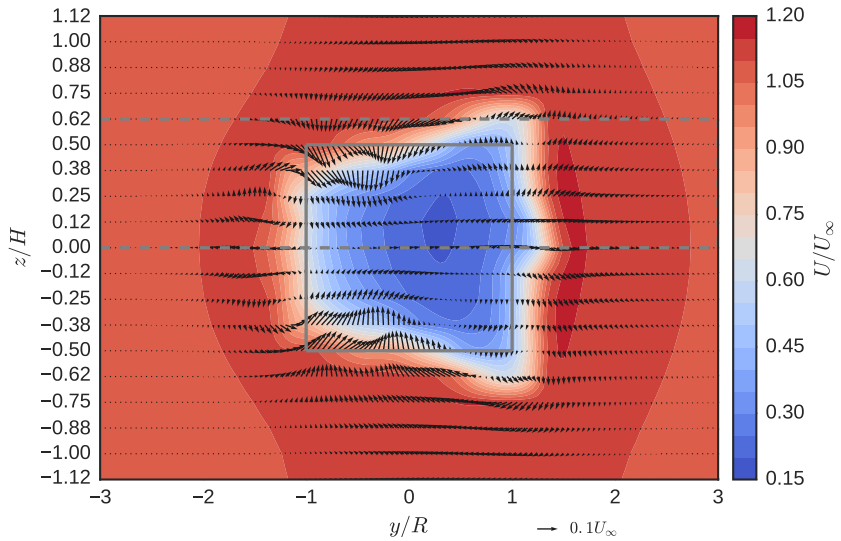

(b) Mean velocity at $x/D = 1$ computed by the 3-D SST model.

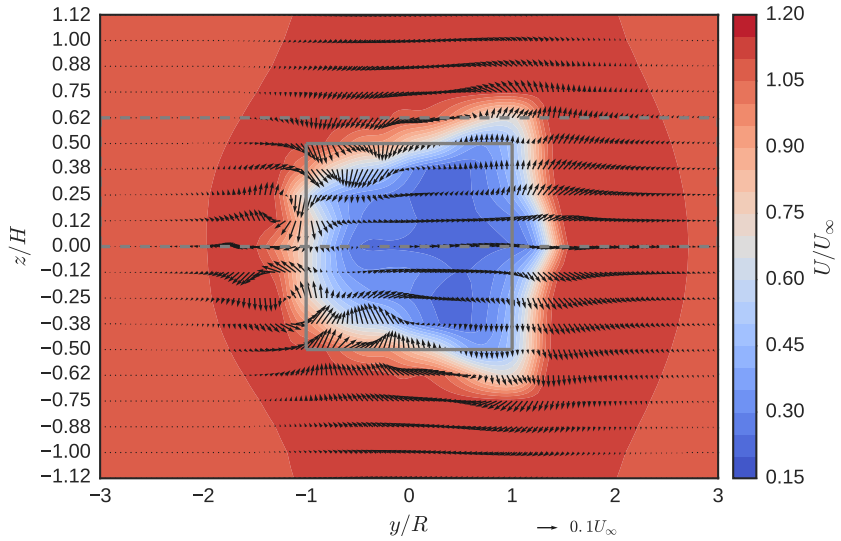

(c) Mean velocity at $x/D = 1$ computed by the 3-D SA model.

Figure 6.9: Mean velocity from experiments and 3-D CFD cases. Solid gray lines indicate turbine frontal area and dashed lines indicate experimental measurement plane.

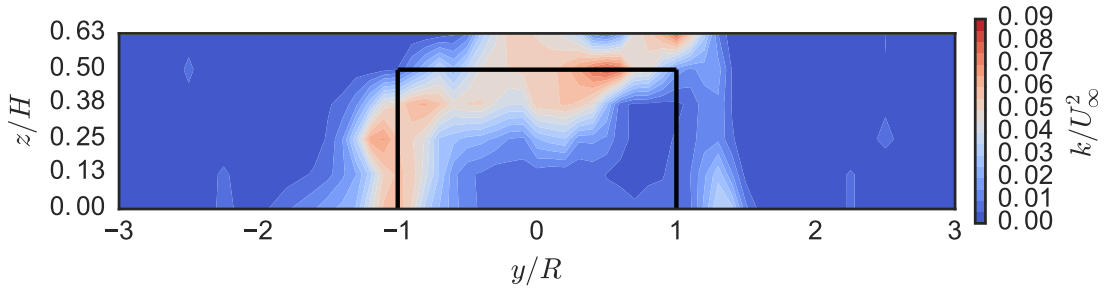

(a) Turbulence kinetic energy at $x/D = 1$ from experiments [34].

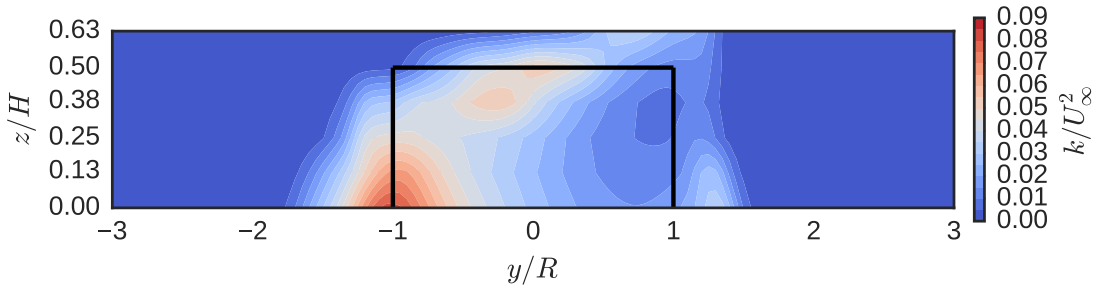

(b) Turbulence kinetic energy at $x/D = 1$ computed by the 3-D SST model.

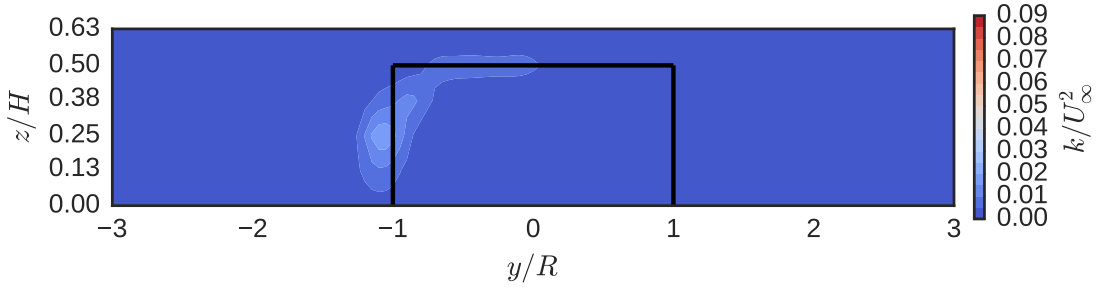

(c) Turbulence kinetic energy at $x/D = 1$ computed by the 3-D SA model.

Figure 6.10: Turbulence kinetic energy from experiments and 3-D CFD cases. Solid black lines indicate turbine frontal area.

6.3.2.3 Momentum recovery

To get an overall idea of the wake recovery predicted by each model, we rearrange the streamwise component of the Navier–Stokes equation to isolate $\partial U/\partial x$—following Bachant and Wosnik [29]—and compute each term at $X/D = 1$ to compare with the experimental results.

We use the RANS models' eddy viscosity to calculate the turbulent transport via

$$\text{Turb. trans.} = \nu_t \nabla^2 \vec{U}, \tag{6.2}$$

which is a different approach from those taken on the experiments, where Reynolds stresses were measured, but x-derivatives were not:

$$\text{Turb. trans. (exp.)} = -\left(\frac{\partial}{\partial y}\overline{u'v'} + \frac{\partial}{\partial z}\overline{u'w'}\right). \tag{6.3}$$

As such, we should not be surprised if the CFD models predict higher levels of turbulent transport than the experiments.

Normalized weighted averages for each recovery term at $x/D = 1$ are computed and multiplied by the cross-sectional area of the measurement plane, or the channel width in the 2-D cases. Results are shown in a bar chart in Figure 6.11. Consistent with the relatively large Reynolds number regime, viscous transport is essentially negligible compared with other mechanisms. Cross-stream advection—or the tendency of streamlines to diverge and reduce the streamwise momentum—produces a negative effect for all cases, though the 3-D SST model predicts significantly lower values. Vertical advection is by definition zero for the 2-D cases. The 3-D cases show varying results—with the SST model overpredicting and SA underpredicting the vertical velocity's effect on replenishing streamwise momentum.

Turbulent transport and streamwise pressure gradient terms show the largest discrepancy between results. The 3-D SST case, despite doing a good job predicting turbulence kinetic energy, significantly overpredicts the turbulent transport term, while other CFD cases are comparable with the experiment. This seems to be balanced by a large adverse pressure gradient, which is also

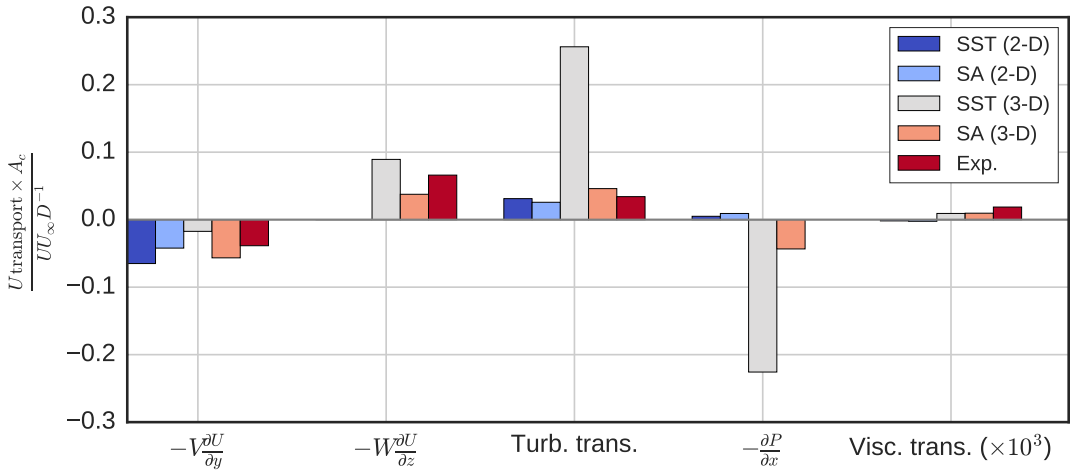

Figure 6.11: Weighted sum normalized momentum recovery terms for each CFD case and experiments[34] at $x/D = 1$.

present to a smaller degree in the 3-D SA case. Interestingly, in contrast, both 2-D CFD cases create a wake where the pressure gradient is acting to slightly accelerate the flow at $x/D = 1$. Unfortunately, pressure data were not acquired from the experiment, though results from the 3-D delayed detached eddy simulation (DDES) of Boudreau and Dumas [46] concur with the adverse pressure gradient condition.

6.4 Conclusions

A cross-flow turbine was modeled using the k–ω SST and Spalart–Allmaras (SA) Reynolds-averaged Navier–Stokes turbulence models to test their abilities to predict turbine performance and near-wake dynamics. It was observed that when modeled in 2-D, the performance is over-predicted compared to the data from the tow tank experiments, which was expected due to omission of blade end effects, support strut drag, and increased blockage. Vertical (or axial) wake dynamics were unresolved in the 2-D model, despite being identified as a significant contributor to streamwise wake recovery, which casts doubt on the 2-D model's applicability as a tool to study array spacing effects.

The 3-D blade-resolved RANS simulations predicted turbine performance and near-wake quite well, where the SA model results were closest to the experimentally measured performance. The SA model's effectiveness gives hope for the prospect of replacing some physical modeling with blade-resolved CFD. However, the overprediction of power coefficient by the SST model highlights the level of technological and economic risk involved with CFD. That is to say, the SST model, despite being considered relatively trustworthy in these flow conditions, would overestimate power output by 30%.

Both the SST and SA models did a good job predicting the mean velocity field at one turbine diameter downstream, but the SST model was more effective at predicting turbulence kinetic energy, since it is solved for in the turbulence model equations. Streamwise momentum recovery terms were computed from the CFD results over an entire cross-section of the domain at $x/D = 1$. Values for transport due to the mean pressure gradient and turbulent fluctuations varied a lot between the two turbulence models. Both models, however, we able to at least qualitatively resolve the vertical velocity field, which will be crucial to predicting the performance of closely spaced CFTs.

The effectiveness at predicting the mean velocity field gives credibility to the prospect of using the computed flow field to extrapolate the experimental results, such that the CFD results can be used as a target for a low-order wake generator or force parameterization. These results may also help develop new tip loss corrections for blade element type models, which currently only exist for axial-flow rotors, since they provide access to the pressure and shear forces over the entire blade surface, which were not measured experimentally. Ultimately, however, the computational cost of 3-D simulations—about 1,000 CPU hours per simulated second (or roughly 10,000 CPU hours per operating point)—may be too expensive to be used for CFT engineering work, especially considering the uncertainty involved compared with physical model studies. Since the 3-D wake results appeared to be only weakly asymmetrical in the x–y plane about $z/H = 0$, it may be possible to reduce computing power by only modeling the top half of the rotor and using a symmetry boundary condition at the mid-plane. However, 3-D blade-resolved RANS will likely not be practical for

turbine array simulations for quite some time, and until they are, low-order models will need to be developed and improved for this purpose.

6.5 Acknowledgments

Thanks to Dr. Vincent S. Neary and Sandia National Labs for the use of their Red Mesa high performance computing cluster to run the simulations.

CHAPTER 7

DEVELOPMENT AND EVALUATION OF AN ACTUATOR LINE MODEL FOR CROSS-FLOW TURBINES

Despite its apparent—but not completely certain—effectiveness for predicting the performance and wake of a single turbine, blade-resolved CFD presents a huge computational expense since it must resolve fine details of the blade boundary layers, and must be performed in three dimensions, which will preclude its use for array analysis until the availability of computing power increases sufficiently. It is therefore necessary to explore simpler models that can predict the turbine loading and flow field with acceptable fidelity, but that are economical enough to not require high performance computing, at least for individual devices.

Very fast solution times can be obtained with blade element momentum (BEM) models, such as the double multiple streamtube (DMST) approached developed by Paraschivoiu [147]. However, their poor performance for rotors with high solidity [103] Nc/R (and/or chord-to-radius ratio c/R), where N is the number of blades, c is the chord length, and R is the maximum rotor radius, makes them less attractive, particular for marine hydrokinetic applications where rotors of the same size will encounter approximately an order of magnitude higher torque compared to wind turbines. Their description of the flow field is very crude as well, simply computing the momentum contained within discretized streamtubes, which cannot resolve any of the complicated flow structures shed by the rotor, limiting their applicability for array analysis.

Blade element based potential flow vortex line methods, e.g., [178, 138], can be solved with reasonable computational effort—ranging from an expense close to BEM up to that of 2-D blade-resolved CFD. The cost is a function of the number of vortex elements, which for free vortex methods increases at each time step, slowing down the calculation as it marches forward in time. Vortex methods can resolve more flow details than BEM. However, since the flow is governed

by the Laplace equation, nonlinear effects such as the turbulent transport will not be included, which we have determined in experiments to be the same order of magnitude as the mean vertical advection.

It is therefore desirable to retain a Navier–Stokes description of the flow field and use an actuator-type model for parameterizing the turbine loading, which dramatically drives down computational expense by removing the need for complicated meshes with many fine cells to resolve the boundary layers near the blade surfaces. As shown in Chapter 3, the conventional uniform actuator disk is not a good candidate for a cross-flow turbine wake generator, never mind the fact that it does not typically compute performance predictions. There are then two actuator methods that use blade element theory to compute blade loading and therefore generate a wake that more closely resembles that of an actual turbine. These are the actuator cylinder or swept-surface model (ASSM) and the actuator line model (ALM). The ASSM solves for the average blade loading along its path and applies this as a constant body force term in the momentum equation. The ALM takes a similar approach but is an unsteady method, resolving the blade element locations in time.

The ALM, originally developed by Sorensen and Shen [174], has become popular for modeling axial-flow or horizontal-axis turbines, and has been shown in blind tests to be competitive with blade-resolved CFD [108, 151]. The ALM combined with large eddy simulation has become the state-of-the-art for modeling entire wind farms [10, 62, 173, 80, 81]. Like other blade element techniques, the effectiveness of the ALM for AFTs is in part due to the quasi-steady nature of the flow in the blade reference frame, and the relatively rare occurrence of stall.

The ASSM and ALM were implemented to model a very low Reynolds number 2-D cross-flow turbine experiment in a flume using large eddy simulation (LES) [164]. Performance predictions for this case were not reported, but the ALM was shown to be more effective at postdicting the wake characteristics measured in the experiments by Brochier et al. [50].

It is therefore proposed that an actuator line model may be the optimal combination of high-fidelity flow modeling that includes performance predictions, but with reduced computational expense. Here we will develop and evaluate the effectiveness of an ALM for cross-flow turbines

inside both RANS and LES simulations, implemented as an extension for the OpenFOAM open-source CFD library. Note that the content here has been submitted for publication as [21].

7.1 Theory

The actuator line model is based on the classical blade element theory combined with a Navier–Stokes description of the flow field. The ALM treats turbine blades as lines of blade elements, for which 2-D profile lift and drag coefficients are given. For each blade element, relative flow velocity and angle of attack are computed by adding the vectors of relative blade motion and the local fluid velocity. The blade element lift force, drag force, and pitching moment are calculated as

$$F_l = \frac{1}{2}\rho A_{\text{elem}} C_l |\vec{U}_{\text{rel}}|^2, \tag{7.1}$$

and

$$F_d = \frac{1}{2}\rho A_{\text{elem}} C_d |\vec{U}_{\text{rel}}|^2, \tag{7.2}$$

$$M = \frac{1}{2}\rho A_{\text{elem}} c C_m |\vec{U}_{\text{rel}}|^2, \tag{7.3}$$

respectively, where ρ is the fluid density, A_{elem} is the blade element planform area (span $\times$ chord), $\vec{U}_{\text{rel}}$ is the local relative velocity projected onto the plane of the element profile cross-section (i.e., the spanwise component is neglected), and C_l, C_d, and C_m are the sectional lift, drag, and pitching moment coefficients, respectively, which are linearly interpolated from a table per the local angle of attack. The forces are then projected onto the rotor coordinate system to calculate torque, overall drag, etc. Forces from the turbine shaft and blade support struts are computed in a similar way. After the force on the actuator lines from the flow is computed, it is then added to the Navier–Stokes equations as a body force or momentum source (per unit density, assuming incompressible flow):

$$\frac{\mathrm{D}\vec{u}}{\mathrm{D}t} = -\frac{1}{\rho}\nabla p + \nu\nabla^2\vec{u} + F_{\text{turbine}}. \tag{7.4}$$

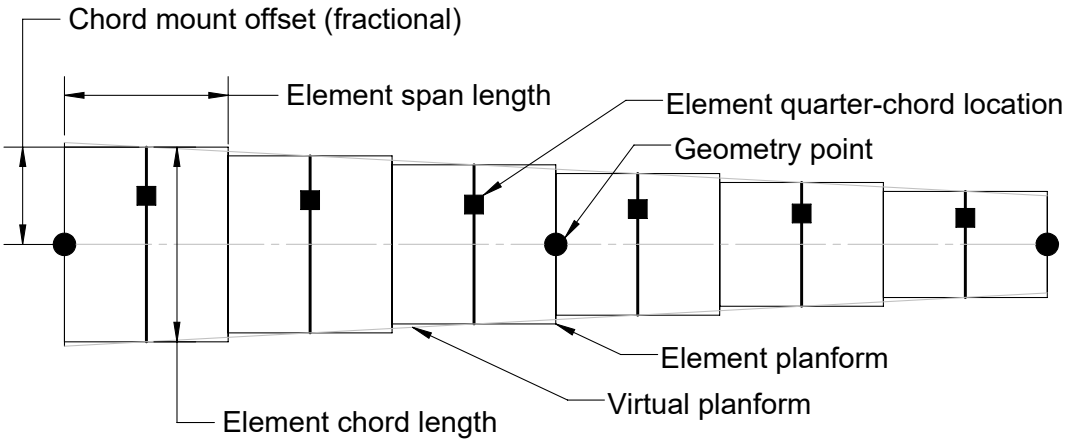

Figure 7.1: Actuator line geometry. Filled circles indicate points where geometry is defined whereas squares indicate actuator line element quarter-chord locations. Chord mount offset is defined as the distance from an element's leading edge to each geometry point in chord lengths, which was 0.5 for both rotors modeled in this study.

7.2 Blade element discretization

In the ALM, a turbine is a collection of actuator lines, which themselves are collections of actuator line elements (ALEs). The position of each ALE is a point in space indicating its quarter-chord location. The element is further defined by its chord direction vector, chord length, span direction vector, span length, and velocity vector.

An actuator line is created from defined geometry points, between which ALE parameters are interpolated linearly. This way, an actuator line can be defined by fewer geometry points than element locations. For example, an AL with straight planform boundaries—e.g. a straight or tapered wing—only needs two geometry points to be fully defined. Figure 7.1 shows and example schematic of a tapered actuator line with three geometry points at the half-chord locations and six total elements. Note that the middle geometry point is technically redundant, but is shown for illustrative purposes. For actuator lines that represent bluff bodies, e.g., shafts, the chord mount offset is set to 1/4, such that the element location is centered along the line of geometry points.

7.3 Determining inflow velocity

In momentum methods, the inflow velocity is determined by solving for the axial and angular induction factors [121]. However, using Navier–Stokes methods, it is somewhat unclear how to calculate the velocity vector used to compute the angle of attack and relative velocity, though we have access to much more information about the flow. Sorensen and Shen used an actuator line element's position to determine the inflow velocity for an axial-flow turbine [174]. Similarly, Shamsoddin and Porte-Agel use the velocity at a blade element's location in their actuator line simulation of a vertical-axis turbine using LES [164]. The US National Renewable Energy Lab (NREL) SOWFA ALM for OpenFOAM also uses the velocity at the actuator line element location for computing inflow velocity and local angle of attack with no corrections [63].

Schito and Zasso developed an effective velocity model (EVM) for computing actuator forces in Navier–Stokes simulations [162]. Their EVM proposes that inflow velocity should be sampled along a line perpendicular to the mean relative flow direction. They ultimately determined that the sampling line should be 1.5 chord lengths upstream of the actuator point (i.e. quarter-chord location). A sampling line was chosen to be 5 times the local mesh cell length. Finally, an angle of attack correction was proposed

$$\Delta\alpha = \frac{c}{M}(1.2553 - 0.0552C_d)C_l, \tag{7.5}$$

where c is the chord length, M is the mesh size, and C_l and C_d are the lift and drag coefficients, respectively. Note that the constants in Equation 7.5 were determined from a calibration with 2-D blade-resolved CFD for a NACA 0012 foil and are not assumed to be universal.

The EVM, despite showing robustness for its chosen validation case, unfortunately involves determination of two unknown tuning parameters. To avoid the additional effort and uncertainty in determining these, the inflow velocity was sampled at the element quarter-chord location using OpenFOAM's `interpolationCellPoint` class, which provides a linear weighted interpolation using cell values. This algorithm helps keep the sampled velocity "smooth" compared with using

the cell values themselves, especially when elements are moving in space as they are in a turbine, since meshes will likely have a cell size on the same order as the chord length, and will move on the order of one cell length per time step.

7.4 Static foil coefficient data

Static input foil coefficient data were taken from Sheldahl and Klimas [165]—a popular database developed for CFTs, which contains values over a wide range of Reynolds numbers. The Sheldahl and Klimas dataset has some limitations, namely that data for some foil and/or Reynolds numbers were "synthesized" numerically from other measurements. Despite its flaws, this dataset is the likely most comprehensive available with respect to variety of profiles and ranges of Reynolds numbers. Surprisingly, considering the maturity and popularity of NACA foils, data remains scarce, especially for $Re_c \sim 10^5$.

NACA 0021 coefficients were used for both turbines, despite the fact that the UNH-RVAT is constructed from NACA 0020 foils, as a NACA 0020 dataset is not available—it is assumed the small difference in foil thickness is negligible. Since pitching moment data were only available at limited Reynolds numbers, two datasets were used: The lowest for $Re_c \leq 3.6 \times 10^5$ and highest $Re_c \geq 6.8 \times 10^5$. For each actuator line element, blade chord Reynolds number is computed based on the sampled inflow velocity, and the static coefficients are then interpolated linearly within the database.

7.5 Force projection

After the force on the ALE from the flow is calculated, it is then projected back onto the flow field as a source term in the momentum equation. To avoid instability due to steep gradients, the source term is tapered from its maximum value away from the element location by means of a spherical Gaussian function. The width of this function η is controlled by a single parameter ε, which is then multiplied by the actuator line element force and imparted on a cell with distance $|\vec{r}|$ from the actuator line element quarter chord location:

$$\eta = \frac{1}{\varepsilon^3 \pi^{3/2}} \exp\left[-\left(\frac{|\vec{r}|}{\varepsilon} \right)^2 \right]. \tag{7.6}$$

Troldborg [185] proposed that the Gaussian width should be set to twice the local cell length Δx in order to maintain numerical stability. Schito and Zasso [162] found that a projection ε equal to the local mesh length was optimal. Jha et al. [102] investigated the ideal projection width for HAWT blades, recommending an equivalent elliptic planform be constructed and used to calculate a spanwise ε distribution.

Martinez-Tossas and Meneveau [126] used a 2-D potential flow analysis to determine that the optimal projection width for a lifting surface is 14–25% of the chord length. The width due to the wake caused by the foil drag force was recommended to be on the order of the momentum thickness θ, which for a bluff body or foil at large angle of attack is related to the drag coefficient ($O(1)$) by [183]

$$C_d = 2\theta / l, \tag{7.7}$$

where l is a reference length, e.g., diameter for a cylinder or chord length for a foil.

Using these guidelines, three Gaussian width values were determined: one relative to the chord length, one to the mesh size, and one to the momentum thickness due to drag force. Each three were computed for all elements at each time step, and the largest was chosen for the force projection algorithm. Using this adaptive strategy, fine meshes could benefit from the increased accuracy of more concentrated momentum sources, and coarse meshes would be protected from numerical instability.

The Gaussian width due to mesh size $\varepsilon_{\text{mesh}}$ was determined locally on an element-wise basis by estimating the size of the cell containing the element as

$$\Delta x \approx \sqrt[3]{V_{\text{cell}}}, \tag{7.8}$$

where V_{cell} is the cell volume. To account for the possibility of non-unity aspect ratio cells, an additional factor C_{mesh} was introduced, giving

$$\varepsilon_{\text{mesh}} = 2C_{\text{mesh}}\Delta x. \tag{7.9}$$

C_{mesh} was set to 2.0 for the simulations presented here—determined by trial-and-error to provide stability on the finest grids. However, in the ALM code C_{mesh} is selectable at run time for each profile used.

7.6 Unsteady effects

In the context of a turbine—especially a cross-flow turbine—the actuator lines will encounter unsteady conditions, both in their angle of attack and relative velocity. These conditions necessitate the use of unsteady aerodynamic models to augment the static foil characteristics, both to capture the time resolved response of the attached flow loading and effects of flow acceleration, also know as added mass. Furthermore, the angles of attack encountered by a CFT blade will often be high enough to encounter dynamic stall (DS). It is therefore necessary to model both unsteady attached and detached flow to obtain accurate loading predictions.

7.6.1 Dynamic stall

Dynamic stall is encountered when the blade angle of attack changes rapidly in time and exceeds a certain threshold, often near the static stall angle [128]. The stall is characterized by an initial increase in lift beyond static values as a vortex is shed from the foil's leading edge, after which a drop in lift and large nose-down pitching moment occurs as the vortex is advected downstream. As the angle of attack drops below the critical value, flow reattaches, closing the so-called hysteresis loop. Dynamic stall has been shown to be a significant positive contributor to performance in CFTs [148, 187], therefore an accurate model is key.

DS models were first developed to improve predictive capability for helicopter rotors, on which DS has significant effects on maneuverability and operational envelope [47]. A summary of dynamic stall models developed for helicopter rotors is presented in [112]. The simplest dynamic stall models rely on semi-empirical correlations, e.g., the Gormont model [87], developed at the

Boeing–Vertol Company. Several variants of the Gormont model were developed for vertical-axis wind turbines, with varying degrees of success; a summary is presented in [148].

Leishman and Beddoes (LB) [113] developed a semi-empirical model for unsteady aerodynamics and dynamic stall, which is derived from the phenomenology of the physics instead rather than pure empiricism. Beddoes then updated the model to the so-called third generation or "3G" version [43]. The LB DS models can be summarized conceptually based on the following principles:

- Dynamic conditions cause a time lag in effective angle of attack and lift force.
- Separation is determined by the Kirchoff flow approximation, which is also used to parameterize the normal force coefficient table based on the trailing edge separation point. This separation point also encounters a time lag.
- The separation initiates a vortex shedding cycle that causes an overshoot and subsequent undershoot in lift before returning to an attached flow condition.

Sheng et al. [168] developed an LB DS model variant targeted at low Mach numbers. This model, along with the original and 3G LB DS model variants, was tested for its effectiveness in cross-flow turbine conditions by Dyachuk et al. [76], who concluded that the Sheng et al. variant results matched most closely with experiments. In a similar study, the Sheng et al. model also faired better than the Gormont model [75], which inspired its adoption here for the ALM.

Before the dynamic stall subroutine is executed, the static profile data for each element is interpolated linearly based on local chord Reynolds number. The profile data characteristics—static stall angle, zero-lift drag coefficient, and separation point curve fit parameters—are then recomputed each time step such that the effects of Reynolds number on the static data are included.

Inside the ALM, angle of attack is sampled from the flow field rather than calculated based on the geometric angle of attack. Therefore, the implementation of the LB DS model was such that the equivalent angle of attack α_{equiv} was taken as the sampled rather than the lagged geometric value. A similar implementation was used by Dyachuk et al. [77] inside a vortex model.

7.6.2 Added mass

A correction for added mass effects, or the effects due to accelerating the fluid, was taken from Strickland et al. [178], which was derived by considering a pitching flat plate in potential flow. In the blade element coordinate system, the normal and chordwise (pointing from trailing to leading edge, which is opposite the x-direction used by Strickland *et al.*) coefficients due to added mass are

$$C_{n_{\mathrm{AM}}} = -\frac{\pi c \dot{U}_n}{8|U_{\mathrm{rel}}|^2}, \tag{7.10}$$

and

$$C_{c_{\mathrm{AM}}} = \frac{\pi c \dot{\alpha} U_n}{8|U_{\mathrm{rel}}|^2}, \tag{7.11}$$

respectively, where U_n is the normal component of the relative velocity, and dotted variables indicate time derivatives, which were calculated using a simple first order backward finite difference. Similarly, the quarter-chord moment coefficient due to added mass was calculated as

$$C_{m_{\mathrm{AM}}} = -\frac{C_{n_{\mathrm{AM}}}}{4} - \frac{U_n U_c}{8|U_{\mathrm{rel}}|^2}, \tag{7.12}$$

where U_c is the chordwise component of relative velocity. Note that the direction of positive moment is "nose-up," which is opposite that used by Strickland et al..

The normal and chordwise added mass coefficients translate to lift and drag coefficients by

$$C_{l_{\mathrm{AM}}} = C_{n_{\mathrm{AM}}} \cos\alpha + C_{c_{\mathrm{AM}}} \sin\alpha, \tag{7.13}$$

and

$$C_{d_{\mathrm{AM}}} = C_{n_{\mathrm{AM}}} \sin\alpha - C_{c_{\mathrm{AM}}} \cos\alpha, \tag{7.14}$$

respectively. The added mass coefficients were then added to those calculated by the dynamic stall model.

7.7 Flow curvature corrections

The rotating blades of a cross-flow turbine will have non-constant chordwise angle of attack distributions due to their circular paths—producing so-called flow curvature effects [137]. This makes it difficult to define a single angle of attack for use in the static coefficient lookup tables. Furthermore, this effect is more pronounced for high solidity (c/R) turbines. Two different flow curvature corrections were considered: one derived in Goude [88] and one by Mandal and Burton [120].

The Goude correction is derived by considering a flat plat moving along a circular path in potential flow, for which the effective angle of attack including flow curvature effects is given by

$$\alpha = \delta + \arctan \frac{V_{\text{abs}} \cos(\theta_b - \beta)}{V_{\text{abs}} \sin(\theta_b - \beta) + \Omega R} - \frac{\Omega x_{0r} c}{V_{\text{ref}}} - \frac{\Omega c}{4 V_{\text{ref}}}, \tag{7.15}$$

where δ is the blade pitch angle, V_{abs} is the magnitude of the local inflow velocity at the blade, θ_b is the blade azimuthal position, β is the direction of the inflow velocity, Ω is the turbine's angular velocity, R is the blade element radius, x_{0r} is a normalized blade attachment point along the chord (or fractional chord distance of the mounting point from the quarter-chord), c is the blade chord length, and V_{ref} is the reference flow velocity for calculating angle of attack.

In the actuator line model, each element's angle of attack is calculated using vector operations, which means the first two terms in Equation 7.15 are taken care of automatically since each element's inflow velocity, chord direction, and element velocity vectors are tracked. Therefore, the last two terms in Equation 7.15 were simply added to the scalar angle of attack value. Note that for a cross-flow turbine, this correction effectively offsets the angle of attack, which therefore increases its magnitude on the upstream half of the blade path, and decreases its magnitude on the downstream half, where the angle of attack is negative.

The Mandal–Burton flow curvature correction assumes that since the blade is encountering a curvilinear flow, it can be treated as having virtual camber. They introduce a factor to describe the variation of angle of attack from the leading to trailing edge

$$\Delta\alpha = \alpha_{\text{TE}} - \alpha_{\text{LE}}, \tag{7.16}$$

where TE and LE subscripts denote the values of angle of attack at the trailing and leading edge, respectively. Calculating these values for an actuator line element can be done by tracking the leading and trailing edge locations and velocities, then performing the same vector arithmetic used to calculate the quarter-chord angle of attack.

An incidence correction factor

$$\alpha_c = \arctan\left(\frac{1-\cos(\Delta\alpha/2)}{\sin(\Delta\alpha/2)}\right) \tag{7.17}$$

is introduced and added to the uncorrected angle of attack. Like the Goude model, α_c is positive on the upstream half of the turbine rotation and negative on the downstream half.

It was determined that the Goude model performed best with respect to matching the near-wake characteristics measured in the experiments, while the performance predictions from both flow curvature models were relatively close to each other. Thus, the Goude model was used for all simulations reported here.

7.8 End effects

Helmholtz's second vortex theorem states that vortex lines may not end in a fluid, but must either form closed loops or extend to boundaries. Consequently the lift distribution due to the bound vortex from foils of finite span must drop to zero at the tips.

Glauert [85] used Prandtl's lifting line theory [154] to develop a tip loss correction factor F to be applied to the local lift of an axial-flow rotor blade element:

$$F = \frac{2}{\pi}\cos^{-1}\left[\exp\left(-\frac{N(R-r)}{2R\sin\phi_R}\right)\right], \tag{7.18}$$

where F is the correction factor applied to the local lift, N is number of blades, R is the rotor radius, r is the local blade element radius, and ϕ_R is the flow angle at the tip.

The Glauert correction was further refined for horizontal-axis wind turbines by Shen et al. [167] as

$$F_1 = \frac{2}{\pi}\cos^{-1}\left[\exp\left(-g\frac{N(R-r)}{2R\sin\phi_R}\right)\right], \tag{7.19}$$

where g is an additional function depending on the tip speed ratio and two tuning constants:

$$g = \exp[-c_1(B\lambda - c_2)]. \tag{7.20}$$

Despite their success for the blade element analysis of axial-flow rotors, these corrections both depend on rotor parameters—tip speed ratio, number of blades, element radius, tip flow angle—that do no necessarily translate directly to the geometry and flow environment of a cross-flow rotor. Therefore, a more general end effects model was sought.

From Prandtl's lifting line theory, the geometric angle of attack α of a foil with an arbitrary circulation distribution can be expressed as a function of nondimensional span θ as [7]

$$\alpha(\theta) = \frac{2S}{\pi c(\theta)}\sum_1^N A_n \sin\theta + \sum_1^N nA_n\frac{\sin n\theta}{\sin\theta} + \alpha_{L=0}(\theta), \tag{7.21}$$

where S is the span length, $c(\theta)$ is the chord length, and N is the number of locations or elements sampled along the foil. This relationship can be rearranged into a matrix equation to solve for the unknown Fourier coefficients A_n,

$$[\alpha_m] - \alpha_{L=0} = [D_{mn}][A_n], \tag{7.22}$$

where

$$D_{mn} = \sum_1^N\left[\frac{2b}{\pi c_m}\sin n\theta_m + n\frac{\sin n\theta_m}{\sin\theta_m}\right]. \tag{7.23}$$

With the Fourier coefficients, the circulation distribution can be calculated as

$$\Gamma(\theta) = 2SU_\infty\sum_1^N A_n \sin n\theta, \tag{7.24}$$

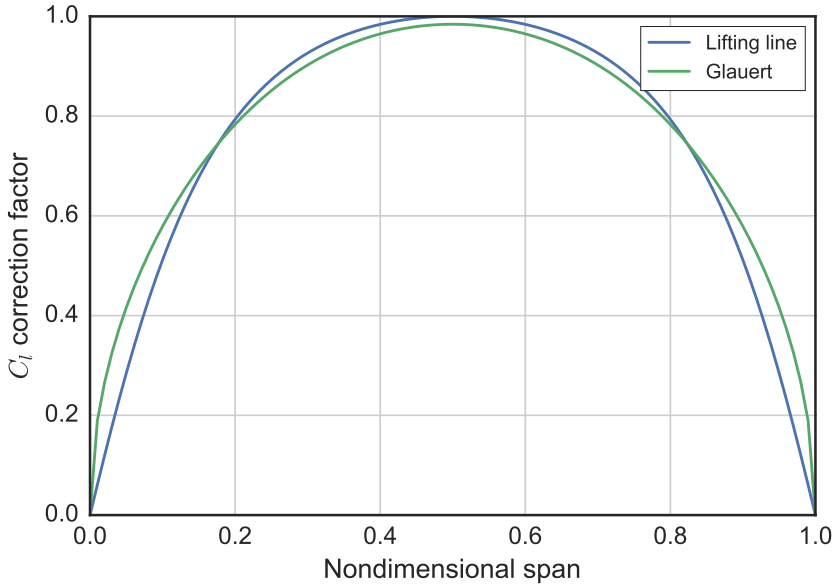

Figure 7.2: End effect correction function values for the Glauert and lifting line methods using UNH-RVAT parameters at 20 degrees tip angle of attack and $\lambda = 1.9$.

which, via the Kutta–Joukowski theorem, provides the lift coefficient distribution

$$C_l(\theta) = \frac{-\Gamma(\theta)}{\frac{1}{2}cU_\infty}. \tag{7.25}$$

We can therefore compute a correction function based on the normalized spanwise lift coefficient distribution

$$F = C_l(\theta)/C_l(\theta)_{\max}, \tag{7.26}$$

which will be in the range $[0,1]$, similar to the Glauert corrections, but does not contain rotor parameters.

The correction functions for the standard Glauert and lifting line methods are plotted for comparison in Figure 7.2. Function values were computed using the UNH-RVAT geometry, $\lambda = \lambda_0 = 1.9$, and a 20 degree tip angle of attack. Both end effects corrections produce similar results for this specific case, which gives confidence that the lifting line method will produce reasonable results without the uncertainty of translating axial-flow to cross-flow rotor parameters.

```
tmp<fvVectorMatrix> UEqn
(
    fvm::ddt(U)
    + fvm::div(phi, U)
    + turbulence->divDevReff(U)
    ==
    fvOptions(U)
);
```

Listing 7.1: Adding source terms to the momentum equation in OpenFOAM.

7.9 Software implementation

NREL has developed and released an actuator line modeling library, SOWFA [61], for simulating horizontal-axis wind turbine arrays using the OpenFOAM finite volume CFD library. OpenFOAM is free, open-source, widely used throughout industry and academia, and has grown a very active support community around itself [13]. Though SOWFA is also open-source, and has the ability to be coupled to NREL's FAST HAWT BEM code, its mostly procedural style would have required significant effort and duplicate code to adapt for cross-flow turbines. Thus, a new and more general ALM library was developed from the ground up that could model both cross- and axial-flow turbines, as well as standalone actuator lines. The actuator line model developed here, dubbed turbinesFoam [22], was also written as an extension library for OpenFOAM, and was developed freely and openly from its inception in order to increase community engagement and research efficiency.

turbinesFoam was written in OpenFOAM's style, using OpenFOAM's `fvOptions` framework for adding source terms to equations at runtime—see Listing 7.1 for an example implementation within the Navier–Stokes' momentum equation. Using the `fvOptions` framework allows the CFT-ALM to be added to many of the solvers included in OpenFOAM, meaning it can be readily used with RANS or LES, multiphase models (e.g., for simulating the free surface in MHK installations), and even with heat transfer. This is in contrast to SOWFA's implementation, which requires custom flow solvers to be developed and maintained.

OpenFOAM and turbinesFoam are written in the C++ programming language, which follows the object oriented programming paradigm. This characteristic helped modularize the ALM code for increased readability and reuse. In turbinesFoam, a turbine is a software object that is composed of actuator line objects, which themselves are composed of actuator line element objects. Structuring the code this way allows isolation and reuse of the functionality of individual components. For example, the actuator line object was written such that is could be used outside the turbine context to ensure it produces the correct forcing, without adding the complexity of rotation, other actuator lines, etc. that would be present in a turbine rotor. The very same actuator line objects can be used in both axial-flow and cross-flow rotors, without having to copy code from one to the other. In contrast, the actuator line model in SOWFA uses a single software object to represent an entire array of turbines, which necessitates iterating through many nested lists down to the element level, which can be confusing to read.

OpenFOAM's data structures are designed to be inherently parallel via message passing interface (MPI). By working within the library infrastructure the ALM code was easily parallelized, which will facilitate its deployment on high performance computing clusters for large flow simulations.

Since all applications are run from a command line and all input data is text based, automation and integration with other tools is relatively straightforward. Future enhancements could include coupling with software for generating static foil data, e.g., XFOIL [71] or other OpenFOAM solvers, turbine controller models, structural analysis codes, and optimization tools, e.g., SNL's DAKOTA [2] or OpenMDAO [90], for both individual turbines and array layouts.

7.10 Results

Both the high solidity UNH-RVAT and medium-low solidity RM2 turbines were modeled using the ALM inside a Reynolds-averaged Navier–Stokes (RANS) simulation, closed with the standard k–ε turbulence model. These rotors provide diverse parameters, which helped evaluate the robustness of the ALM. The simulations were performed inside a domain similar in size to that used in Chap-

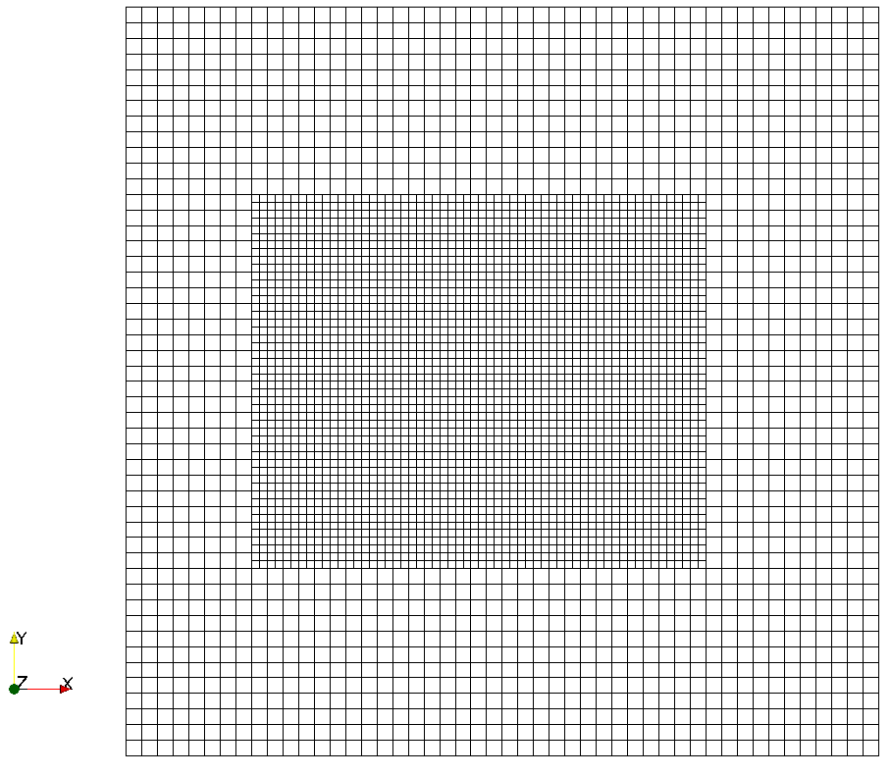

Figure 7.3: *x*–*y* planar slice of the mesh used for the ALM RANS simulations.

ter 6 to mimic the tow tank (3.66 m wide, 2.44 m tall, 1.52 m upstream and 2.16 m downstream), with similar boundary conditions (1 m/s inflow, no-slip walls and bottom, and a rigid slip for the top). Simulations were run for a total of 6 seconds, with the latter half used to calculate performance and wake statistics. Pressure–velocity coupling for the momentum equation was achieved using the PISO (pressure implicit splitting of operators) method. A slice of the mesh in the *x*–*y* plane is shown in Figure 7.3.

Similar numerical settings were used for each turbine as well. The Sheng et al. DS model was used with the default coefficients given in [168], and the Goude flow curvature correction was employed. A second order backward difference was used for advancing the simulation in time, and second order linear schemes were used for the majority of the terms' spatial discretizations. The only major difference between the two simulation configurations was that the end effects model was deactivated for the RM2, since it reduced C_P far below the experimental measurements. This

modification is consistent with the RM2 blades' higher aspect ratio (15 versus the UNH-RVAT's 7.1) and tapered planform, though will need to be investigated further. The number of elements per actuator line was set to be approximately equal to the total span divided by the Gaussian force projection width ε. Case files for running all the simulations presented here with OpenFOAM 3.0.x are available from [19, 14, 20].

The same foil coefficient data were used for all simulations—those for a NACA 0021 as reported by Sheldahl and Klimas [165]. Each rotor's shaft was assumed to have a drag coefficient $C_d = 1.1$, and the blade support strut end element drag coefficients were set to 0.05, to approximate the effects of separation in the corners of the blade–strut connections.

Since the ALM is intended to be an engineering tool when coupled with RANS, it was assumed that information about tip speed ratio due to control details—that is, sinusoidally oscillating λ—would not be known a priori, and was excluded, unlike the 3-D blade-resolved cases in Chapter 6. Note that a systematic investigation of the effects of sinusoidal λ was not undertaken, but for the UNH-RVAT a one to two percentage point increase in C_P was observed when running with similar parameters as the blade-resolved simulation.

Compared to 3-D blade-resolved RANS, the ALM can solve a standalone turbine case on the order of CPU minutes per second of simulated time versus 1,000 CPU hours per second—a savings of 4 orders of magnitude.

7.10.1 Verification

Verification for sensitivity to spatial and temporal grid resolution was performed for both the UNH-RVAT and RM2 RANS cases at their optimal tip speed rations, the results from which are plotted in Figure 7.4 and Figure 7.5, respectively. Similar to the verification strategy employed in Chapter 6, the mesh topology was kept constant, and the resolution was scaled proportional to the number of cells in the x-direction N_x for the base hexahedral mesh. Both models displayed low sensitivity to the number of time steps per revolution. Spatial grid dependence, however, was more important.

Final spatial grid resolutions were chosen as $N_x = 48$ for both the UNH-RVAT and RM2 cases. Time steps were chosen as $\Delta t = 0.01$ and $\Delta t = 0.005$ seconds for the UNH-RVAT and RM2 re-

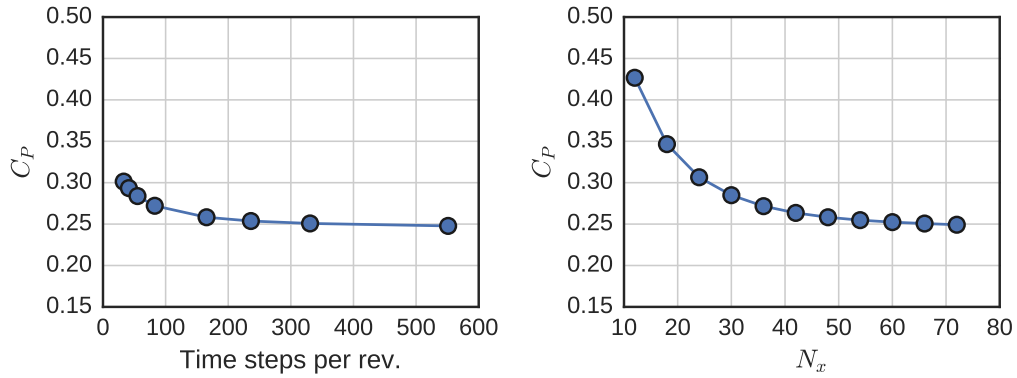

Figure 7.4: Temporal (left) and spatial (right) grid resolution sensitivity results for the UNH-RVAT ALM RANS model.

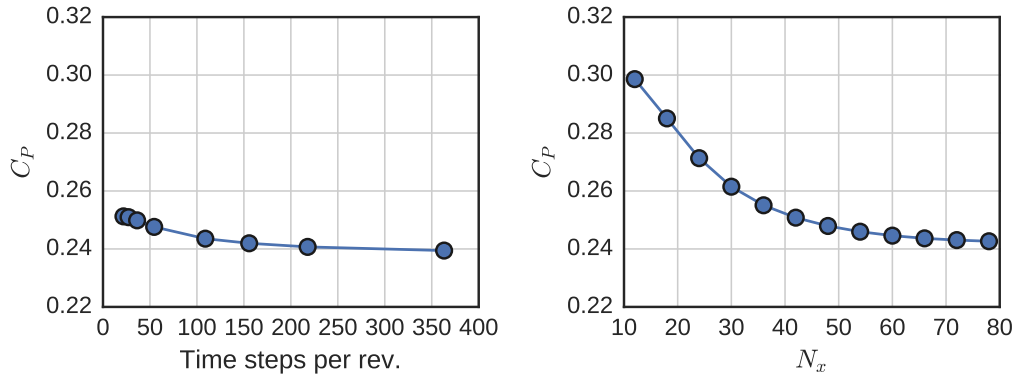

Figure 7.5: Temporal (left) and spatial (right) grid resolution sensitivity results for the RM2 ALM RANS model.

spectively, which correspond to approximately 200 steps per revolution. The chosen values should provide C_P predictions within one percentage point of the true solution, which is on the order of the expanded uncertainty of the experimental measurements. Note that for computing performance curves, the number of steps per revolution was kept constant, i.e., the time step was adjusted to $\Delta t = \Delta t_0 \lambda_0 / \lambda$.

7.10.2 UNH-RVAT RANS

Power and drag coefficient curves are plotted for the UNH-RVAT in Figure 7.6. The ALM was successful at predicting the performance tip speed ratios up to λ_0, which suggests that dynamic stall

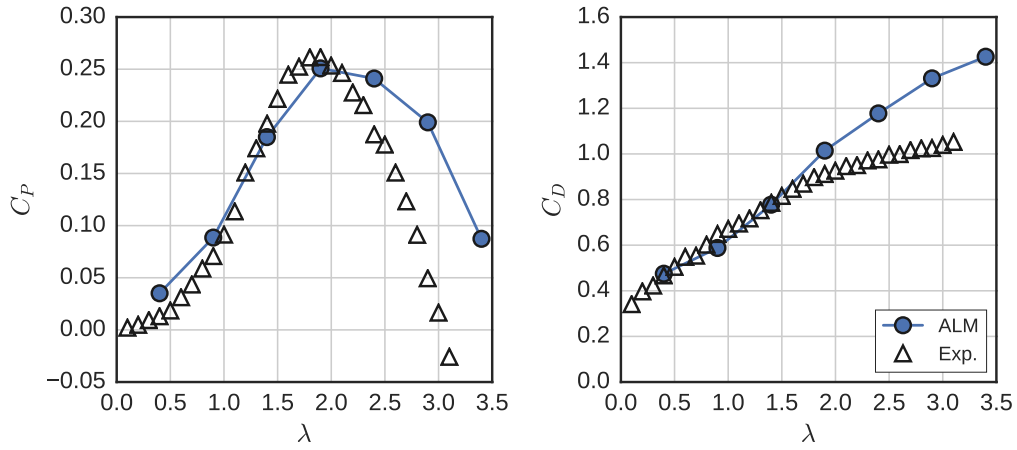

Figure 7.6: Power and drag coefficient curves computed for the UNH-RVAT using the actuator line model with RANS.

was being modeled accurately, but C_P was overpredicted at high λ. This may have been caused by the omission of additional parasitic drag sources such as roughness from exposed bolt heads located far enough from the axis to have a large effect at high rotation rates, or an underestimation of the blade–strut connection corner drag coefficient. In Chapter 5 we showed how these losses can be significant even with carefully smoothed struts and strut-blade connections. Overprediction of performance at high tip speed ratio could also be a consequence of the Leishman–Beddoes dynamic stall model, which can also be seen in the Darrieus VAWT momentum model results shown in Figure 6.70 of [148].

Figure 7.7 shows mean velocity field for the UNH-RVAT computed by the ALM RANS model. The asymmetry was captured well, along with some of the vertical flow due to blade tip vortex shedding, though the flow structure is missing the detail present in the experiments and blade-resolved RANS simulations. Overall, the wake appears to be over-diffused, which could be a consequence of the relatively coarse mesh. Note that with the DS and flow curvature corrections turned off, the direction of the mean swirling motion reverses, which highlights the importance of resolving the correct azimuthal location of blade loading.

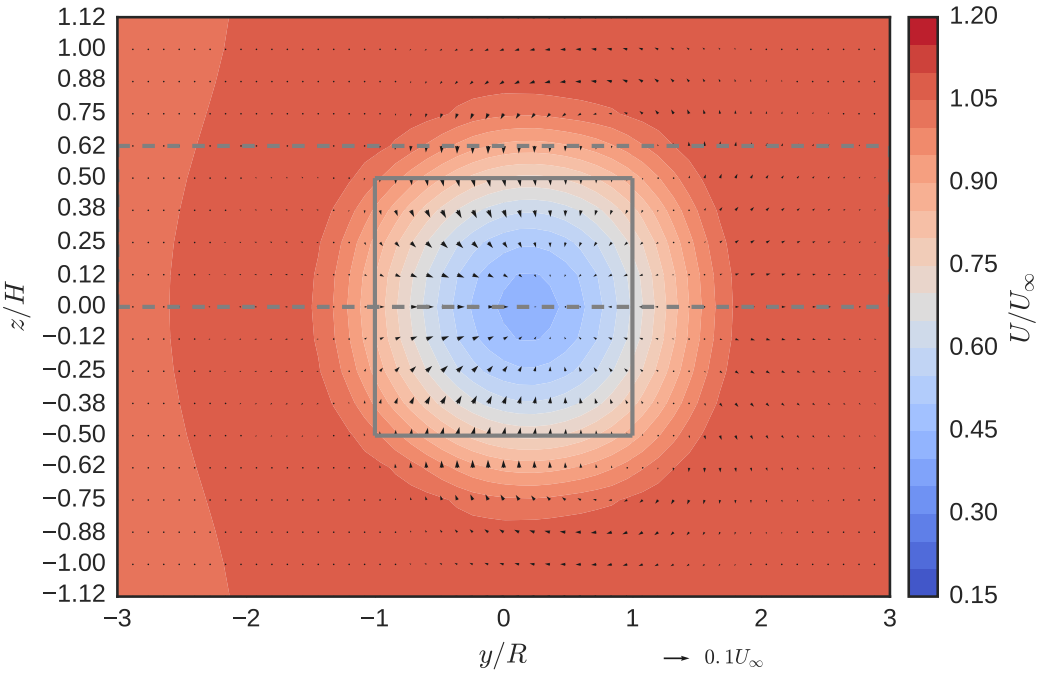

Figure 7.7: UNH-RVAT mean velocity field at $x/D = 1$ computed with the ALM coupled with a k–ε RANS model.

Turbulence kinetic energy contours (including resolved and modeled energy) are shown in Figure 7.8. The ALM was able to resolve the concentrated area of k on the $+y$ side of the turbine, but the turbulence generated by the dynamic stall vortex shedding process is absent. This makes sense since in the ALM, the DS model only modulates the body force term in the momentum equation, which does not provide a mechanism for mimicking shed vortices or turbulence.

Profiles of mean streamwise velocity and turbulence kinetic energy are shown in Figure 7.9. Here the over-diffused or over-recovered characteristic of the mean velocity deficit seen in Figure 7.7 is more apparent. This effect is also seen in the profile of k, where energy is smeared over the center region of the rotor.

Weighted averages for the momentum recovery terms were computed identically as they were in Chapter 6, and are plotted in Figure 7.10 along with the actuator disk (AD) results from Chapter 3, 3-D blade-resolved RANS results from Chapter 6 and experiments. The most glaring discrepancy is the ALM's prediction of positive cross-stream advection, which is caused by the lack

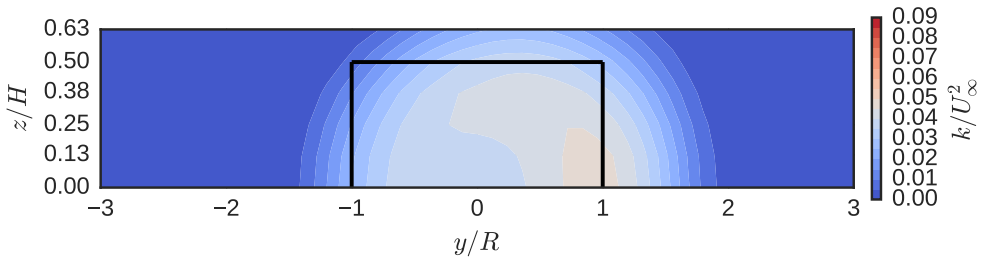

Figure 7.8: UNH-RVAT turbulence kinetic energy contours at $x/D = 1$ predicted by the ALM inside a k–ε RANS model.

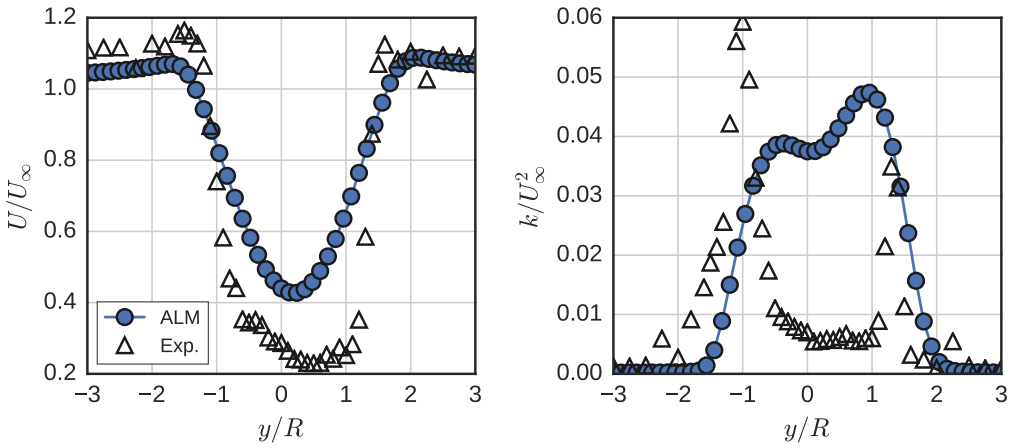

Figure 7.9: Mean streamwise velocity (left) and turbulence kinetic energy (right) profiles at $z/H = 0$ for the UNH-RVAT ALM.

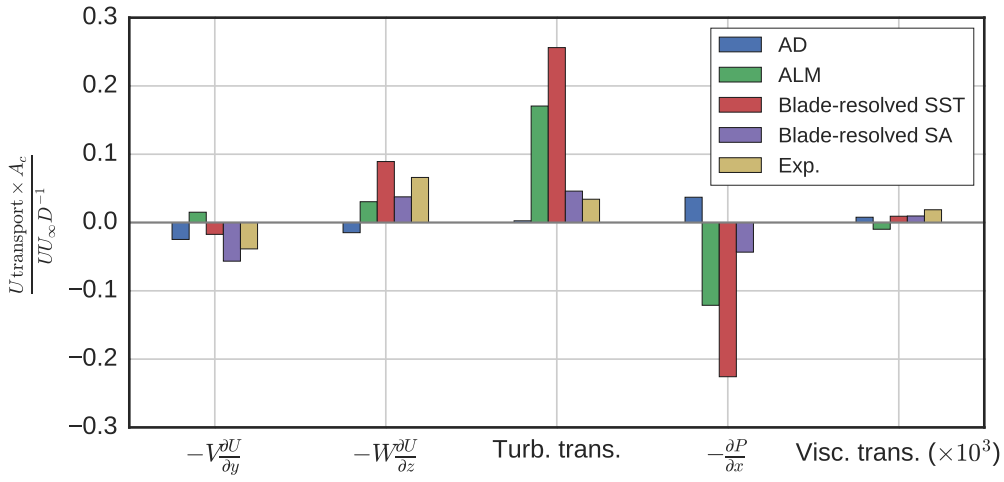

Figure 7.10: Weighted average momentum recovery terms for the actuator disk (AD) simulation from Chapter 3, UNH-RVAT actuator line model with a k–ε RANS closure, the two 3-D blade resolved RANS models described in Chapter 6, and the experiments in Chapter 3.

of detail in the tip vortex shedding. The total for vertical advection, however, is close to that predicted by the 3-D blade-resolved Spalart–Allmaras model. Levels of turbulent transport due to eddy viscosity and deceleration due to the adverse pressure gradient are between those predicted by the 3-D blade-resolved k–ω SST and SA models. Overall, however, one might expect the total wake recovery rate to be comparable between all models except the actuator disk, which induces negative vertical advection, very little turbulent transport, and has a positive pressure gradient contribution. These results suggests the ALM would be an effective tool—much better than an actuator disk—for assessing downstream spacing of subsequent CFTs, though blade–vortex interaction for very tightly spaced rotors may not be captured, at least on relatively coarse meshes as used here.

7.10.3 RM2 RANS

Figure 7.11 shows the performance curves computed for the RM2 by the ALM, and those from the tow tank experiments. As with the high solidity RVAT, C_P is overpredicted at high λ. However, λ_0, the tip speed ratio of peak power coefficient, is also shifted to the right. This is indicative of inaccurate dynamic stall modeling, which could be attributed to one of the models' tuning constants, e.g., the time constant T_α for the lagged angle of attack α', the change of which per time

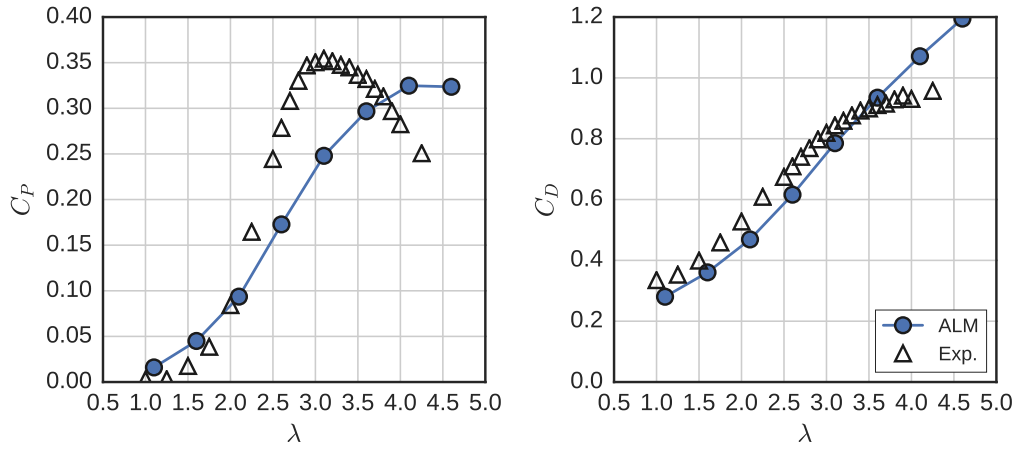

Figure 7.11: Power and drag coefficient curves computed for the RM2 using the ALM.

step is given by [168]

$$\Delta\alpha' = \Delta\alpha(s)(1 - \mathrm{e}^{-s/T_\alpha}), \tag{7.27}$$

where s is a nondimensional time, defined as [113]

$$s = \frac{2|\vec{U}_{\mathrm{rel}}|t}{c}. \tag{7.28}$$

Limited ad hoc testing revealed that the mean C_P at λ_0 more closely matched experimental measurements with T_α roughly double the default value given in [168]. This could be investigated further by looking at the phase of, e.g., maximum C_P peaks compared to the experimental values (or possibly those from blade-resolved CFD), but for the present study only mean values were considered.

Figure 7.12 shows the mean velocity field at 1 m downstream or $x/D = 0.93$ computed by the ALM for the RM2. The mean near-wake structure looks similar to the RVAT ALM RANS case, but for the RM2, the lack of detail from blade tip vortex shedding matches more closely with experiments. However, the vertical flow towards the x–y center plane was captured, which is an important qualitative feature of both CFT near-wakes.

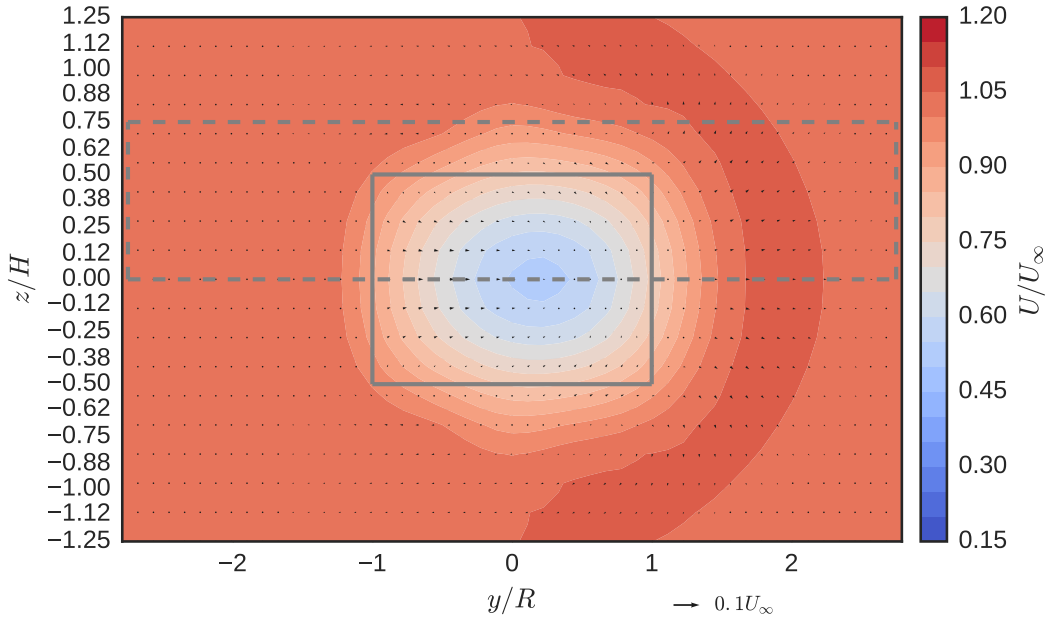

Figure 7.12: Mean velocity field at $x/D = 0.93$ for the RM2 predicted by the ALM.

Figure 7.13 shows the ALM's turbulence kinetic energy predictions in the near-wake of the RM2. Like for the UNH-RVAT, k appears to be concentrated on the $+y$ side of the rotor. However, overall levels of turbulence are lower than for the UNH-RVAT, which is consistent with the experimental results. However, turbulence generated by the RM2's blade tip vortex shedding was not captured by the ALM.

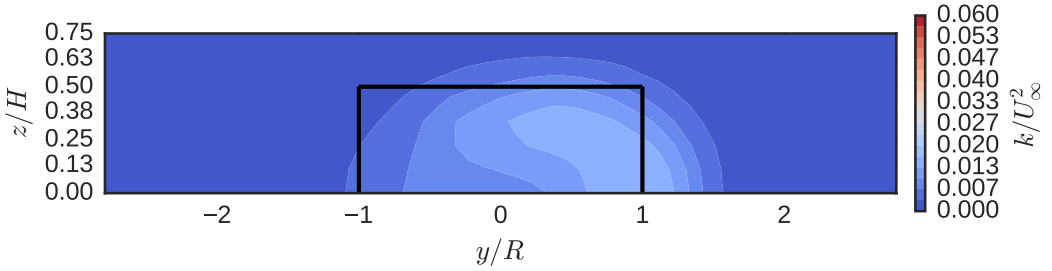

Figure 7.13: Turbulence kinetic energy contours at $x/D = 0.93$ behind the RM2 predicted by the ALM.

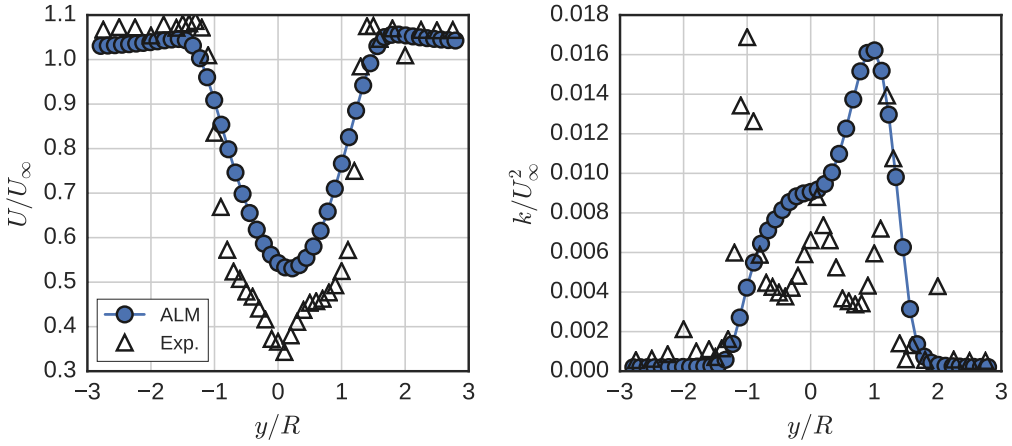

Figure 7.14: Mean streamwise velocity (left) and turbulence kinetic energy (right) profiles at $x/D = 0.93$ and $z/H = 0$ computed for the RM2 using the ALM inside a k–ε RANS model.

Wake profiles at turbine mid-height in the x–y center plane are shown in Figure 7.14. Like the UNH-RVAT case, the mean velocity deficit appears to be recovering too quickly, which may similarly be due to coarseness of the grid or overprediction of the eddy viscosity. The peak in turbulence kinetic energy on the $-y$ side of the turbine was also underpredicted, though was much lower in magnitude compared to the UNH-RVAT, even in the experimental measurements.

Finally, a similar mean streamwise momentum transport analysis was undertaken by computing weighted sums of each term across the entire domain in the y–z directions. Similar results as for the UNH-RVAT were obtained, i.e., cross-stream advection was predicted to be positive where it should have been negative, vertical advection was predicted reasonably well, and turbulent transport due to the eddy viscosity was also relatively large. The ratio of wake transport compared with the UNH-RVAT RANS case (approximately 60% to 70% lower for the RM2) matches well with that computed from the experiments, which shows the ALM may successfully predict larger optimal array spacing for the RM2 versus UNH-RVAT.

7.10.4 UNH-RVAT LES

The state-of-the-art in high fidelity turbine array modeling uses the actuator line method coupled with large eddy simulation (LES), which allows more of the turbulent energy spectrum to be di-

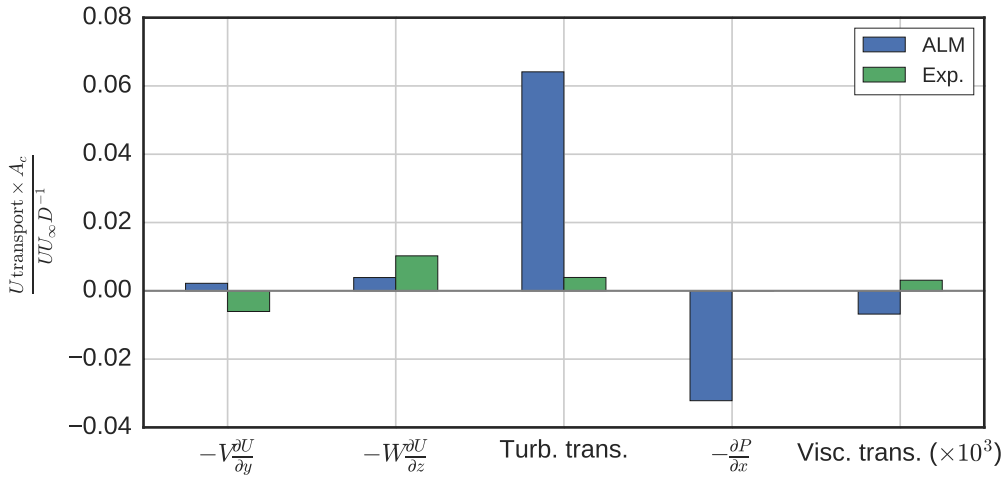

Figure 7.15: Weighted average momentum recovery terms at $x/D = 0.93$ for the RM2 actuator line model with a k–ε RANS closure and the experiments described in Chapter 5.

rectly resolved, only requiring the dynamics of the smallest scales—where dissipation occurs—to be computed by the so-called subgrid-scale (SGS) model. Since the ALM LES approach has only been reported in the literature for a very low Reynolds number 2-D CFT [164], and CFTs may provide unique opportunities to array optimization, which could be explored with LES, it was of interest to determine how well the ALM coupled with LES might predict wake dynamics of a higher *Re* 3-D CFT rotor.

Thus, the UNH-RVAT baseline case was simulated using the Smagorinsky LES turbulence model [171], which was the first of its kind, and serves as a good standard for LES modeling since its behavior is well-reported in the literature. Default Smagorinsky model coefficients were used, LES filter width was set as the cube root of the local cell volume. The tip speed ratio was set to oscillate sinusoidally about λ_0 with a 0.19 magnitude and the angle of the first peak at 1.4 radians—similar to the rotation presribed in the blade-resolved RANS simulations discussed in Chapter 6.

Since the computational cost of LES is significantly higher than RANS, verification with respect to grid dependence was not performed. Instead, mesh resolution was chosen relative to similar studies of turbine wake ALM LES. Of the studies surveyed [164, 10, 125, 186], the mesh

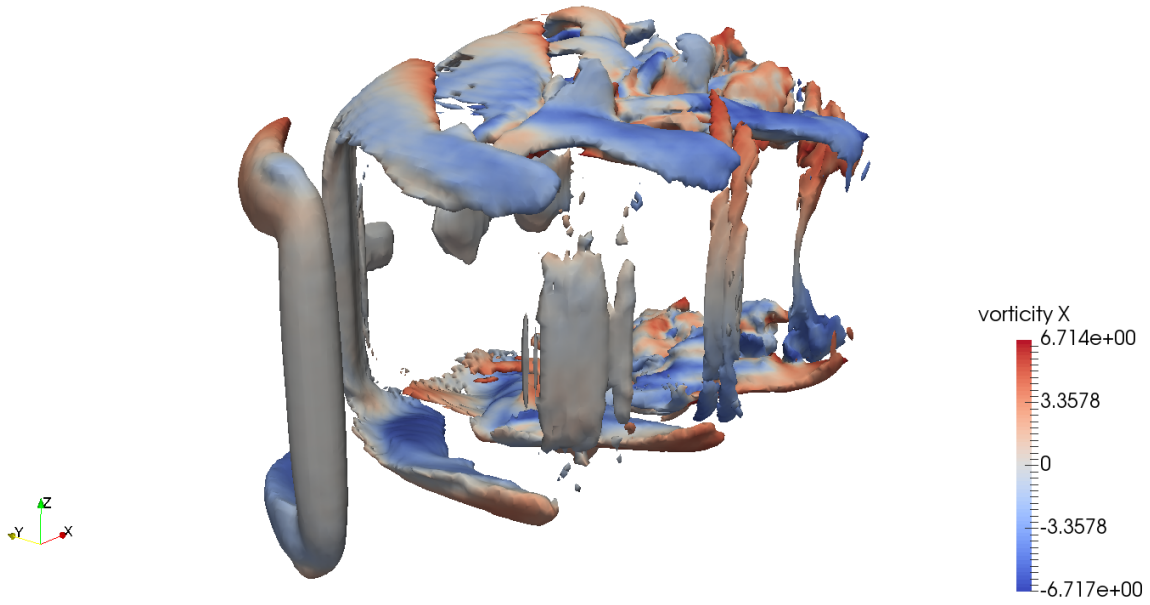

Figure 7.16: Snapshot of vorticity isosurfaces (colored by their streamwise component) at $t = 6$ s for the UNH-RVAT LES case.

resolution ranged from 18–64 points per turbine diameter. The mesh here was set accordingly by using a 16 point per meter base mesh, and refining twice in a region containing the turbine to produce a 64 point per turbine diameter/height resolution. The solver was run with a 0.002 second time step, which is significantly within the limit described by [124], where an actuator line element may not pass through more than one cell per time step. With these resolutions computation times were $O(10)$ CPU hours per second of simulated time, which is approximately two orders of magnitude lower than for blade-resolved RANS.

Mean power coefficient predictions for the UNH-RVAT at its optimal mean tip speed ratio dropped to 0.20 using the ALM within the large eddy simulation. However, the amount of information regarding the wake dynamics was greatly increased, even beyond that of the 3-D blade-resolved RANS. Figure 7.16 shows an instantaneous snapshot of isosurfaces of vorticity produced by the actuator lines.

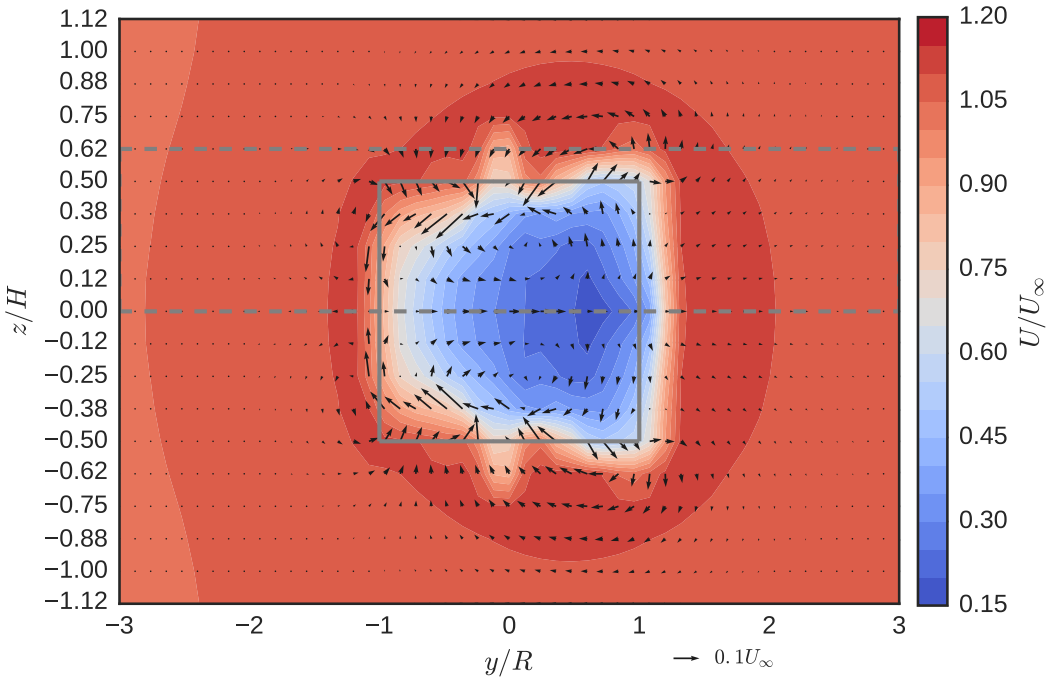

Figure 7.17: Mean velocity field in the UNH-RVAT near-wake at $x/D = 1$ computed with the Smagorinsky LES model.

The near-wake's mean velocity field at $x/D = 1$ is shown in Figure 7.16. Compared with the RANS ALM results, the LES looks much more like the blade-resolved and experimental results, showing the clockwise and counterclockwise mean swirling motion on the $-y$ and $+y$ sides of the rotor, respectively.

Contours of turbulence kinetic energy sampled at $x/D = 1$ from the large eddy simulation are plotted in Figure 7.18. Compared with RANS, LES is more able to predict the turbulence generated by the blade tip vortex shedding and dynamic stall effects, though the overall level of unsteadiness generated was much lower, especially on the $+y$ side of the rotor. This is likely a consequence of the SGS modeling, where the vortical structures generated by the blades remain stable further downstream. Similar effects were seen in [125, 164], where higher levels of the Smagorinsky coefficient delayed vortex breakdown and subsequent higher levels of turbulence. Figure 7.16 shows evidence of these effects, where the blade bound and tip vortices are still relatively coherent at $x/D = 1$.

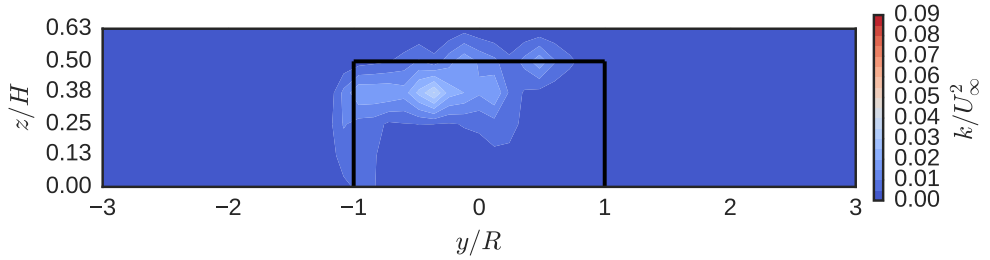

Figure 7.18: Turbulence kinetic energy in the UNH-RVAT near-wake at $x/D = 1$ computed with the Smagorinsky LES model.

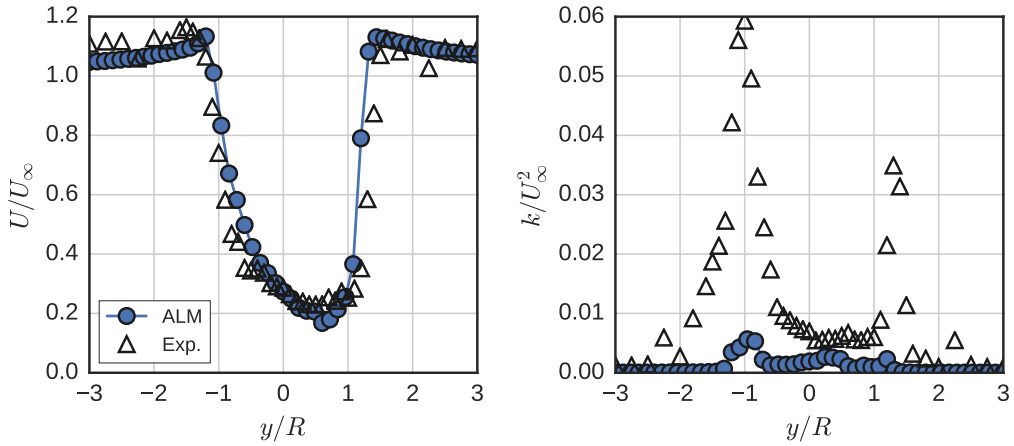

Figure 7.19: Mean velocity profiles in the UNH-RVAT near-wake at $x/D = 1$ and $z/H = 0$ computed with the Smagorinsky LES model.

Mean velocity profiles at the turbine center plane, plotted in Figure 7.19, were predicted more accurately using LES versus RANS, and rival those of the 3-D blade-resolved models. However, turbulence kinetic energy profiles did not match as closely with experiments. Though the qualitative shape was resolved better than that by the RANS ALM simulation, notably the asymmetric peaks around $y/R = \pm 1$, the turbulence generated in the large eddy simulation was approximately an order of magnitude too low. Once again this was probably a result of the subgrid-scale modeling and its effect on the stability of vortex structures.

The planar weighted sums of streamwise momentum recovery terms were computed in the same way as for the RANS cases with the exception of the turbulent transport term, which for the

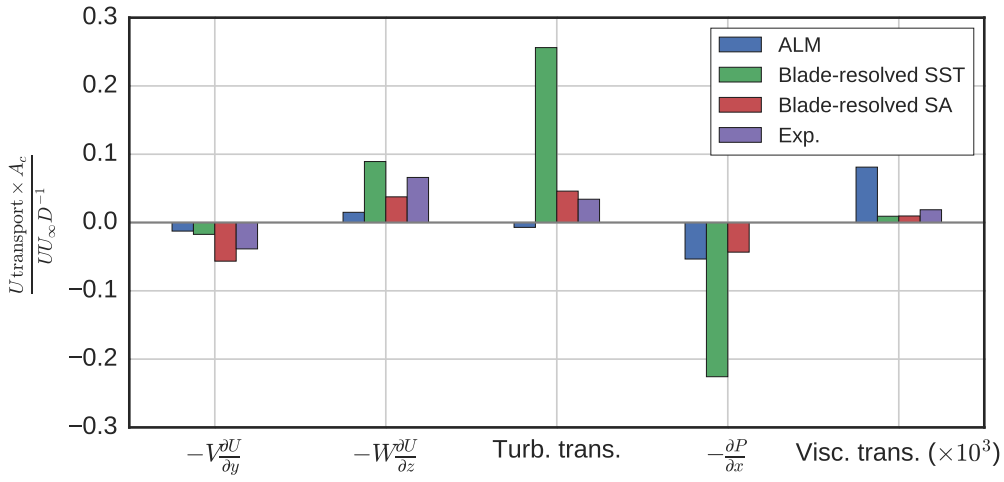

Figure 7.20: Weighted average momentum recovery terms at $x/D = 1$ for the RVAT ALM LES using the Smagorinsky SGS model.

LES was computed from the x-components of the divergence of the resolved and SGS Reynolds stress tensors:

$$\text{Turb. trans.} = -\left(\frac{\partial}{\partial x_j}\overline{u_x' u_j'} + \frac{\partial}{\partial x_j} R_{xj}\right), \tag{7.29}$$

where u indicates the resolved or filtered velocity, and R is the subgrid-scale Reynolds stress.

Transport term weighted sums computed from the LES results are shown in Figure 7.20. Unlike the RANS ALM cases, the cross-stream advection contributions are negative, as they are in the experiment and blade-resolved CFD models. The vertical advection term is positive as expected, though smaller than in other cases. Interestingly, the turbulent transport is negative in the LES, meaning the combined effects of the resolved and SGS stressed are transferring momentum out of the wake. The low turbulent transport appears to be partially balanced by higher levels of viscous diffusion—about an order of magnitude larger than the 3-D blade-resolved RANS models and experiments. These discrepancies highlight the difficulty of predicting the near-wake dynamics, the importance of the SGS model in LES, and the need for data further downstream to test and refine predictions for wake evolution. For example, setting the Smagorinsky coefficient higher may induce vortex breakdown earlier, which would raise the turbulence levels significantly.

7.11 Conclusions

An actuator line model for cross-flow turbines, including a Leishman–Beddoes type dynamic stall model, flow curvature, added mass, and lifting-line based end effects corrections, was developed and validated against experimental datasets acquired for high and medium-low solidity rotors at scales where the performance and near-wake dynamics were essentially Reynolds number independent. When coupled to a k–ε RANS solver ALM simulations took $O(0.1)$ CPU hours per second of simulated time, while when coupled with a Smagorinsky LES model the computing time was $O(10)$ hours per second, which represent a four and two order of magnitude decrease in computational expense versus 3-D blade-resolved RANS, respectively.

The RANS ALM predicted the UNH-RVAT performance well at tip speed ratios up to and including that of max power coefficient. The RM2 power coefficient on the other hand was underpredicted at lower λ. Both models overestimated C_P at the highest tip speed ratios, which has been observed in other simulations using Leishman–Beddoes type dynamic stall models. Possible explanations include underestimation of added mass effects or blade–strut connection corner drag, incorrect time constants in the LB DS model, and/or inaccuracy due to the virtual camber effect. In the present flow curvature model, the angle of attack is corrected, but the foil coefficient data is not transformed, meaning the LB DS separation point curve fit parameters are equal for both positive and negative angles of attack. A foil data transformation algorithm based on virtual camber should be investigated for future improvement of the ALM.

The RANS ALM cases were able to match some important qualitative near-wake flow features, e.g., the mean vertical advection velocity towards the mid-rotor plane. However, the mean flow structure and turbulence generation due to blade tip and dynamic stall vortex shedding shows some discrepancy with experimental and blade-resolved CFD. Extensions to the ALM to deal with these shortcomings should be developed, e.g., a turbulence injection model as employed by James et al. [100] or a model that will "turn" the ALM body force vectors to approach the effects of leading and trailing edge vortex shedding during dynamic stall.

The UNH-RVAT was simulated with the ALM embedded within a typical Smagorinsky LES, which thanks to its lower diffusion and/or dissipation was able to more accurately capture the large scale vortical flow structures shed by the rotor blades. Turbulence generated by the blade tip vortex shedding and dynamic stall region of the blade path was better resolved, but overall lower levels of turbulence were predicted, which is likely a consequence of the subgrid-scale model's influence on the stability of shed vortices. This effect was also apparent in the negative predictions of turbulent transport on the streamwise momentum recovery. Therefore, subgrid-scale modeling should be investigated further before applying the ALM LES to array analyses.

The ALM provides a more physical flow description compared to momentum and potential flow vortex models, at a reasonable cost. The ALM also drastically reduces computational effort compared to blade-resolved CFD, while maintaining the unsteadiness of the wake not resolved by a conventional actuator disk. Furthermore, its implementation within finite volume CFD provides a convenient way to study turbine array siting, since effects like terrain and buildings can be included, as can no-slip boundary conditions and boundary layer inflow profiles. Since the turbinesFoam library developed here uses OpenFOAM's modular `fvOptions` framework, the ALM body force term can be added as-is to compressible or multiphase solvers, for exploring more complicated physics. These features would be difficult or impossible to implement in a momentum or vortex models.

Ultimately, the ALM retains some of the disadvantages of other blade element methods, but is a the next logical step bridging the gap between low- and high-fidelity flow modeling, and has been shown to be a method worthy of further advancement. The prospect of using ALM simulations to drive down computational cost of RANS by roughly four orders of magnitude—enabling 3-D unsteady Navier–Stokes simulations to be performed on a typical PC—itself justifies further development.

At contemporary levels of computing power, the ALM is a useful tool for studying individual turbines when HPC is not feasible—requiring similar resources as 2-D blade-resolved RANS, but with improved performance predictions. Furthermore, if arrays of CFTs advance to commercial

scale, the ALM combined with LES represents one of the highest fidelity tools available, and will improve as turbulence modeling improves. It is therefore expected that this tool will prove valuable for both the engineering and research of wind and MHK turbines.

7.12 Future work

The actuator line model shows great potential for use in cross-flow turbine engineering, and this study has inspired many avenues for its improvement.

Firstly, since the fundamental premise of the ALM relies on accurate static foil coefficient data, it is crucial that more be measured and published openly, to allow the exploration of new rotor designs with various profiles. There is some doubt regarding the veracity of the Sheldahl and Klimas NACA foil data [44]. However, competing datasets at large laboratory scale Reynolds numbers are rare, even for the standard symmetrical foils. CFD may play a role in generating new data, but models must be rigorously validated, given the difficulty in predicting stall and its importance on CFT blade loading.

Profile coefficient databases could be expanded to include more dimensions, or independent variables. For example, since the ALM will almost always involve turbulence modeling, the effects of local turbulence levels on foil coefficient data could be included, since stall delay could affect loading significantly, especially for a cross-flow turbine.

Dynamic stall model empirical constants should be further investigated for their optimal values within the cross-flow turbine context. Though the Leishman–Beddoes type models are formulated in terms of a nondimensional time, there may be a dependence of the various time constants on the pitch rate, as indicated by the improvement in predictions for the RM2 at optimal tip speed ratio when using a higher angle of attack lag time constant. Machine learning techniques could be employed to "train" the constants (and/or their λ-dependence) to one turbine's power curve, and they could be validated against the other turbine's data. A more data-intensive alternative could be to develop dynamic cyclic profile coefficient databases—either experimentally or numerically—for many reduced frequencies, though this would be a difficult task, even for a single profile.

Flow curvature corrections should be examined in more detail, and it may be beneficial to develop models to transform entire foil datasets to match their virtual camber, as suggested by Migliore et al. [137]. It also may be advantageous to implement a complementary model to adjust the direction of the resultant force vector to more accurately generate the blade's shed vorticity.

Rotor angular speed control via generator models could be included to test the effectiveness of various control schemes, e.g., sinusoidal λ set points, which have been shown in some cases to improve mean power coefficient [180]. Free stream velocity sampling could be implemented to determine the optimal location for sensing reference velocity used to compute tip speed ratio and power coefficient, which can become difficult in sheared or otherwise nonuniform flows [82].

Since turbinesFoam is compatible with OpenFOAM's volume of fluid (VOF) multiphase flow solver interFoam, the ALM's effectiveness should be assessed for predicting the generation and interaction of turbines with surface waves. The ADV positioning system developed in Chapter 2 could be retrofitted with a wave staff to measure and validate the free surface disturbance, which could be key to predicting the effects of placing turbines in channels at high blockage ratio.

Possibly most importantly, the ALM should be validated with far-wake velocity measurements and/or performance data from two CFTs operating in proximity of each other. Next, the ALM should be evaluated for its use in modeling CFT arrays using both RANS and LES. If either can successfully postdict experimentally measured performance of closely-spaced physical model CFTs, they should then be coupled with optimization algorithms to automatically explore the design space, and ultimately drive down the cost of energy.

CHAPTER 8

CONCLUSIONS

To help meet the need for more high quality cross-flow turbine performance and wake data—especially for higher solidity rotors—an automated turbine test bed was developed as part of UNH's wave and tow tank, which increased the number of possible tows per experiment by an order of magnitude while improving repeatability. Two "large laboratory scale" turbines ($\sim$ 1 m scale) were designed, built, and tested: the high solidity UNH-RVAT, and the medium solidity DOE/SNL RM2.

A baseline performance and near-wake measurement dataset was acquired for the UNH-RVAT. A new method for assessing wake recovery was developed by rearranging the streamwise mean momentum and mean kinetic energy equations to examine their streamwise partial derivatives [29]. Weighted averages of these terms were calculated from experimental data to assess the relative balance of various transport mechanisms. For the UNH-RVAT, it was shown that the mean vertical advection dominated in the near-wake region, which is caused by the unique vorticity field generated by the bound and tip vortices.

Scale, or Reynolds number effects on the UNH-RVAT data were examined by remeasuring performance and near-wake data at multiple tow speeds. It was shown that the measurements became nearly *Re*-independent at a turbine diameter Reynolds number $Re_D \sim 10^6$ or blade chord Reynolds number $Re_c \approx 2 \times 10^5$, which provides a convenient guideline for ensuring physical model tests are relevant to full scale behavior.

A similar experimental campaign was undertaken for the RM2. Reynolds number dependence showed a similar threshold, though the performance retained weak linear *Re*-dependence at the highest speeds tested. This effect was also seen when inspecting the maximum geometric torque coefficient computed from 2-D static foil coefficient data produced by the XFOIL viscous panel

code. Since the UNH-RVAT has a higher solidity or chord-to-radius ratio, and therefore higher virtual camber, the Reynolds number independence of its performance—estimated by the geometric torque coefficient calculation—is more dramatic. The near-wake of the RM2 overall showed lower levels of streamwise recovery, though mean vertical advection was still dominant. The turbulence was generated more symmetrically due to the rotors higher operational tip speed ratio, caused by its lower solidity. Additionally, measurements were taken to assess the effects of blade support strut drag, showing that even for streamlined foil struts, parasitic losses can be equivalent to several C_P percentage points, and increase faster than quadratically with tip speed ratio.

A blade-resolved RANS CFD model was evaluated for its ability to postdict the UNH-RVAT baseline data, using both 2-D and 3-D configurations, and the Spalart–Allmaras and k–ω SST turbulence models. As expected, the 2-D models overestimated performance due to higher blockage and lack of end effects. The lack of the vertical dimension made them unable to realize the strongest contribution to wake recovery—mean vertical advection—-which precludes their use for analyzing arrays of low aspect ratio turbines, despite the computational feasibility.

The 3-D blade-resolved RANS models performed better—the Spalart–Allmaras model postdicting mean performance just 6% below the experimental results, where k–ω overpredicted by 30%. Both models were able to resolve the effects of blade tip vortex shedding in the near-wake's mean velocity field, and therefore the vertical advection. Overall, 3-D blade-resolved RANS presents a potentially less expensive alternative to *Re*-independent physical model testing, though there is still some uncertainty with respect to turbulence model selection. However, the cost of 3-D blade-resolved CFD really depends on availability of high performance computing resources, much like physical model testing depends on the availability of experimental facilities.

Motivated by the prospect of reducing the computational cost of 3-D CFD simulations, an actuator line model was developed for cross-flow turbines and implemented in a standard k–ε RANS model. The ALM was coupled with a Leishman–Beddoes type semi-empirical dynamic stall model, end effects correction, flow curvature correction, and an added mass model. Both the UNH-RVAT and RM2 turbines were modeled with the RANS ALM. The performance curve for the

UNH-RVAT matched the experiments almost perfectly for tip speed ratios below that of maximum power output, but was overpredicted above. For the RM2, however, the shape of the C_P–λ curve was "stretched" such that $C_{P_{\max}}$ occurred at higher λ, though $C_{P_{\max}}$ was only underpredicted by approximately 9% compared with experiments. To address this issue, it is recommended that a more rigorous validation be performed with respect to the Leishman–Beddoes dynamic stall model time constants. It is hypothesized that tip speed ratio dependent time constants may improve mean performance predictions.

Wake predictions with the RANS ALM matched some of the qualitative near-wake flow field characteristics seen in experiments, e.g., the mean vertical advection, and production of turbulence kinetic energy on the $+y$ or upwind facing side of the rotor. Neither of these matched perfectly with experiments, but did a much better job representing a CFT wake than a simple actuator disk, with minimal additional computational effort.

The UNH-RVAT was also modeled using large eddy simulation with a typical Smagorinsky subgrid-scale model. Inside the LES, the ALM's mean performance coefficient predictions at $\lambda = \lambda_0 = 1.9$ dropped about five percentage points compared with RANS. However, the LES was able to resolve some of the important qualitative features of the near-wake's mean velocity field, i.e., the apparent mean vortex pair created by the blade tip vortex shedding. On the other hand, levels of turbulence were significantly lower than those measured in the experiment, which is thought to be an effect of the subgrid-scale modeling delaying vortex breakdown. Therefore, it is recommended that wake measurements be taken further downstream, and deeper investigation of SGS modeling be undertaken in order to recommend which LES model might be most effective for modeling arrays of cross-flow turbines.

On the whole, the work described here helps engineers better select initial CFT rotor concepts, as well as methods to predict their suitability. When full scale prototyping is not feasible, physical modeling at $Re_D \sim 10^6$ can be effective. Both of these methods are expensive, so it may be desirable to use 3-D blade-resolved RANS, despite also being expensive, and its uncertainty with respect to turbulence modeling. The actuator line model presents a good alternative when bud-

gets are constrained, allowing turbines to be simulated in a 3-D Navier–Stokes model with typical computing resources, i.e., dropping the expense by two to four orders of magnitude versus blade-resolved CFD for LES and RANS, respectively. For designing arrays of turbines, the ALM at present is probably the best balance between cost and accuracy, as its computational expense can be adjusted by the turbulence modeling fidelity. Furthermore, the effects of, e.g., a free surface or temperature/density stratification can easily be incorporated into ALM simulations, opening up many opportunities for future investigation.

The products of this research—datasets, processing code, CAD files, simulation case files, and the newly developed ALM software library turbinesFoam—have been made freely and openly available. Besides improving transparency and reproducibility, the open research paradigm also accelerates progress through collaboration, allowing researchers to build on each other's work rather than start anew. Working openly has already improved this research thanks to external contributions, and it will hopefully improve others' as time goes on.

8.1 Future work

To make cross-flow turbines viable, optimal designs must be established, which is especially true for MHK applications, where concepts have not yet matured to the level of wind turbines. The ability to predict the fatigue life of MHK rotor blades is paramount here, and will help reduce necessary rotor solidities to enhance performance. Towards that end, it is of interest to determine if 2-D blade-resolved CFD can rank relative rotor performance, e.g., for determining optimal preset blade pitch.

Experimental velocity measurements should be taken further downstream in the cross-flow turbine wakes. From these, streamwise derivatives in the RANS equations could be computed to evaluate our estimates of near-wake recovery, and observe how the balance of the recovery mechanisms evolves downstream. If possible, it would be helpful to obtain pressure measurements—possibly even local pressure gradient measurements. Particle image velocimetry (PIV) could be employed

to investigate the breakdown of the vortex structures shed by the rotor, ultimately helping to inform ideal subgrid scale modeling for LES.

Finally, multi-CFT (small array) experiments should be performed, preferably with an experimental setup capable of automating—and therefore optimizing—rotor positions. With these measurements, the ALM can be validated to assess its ability to predict interaction between rotors, and the momentum and energy recovery between. Furthermore, the trade-off between more efficient rotors and faster wake recovery, e.g., the RM2 versus UNH-RVAT, can be considered. With enhanced physical understanding and numerical modeling techniques, cross-flow turbine arrays may become an attractive option for both the wind and MHK industries.

BIBLIOGRAPHY

[1] D. Acheson. *Elementary Fluid Dynamics*. Oxford University Press, Oxford, UK, 1990.

[2] B. Adams, L. Bauman, W. Bohnhoff, K. Dalbey, M. Ebeida, J. Eddy, M. Eldred, P. Hough, K. Hu, J. Jakeman, L. Swiler, , and D. Vigil. DAKOTA, a multilevel parallel object-oriented framework for design optimization, parameter estimation, uncertainty quantification, and sensitivity analysis: Version 5.4 user's manual. Technical Report SAND2010-2183, Sandia National Laboratories, December 2009.

[3] J. Ainslie. Calculating the flowfield in the wake of wind turbines. *Journal of Wind Engineering and Industrial Aerodynamics*, 27:213–224, 1988.

[4] R. Akins. Measurement of surface pressure on an operating vertical-axis wind turbine. Technical Report SAND89-7051, Sandia National Laboratories, 1989.

[5] A. Alaimo, A. Esposito, A. Messineo, C. Orlando, and D. Tumino. 3D CFD analysis of a vertical axis wind turbine. *Energies*, 8(4):3013–3033, 2015.

[6] E. Amet, T. Maître, C. Pellone, and J.-L. Achard. 2D numerical simulations of blade-vortex interaction in a Darrieus turbine. *Journal of Fluids Engineering*, 131, November 2009.

[7] J. D. Anderson. *Fundamentals of aerodynamics*. McGraw-Hill, 3rd edition, 2001.

[8] S. Antheaume, T. Maître, and J.-L. Achard. Hydraulic Darrieus turbines efficiency for free fluid flow conditions versus power farms conditions. *Renewable Energy*, 33:2186–2198, 2008.

[9] D. B. Araya, A. E. Craig, M. Kinzel, and J. O. Dabiri. Low-order modeling of wind farm aerodynamics using leaky rankine bodies. *Journal of Renewable and Sustainable Energy*, 6, 2014.

[10] C. L. Archer, S. Mirzaeisefat, and S. Lee. Quantifying the sensitivity of wind farm performance to array layout options using large-eddy simulation. *Geophysical Research Letters*, 40:4963–4970, 2013.

[11] T. D. Ashwill. Measured data for the Sandia 34-meter vertical axis wind turbine. Technical Report SAND91-2228, Sandia National Laboratories, Albuquerque, NM 87185, 1992.

[12] P. Bachant. Experimental investigation of helical cross-flow axis hydrokinetic turbines, including effects of waves and turbulence. Master's thesis, University of New Hampshire, 2011.

[13] P. Bachant. CFD online forums analysis. fig**share**. http://dx.doi.org/10.6084/m9.figshare.1606310.v1, November 2015.

[14] P. Bachant. RM2-turbinesFoam: v1.0.0. Zenodo. http://dx.doi.org/10.5281/zenodo.50594, 2016.

[15] P. Bachant. UNH-RVAT-2D-OpenFOAM: v1.0.0-SA. Zenodo. http://dx.doi.org/10.5281/zenodo.47929, 2016.

[16] P. Bachant. UNH-RVAT-2D-OpenFOAM: v1.0.0-SST. Zenodo. http://dx.doi.org/10.5281/zenodo.47928, 2016.

[17] P. Bachant. UNH-RVAT-3D-OpenFOAM: v1.0.0-SA. Zenodo. http://dx.doi.org/10.5281/zenodo.47927, 2016.

[18] P. Bachant. UNH-RVAT-3D-OpenFOAM: v1.0.0-SST. Zenodo. http://dx.doi.org/10.5281/zenodo.47926, 2016.

[19] P. Bachant. UNH-RVAT-turbinesFoam: v1.0.0. Zenodo. http://dx.doi.org/10.5281/zenodo.50592, 2016.

[20] P. Bachant. UNH-RVAT-turbinesFoam: v1.0.0-LES. Zenodo. http://dx.doi.org/10.5281/zenodo.50593, 2016.

[21] P. Bachant, A. Goude, and M. Wosnik. Actuator line modeling of vertical-axis turbines. *arXiv preprint arXiv:1605.01449 Submitted to Wind Energy*, 2016.

[22] P. Bachant, A. Goude, and M. Wosnik. turbinesFoam: v0.0.7. Zenodo. http://dx.doi.org/10.5281/zenodo.49422, 2016.

[23] P. Bachant, V. Lyon, and M. Wosnik. UNH tow tank and turbine test bed CAD files. fig**share**. https://dx.doi.org/10.6084/m9.figshare.3309424.v1, 2016.

[24] P. Bachant and M. Wosnik. Performance and near-wake measurements for a vertical axis turbine at moderate Reynolds number. In *Proceedings of the ASME Fluids Engineering Division Summer Meeting*, number FEDSM2013-16575, Incline Village, NV, July 2013.

[25] P. Bachant and M. Wosnik. OpenFOAM cylindrical actuator surface case files. fig**share**. http://dx.doi.org/10.6084/m9.figshare.1080780, 2014.

[26] P. Bachant and M. Wosnik. Reynolds number dependence of cross-flow turbine performance and near-wake characteristics. In *Proceedings of the 2nd Marine Energy Technology Symposium METS2014*, Seattle, WA, April 15–18 2014.

[27] P. Bachant and M. Wosnik. UNH-RVAT baseline performance and near-wake measurements: Reduced dataset and processing code. fig**share**. http://dx.doi.org/10.6084/m9.figshare.1080781, 2014.

[28] P. Bachant and M. Wosnik. UNH-RVAT CAD models. fig**share**. http://dx.doi.org/10.6084/m9.figshare.1062009, 2014.

[29] P. Bachant and M. Wosnik. Characterising the near-wake of a cross-flow turbine. *Journal of Turbulence*, 16(4):392–410, January 2015.

[30] P. Bachant and M. Wosnik. Performance measurements of cylindrical- and spherical-helical cross-flow marine hydrokinetic turbines, with estimates of exergy efficiency. *Renewable Energy*, 2015.

[31] P. Bachant and M. Wosnik. Effects of reynolds number on the energy conversion and near-wake dynamics of a high solidity vertical-axis cross-flow turbine. *Energies*, 9(73), 2016.

[32] P. Bachant and M. Wosnik. Modeling the near-wake of a vertical-axis cross-flow turbine with 2-D and 3-D RANS. *arXiv preprint arXiv:1604.02611 Submitted to Journal of Renewable and Sustainable Energy*, 2016.

[33] P. Bachant and M. Wosnik. NACA XX20 XFOIL coefficients. Zenodo. `http://dx.doi.org/10.5281/zenodo.45099`, January 2016.

[34] P. Bachant and M. Wosnik. UNH-RVAT Reynolds number dependence experiment: Reduced dataset and processing code. fig**share**. `http://dx.doi.org/10.6084/m9.figshare.1286960`, January 2016.

[35] P. Bachant, M. Wosnik, B. Gunawan, and V. Neary. 1:6 scale RM2 cross-flow turbine CAD package. fig**share**. `http://dx.doi.org/10.6084/m9.figshare.1373870`, 2015.

[36] P. Bachant, M. Wosnik, B. Gunawan, and V. Neary. UNH RM2 tow tank experiment: Reduced dataset and processing code. fig**share**. `http://dx.doi.org/10.6084/m9.figshare.1373899`, 2016.

[37] P. Bachant, M. Wosnik, B. Gunawan, and V. S. Neary. Experimental study of a reference model vertical-axis cross-flow turbine. *Submitted to PLOS ONE*, 2016.

[38] C. Baker and N. Brockie. Wind tunnel tests to obtain train aerodynamic drag coefficients: Reynolds number and ground simulation effects. *Journal of Wind Engineering and Industrial Aerodynamics*, 38:23–28, 1991.

[39] F. Balduzzi, A. Bianchini, R. Maleci, G. Ferrara, and L. Ferrari. Critical issues in the CFD simulation of Darrieus wind turbines. *Renewable Energy*, 85:419–435, 2016.

[40] M. Barone, T. Griffith, and J. Berg. Reference model 2: "rev 0" rotor design. Technical Report SAND2011-9306, Sandia National Laboratories, November 2011.

[41] L. Battisti, L. Zanne, S. Dell'Anna, V. Dossena, G. Persico, and B. Paradiso. Aerodynamic measurements on a vertical axis wind turbine in a large scale wind tunnel. *Journal of Energy Resources Technology*, 133, 2011.

[42] M. J. Beam, B. R. Elbing, T. K. Fetterolf, B. L. Kline, D. F. Kerstetter, J. A. Mickey, A. A. Fontaine, and W. A. Straka. Power take-off system design SNL reference turbine 2. Technical report, Penn State Applied Research Lab, 2011.

[43] T. S. Beddoes. A third generation model for unsteady aerodynamics and dynamic stall. Technical Report RP 908, Westland Helicopters Limited, Yeovil, Somerset, November 1993.

[44] G. Bedon, E. G. Antonini, S. D. Betta, M. R. Castelli, and E. Benini. Evaluation of the different aerodynamic databases for vertical axis wind turbine simulations. *Renewable and Sustainable Energy Reviews*, 40, 2014.

[45] B. Blackwell, R. Sheldahl, and L. Feltz. Wind tunnel performance data for the Darrieus wind turbine with NACA 0012 blades. Report SAND76-0130, Sandia National Laboratories, Albuquerque, NM, May 1976.

[46] M. Boudreau and G. Dumas. Wake analysis of various hydrokinetic turbine technologies through numerical simulations. In *Proceedings of AERO 2015*, 2015.

[47] W. G. Bousman. Airfoil dynamic stall and rotorcraft maneuverability. Technical Report NASA/TM-2000-209601, NASA Ames Research Center, 2000.

[48] W. G. Bousman. Evaluation of airfoil dynamic stall characteristics for maneuverability. In *Proceedings of the 26th European Rotorcraft Forum*, The Hague, Netherlands, September 26–29 2000.

[49] R. Bravo, S. Tullis, and S. Ziada. Performance testing of a small vertical-axis wind turbine. In *Proceedings of the 21st Canadian Congress of Applied Mechanics CANCAM*, Toronto, Ontario, Canada, June 3–7 2007.

[50] G. Brochier, P. Fraunie, C. Beguier, and I. Paraschivoiu. Water channel experiments of dynamic stall on darrieus wind turbine blades. *AIAA Journal of Propulsion and Power*, 2(5):46–510, September–October 1986.

[51] S. C. Cakmakcioglu, I. O. Sert, O. Tugluk, and N. Sezer-Uzol. 2-D and 3-D CFD investigation of NREL S826 airfoil at low Reynolds numbers. In *Journal of Physics: Conference Series*, 2014.

[52] R. B. Cal, J. Lebron, L. Castillo, H. S. Kang, and C. Meneveau. Experimental study of the horizontally averaged flow structure in a model wind-turbine array boundary layer. *Journal of Renewable and Sustainable Energy*, 2:1–25, 2010.

[53] B. H. Carmichael. Low Reynolds number airfoil survey volume I. Technical report, National Aeronautics and Space Administration, Capistrano Beach, California, USA, 1981.

[54] M. R. Castelli, F. Garbo, and E. Benini. Numerical investigation of laminar to turbulent boundary layer transition on a Naca 0012 airfoil for vertical-axis wind turbine applications. *Wind Engineering*, 35(6):661–686, 2011.

[55] R. Cavagnaro and B. Polagye. An evaluation of blockage corrections for a helical cross-flow turbine. In *Proceedings of the 3rd Oxford Tidal Energy Workshop*, Oxford, UK, April 7–8 2014.

[56] L. Chamorro, M. Guala, R. Arndt, and F. Sotiropoulos. On the evolution of turbulent scales in the wake of a wind turbine model. *Journal of Turbulence*, 13:1–13, 2012.

[57] L. P. Chamorro, R. E. A. Arndt, and F. Sotiropolous. Reynolds number dependence of turbulence statistics in the wake of wind turbines. *Wind Energy*, 15:733–742, 2012.

[58] L. P. Chamorro, R. E. A. Arndt, and F. Sotiropoulos. Turbulent flow properties around a staggered wind farm. *Boundary-Layer Meteorol*, 2011.

[59] L. P. Chamorro and F. Porté-Agel. Turbulent flow inside and above a wind farm: A wind-tunnel study. *Energies*, 2011.

[60] J. Choi and M. Shan. Advancement of Jensen (Park) wake model. In *Proceedings of the EWEA conference*, February 2013.

[61] M. Churchfield, S. Lee, and P. Moriarty. Overview of the simulator for wind farm application (SOWFA). http://wind.nrel.gov/designcodes/simulators/sowfa/SOWFA_tutorial_05-20-2014.pdf, May 2014.

[62] M. J. Churchfield, S. Lee, J. Michalakes, and P. J. Moriarty. A numerical study of the effects of atmospheric and wake turbulence on wind turbine dynamics. *Journal of Turbulence*, 13:1–32, 2012.

[63] M. J. Churchfield, Y. Li, and P. J. Moriarty. A large-eddy simulation study of wake propagation and power production in an array of tidal-current turbines. *Phil. Trans. R. Soc. A*, 2013.

[64] H. W. Coleman and W. G. Steele. *Experimentation, Validation, and Uncertainty Analysis for Engineers*. John Wiley & Sons,, third edition, 2009.

[65] A. Crivellini and V. D'Alessandro. Spalart–Allmaras model apparent transition and RANS simulations of laminar separation bubbles on airfoils. *International Journal of Heat and Fluid Flow*, 47:70–83, 2014.

[66] J. Dabiri. Potential order-of-magnitude enhancement of wind farm power density via counter-rotating vertical-axis wind turbine arrays. *Journal of Renewable and Sustainable Energy*, 3:1–13, 2011.

[67] L. Darnell. A towing carriage for the University of New Hampshire towing and wave making basin. Master's thesis, University of New Hampshire, 1996.

[68] G. J. M. Darrieus. Turbine having its rotating shaft transverse to the flow of the current, 1931.

[69] K. Dixon, C. J. Simao Ferreira, C. Hofemann, G. J. W. van Bussel, and G. A. M. Van Kuik. A 3d unsteady panel method for vertical axis wind turbines. In *Proceedings of the European Wind Energy Conference & Exhibition EWEC Brussels, 1-10*, 2008.

[70] V. Dossena, G. Persico, B. Paradiso, L. Battisti, S. Dell'Anna, A. Brighenti, and E. Benini. An experimental study of the aerodynamics and performance of a vertical axis wind turbine in a confined and unconfined environment. *Journal of Energy Resources Technology*, 2015.

[71] M. Drela. XFOIL: An analysis and design system for low reynolds number airfoils. In *Low Reynolds Number Aerodynamics*, volume 54 of *Lecture Notes in Engineering*. Springer Verlag, 1989.

[72] S. Drzewiecki. In *Bulletin de l'Association Technique Maritime*, 1892.

[73] S. Drzewiecki. *Théorie Générale de l'Hélice*. Paris, 1920.

[74] N. Durrani, N. Qin, H. Hameed, and S. Khushnood. 2d numerical analysis of a vawt wind farm for different configurations. In *Proceedings of 49th AIAA Aerospace Sciences Meeting including the New Horizons Forum and Aerospace Exposition*, number AIAA 2011-461, Orlando, FL, January 2011.

[75] E. Dyachuk and A. Goude. Simulating dynamic stall effects for vertical axis wind turbines applying a double multiple streamtube model. *Energies*, 8:1353–1372, 2015.

[76] E. Dyachuk, A. Goude, and H. Bernhoff. Dynamic stall modeling for the conditions of vertical axis wind turbines. *AIAA Journal*, 52, 2014.

[77] E. Dyachuk, A. Goude, and H. Bernhoff. Simulating pitching blade with free vortex model coupled with dynamic stall model for conditions of straight bladed vertical axis turbines. *Journal of Solar Energy Engineering*, 137:1–7, August 2015.

[78] C. S. Ferreira, H. Bijl, G. van Bussel, and G. van Kuik. Simulating dynamic stall in a 2d vawt: Modeling strategy, verification and validation with particle image velocimetry data. *Journal of Physics: Conference Series, The Science of Making Torque from Wind*, 75:1–13, 2007.

[79] A. J. Fiedler and S. Tullis. Blade offset and pitch effects on a high solidity vertical axis wind turbine. *Wind Engineering*, 33:237–246, 2009.

[80] P. Fleming, S. Lee, M. Churchfield, A. Scholbrock, J. Michalakes, K. Johnson, P. Moriarty, P. Gebraad, and J. van Wingerden. The sowfa super-controller: A high-fidelity tool for evaluating wind plant control approaches. In *Proceedings of EWEA*, 2013.

[81] P. A. Fleming, P. M. Gebraad, S. Lee, J.-W. van Wingerden, K. Johnson, M. Churchfield, J. Michalakes, P. Spalart, and P. Moriarty. Evaluating techniques for redirecting turbine wakes using sowfa. *Renewable Energy*, 2014.

[82] D. Forbush, B. Polagye, J. Thomson, B. Fabien, J. Donegan, and J. McEntee. Characterization and control of cross-flow turbine in shear flow. In *Proceedings of the 3rd Marine Energy Technology Symposium*, 2015.

[83] N. Fujisawa and S. Shibuya. Observations of dynamic stall on darrieus wind turbine blades. *Journal of Wind Engineering and Industrial Aerodynamics*, 89:201–214, 2001.

[84] S. Giorgetti, G. Pellegrini, and S. Zanforlin. CFD investigation on the aerodynamic interferences between medium-solidity Darrieus vertical axis wind turbines. *Energy Procedia*, 81:227–239, 2015.

[85] H. Glauert. Airplane propellers. In *Aerodynamic theory*, pages 169–360. Springer, 1935.

[86] J. Goldenberg and G. Fekete. Mean flow energy content of boundary layer downstream of vertical-axis wind-turbine simulators. *Journal of Wind Engineering and Industrial Aerodynamics*, 12:1–14, 1983.

[87] R. E. Gormont. A mathematical model of unsteady aerodynamics and radial flow for application to helicopter rotors. Technical Report USAAMRDL 72-67, The Boeing Company, Vertol Division, Philadelphia, Pennsylvania, May 1973.

[88] A. Goude. *Fluid Mechanics of Vertical Axis Turbines, Simulations and Model Development*. PhD thesis, Uppsala University, 2012.

[89] A. Goude and O. Agren. Numerical simulation of a farm of vertical axis marine current turbines. In *Proceedings of the ASME 2010 29th International Conference on Ocean, Offshore and Arctic Engineering*, Shanghai, China, June 2010.

[90] J. Gray, K. T. Moore, and B. A. Naylor. OpenMDAO: An open source framework for multidisciplinary analysis and optimization. In *Proceedings of the 13th AIAA/ISSMO multidisciplinary analysis and optimization conference*, number AIAA-2010-9101, Forth Worth, TX, August 2010.

[91] B. Gunawan, V. Neary, J. Roberts, A. Dallman, S. Grovue, J. Mortensen, and B. Heiner. Field measurement test plan to determine effects of hydrokinetic turbine deployment on canal test site in Yakima, WA, USA. In *Proceeding of the 2nd Marine Energy Technology Symposium*, 2014.

[92] K. A. Haas, H. M. Fritz, S. P. French, and V. S. Neary. Assessment of energy production potential from ocean currents along the United States coastline. Technical Report DE-EE0002661, Georgia Tech Research Corporation, September 2013.

[93] K. A. Haas, H. M. Fritz, S. P. French, B. T. Smith, and V. Neary. Assessment of energy production potential from tidal streams in the united states. Technical Report DE-FG36-08GO18174, Georgia Tech Research Corporation, June 2011.

[94] J. Hansen, P. Kharecha, M. Sato, V. Masson-Delmotte, F. Ackerman, D. J. Beerling, P. J. Hearty, O. Hoegh-Guldberg, S.-L. Hsu, C. Parmesan, J. Rockstrom, E. J. Rohling, J. Sachs, P. Smith, K. Steffen, L. Van Susteren, K. von Schuckmann, and J. C. Zachos. Assessing "dangerous climate change": Required reduction of carbon emissions to protect young people, future generations and nature. *PLoS ONE*, 8, 2013.

[95] C. Hill, V. Neary, B. Gunawan, M. Guala, and F. Sotiropoulos. U.S. Department of Energy Reference Model Program RM2: Experimental results. Technical report, St. Anthony Falls Laboratory for Wind and Water Technologies Program, Office of Energy Efficiency and Renewable Energy, U.S. Department of Energy, June 2014.

[96] R. Howell, N. Qin, J. Edwards, and N. Durrani. Wind tunnel and numerical study of a small vertical axis wind turbine. *Renewable Energy*, 35:412–422, 2010.

[97] Interface Inc. T8 general purpose rotary torque transducer specifications. http://www.interfaceforce.com/index.php?T8-General-Purpose-Rotary-Torque-Transducer&mod=product&show=65, Accessed December 2014.

[98] E. N. Jacobs and A. Sherman. Airfoil section characteristics as affected by variation of the reynolds number. Technical report, National Advisory Committee for Aeronautics, Langley Aeronautical Lab.; Langley Field, VA, United States, 1937.

[99] S. C. James, S. Lefantzi, J. Barco, E. Johnson, and J. D. Roberts. Verifying marine-hydrokinetic energy generation simulations using snl-efdc. In *OCEANS*, Waikoloa, HI, September 2011.

[100] S. C. James, E. Seetho, C. Jones, and J. Roberts. Simulating environmental changes due to marine hydrokinetic energy installations. In *OCEANS*, Seattle, WA, September 2010.

[101] N. Jensen. A note on wind generator interaction. Technical Report RISO-M-2411, RISO, 1983.

[102] P. K. Jha, M. J. Churchfield, P. J. Moriarty, and S. Schmitz. Guidelines for volume force distributions within actuator line modeling of wind turbines on large-eddy simulation-type grids. *Journal of Solar Energy Engineering*, 136(3):1–11, 2014.

[103] S. Joo, H. Choi, and J. Lee. Aerodynamic characteristics of two-bladed h-darrieus at various solidities and rotating speeds. *Energy*, pages 1–13, 2015.

[104] M. Kinzel, Q. Mulligan, and J. O. Dabiri. Energy exchange in an array of vertical-axis wind turbines. *Journal of Turbulence*, 13:1–13, 2012.

[105] Kollmorgen. AKD user guide. http://www.kollmorgen.com/en-us/products/drives/servo/akd/_manuals/kollmorgen-akd-user-guide-en-rev-m/, Accessed December 2014.

[106] S. Kooiman and S. Tullis. Response of a vertical axis wind turbine to time varying wind conditions found within the urban environment. *Wind Engineering*, 34(4):389–401, 2010.

[107] P. Krogstad and M. S. Adaramola. Performance and near wake measurements of a model horizontal axis wind turbine. *Wind Energy*, 15:743–756, 2012.

[108] P.-Å. Krogstad and P. E. Eriksen. "Blind test" calculations of the performance and wake development for a model wind turbine. *Renewable Energy*, 50:325–333, 2013.

[109] H. Lam and H. Peng. Study of wake characteristics of a vertical axis wind turbine by two- and three-dimensional computational fluid dynamics simulations. *Renewable Energy*, 90:386–398, 2016.

[110] K. Lam. Vortex shedding flow behind a slowly rotating circular cylinder. *Journal of Fluids and Structures*, 25:245–262, 2009.

[111] A. Laneville and P. Vittecoq. Dynamic stall: The case of the vertical axis wind turbine. *Journal of Solar Energy Engineering*, 108:140–145, May 1986.

[112] J. G. Leishman. *Principles of Helicopter Aerodynamics*. Cambridge, 2006.

[113] J. G. Leishman and T. S. Beddoes. A semi-empirical model for dynamic stall. *Journal of the American Helicopter Society*, 34(3):3–17, July 1989.

[114] C. Li, S. Zhu, Y. lin Xu, and Y. Xiao. 2.5D large eddy simulation of vertical axis wind turbine in consideration of high angle of attack flow. *Renewable Energy*, 51:317–330, 2013.

[115] Y. Li and S. M. Calisal. Modeling of twin-turbine systems with vertical axis tidal current turbines: Part I—power output. *Ocean Engineering*, 37:627–637, 2010.

[116] P. B. S. Lissaman. Low-Reynolds-number airfoils. *Annual Review of Fluid Mechanics*, 15:223–239, 1983.

[117] W.-Q. Liu, I. Paraschivoiu, and R. Martinuzzi. Calculation of dynamic stall on Sandia 34-m VAWT using an indicial model. *Wind Engineering*, 1992.

[118] A. Lopez, B. Roberts, D. Heimiller, N. Blair, and G. Porro. U.S. renewable energy technical potentials: A GIS-based analysis. Technical Report NREL/TP-6A20-51946, National Renewable Energy Laboratory, July 2012.

[119] M. C. Lott. Eiffel tower going green with two new wind turbines. `http://blogs.scientificamerican.com/plugged-in/eiffel-tower-going-green-with-two-new-wind-turbines/`, March 2015.

[120] A. C. Mandal and J. D. Burton. The effects of dynamic stall and flow curvature on the aerodynamics of Darrieus turbines applying the cascade model. *Wind engineering*, 18(6):267–282, 1994.

[121] J. Manwell, J. McGowan, and A. Rogers. *Wind Energy Explained*. John Wiley, UK, 2002.

[122] P. Marsh, D. Ranmuthugala, I. Penesis, and G. Thomas. Three-dimensional numerical simulations of straight-bladed vertical axis tidal turbines investigating power output, torque ripple and mounting forces. *Renewable Energy*, 83:67–77, 2015.

[123] D. Marten, J. Wendler, G. Pechlivanoglou, C. Nayeri, and C. Paschereit. QBlade: An open source tool for design and simulation of horizontal and vertical axis wind turbines. *International Journal of Emerging Technology and Advanced Engineering*, 3(3):264–269, February 2013.

[124] L. A. Martínez-Tossas, M. J. Churchfield, and S. Leonardi. Large eddy simulations of the flow past wind turbines: actuator line and disk modeling. *Wind Energy*, 18:1047–1060, 2015.

[125] L. A. Martínez-Tossas, M. J. Churchfield, and C. Meneveau. Large eddy simulation of wind turbine wakes: detailed comparisons of two codes focusing on effects of numerics and subgrid modeling. *Journal of Physics: Conference Series*, 625, 2015.

[126] L. A. Martínez-Tossas and C. Meneveau. Optimal smoothing length scale for actuator line models of lifting surfaces. *arXiv preprint arXiv:1511.04117*, (arXiv:1511.04117), 2015.

[127] I. D. Mays, C. A. Morgan, M. B. Anderson, and S. Powles. Experience with the VAWT 850 demonstration project. In *Proceedings of European Community Wind Energy Conference*, 1990.

[128] W. J. McCroskey. The phenomenon of dynamic stall. Technical report, Nationa Aeronautics and Space Administration, March 1981.

[129] K. W. McLaren. *A Numerical and Experimental Study of Unsteady Loading of High Solidity Vertical Axis Wind Turbines*. PhD thesis, McMaster University, 2011.

[130] J. H. McMasters and M. L. Henderson. Low-speed single-element airfoil synthesis. *Tech. Soaring*, 6(2):1–21, 1980.

[131] S. McTavish, D. Feszty, and F. Nitzsche. Evaluating Reynolds number effects in small-scale wind turbine experiments. *J. Wind Eng. Ind. Aerodyn.*, 120:81–90, 2013.

[132] F. Menter. Two-equation eddy-viscosity turbulence models for engineering applications. *AIAA Journal*, 32:1598–1605, 1994.

[133] F. Menter and T. Esch. Elements of industrial heat transfer predictions. In *Proceedings of the 16th Brazilian Congress of Mechanical Engineering*, pages 117–127, November 2001.

[134] F. R. Menter, M. Kuntz, and R. Langtry. Ten years of industrial experience with the sst turbulence model. *Turbulence, Heat and Mass Transfer*, 4, 2003.

[135] S. Mertens, G. van Kuik, and G. van Bussel. Performance of an H-Darrieus in the skewed flow on a roof. *Journal of Solar Energy Engineering*, 125:443–440, 2003.

[136] C. Michelen, V. S. Neary, J. C. Murray, and M. Barone. CACTUS open source code for hydrokinetic turbine design and analysis: model performance evaluation and public dissemination as open source design tool. In *Proceedings of the 2nd Marine Energy Technology Symposium*, 2014.

[137] P. G. Migliore, W. P. Wolfe, and J. B. Fanucci. Flow curvature effects on Darrieus turbine blade aerodynamics. *J. Energy*, 4(2):49–55, 1980.

[138] J. Murray and M. Barone. The development of cactus, a wind and marine turbine performance simulation code. In *Proceedings of the 49th AIAA Aerospace Sciences Meeting including the New Horizons Forum and Aerospace Exposition*, 2011.

[139] V. Neary. Reference inflow characterization for river resource reference model (rm2). Technical Report ORNL/TM-2011/360, Oak Ridge National Laboratory, 2011.

[140] V. Neary, M. Lawson, M. Previsic, A. Copping, K. Hallett, L. A., J. Rieks, and D. Murray. Methodology for design and economic analysis of marine energy conversion (mec) technologies. In *Proceedings of the Marine Energy Technology Symposium (METS2014)*, Seattle, WA, April 2014.

[141] V. S. Neary, M. Previsic, R. A. Jepsen, M. J. Lawson, Y.-H. Yu, A. E. Copping, A. A. Fontaine, K. C. Hallett, and D. K. Murray. Methodology for design and economic analysis of marine energy conversion (MEC) technologies. Technical Report SAND2014-9040, Sandia National Laboratories, Albuquerque, NM, USA, March 2014.

[142] K. Nelson, C. Jones, and J. Roberts. FY13 Q3 Water Power Report; MHK Array Placement Analysis: SNL-EFDC Model Application at Cobscook Bay. Technical report, Water Power Technologies, Sandia National Laboratories, Albuquerque, NM, 2013.

[143] M. Nini, V. Motta, G. Bindolino, and A. Guardone. Three-dimensional simulation of a complete vertical axis wind turbine using overlapping grids. *Journal of Computational and Applied Mechanics*, 2014.

[144] Nortek-AS. Vectrino 3D water velocity sensor lab probe datasheet. `http://www.nortekusa.com/lib/data-sheets/datasheet-vectrino-lab`, Accessed December 2014.

[145] Ocean Renewable Power Company. America's first ocean energy delivered to the grid, September 2012.

[146] A. Orlandi, M. Collu, S. Zanforlin, and A. Shires. 3D URANS analysis of a vertical axis wind turbine in skewed flows. *J. Wind Eng. Ind. Aerodyn.*, 147:77–84, 2015.

[147] I. Paraschivoiu. Double-multiple streamtube model for studying vertical-axis wind turbines. *J. Propulsion*, 4:370–377, 1988.

[148] I. Paraschivoiu. *Wind Turbine Design with Emphasis on Darrieus Concept*. Polytechnic International, Montreal, Quebec, Canada, 1st edition, 2002.

[149] U. S. Paulsen, T. F. Pedersen, H. A. Madsen, K. Enevoldsen, P. H. Nielsen, J. Hattel, L. Zanne, L. Battisti, A. Brighenti, M. Lacaze, V. Lim, J. W. Heinen, P. A. Berthelsen, S. Carstensen, E.-J. de Ridder, G. van Bussel, and G. Tescione. Deepwind- an innovative wind turbine concept for offshore. In *Proceedings of EWEA*, Brussels, Belgium, March 2011.

[150] B. Pierce, P. Moin, and J. Dabiri. Evaluation of point-forcing models with application to vertical axis wind turbine farms. Technical report, Center for Turbulence Research, Stanford University, Stanford, CA, 2013.

[151] F. Pierella, P.-Å. Krogstad, and L. Sætran. Blind test 2 calculations for two in-line model wind turbines where the downstream turbine operates at various rotational speeds. *Renewable Energy*, 70:62–77, 2014.

[152] B. L. Polagye, R. J. Cavagnaro, and A. L. Niblick. Micropower from tidal turbines. In *Proceedings of ASME Fluids Engineering Division Summer Meeting*, number FEDSM2013-16604, Incline Village, NV, July 7–11 2013.

[153] F. L. Ponta and P. M. Jacovis. A vortex model for darrieus turbine using finite element techniques. *Renewable Energy*, 24:1–18, 2001.

[154] L. Prandtl and A. Betz. *Vier Abhandlungen zur Hydrodynamik und Aerodynamik*. GÃűttinger Nachr., GÃűttingen, 1927.

[155] T. Ravens, K. Cunningham, and G. Scott. Assessment and mapping of the riverine hydrokinetic energy resource in the continental United States. Technical Report 1026880, Electric Power Research Institute, Palo Alto, CA, December 2012.

[156] G. W. Rawlings. Parametric characterization of an experimental vertical axis hydro turbine. Master's thesis, University of British Columbia, 2008.

[157] Renishaw. LM15 linear encoder datasheet. `http://resources.renishaw.com/download.aspx?lang=en&data=49238&btn=1`, Accessed December 2014.

[158] S.-C. Roh and S.-H. Kang. Effects of a blade profile, the Reynolds number, and the solidity on the performance of a straight bladed vertical axis wind turbine. *Journal of Mechanical Science and Technology*, 2013.

[159] Sandia National Laboratories. Offshore use of vertical-axis wind turbines gets closer look, July 2012.

[160] F. Scheurich and R. E. Brown. Effect of dynamic stall on the aerodynamics of vertical-axis wind turbines. *AIAA Journal*, 49:2511–2521, 2011.

[161] F. Scheurich, T. M. Fletcher, and R. E. Brown. Simulating the aerodynamic performance and wake dynamics of a vertical-axis wind turbine. *Wind Energ.*, 14:159–177, 2011.

[162] P. Schito and A. Zasso. Actuator forces in CFD: RANS and LES modeling in OpenFOAM. *Journal of Physics: Conference Series, The Science of Making Torque from Wind*, 524, 2014.

[163] Sentran. ZB S beam load cell datasheet. `http://www.sentranllc.com/pdfs/zb1.pdf`, Accessed December 2014.

[164] S. Shamsoddin and F. Porté-Agel. Large eddy simulation of vertical axis wind turbine wakes. *Energies*, 7:890–912, 2014.

[165] R. Sheldahl and P. Klimas. Aerodynamic characteristics of seven symmetrical airfoil sections through 180-degrees angle of attack for use in aerodynamic analysis of vertical axis wind turbines. Final report SAND80-2114, Sandia National Laboratories, Albuquerque, NM, March 1981.

[166] R. E. Sheldahl and B. F. Blackwell. Free-air performance tests of a 5-metre-diameter darrieus turbine. Technical report, Sandia Laboratories, 1977.

[167] W. Z. Shen, R. Mikkelsen, and J. N. SÃżrensen. Tip loss corrections for wind turbine computations. *Wind Energy*, 8:457–475, 2005.

[168] W. Sheng, R. A. M. Galbraith, and F. N. Coton. A modified dynamic stall model for low Mach numbers. *Journal of Solar Energy Engineering*, 130, 2008.

[169] J. D. Singleton and W. T. Yeager, Jr. Important scaling parameters for testing model-scale helicopter rotors. *Journal of Aircraft*, 37(3):396–402, May–June 2000.

[170] J. Slotnick, A. Khodadoust, J. Alonso, D. Darmofal, W. Gropp, E. Lurie, and D. Mavriplis. CFD vision 2030 study: A path to revolutionary computational aerosciences. Technical report, NASA, 2014.

[171] J. Smagorinsky. General circulation experiments with the primitive equations: I. the basic experiment. *Monthly Weather Review*, 91(3):99–164, March 1963.

[172] J. Smith, T. Forsyth, K. Sinclair, and F. Oteri. Built-environment wind turbine roadmap. Technical Report NREL/TP-5000-50499, National Renewable Energy Laboratory, November 2012.

[173] J. N. Sørensen, R. F. Mikkelsen, D. S. Henningson, S. Ivanell, S. Sarmast, , and S. J. Andersen. Simulation of wind turbine wakes using the actuator line technique. *Phil Trans R Soc A*, 373, 2015.

[174] J. N. Sørensen and W. Z. Shen. Numerical modeling of wind turbine wakes. *Journal of Fluids Engineering*, 2002.

[175] P. Spalart and S. Allmaras. A one-equation turbulence model for aerodynamic flows. Technical Report AIAA-92-0439, American Institute for Aeronautics and Astronautics, 1992.

[176] R. J. A. M. Stevens, D. F. Gayme, and C. Meneveau. Coupled wake boundary layer model of wind-farms. *Submitted to Journal of Renewable and Sustainable Energy*, 2014.

[177] R. J. A. M. Stevens, D. F. Gayme, and C. Meneveau. Large eddy simulation studies of the effects of alignment and wind farm length. *Journal of Renewable and Sustainable Energy*, 6:1–14, 2014.

[178] J. Strickland, T. Smith, and K. Sun. A vortex model of the darrieus turbine: An analytical and experimental study. Final report SAND81-7017, Texas Tech University, Lubbock, TX, June 1981.

[179] J. H. Strickland, B. T. Webster, and T. Nguyen. A vortex model of the darrieus turbine: An analytical and experimental study. *Journal of Fluids Engineering*, 101:500–505, 1979.

[180] B. Strom, S. Brunton, and B. Polagye. Phase resolved angular velocity control of cross flow turbines. In *Bulletin of the American Physical Society*, volume 60. American Physical Society, 2015.

[181] D. Sumner, J. Heseltine, and O. Dansereau. Wake structure of a finite circular cylinder of small aspect ratio. *Experiments in Fluids*, 37:720–730, 2004.

[182] R. J. Templin. Aerodynamic performance theory for the nrc vertical axis wind turbine. Technical Report LTR-LA-160, National Research Council Canada, Ottawa, Canada, 1974.

[183] H. Tennekes and J. L. Lumley. *A First Course in Turbulence*. The MIT Press, Cambridge, MA, 1972.

[184] G. Tescione, D. Ragni, C. He, C. S. Ferreira, and G.J. Near wake flow analysis of a vertical axis wind turbine by stereoscopic particle image velocimetery. *Renewable Energy*, 70:47–61, October 2014.

[185] N. Troldborg. *Actuator Line Modeling of Wind Turbine Wakes*. PhD thesis, Technical University of Denmark, 2008.

[186] N. Troldborg, J. N. Sørensen, and R. Mikkelsen. Actuator line simulation of wake of wind turbine operating in turbulent inflow. *Journal of Physics: Conference Series*, 75, 2007.

[187] R. Urbina, M. L. Peterson, R. W. Kimball, G. S. deBree, and M. P. Cameron. Modeling and validation of a cross flow turbine using free vortex model and a modified dynamic stall model. *Renewable Energy*, 50:662–669, 2013.

[188] U.S. Energy Information Administration. Annual energy outlook 2015 with projections to 2040. Technical Report DOE/EIA-0383(2015), U.S Department of Energy, April 2015.

[189] P. Vermeulen, P. Builtjes, J. Dekker, and G. Bueren. An experimental study of the wake behind a full scale vertical-axis wind turbine. Technical Report 79-06118, Netherlands Organization for Applied Scientific Research, Apeldoorn, NL, June 1979.

[190] J. M. Walker, K. A. Flack, E. E. Lust, and M. P. S. L. Luznik. Experimental and numerical studies of blade roughness and fouling on marine current turbine performance. *Renewable Energy*, 66:257–267, 2014.

[191] D. C. Wilcox. *Turbulence Modeling for CFD*. DCW Industries, Inc., 1st edition, 1994.

[192] M. H. Worstell. Aerodynamic performance of the 17 meter diameter Darrieus wind turbine. Technical Report SAND78-1737, Sandia National Laboratories, September 1978.

[193] Y.-T. Wu and F. Porté-Agel. Large-eddy simulation of wind-turbine wakes: Evaluation of turbine parametrisations. *Boundary-Layer Meteorology*, 138:345–366, 2011.

[194] H. Yoon, D. Hill, S. Balachandar, R. Adrian, and M. Ha. Reynolds number scaling of flow in a rushton turbine stirred tank. Part I—mean flow, circular jet and tip vortex scaling. *Chemical Engineering Science*, 60:3169–3183, 2005.

[195] A. Zanon, P. Giannattasio, and C. J. S. Ferreira. A vortex panel model for the simulation of the wake flow past a vertical axis wind turbine in dynamic stall. *Wind*, 2012.

APPENDIX A

EXPERIMENTAL UNCERTAINTY

For each set of experimental measurements, uncertainty was estimated from both systematic and random errors. Random error was computed on a per-rotor-revolution basis and systematic errors were estimated from the sensor calibrations or datasheets. Computation and combination of both error sources and their propagation into derived quantities, followed Coleman and Steele [64], which is summarized below.

An expanded uncertainty interval with 95% confidence

$$U_{95} = t_{95} u_c, \tag{A.1}$$

was computed for mean power coefficient C_P, mean rotor drag coefficient C_D, and mean wake velocities, where t_{95} is the value from the Student t-distribution for a 95% confidence interval and u_c is the combined standard uncertainty, which is given by

$$u_{\bar{X}}^2 = s_{\bar{X}}^2 + b_{\bar{X}}^2, \tag{A.2}$$

where $s_{\bar{X}} = s_X/\sqrt{N}$ is the sample standard deviation of the mean per turbine revolution, the total of which is N. The systematic uncertainty b_X is computed as

$$b_X^2 = \sum_{i=1}^{J} \left(\frac{\partial X}{\partial x_i} \right)^2 b_{x_i}^2, \tag{A.3}$$

where x_i is a primitive quantity used to calculate X (e.g., T, ω, and U_∞ for calculating C_P), and b_{x_i} is the primitive quantity's systematic uncertainty, estimated as half the value listed on the sensor manufacturer's documentation. Values for each of the sensors are listed in Table 2.2.

Selecting the Student t-statistic t_{95} requires an estimate for the number of degrees of freedom ν_X, which was obtained using the Welch–Satterthwaite formula [64]:

$$\nu_X = \frac{\left(s_X^2 + \sum_{k=1}^{M} b_k^2\right)^2}{s_X^4/\nu_{s_X} + \sum_{k=1}^{M} b_k^4/\nu_{b_k}}, \tag{A.4}$$

where ν_{s_X} is the number of degrees of freedom associated with s_X and ν_{b_k} is the number of degrees of freedom associated with b_k. ν_{s_X} is assumed to be $(N-1)$. ν_{b_k} was estimated as

$$\nu_{b_k} = \frac{1}{2}\left(\frac{\Delta b_k}{b_k}\right)^{-2}, \tag{A.5}$$

where the quantity in parentheses is the relative uncertainty of b_k, which was assumed to be 0.25.

APPENDIX B

TURBINE TEST BED OPERATING PROCEDURES

This appendix contains instructions for operating the turbine test bed system as of its latest iteration, which was used to perform the RM2 experiments described in Chapter 5. Note that any links or URLs used here are valid at the time of this writing, but are subject to change.

B.1 Software setup

A custom Python desktop application, TurbineDAQ, was developed to operate and automate the turbine test bed systems. Its operation is described below. Note that this software has not been tested and debugged to "consumer" standards, so it is highly recommended its source code, presently available from `https://github.com/petebachant/TurbineDAQ`, be inspected and understood by prospective users.

B.1.1 Dependencies

So far, TurbineDAQ has been used at UNH with the Python(x,y) distribution, though it should work elsewhere as well. Additional Python dependencies (beyond Python(x,y)) can be installed with

```
pip install pydaqmx daqmx acspy nortek micronopt
```

The ACS Motion Control SPiiPlus MMI Application Studio, National Instruments DAQmx drivers, and the Nortek PdCommATL library will also need to be installed separately.

B.1.2 Running

TurbineDAQ is designed to be portable, i.e., it does not need to be installed. Simply clone the repository and execute `turbinedaq.py`.

B.1.3 Creating a new project

1. Clone the TurbineDAQ project template repo:

```
git clone https://github.com/petebachant/TurbineDAQ-project-template
   my-new-experiment
```

2. Rename the `origin` remote to `template`:

```
cd my-new-experiment
git remote rename origin template
```

   Note: This allows any updates to the template to be incorporated with `git pull template master`.

3. Create a new repository and add this as the origin remote (optional, but highly recommended):

```
git remote add origin https://github.com/myusername/my-new-experiment.git
git push origin master -u
```

   For this example, a new repo named `my-new-experiment` would have already been created on GitHub by the user `myusername`.

4. Edit `Config/turbine_properties.json` with a text editor to reflect the turbines to be used in the experiment.

5. Create/edit CSVs of test matrix sections in `Config/Test plan`. This can be done with a text editor or spreadsheet application (be sure to export to CSV, not e.g. *.xlsx). Note that currently run numbers should start from zero, until issue #56 is fixed. See the RM2 tow tank experiment repo for examples, which include matrix sections for tare drag, tare torque, and settling runs.

B.2 Installation

B.2.1 Tools and parts needed

- 8 mm, 1/4 inch drive hex key
- Torque wrench with 70 Nm capacity—either 1/4 inch drive or adapted down to 1/4 inch
- 1/4 inch ratchet
- Bar clamp
- 9/16 inch ratchet wrench or socket
- 5 mm, 1/4 inch drive hex key
- Necessary parts are kept in a plastic container labeled “Turbine test bed” stored on the control platform shelves.

B.2.2 Mechanical

This process should take two people about one hour to complete. Note: The beach must be installed before the tow frame can be installed.

1. Install turbine in test bed frame assembly while on its rolling stand.
2. On the tow carriage, move drag slides (mounted below carriage) out to the outer edge of the carriage on the beach side by loosening the top 8 socket-head cap screws on each side with a 5 mm hex key.
3. Home the tow axis. This will make the tow carriage stop at the limit switch. Back up the tow carriage until there is approximately 0.7–1.0 m between the ends of the beach and the edge of the tow carriage.
4. Lift frame with beach gantry hoists and move towards the carriage. **CAUTION**: When lifting, make sure tow frame and turbine clear tank walls, make sure lift hooks are installed such that steel cables do not cross.
5. Lower frame and insert the 3/8-24 hex bolts through the upper clevis brackets, through the rod end at the top of the frame. Tighten these by hand.
6. Take load off gantry hoists.

7. Swing lower drag slide arms downward to engage with the self-clinching nuts on the vertical foil sections of the main frame.
8. Insert and tighten the 3/8-16 hex bolts through the lower clevis bracket and the self-clinching nuts.
9. Slide the frame back under the carriage, towards the wavemaker, until the front edge of the front drag slide mounting plates are aligned with the mark on the carriage's 80/20 members. This mark should be 24" from the beach end of the 80/20 extrusions, for reference. See Figure 1 for details.
10. Attach a bar clamp to the bottom of the 80/20 extrusions mounting the drag slides and pull them up flush against the top 80/20 extrusions attached to the tow carriage. Tighten the 8 screws on each side using a 5 mm hex key.
11. Attach outer guy wires to outer linear bearings and tension by hand. Be sure to tension uniformly so the frame remains square and vertical.
12. Attach inner guy wires. This involves turning the cable end counterclockwise roughly 5 turns before engaging the threads so that the torsion preload tensions the cable as it unwinds in the clockwise direction while threading into the rod end at the drag slide.
13. If taking wake measurements install the YZ traverse.

B.2.3 Connecting instrumentation

Connect torque and drag measurement instrumentation cables to the modules installed in the NI CompactDAQ according to the following table:

Sensor	NI module	Phys. chan.
Torque trans.	NI-9205	0
Torque arm	NI-9237	0
Drag left (facing beach)	NI-9237	1
Drag right (facing beach)	NI-9237	2

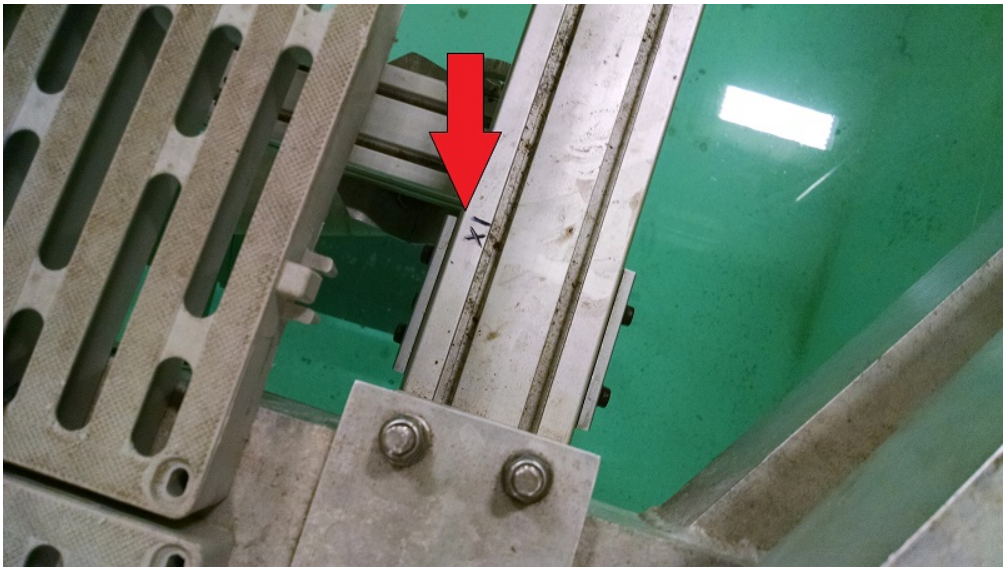

Figure B.1: Drag slide (right) mounting distance.

B.2.4 Installing servo motor

1. Turn off the onboard electronics cabinet using the disconnect handle on the front of the door.
2. Slowly drop motor into position such that the flexible coupling engages with the torque transducer.
3. Insert and tighten 4 socket head cap screws with an 8 mm hex key socket on a 1/4 inch ratchet.
4. Torque flexible coupling screws to 70 Nm to clamp onto the torque transducer shaft.
5. Attach servo cables to motor and the beach-facing side of the onboard electronics cabinet. **Note: the connectors on the motor-ends of the cables are similar, and pin damage can occur if these are mismatched.** The power cable mates to the "MOTOR POWER" connector and feedback cable mates to the "MOTOR FEEDBACK" connector on the cabinet.
6. Turn on the onboard electronics cabinet and restart the controller via SPiiPlus MMI Application Studio (on the Tow Tank PC).

B.3 Running

B.3.1 Pre-run checklist

1. Check that the tank depth is 2.44 m and fill or drain as necessary.
2. Home tow axis. This should have been done as part of the installation process, but must be repeated each time the controller is restarted, e.g., when starting a new day of runs.
3. Launch the TurbineDAQ application. See the TurbineDAQ wiki for more information.
4. With the turbine axis disabled, rotate turbine by hand to an azimuthal angle of zero, then home the turbine axis from the TurbineDAQ "Homing" menu.
5. If taking Vectrino measurements, home the y- and z- axes from the TurbineDAQ "Homing" menu.
6. Ensure the NI DAQ and Vectrino (if applicable) are powered on.
7. Select the experiment working directory using the folder icon next to the address bar. If test matrix CSVs are located in the appropriate directory, these will be loaded automatically into the test plan table.
8. Using the icons in the TurbineDAQ toolbar, check that each DAQ system (ACS motion controller, NI, and Vectrino) can acquire data. Signals will be plotted as they are acquired.
9. Move the tow axis back to zero using the Tow application or the SPiiPlus MMI Application Studio terminal with the command `ptp tow, 0`.
10. Ensure that the carriage path is clear.
11. Switch to shakedown mode and select some conservative parameters for an initial test run, e.g., a tow speed of 0.5 m/s or so.
12. Perform a shakedown run. If the experiment processing software has been setup correctly, the run will be processed automatically and the results printed to the terminal.

B.3.2 Seeding the tank

Note: This is only necessary if taking velocity measurements with the Vectrino.

1. Mix approximately 1 cup of 11 micron mean diameter hollow glass spheres with approximately 1 gallon of water.

2. Using the Tow application, turn on the jog pendant.
3. While on board the carriage, jog to the beach end of the tank.
4. Jog the tank slowly towards the wavemaker, pouring the seeding mixture into the center (cross-stream direction) of the tank.
5. Return to the control platform and perform a couple turbine tows at ~1 m/s, either as a TurbineDAQ shakedown run, or using one of the motion control buffers via SPiiPlus MMI Application Studio.
6. Using the Nortek Vectrino Plus application or the TurbineDAQ Vectrino monitoring feature, sample velocity data and observe the signal-to-noise ratio (SNR) and correlation values. Continue adding seeding and mixing until the SNR reaches approximately 12 dB. Note that the YZ traverse axes should be disabled while the Vectrino is sampling.

B.3.3 Determining tank settling time

Before undertaking regular performance and wake measurement runs, tank settling times should be established. In principle this should only need to be done once for each turbine. TurbineDAQ is setup to perform "settling runs," the test matrix for which is tabulated in `Config/Test plan/Settling.csv`, where a turbine is towed and returned to the control platform. The Vectrino will then acquire wake data for an extended period of time. This data can then be inspected manually to determine when mean and turbulence quantities have decayed below an acceptable threshold. After determining a settling time (in seconds) for each speed, TurbineDAQ will automatically read these values from the `Config/settling_times.csv` file. For an example, see `Settling.csv` from the RM2 tow tank experiment repository.

B.3.4 Acquiring performance and wake data

If test matrix sections have been loaded properly, and settling times have been tabulated in the correct file, pressing the "play" icon in the TurbineDAQ toolbar with the "Test Plan" tab visible will start the next unfinished run in the table. So long as the "play" button is depressed, TurbineDAQ will continue executing runs, idling in between according the specified settling times.

B.3.5 Acquiring tare torque data

1. Move the carriage to the beach end of the tank near the gantry hoists.
2. Remove the turbine and mounting frame from the carriage. See below for removal instructions.
3. With the frame suspended out of the water by the gantry hoists, remove the turbine blades.
4. Reinstall the servo motor and cables (note that the onboard electronics cabinet should be turned off whenever plugging or unplugging cables).
5. Switch to the `Tare torque` test matrix section from the "Test Plan" tab in TurbineDAQ.
6. Ensure the turbine shaft is free to rotate, and press the "play" icon in the TurbineDAQ toolbar. Similar to the standard performance and wake measurement runs, the table will be executed automatically.

B.3.6 Acquiring tare drag data

1. After acquiring tare torque data (see above), remove the turbine shaft from the frame.
2. Remove the servo motor and place back at the control platform. Note that the ACS motion controller will need to be restarted after turning the onboard electronics cabinet on/off.
3. Reinstall the turbine mounting frame under the carriage and attach all four guy wires.
4. Switch to the `Tare drag` test matrix section from the "Test plan" tab in TurbineDAQ.
5. Ensure the carriage path is clear, and press the "play" icon in the TurbineDAQ toolbar. The table of tare drag runs will then be executed automatically.

B.4 Removal

1. Turn off the onboard electronics cabinet.
2. Disconnect the torque arm and torque transducer sensor cables. Coil up and wrap around the torque arm load cell mounting bracket.
3. After at least 10 mins with the electronics cabinet powered-off, remove the servo cables and put these back on the shelf on the control platform.

4. Loosen but don't remove the bottom two screws of the upper flexible servo coupling (the one torqued to 70 Nm during installation.
5. Remove the four socket head cap screws fixing the servo gearhead to the torque arm mounting block.
6. Pull up to remove the servo and gearhead, then place this on the small desk in the corner of the control platform.
7. Remove all four guy wires and attach these back to the frame, as it was in storage.

APPENDIX C

DATASET AVAILABILITY AND USAGE

Three open experimental datasets were produced from the work described in Chapters 3, 4, and 5. These datasets are based around Git version control repositories, which include histories of all changes made to configuration files, documentation, processed or derived data, and code used to process and visualize the data. At the time of writing, these are primarily distributed via the Git repository hosting site GitHub.com. Specific releases or snapshots of the repositories have been archived via Figshare.com, which provides digital object identifiers (DOIs). The Figshare archives thereby provide persistent links, which are cited in the publications where the data was used. Note that presently, prospective users are pointed to the repositories on GitHub to ensure they obtain the most recent version, and may take advantage of some of GitHub's collaboration features, e.g., issues, wikis, and pull requests.

This appendix contains instructions for using the RM2 tow tank dataset, though instructions for the UNH-RVAT baseline and UNH-RVAT Reynolds number dependence datasets are similar. However, it should be noted that an object-oriented interface was not implemented for the UNH-RVAT baseline processing software, though the top-level scripts are similar. Also note that the documentation below was automatically generated from the RM2 tow tank experiment's wiki on GitHub (`https://github.com/UNH-CORE/RM2-tow-tank/wiki`), which was deemed to be as accurate as possible at the time of this writing, though may evolve as the repository evolves. Therefore, the wiki should be consulted for the most up-to-date documentation, if possible.

C.1 Getting started

See the experimental repository's `README.md` for necessary software dependencies and how to install these.

C.2 Downloading (cloning) to local machine

The experiment repository ("repo") may be cloned via Git with

```
git clone https://github.com/UNH-CORE/RM2-tow-tank.git
```

or downloaded as a ZIP file from GitHub. The benefit of using Git is that all changes to the processed data or code can be pulled in automatically with `git pull origin master`, without having to re-download and unzip the entire repository.

C.3 Generating figures

1. Open a terminal or command prompt in the experiment root directory.
2. Execute `python plot.py -h` to see plotting script options.

To generate and save all figures without opening them in new windows, execute

```
python plot.py --all --save --no-show
```

C.3.1 Generating figures for a different project

The `plotting` module inside the experiment's `pyrm2tt` Python package can be used to generate plots elsewhere, e.g., if running in a Jupyter Notebook, IPython shell, or Jupyter Qt Console. In the example below, the performance coefficient curve is plotted at a tow speed of 1.0 m/s, with the assumption that the user is working in a different directory (`notebook_dir`).

```
import os

# Define some paths
notebook_dir = "C:/Users/Frank/Notebooks/RM2-numerical-modeling"
rm2_dir = "C:/Users/Frank/Experiments/RM2-tow-tank"

# Move into the experiment directory
os.chdir(rm2_dir)

# Import the experiment's plotting module
import pyrm2tt.plotting

# Create an instance of a performance curve object and plot C_P
pc = pyrm2tt.plotting.PerfCurve(tow_speed=1.0)
pc.plotcp(marker="o")
```

```
# Move back into the notebook directory
os.chdir(notebook_dir)

# View the performance curve C_P data as a table
print(pc.df.mean_cp)
```

C.4 Working with the data

The experiment repo includes all the code used to process and visualize the data inside of a Python package called `pyrm2tt`, which contains `processing` and `plotting` modules. The best way to figure out how these work is to look at the functions called in the top level `plot.py` and `process.py` scripts. Inside the `pyrm2tt.processing` module there is a `Run` class, which encapsulates the data from an individual tow, and includes all the methods used to load the raw data, extract the quasi-steady duration, compute statistics, etc. Note that to import and use the Python package, you must be running inside the experiment root directory.

C.4.1 Examples

Access the instantaneous power coefficient time series of run 12 from the `Perf-1.0` test matrix section:

```
from pyrm2tt.processing import Run

run = Run("Perf-1.0", 12)
cp = run.cp
```

C.5 Contributing

Upgrades and bug fixes can be submitted via pull request on GitHub. The steps to submitting a pull request are:

1. Fork the experiment repo using the button on the GitHub website.

2. Clone the forked repo locally.

3. Checkout a new branch with a name representing the proposed change, e.g.,

```
git checkout -b analyze-new-thing
```

4. Commit some changes and push them up to the new branch on GitHub.

5. Visit the forked repo on GitHub, and click the "pull request" button. In the form, describe the proposed changes.

6. The repository maintainers will review the pull request, and suggest modifications if necessary. The pull request can be automatically updated by pushing up to the appropriate branch.

C.6 Issues, feature requests, and questions

To report issues, suggest enhancements, or even to simply ask questions, use the project's issue tracker on GitHub. This issue tracker also serves as a public forum for discussing the results and ideas for new analyses.

APPENDIX D

TURBULENCE MODELS

In this chapter the three eddy viscosity RANS and one LES turbulence models used throughout this work are detailed. Note that since all of these were applied via OpenFOAM, their exact implementation can be interrogated by looking at the source code, which is freely available.

The exact incompressible RANS equations are written as

$$\frac{\partial U_i}{\partial t} + U_j \frac{\partial U_i}{\partial x_j} = -\frac{1}{\rho}\frac{\partial P}{\partial x_i} - \frac{\partial}{\partial x_j}\overline{u_i' u_j'} + \nu \frac{\partial^2 U_i}{\partial x_j \partial x_j} \tag{D.1}$$

The RANS equations with the eddy viscosity formulation are modified with the relation $-\overline{u_i' u_j'} = 2\nu_t S_{ij}$, where ν_t is the turbulence viscosity and S_{ij} is the mean strain rate tensor. The RANS equations with the eddy viscosity approximation then become

$$\frac{\partial U_i}{\partial t} + U_j \frac{\partial U_i}{\partial x_j} = -\frac{1}{\rho}\frac{\partial P}{\partial x_i} + (\nu + \nu_t)\frac{\partial^2 U_i}{\partial x_j \partial x_j}. \tag{D.2}$$

D.1 Spalart–Allmaras

The Spalart–Allmaras turbulence model is based on the transport of a single scalar $\tilde{\nu}$ [175], which is designed to behave linearly near the wall. The transport equation for $\tilde{\nu}$ is defined as

$$\frac{\mathrm{D}\tilde{\nu}}{\mathrm{D}t} = c_{b1}\tilde{S}\tilde{\nu} + \frac{1}{\sigma}\left[\nabla\cdot((\nu+\tilde{\nu})\nabla\tilde{\nu}) + c_{b2}(\nabla\tilde{\nu})^2\right] - c_{w1}f_w\left[\frac{\tilde{\nu}}{d}\right]^2, \tag{D.3}$$

with

$$\tilde{S} = f_{v3}\sqrt{2}|\mathrm{skew}\nabla U| + f_{v2}\frac{\tilde{\nu}}{\kappa^2 d^2}, \tag{D.4}$$

where $\mathrm{skew}\nabla U$ is the skew-symmetric component of the velocity gradient tensor.

Auxiliary relations are defined by:

$$f_{v2} = 1 - \frac{\chi}{1+\chi f_{v1}},\ f_{v3} = 1, \tag{D.5}$$

$$c_{w1} = c_{b1}/\kappa^2 + \frac{1+c_{b2}}{\sigma}, \tag{D.6}$$

$$f_w(r) = g\left[\frac{1+c_{w3}^6}{g^6+c_{w3}^6}\right]^{1/6}, \tag{D.7}$$

$$g = r + c_{w2}(r^6 - r), \tag{D.8}$$

and

$$f = \frac{\tilde{\nu}}{\tilde{S}\kappa^2 d^2}, \tag{D.9}$$

where d is the distance to the wall. The SA turbulent viscosity is calculated as $\nu_t = f_{v1}\tilde{\nu}$. Typical coefficients are

$$c_{b1} = 0.1355,\ c_{b2} = 0.622,\ c_{w2} = 0.3,\ c_{w3} = 2.0,\ c_{v1} = 7.1,\ c_{v2} = 5.0,\ \sigma = 0.66666,\ \kappa = 0.41. \tag{D.10}$$

D.2 k–ω SST

Menter's k–ω SST is defined in [133]. The transport equation for the turbulence kinetic energy k is

$$\rho\frac{\partial k}{\partial t} + \rho U_j\frac{\partial k}{\partial x_j} = \tilde{P}_k - \rho\beta^*\omega k + \frac{\partial}{\partial x_j}\left(\Gamma_k\frac{\partial k}{\partial x_j}\right), \tag{D.11}$$

and for the specific dissipation ω:

$$\rho\frac{\partial \omega}{\partial t} + \rho U_j\frac{\partial \omega}{\partial x_j} = \frac{\gamma}{\nu_t}P_k - \rho\beta\omega^2 + \frac{\partial}{\partial x_j}\left(\Gamma_\omega\frac{\partial \omega}{\partial x_j}\right) + 2\rho(1-F_1)\sigma_{\omega 2}\frac{1}{\omega}\frac{\partial k}{\partial x_j}\frac{\partial \omega}{\partial x_j}. \tag{D.12}$$

Auxiliary relations include:

$$\Gamma_k = \mu + \frac{\mu_t}{\sigma_k},\ \Gamma_\omega = \mu + \frac{\mu_t}{\sigma_\omega},\ P_k = \tau_{ij}\frac{\partial U_i}{\partial x_j},\ \tilde{P}_k = \min(P_k; c_l\varepsilon),\ \mu_t = \rho\frac{a_1 k}{\max(a_1\omega; S\cdot F_2)}. \tag{D.13}$$

Coefficients ϕ are blended with $\phi = F_1\phi_1 + (1-F_1)\phi_2$, where the 1 and 2 subscripts denote values from the k–ω and k–ε models, respectively:

$$F_1 = \tanh(\arg_1^4), \tag{D.14}$$

$$\arg_1 = \min\left(\max\left(\frac{\sqrt{k}}{\beta^*\omega y}; \frac{500\nu}{y^2\omega}\right); \frac{4\rho\sigma_{\omega 2}k}{CD_{k\omega}y^2}\right), \tag{D.15}$$

$$CD_{k\omega} = \max\left(2\rho\sigma_{\omega 2}\frac{1}{\omega}\frac{\partial k}{\partial x_j}\frac{\partial \omega}{\partial x_j}; 10^{-10}\right). \tag{D.16}$$

OpenFOAM's implementation of the SST model features updated coefficients from [134], with the consistent production terms from [133]. OpenFOAM also uses coefficients in terms of $\alpha = 1/\sigma$ to apply blending functions. Default coefficients are

$$\begin{aligned}&\alpha_{k1} = 0.85,\ \alpha_{k2} = 1.0,\ \alpha_{\omega 1} = 0.5,\ \alpha_{\omega 2} = 0.856,\ \beta_1 = 0.075,\ \beta_2 = 0.0828,\ \beta^* = 0.09,\\ &\gamma_1 = 5/9,\ \gamma_2 = 0.44,\ a_1 = 0.31,\ b_1 = 1.0,\ c_1 = 10.0.\end{aligned} \tag{D.17}$$

D.3 k–ε

The standard k–ε model is defined in [191]. The equation for the turbulence kinetic energy is

$$\rho\frac{\partial k}{\partial t} + \rho U_j\frac{\partial k}{\partial x_j} = \tau_{ij}\frac{\partial U_i}{\partial x_j} - \rho\varepsilon + \frac{\partial}{\partial x_j}\left[(\mu + \mu_t/\sigma_k)\frac{\partial k}{\partial x_j}\right]. \tag{D.18}$$

and for the dissipation ε:

$$\rho\frac{\partial \varepsilon}{\partial t} + \rho U_j\frac{\partial \varepsilon}{\partial x_j} = C_{\varepsilon 1}\frac{\varepsilon}{k}\tau_{ij}\frac{\partial U_i}{\partial x_j} - C_{\varepsilon 2}\rho\frac{\varepsilon^2}{k} + \frac{\partial}{\partial x_j}\left[(\mu + \mu_t/\sigma_k)\frac{\partial \varepsilon}{\partial x_j}\right]. \tag{D.19}$$

The eddy-viscosity is defined as

$$\nu_t = C_\mu k^2/\varepsilon, \tag{D.20}$$

and typical closure coefficients are

$$C_{\varepsilon 1} = 1.44,\ C_{\varepsilon 2} = 1.92,\ C_\mu = 0.09,\ \sigma_k = 1.0,\ \sigma_\varepsilon = 1.3. \tag{D.21}$$

D.4 Smagorinsky LES model

Large eddy simulation solves for the filtered velocity field $\tilde{u}$. The filtered Navier–Stokes equations are

$$\frac{\partial \tilde{u}_i}{\partial t} + \tilde{u}_j \frac{\partial \tilde{u}_i}{\partial x_j} = -\frac{1}{\rho}\frac{\partial \tilde{p}}{\partial x_i} + \nu \frac{\partial^2 \tilde{u}_i}{\partial x_j \partial x_j} - \frac{\partial \tau_{ij}}{\partial x_j}. \tag{D.22}$$

Smagorinsky [171] proposed an eddy viscosity type relation for the computing the subgrid scale (SGS) stress tensor τ_{ij}:

$$\tau_{ij} = 2\mu_t S_{ij},\ S_{ij} = \frac{1}{2}\left(\frac{\partial \tilde{u}_i}{\partial u_j} + \frac{\partial \tilde{u}_j}{\partial u_i}\right). \tag{D.23}$$

The eddy viscosity is then

$$\nu_t = (C_S \Delta)^2 \sqrt{\tilde{S}_{ij}\tilde{S}_{ij}}, \tag{D.24}$$

where Δ is the filter width (e.g., the cube root of the local cell volume) and C_S is the Smagorinsky coefficient, which is not universal, i.e., will vary for different flow conditions. Note that OpenFOAM's implementation of the Smagorinsky model is based on two coefficients, which by default are

$$C_k = 0.094,\ C_\varepsilon = 1.048. \tag{D.25}$$

These are related to C_S by

$$C_S = \left(C_k \left(C_k/C_\varepsilon\right)^{1/2}\right)^{1/2}. \tag{D.26}$$